



HAL
open science

Sensitivity of the mass balance of glaciers in the eastern part of the central Himalayas (eastern Nepal) to variations in air temperature and precipitation

Arbindra Khadka

► **To cite this version:**

Arbindra Khadka. Sensitivity of the mass balance of glaciers in the eastern part of the central Himalayas (eastern Nepal) to variations in air temperature and precipitation. Hydrology. Université Grenoble Alpes [2020-..], 2024. English. NNT : 2024GRALU021 . tel-04710422

HAL Id: tel-04710422

<https://theses.hal.science/tel-04710422v1>

Submitted on 26 Sep 2024

HAL is a multi-disciplinary open access archive for the deposit and dissemination of scientific research documents, whether they are published or not. The documents may come from teaching and research institutions in France or abroad, or from public or private research centers.

L'archive ouverte pluridisciplinaire **HAL**, est destinée au dépôt et à la diffusion de documents scientifiques de niveau recherche, publiés ou non, émanant des établissements d'enseignement et de recherche français ou étrangers, des laboratoires publics ou privés.

THÈSE

Pour obtenir le grade de

DOCTEUR DE L'UNIVERSITÉ GRENOBLE ALPES

École doctorale : STEP - Sciences de la Terre de l'Environnement et des Planètes

Spécialité : Sciences de la Terre et de l'Environnement

Unité de recherche : Institut des Géosciences de l'Environnement (IGE)

Sensibilité du bilan de masse des glaciers de la partie orientale de l'Himalaya central (Népal oriental) aux variations de la température de l'air et des précipitations

Sensitivity of the mass balance of glaciers in the eastern part of the central Himalayas (eastern Nepal) to variations in air temperature and precipitation

Présentée par :

Arbindra KHADKA

Direction de thèse :

Patrick WAGNON

DIRECTEUR DE RECHERCHE, Université Grenoble Alpes

Directeur de thèse

Fanny BRUN

CHARGE DE RECHERCHE, Université Grenoble Alpes

Co-encadrante de thèse

Rapporteurs :

Fabien MAUSSION

ASSOCIATE PROFESSOR, University of Bristol

Tobias SAUTER

ASSISTANT PROFESSOR, Humboldt-Universität zu Berlin, Berlin (HU Berlin)

Thèse soutenue publiquement le **20 juin 2024**, devant le jury composé de :

Patrick WAGNON,

DIRECTEUR DE RECHERCHE, IRD

Directeur de thèse

Fanny BRUN,

CHARGE DE RECHERCHE, IRD

Co-encadrante de thèse

Fabien MAUSSION,

ASSOCIATE PROFESSOR, University of Bristol

Rapporteur

Tobias SAUTER,

ASSISTANT PROFESSOR, Humboldt-Universität zu Berlin, Berlin (HU Berlin)

Rapporteur

Koji FUJITA,

FULL PROFESSOR, Nagoya University

Examineur

Deepak ARYAL,

FULL PROFESSOR, Tribhuvan University

Examineur

Delphine SIX,

PHYSICIENNE, UGA

Présidente



*Dedicated to my little brother **Bikalpa Khadka**,
who passed away on March 2, 2024.*

Acknowledgments

The past three and half years have been some of the best of my life, filled with physical and educational adventures. I want to thank everyone who contributed to this journey.

Firstly, I would like to express my gratitude to Patrick Wagnon and Fanny Brun for their invaluable guidance and support throughout this endeavour. Their trust, motivation, and unwavering assistance have been instrumental in my personal and professional growth. I will never forget the memories we shared, the spaghetti, KhusKhus, Tonba, and a shoe from Amphu Lapcha. I am immensely thankful to Dibas Shrestha, Yves (Karki dai), and Adina Didi for your constant support.

I would like to thank Baker Perry, Aurora Elmore, Tom Mathews, Sandra Elvin, and the National Geographic Society's Perpetual Planet program for supporting my PhD. I sincerely thank all my colleagues from CDHM and ICIMOD. It was a privilege to work with you and to learn the cryospheric science together. Thanks to Simon and Jakob for following my work and guiding me over the past three years. I would also like to thank the jury members for their evaluation of my work.

Since 2016, I have been fortunate to participate in unforgettable expeditions and collaborate with a fantastic team of professionals, including Maxim, Emmy, Walter, Marin, Guilhem, Thibaut, Delphine, and Vincent. I am grateful to Tenzing Gyaljen, Kami Temba, and all others who were part of the Everest expedition.

I would like to thank Ailsa and Sara. I hope we will have the chance to climb, ski, and travel together again. I am also grateful to Luc for his constant support and for singing J'aim le chat. I am grateful to all the IGE family.

I would also like to thank Shree Dai, Ujjwal Dai, Sudishna, Subas, Bandana, Anil, Binod, Sandip, Garima, Bishal, and all the Nepali community in Grenoble. I would like to thank Anushilan, Pragma, Sailen, Kalpana, and Pan for always listening to me.

I just wanted to take a moment to express my gratitude to my family, who have been incredibly supportive throughout my life. And, of course, I cannot forget to thank my amazing mother for everything she has done for me.

I feel truly blessed to have such wonderful people in my life.

Abstract

The large quantities of glaciers, snow, and permafrost provide fresh water for millions of people in the Himalayas and downstream. In recent decades, the Himalayan glaciers have been rapidly losing mass. However, studies of the links between local meteorology, climate, and glaciers in this region are limited by the paucity of high-altitude observations.

In this thesis, we take advantage of the long series of meteorological and glaciological observations collected in the upper Dudh Koshi basin (Everest region) and on Mera Glacier since 2007 as part of the GLACIOCLIM Observatory, to evaluate the performance of reanalysis data (ERA5 Land and HARv2) and to estimate the sensitivity of the glacier mass balance to meteorological variables. In the first part, we carried out a detailed analysis of these meteorological records. We observe a negative horizontal gradient of annual precipitation in south-to-north direction across the range, with a 28 % decrease in precipitation at ~ 5000 m above sea level (a.s.l.) between Mera Glacier and Pyramid Observatory, ~ 30 km further north. Comparison of the ERA5 Land and HARv2 datasets with the in-situ data shows that both gridded datasets are able to resolve the mesoscale atmospheric processes, with HARv2 performing slightly better than ERA5-Land. Due to the complex topography, they fail to reproduce local to microscale processes recorded at individual weather stations, especially for variables with large spatial variability such as precipitation or wind speed. Air temperature is the variable that is best captured by reanalyses, as long as an appropriate elevational gradient of air temperature above ground, spatiotemporally variable and preferably assessed by local observations, is used to extrapolate it vertically. A cold bias is still observed but attenuated over clean-ice glaciers. The atmospheric water content is well represented by both gridded datasets although we observe a small wet bias and a spectacular overestimation of precipitation during the monsoon (June to September). The agreement between reanalyzed and observed shortwave and longwave incoming radiation depends on the elevation difference between the station location and the reanalysis grid cell. The seasonality of wind speed is only captured by HARv2. The two gridded datasets ERA5-Land and HARv2 are applicable for glacier mass and energy balance studies, as long as either statistical or dynamical downscaling techniques are used to resolve the scale mismatch between coarse mesoscale grids and fine-scale grids or individual sites.

In the second part, we estimate the sensitivity of the mass balance of Mera Glacier to temperature and precipitation. We simulate the glacier-wide mass balance of Mera Glacier with the distributed Coupled Snowpack and Ice surface energy and mass balance model in Python (COSIPY), driven by in-situ meteorological data, from 2016 to 2020. The analysis of the share of the energy fluxes of the glacier shows the radiative fluxes account for almost all the energy available during the melt season (May to October). On an annual scale, melt is the dominant mass flux at all elevations, but 44 % of the melt refreezes across the glacier. Sublimation is another major contributor to the mass balance, except during the monsoon, contributing more than 0.15 m w.e. of the annual mass balance. By reshuffling the available observations, we create 180 synthetic series of hourly meteorological forcings to force the model over a wide range of plausible climate conditions. A $+1$ (-1) $^{\circ}\text{C}$ change in temperature results in a -0.75 ± 0.17 ($+0.93 \pm 0.18$) m w.e. change in glacier-wide mass balance and a $+20$

(-20) % change in precipitation results in a $+0.52 \pm 0.10$ (-0.60 ± 0.11) m w.e. change. Our study highlights the need for physically based approaches to produce consistent forcing datasets, and calls for more meteorological and glaciological measurements in High Mountain Asia (HMA).

Keywords: precipitation, glacier, Himalaya, mass balance

Résumé

Les glaciers, la neige et le pergélisol contribuent à l'alimentation en eau douce de millions de personnes en Himalaya. Au cours des dernières décennies, les glaciers himalayens ont largement perdu de la masse. Cependant, les études concernant la météorologie locale, le climat ou les glaciers de cette région restent limitées par le manque d'observations à haute altitude.

Dans cette thèse, nous profitons de la longue série d'observations météorologiques et glaciologiques collectées dans le bassin supérieur de la Dudh Koshi (région de l'Everest) et sur le glacier Mera depuis 2007, pour évaluer la performance des réanalyses ERA5 Land et HARv2 et pour estimer la sensibilité du bilan de masse du Mera aux variables météorologiques. Dans la première partie, nous avons analysé en détail les données météorologiques. Nous observons un gradient horizontal négatif des précipitations annuelles le long d'un axe sud-nord au travers de la chaîne, avec une diminution de 28 % des précipitations à ~5000 m d'altitude entre le Mera et l'observatoire Pyramid, ~30 km plus au nord. La comparaison des données ERA5 Land et HARv2 avec les données *in-situ* montre que les réanalyses sont capables de résoudre les processus atmosphériques à méso-échelle, HARv2 étant légèrement plus performant qu'ERA5-Land. En raison de la topographie complexe, ces réanalyses ne parviennent cependant pas à reproduire les processus locaux, surtout pour les variables présentant une forte variabilité spatiale comme les précipitations ou la vitesse du vent. La température de l'air est la variable la mieux estimée par les réanalyses, à condition qu'un gradient d'altitude approprié soit utilisé pour l'extrapoler verticalement. Un biais froid est toujours observé, mais il est atténué sur les glaciers blancs. Le contenu en eau de l'atmosphère est bien représenté par les réanalyses, bien que nous observions un léger biais humide et une surestimation spectaculaire des précipitations pendant la mousson (juin à septembre). En ce qui concerne le rayonnement incident courte ou grande longueur d'onde, l'accord entre les données observées et réanalysées dépend de la différence d'altitude entre la station et la grille de la réanalyse. La saisonnalité de la vitesse du vent n'est reproduite que par HARv2. Les jeux de données ERA5-Land et HARv2 sont utilisables dans les études sur le bilan de masse et d'énergie des glaciers, à condition que des méthodes de descente d'échelle statistique ou dynamique soient utilisées pour résoudre la discordance d'échelle entre données grillées et ponctuelles.

Dans la deuxième partie, nous estimons la sensibilité du bilan de masse du glacier Mera à la température et aux précipitations. Nous simulons le bilan de masse du glacier Mera à l'aide du modèle distribué COSIPY (Coupled Snowpack and Ice surface energy and mass balance model in Python), nourri par des données météorologiques *in-situ*, de 2016 à 2020. Les flux radiatifs représentent la quasi-totalité de l'énergie disponible pendant la saison de fonte (mai à octobre). À l'échelle annuelle, la fonte est le flux de masse dominant à toutes les altitudes, mais 44 % de l'eau fondue regèle. La sublimation, même si elle est négligeable pendant la mousson, est un autre facteur important et contribue à 23 % du bilan de masse annuel. En remaniant les observations disponibles, nous créons 180 scénarios de forçages météorologiques pour forcer le modèle sur une large gamme de conditions climatiques réalistes. Un changement de température de +1 (-1) °C se traduit par une variation du bilan

de masse du glacier de -0.75 ± 0.17 ($+0.93 \pm 0.18$) m équivalent eau (m eq. e.) et un changement de +20 (-20) % dans les précipitations entraîne une variation de $+0.52 \pm 0.10$ (-0.60 ± 0.11) m eq. e. Il est nécessaire de produire des forçages de données cohérents pour évaluer la sensibilité des bilans de masse glaciaires, et cela est possible que si des observations sont disponibles sur le long terme.

Table of Contents

Abstract
... iv	
1 Motivation and background.....	1
2 Regional context and previous work	6
2.1 Geographical and geological setting.....	6
2.2 Climatic setting and glacier regimes.....	7
2.2.1 Regional atmospheric circulation patterns.....	7
2.2.2 Temperature and precipitation patterns across the region	9
2.2.3 Glacier regimes	11
2.3 Climate trends and projections across the region.....	11
2.3.1 Observed temperature changes	11
2.3.2 Observed precipitation changes	12
2.4 Glacier mass balance (theoretical concepts).....	13
2.4.1 Glaciological mass balance	14
2.4.2 Geodetic mass balance	15
2.5 Glacier energy balance	17
2.6 Mass balance sensitivity	19
2.7 Present knowledge of Himalaya Karakoram glaciers	20
2.7.1 Glacier mass balance studies in central Himalaya	20
2.7.2 Glacier surface energy balance studies in Himalaya-Karakoram	23
2.7.3 Glacier mass balance sensitivity studies in Himalaya-Karakoram	25
2.8 Summary and objectives.....	28
3 Study area and data.....	30
3.1 Dudh Koshi basin and Mera Glacier.....	30
3.1.1 Mass balance data of Mera Glacier	32
3.1.2 Meteorological data	33
4 Evaluation of ERA5-Land and HARv2 reanalysis data at high elevation in the upper Dudh Koshi basin (Everest region, Nepal)	36
4.1 A short introduction.....	36
4.2 Abstract.....	37
4.3 Introduction	38
4.4 Study site and climatology.....	39
4.5 Data and Methods	40
4.5.1 Data	40
4.5.2 Methods of evaluation	42
4.6 Results.....	45
4.6.1 Meteorology of the upper Dudh Koshi basin	45
4.7 Comparison between reanalysis and observed data in the upper Dudh Koshi basin	47
4.8 Discussion	63
4.8.1 Performances of ERA5L and HARv2 reanalyses in the central Himalaya.....	63

4.8.2	Qualitative relevance for mass and energy balance studies over glaciers	66
4.9	Conclusion.....	67
4.10	Supplementary Material.....	69
5	Surface energy and mass balance of Mera Glacier (Nepal, Central Himalaya) and their sensitivity to temperature and precipitation	81
5.1	A short introduction.....	81
5.2	Abstract.....	82
5.3	Introduction	82
5.4	Study area and climate	84
5.4.1	Mera Glacier	84
5.4.2	Climate.....	84
5.5	Data.....	85
5.5.1	Meteorological Data	85
5.5.2	Spatial distribution of meteorological forcings	87
5.5.3	Mass balance data	88
5.6	Methods.....	89
5.6.1	Model Description (COSIPY)	89
5.6.2	Optimisation	91
5.6.3	Evaluation of the model at point and distributed scale	93
5.6.4	Sensitivity analysis	93
5.7	Results.....	95
5.7.2	SEB and mass balance components	99
5.7.3	Mass balance sensitivity to meteorological forcings	103
5.8	Discussion	107
5.8.1	Surface energy and mass balance components of Mera Glacier, and comparison with other similar studies in HKH	107
5.8.2	Mass balance sensitivity to different meteorological variables and comparison with other studies in HKH	110
5.8.3	Limitations of our approach	112
5.9	Conclusion.....	114
5.10	Supplementary material	115
6	Conclusion and perspectives.....	131
	Annex.....	136
7	References	141



On 9 May 2022, I was standing at the summit of Mt. Everest to install the world's highest AWS.

Photo: After the installation of AWS at 8810 m on Mt Everest (from left: Tenzing Gyaljen, Kami Temba, and myself)

Chapter 1

1 Motivation and background

I am delighted to present this thesis, which is inspired by my personal experiences and growing passion for glaciology. I come from Nuwakot, a village in central Nepal, at an elevation of 900 m a.s.l.; I did not grow up in the mountains above 3,000 m a.s.l. like the Sherpas. Therefore, I never imagined experiencing the breathtaking beauty of high altitudes and glaciers, let alone glaciology. Additionally, glaciological studies are not as common in Nepal as they should be. However, this has not deterred me from pursuing my dreams and making a difference in the world of glaciology.

In May 2016, everything changed for me: I traveled to an altitude of approximately 5,200 a.s.l. to maintain weather stations, for the first time. Subsequently, I had the fortuitous opportunity to participate in a field expedition with the French IRD (Institut de Recherche pour le Développement) team in November 2017. It was then, that I had the opportunity to touch a glacier for the first time, and it was a life-changing experience. This was an unforgettable adventure that allowed me to see the glaciers not just as a visitor but through the eyes of a glaciologist. I had an amazing time doing glacier mass balance fieldwork and learned so much about working on glaciers and their importance. This experience ignited my passion for glaciology, and I have been fortunate enough to subsequently contribute to a dozen fieldwork expeditions and scientific collaborations with both international and national scientific teams. Through these experiences, I gained a deeper understanding of the crucial role that mountains, glaciers, snow, and permafrost play. This has motivated me to pursue a PhD thesis on this topic.

What an incredible experience this has been in the past few years! I have come to understand the importance of mountains as a researcher and also through the eyes of local people, such as Kami Sherpa, Phadindra, Gelu, and many others who live their entire lives in the Himalayas. I firmly believe that glaciers are important to all these people, and I am confident that with the skills and experience I have gathered in the last few years, my contribution to this field will be significant.

Importance of cryosphere in Nepal

Nepal is a mountainous country in the central Himalayas, hosting about one-third (~800 km) of the total extent of the Himalayan range. Eight of the world's 14 highest mountains are located in Nepal, including the world-famous Mt. Everest (8,849 m a.s.l.). A significant area of Nepal above 4,000 m a.s.l. is covered by snow, glaciers, and permafrost (Bajracharya et al., 2014; Jackson et al., 2023). The perennial snow and glaciers of this mountain range play an important role in mountain hydrology, as all the perennial rivers of Nepal (Karnali, Gandaki, and Koshi) originate from these mountains. At lowlands, glacier ice melt contributes ~2-20 % of to the streamflow of major rivers of Nepal, with an average of 10-12 % (Alford and Armstrong, 2010; Lutz et al., 2014). This increases significantly at higher elevation and closer to glaciers. For example, in the Dudh Koshi basin (3712 km²), the total contribution of snow and glacier melt to annual streamflow is ~34 % (Nepal, 2016) and reaches > 85 % in the upper part of the basin (Pheriche outlet) (146 km², Mimeau et al., 2019a).

Furthermore, the cryosphere holds significant socio-economic importance for communities living both in the mountainous regions and downstream areas, as many industries, hydropower plants, ecosystems, and agricultural practices in the region rely heavily on water from the cryosphere (Immerzeel et al., 2010). Hydropower and agriculture, which are to some extent dependent on the snow and glacier ice meltwater, are not only an economic driver of Nepal but also a lifeline for many Nepalese (Nepal et al., 2021). Additionally, over the past 70 years, the Himalayas have become a popular destination for trekking and mountaineering. The high level of tourism creates employment opportunities for communities along the main trekking routes and within the region, thus contributing to the gross domestic product of Nepal (Stevens, 1991; Prasad, 2014). However, increasing number of visitors also lead to increased pressure on water resources.

Nepal also exhibits a large diversity of ethnic groups. In the Khumbu region, the Sherpa ethnic group is an example of a community with strong cultural ties to its natural environment. The Sherpa community lives in mountainous regions and primarily relies on perennial snow and glaciers for freshwater; hence, they are the first to experience the glacier changes and the consequences of these changes. The Sherpas have unique language, and heritage; they also consider glaciers to be sacred and believe that protective deities and spirits inhabit the mountains and glaciers. Mt. Everest (Zyomolangma, or Cho Molungma), for example, is considered to be an abode of the goddesses (Mu et al., 2020; Sherpa & Wengel, 2023). With the increase in tourism and the loss of glacier ice on the mountaintops, these beliefs are unfortunately also disappearing.

Why studying the glacier mass balance sensitivity of Mera Glacier?

In recent decades, the Himalayas have experienced rapid temperature and precipitation changes (Yan and Liu, 2014; Wester et al., 2019). Some of these changes can happen faster or with a larger magnitude at high altitudes than at lower elevations (Pepin et al., 2015; Thakuri et al., 2019). Climate change induces changes in the cryosphere as well as the hydrological cycle (Bolch et al., 2012; Yao et al., 2012; Sakai and Fujita, 2017). Recent studies have already shown significant glacier mass loss over the Himalayas in the last two decades (Brun et al., 2017; Shean et al., 2020; Hugonnet et al., 2021). Over the entire Hindu Kush Himalaya, the overall mass loss in the recent decade (2010 - 2019) was -0.28 ± 0.05 m w.e. a^{-1} , with higher rates of -0.40 ± 0.06 m w.e. a^{-1} in the central Himalaya (Jackson et al., 2023). Furthermore, under the global warming scenarios (+1.5 to +2 °C) outlined in the Paris Agreement, glaciers in this region are estimated to lose 30 to 50 % of their volume by 2100 compared to 2015 levels (Kraaijenbrink et al., 2017; Rounce et al., 2020; Marzeion et al., 2020; Edwards et al., 2021). For higher global warming levels (+3 to +4 °C), the estimated loss is 55 to 80 % of their current volume (Marzeion et al., 2020; Edwards et al., 2021). This wide range of projections of glacier evolution raises several important questions about our understanding of the glacier-climate relationship: *How will glaciers respond to different climate scenarios? What is the sensitivity of glacier mass to various climate variables?* Tackling these questions implies a thorough understanding of the current glacier mass balance patterns and their components, which in turn implies combining systematic field measurements with improved physical models.

However, this understanding is hindered by the limited field-based in-situ data available to address these questions in the Himalaya-Karakoram region. Only 28 out of 31,874 glaciers have been monitored for more than one year across the region, with seven of these glaciers being located in Nepal (RGI6; Azam et al., 2021; Jackson et al., 2023). In Nepal, glacier mass balance studies were initiated in the 1970s by Japanese scientists at Rikha Samba Glacier in Hidden Valley (Fujii et al., 1976) and AX010 Glacier in Dudh Koshi basin (Ageta et al., 1980), but these measurements were discontinuous and interrupted after a few years. From the 2000s, seven different glaciers in Nepal have been more closely monitored in Hidden Valley, Langtang, and the upper Dudh Koshi basin (Jackson et al., 2023). More precisely, Mera, Pokalde, and West Changri Nup glaciers in the upper Dudh Koshi basin have been monitored by the French IRD in collaboration with local institutes in Nepal since 2007, 2009, and 2010, respectively (Sherpa et al., 2017; Wagnon et al., 2021, 2013). These glaciological measurements are complemented by meteorological data collected by automatic weather stations (AWS) installed on/off the glaciers (Khadka et al., 2022). Despite the recent increase in field measurements in areas such as the Langtang and the Khumbu, across the region there remains an important gap in understanding the link between glacier mass balance and meteorological variables and in the knowledge of the specific mass balance components such as melt, sublimation and refreezing (Fujita and Ageta, 2000; Litt et al., 2019). Previous studies on the sensitivity of glacier mass balance to meteorological variables are limited in Nepal (Kayastha et al., 1999; Sunako et al., 2019). It is noteworthy to mention that until the start of this PhD in 2021, only three glaciers were investigated with respect to glacier mass balance sensitivity using the energy balance method (Kayastha et al., 1999; Sunako et al., 2019; Arndt

et al., 2021) and only two glacier mass balance reconstruction was performed using meteorological data in Nepal (Sunako et al., 2019; Arndt et al., 2021).

Given the above-mentioned limitations in the existing studies, a thorough analysis of glacier mass balance components and their sensitivity to climate on the basis of high-quality in-situ measurements is still needed. The extensive record of in-situ measurements on Mera Glacier in the eastern part of Nepal provides an excellent opportunity to address this research gap. Specifically, these measurements serve to understand the different mass balance fluxes, and to assess the mass balance sensitivity to meteorological variables, which constitute the main goal of this thesis.

Organization of the thesis

This thesis is organized as follows:

- Chapter two describes the physical geography, climate, and glaciers of the Himalaya Karakoram, as well as previous studies conducted on glacier surface energy balance in the region;
- Chapter three provides an extensive description of the study site and meteorological stations used in the thesis;
- Chapter four presents the evaluation of reanalysis products with in-situ measurements;
- Chapter five describes the analysis of the Mera Glacier surface energy balance and the calculation of the mass balance sensitivity to climate.
- Chapter six provides a summary of the work and discusses prospects for future research.

The fourth and fifth chapters are based on two journal articles, one published and one under review, with a brief introduction at the beginning of each.

Short notes to the readers

Depending on the consideration of different sub-regions, there are many different names to designate the mountainous regions of Asia in the literature. This thesis followed the region and acronyms given by some recently published work/reports:

- **HMA** stands for High Mountain Asia and includes the Tibetan Plateau and surrounding mountain ranges (Tien Shan, Pamir, Kunlun Shan, Hindu Kush, Karakoram, Himalaya and Nyainqentanglha). For a definition of these regions the reader is referred to Bolch et al. (2019).
- **HKH** Hindu Kush Himalaya region is the same as in the Water, Ice, Society, and Ecosystems in the Hindu Kush Himalaya (HIWISE) report (Jackson et al., 2023), which includes all the regions of HMA except Pamir and Tien Shan
- The **Himalayan-Karakoram** is the same as Bolch et al. (2012) and Azam et al. (2021), which includes eastern Himalaya, central Himalaya, western Himalaya and Karakoram only.

Chapter 2

2 Regional context and previous work

2.1 Geographical and geological setting

The Himalaya-Karakoram region spans ~2500 km, extending from the eastern Hindu Kush to the west of Nyainqentanghla (72.7 - 95.7E), covering more than 778,300 km² of land in Bhutan, Nepal, India, Pakistan, and China (Bolch et al., 2012). The region is highly glacierized (~37,567 km²) and known as the freshwater tower of South Asia (Immerzeel et al., 2010). Snow and glaciers feed the major Asian rivers, such as the Indus, Brahmaputra, and Ganges, and support the billions of people living in the downstream region (Figure 2.1, Lutz et al., 2014; Bolch et al., 2019).

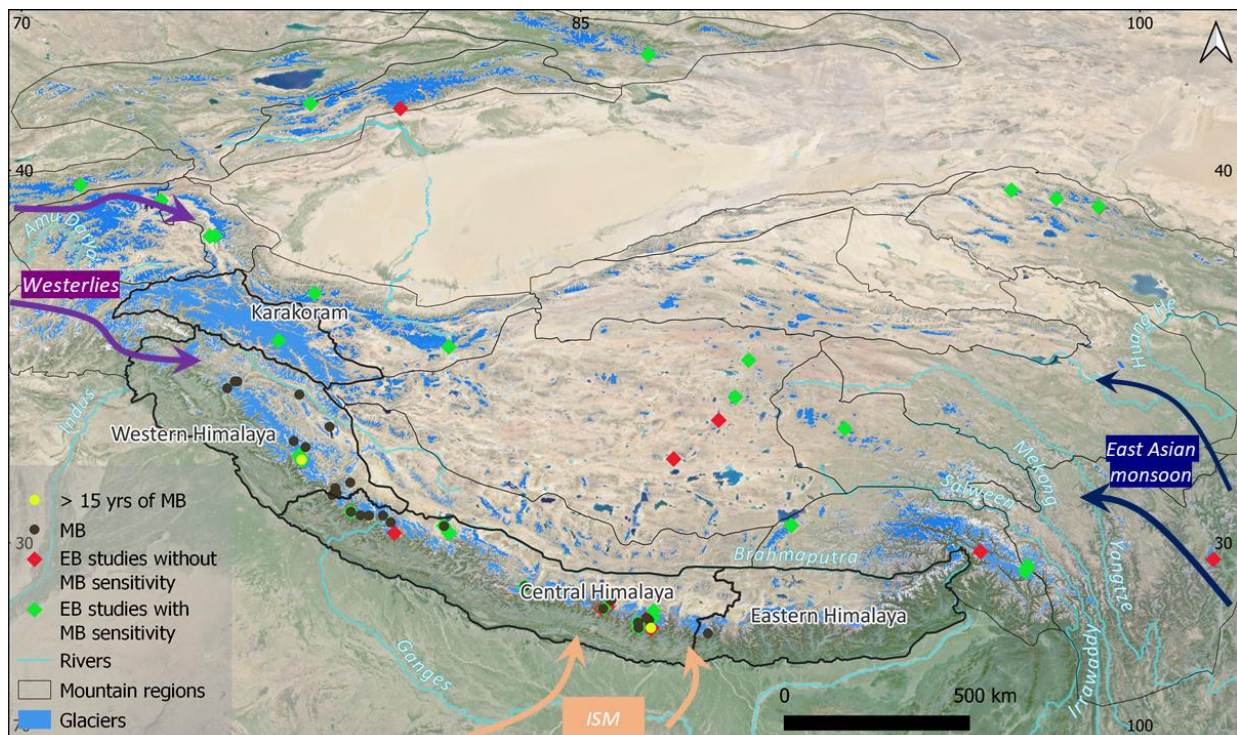


Figure 2.1 Figure showing the entire High Mountain Asia (HMA), with regions as defined in Bolch et al. (2019) with the Himalaya-Karakoram with bold boundary. The main circulation systems, the available glaciological mass balance (MB) studies (updated from Jackson et al., 2023) and all available energy balance (EB) studies. The MB works are divided into two categories: longer than 15 years of measurement and less. Similarly, the energy balance works are divided into two categories, with or without the MB sensitivity, representing the energy balance studies with/without the glacier mass balance sensitivity calculation.

Geologically, the Himalayas and Karakoram are two distinct mountain ranges separated by the Indus river (Figure 2.1). The current topography of these regions is the result of millions of years of tectonic forces, erosion and deposition by glaciers, and long-term climatological erosion. Altogether, there were active glacier movements and climatic variations. The formation of these mountain ranges is attributed to the collision of two large landmasses, namely the Indian and Eurasian plates; this first occurred ~65-60 million years ago, with the continent welding completed by 55-50 million years ago as evidenced by paleomagnetic data (Palzett et al., 1996). After the collision, the northward progress of India slowed down from

18 - 19.5 cm a⁻¹ to 4.5 cm a⁻¹ (Valdiya, 2002). The leading edge of the Indian plate, which is thicker than the Eurasian crust in southern Tibet, did not subduct under Asia; instead, it resisted subduction, causing pressure to build up between the colliding plates. This pressure was eventually relieved by thrusting upwards, which distorted the collision zone and resulted in the formation of the jagged Himalayan peaks and depression on the northern side (Lyon-Caen and Molnar, 1985; Valdiya, 2002). About 6.5 to 0.8 million years ago, an active tectonic event occurred, resulting in the formation of the Himalayas and subsequently further uplift of the region (France-Lanord et al., 1993). The Hindu Kush Himalaya region experienced the last glacial period, the Pleistocene, starting ~3 million years ago until ~0.2 million years ago. After the Pleistocene period, the region experienced an oscillation of dry-cold and wet-warm climates (Valdiya, 2002).

2.2 Climatic setting and glacier regimes

2.2.1 Regional atmospheric circulation patterns

The climate in the Himalaya Karakoram region is under the influence of two primary atmospheric circulation systems: the Westerlies and the Indian Summer Monsoon (ISM) (Bookhagen and Burbank, 2010) (Figure 2.1). The Westerlies refer to the prevailing winds from the west that originate from a high-altitude jet generated by a geopotential height gradient. During the winter, the Inter-Tropical Convergence Zone (ITCZ) moves southward (in response to the position of Sun); consequently, Westerlies also move southward and dominates the regional circulation pattern (Schneider et al., 2014). The Westerlies bring moisture from the Arabian Sea, when the air masses reach the western border of the HMA, the air masses is divided into northward and southward (Figure 2.1, Maussion et al., 2014; Mölg et al., 2014; Huintjes, 2014). The southward westerly air masses mostly falls as snow in the western part (Karakoram and western Himalaya) of the region (Maussion et al., 2014). The eastern part of the region is not much affected by these winter snowfalls, as the air masses are drier when they reach the Central and Eastern Himalaya. In the summer (ISM: defined in the following section), the circulation patterns change dramatically, the ITCZ moves northward and winds flow in the opposite direction of westerly. ITCZ-associated trade winds bring moist air to the land masses of the Indian sub-continent (Yancheva et al., 2007; Maussion et al., 2011). The orographic belt acts as a barrier, resulting in maximum precipitation located at elevations between 1,000 and 3,000 m a.s.l. (Figure 2.1, Bookhagen and Burbank, 2010; Bolch et al., 2012; Yao et al., 2022). The eastern and central Himalaya is largely under the influence of the ISM. The influence of the ISM decreases from the Garhwal range in the western of the central Himalaya to the Karakoram and further westwards. Overall, 80 % of the annual precipitation falls during the ISM in the central Himalayas (Figure 2.2 and 2.3C, Bookhagen and Burbank, 2010). Conversely, winter precipitation consists in the majority of the annual precipitation in Karakoram and the western Himalayas (Figure 2.2, Thayyen and Gergan, 2010; Maussion et al., 2014) These seasonality of precipitation driven by different climate regimes is clearly visible in Figure 2.3. The following section 2.2.2 exemplify this general overview by digging into the details of temperature and precipitation patterns, and their links with glacier regimes.

Furthermore, both the ISM and the westerly climate systems are also influenced by tropical and extra-tropical climate drivers such as the El Niño-Southern Oscillation, the North Atlantic

Oscillation, the Indian Ocean Dipole, the Madden-Julian Oscillation and the Arctic Oscillation (Massoud et al., 2023; Wester et al., 2019). The strength of these climatic drivers are highly variable from year to year, and the influence on regional precipitation varies annually in the region (Hrudya et al., 2021).

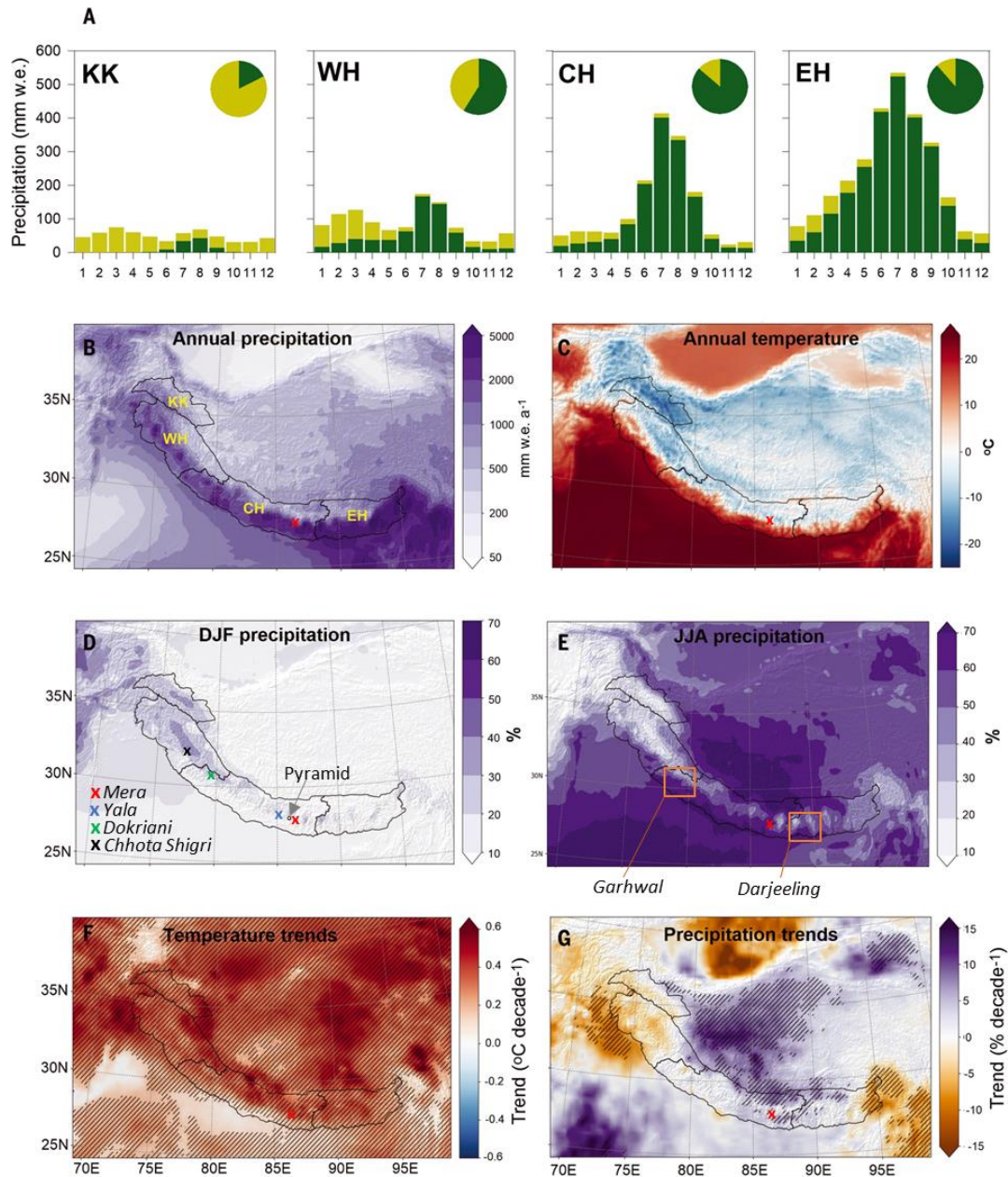


Figure 2.2. Precipitation and temperature patterns and trends over the Himalaya-Karakoram region. (A) Mean monthly precipitation (light green = snow and dark green = rain) sums over 1979-2019, extracted from ERA5 (<https://cds.climate.copernicus.eu/>). Pie charts show the annual contribution of snow and rain. (B to G) mean annual precipitation, mean annual temperature, mean DJF precipitation (%), mean JJA precipitation (%), temperature trends and precipitation trends, respectively. The stippling (diagonal lines) in (F) and (G) denote the areas statistically significant at the 5% level after correction for the false discovery rates. The red cross mark represents the location of Mera Glacier. The three other crosses show the location of three other monitored glaciers. KK, WH, CH, and EH stand for Karakoram, western, central, and eastern Himalaya, respectively. Figure adapted from Azam et al. (2021).

2.2.1.1 Season definition

The hydrological year (October of year N to September of year N+1) is typically divided into four seasons in the Himalaya Karakoram region (Bonasoni et al., 2010; Bookhagen and Burbank, 2010; Brunello et al., 2020). Winter is from December to February; Pre-monsoon is

from March to May; Monsoon or ISM is from June to September; Post-monsoon is from October to November. However, in the literature, depending on the location, precipitation pattern, and the purpose of the study, the length and definition of the seasons vary in different studies (Bollasina et al., 2002; Immerzeel et al., 2014; Brun et al., 2015; Khadka et al., 2021; Mandal et al., 2022). For example, Immerzeel et al. (2014) selected the monsoon for a specific date (June 16 to September 30) for 2012 to determine the seasonal variation in temperature and precipitation gradients at Langtang valley.

2.2.2 Temperature and precipitation patterns across the region

The Himalaya region exhibits specific temperature and precipitation patterns, which are a result of the various circulation systems combined with topographic and geographic characteristics (Figure 2.2; Bookhagen and Burbank, 2006). The mean annual temperature is primarily controlled by elevation (Figure 2.2), leading to large high elevation areas where the summer temperature is below zero degree, as in the Tibetan Plateau (Figure 2.3). The mean temperature also varies with latitude, longitude, and surface conditions (vegetation, snow, glaciers). For instance, the mean annual temperature measured at 5360 m a.s.l. at Mera La AWS (27.73N, 86.89E) in central Himalaya (-3.5°C) is higher than the mean annual temperature measured at 4863 m a.s.l. in Chhota Shigri AWS (32.38N, 77.85E) in western Himalaya (-6.1°C, Srivastava and Azam, 2022). The difference in latitude might explain this observed difference. Similarly, the amplitude of the intra-annual variability of temperature varies across the region (Figure 2.3). For example, the Chhota Shigri glacier (4863 m a.s.l.) in the western Himalaya has mean monthly temperature variations up to 20 °C (Mandal et al., 2022). In contrast, mean monthly temperature variations in Khumbu (east side of central Himalaya, 3570-5035 m a.s.l.) are around 12 °C (Sherpa et al., 2017; Wagnon et al., 2013). This variability in temperature amplitude may be due to differences in latitude and climate dynamics and follows a general pattern of larger temperature amplitude on the western side of the Himalaya Karakoram region than on the eastern side (Figure 2.3).

Regarding precipitation patterns, while the regional pattern of precipitation variability is imposed by the large climatic systems, the orographic barriers are important reasons for precipitation amount and frequency variation, whereas elevation and temperature are responsible for the form of precipitation (Bolch et al., 2012; Immerzeel et al., 2010; Yao et al., 2012). In the Himalayan valleys, precipitation shows significant variations from south to north due to changes in elevation and geography. Southern areas of the Himalayas with an altitude of approximately 1000 to 2000 m a.s.l. generally experience higher amounts (~1500 mm) of precipitation, while the higher Himalayan regions above 3000 m a.s.l. receive less (<1000 mm) precipitation (Bookhagen and Burbank, 2006, 2010). Above 3000 m a.s.l., the precipitation gradients remain very unclear due to the sparse number of measurements and due to the limitations of remote sensing products in mountainous areas (Shrestha et al., 2012; Schauwecker et al., 2017; Khadka et al., 2022). Even in areas with numerous measurements, such as the upper Dudh Koshi basin, contradictory results have been found. For instance, Salerno et al. (2015) demonstrate that the amount of precipitation is higher in Pheriche (4200 m a.s.l.) than in Pyramid (5035 m a.s.l.), whereas Mimeau et al. (2019a) and Perry et al. (2020) report that the precipitation is higher in Pyramid than in Pheriche. In Langtang Valley, located approximately 120 km west of the upper Dudh Koshi basin, Immerzeel et al. (2014) found that

precipitation variations are not homogeneous in a short horizontal distance and with a small altitude difference. In particular, they found an increase in precipitation with the elevation for stations located from 3800 m a.s.l. to 4800 m a.s.l., but the magnitude and frequency varies with seasons. This variation in precipitation is because of the altitudinal dependency of moisture source regions and the drying of air masses as they travel along the valleys (Perry et al., 2020). Similarly, the drying of air masses could explain the 30 % precipitation depletion at Pyramid station, compared with Khare station located ~30 km away upstream of the monsoonal moisture flux (Khadka et al., 2022).

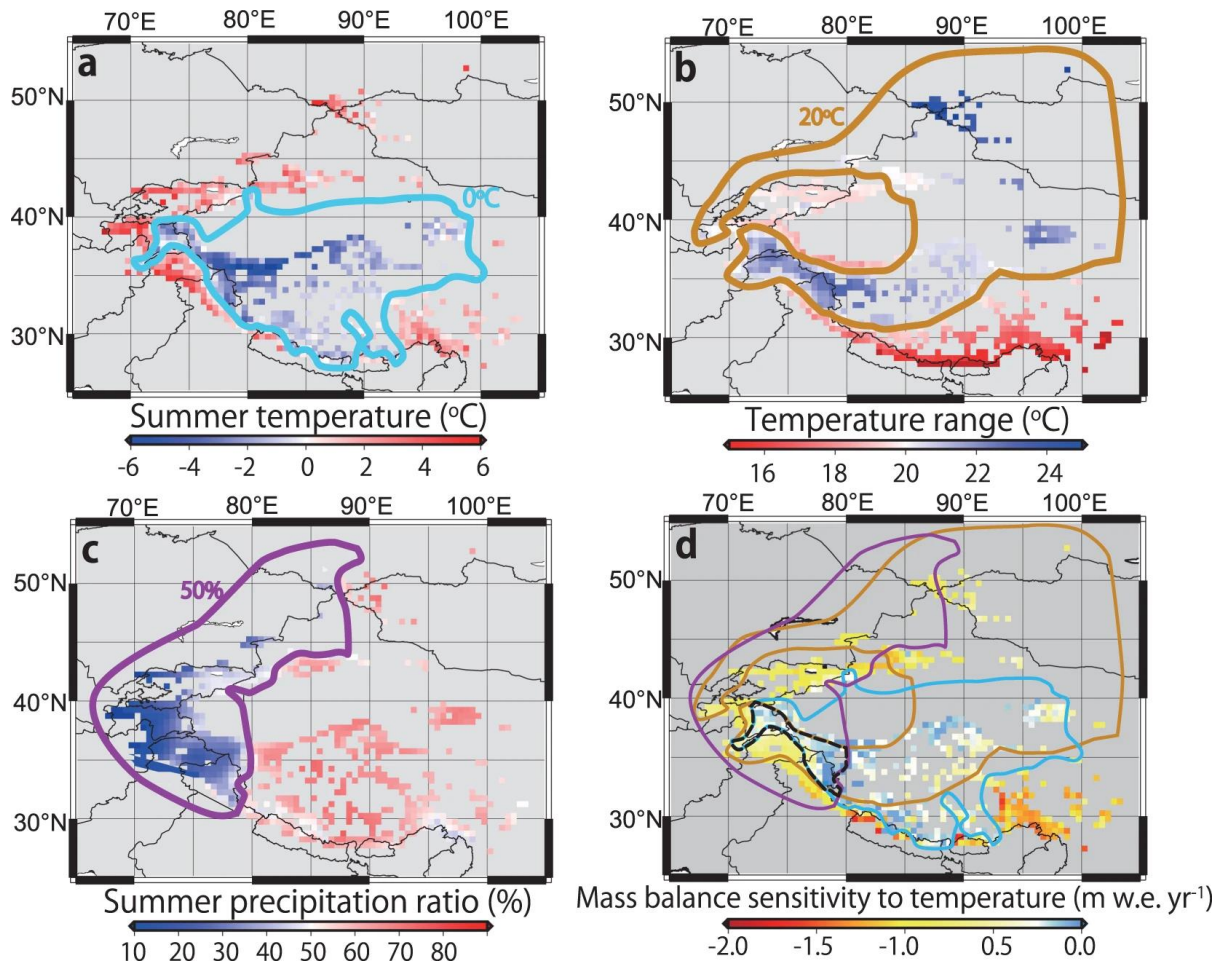


Figure 2.3. Distributions and boundaries of explanatory variables for multi-regression analysis and area boundaries for each explanatory variable with a weaker mass balance sensitivity. (a) The area with summer temperatures $< 0^{\circ}\text{C}$ is encompassed with a light blue line. (b) The areas with an annual range in monthly temperature $> 20^{\circ}\text{C}$ is encompassed with an orange line. (c) The area with a summer precipitation ratio of $< 50\%$ is encompassed with a purple line. (d) MBS distribution showing overlapping areas of lower summer temperature ($< 0^{\circ}\text{C}$), higher temperature ranges ($> 20^{\circ}\text{C}$), and lower summer precipitation ratio ($< 50\%$) with a black dashed line. a-c are depicted based on a 0.5° grid cell. Figure adapted from Sakai and Fujita (2017)

Additionally, the measurements from various stations in the different mountain valleys provide further evidence of precipitation variability at the location of the glaciers (Figure 2.2D), meaning that some glaciers are in much drier climate than others. The mean annual precipitation is 814 mm (2016-2020) near Mera Glacier (Khare AWS; 4888 m a.s.l.) and 540 mm (2012-2019) at Pyramid near Pokalde and Changri Nup glaciers (5035 m a.s.l.) (Khadka et al., 2022). Similarly, Kyanjin (3842 m a.s.l.) near Yala Glacier receives around 867 mm (2011-2013), while Dokriani Glacier (37774 m a.s.l.) receives over 2000 mm (2011-2016) and Chhota Shigri (3850 m a.s.l.) receives over 900 mm (2009-2017) (Immerzeel et al., 2014; Srivastava and Azam, 2022).

2.2.3 Glacier regimes

The amount and seasonality of precipitation determine the glacier regimes across the regions (Maussion et al., 2014; Thayyen & Gergan, 2010). Here, we define the glacier regimes based on two different definitions: the glacio-hydrological regime and the continentality.

Glacio-hydrological regime: Glaciers in the eastern and central Himalaya receive most of the precipitation during the ISM, and they experience maximum accumulation and ablation simultaneously during the summer (Ageta et al., 1980; Sakai et al., 2015; Sherpa et al., 2017). They are referred to as 'summer accumulation' type glaciers and correspond to the snow and monsoon regime of Thayyen & Gergan (2010). Glaciers in the western Himalaya region are in the monsoon transition zone and receive ~50 % of their total precipitation during the ISM, and they are known as the 'monsoon-arid transition zone' glaciers (Thayyen and Gergan, 2010). In the Karakoram, winter snowfall from the Westerlies dominates the annual precipitation. In this area, the ISM activity is low, and glaciers in this area are known as 'winter accumulation' type glaciers, corresponding to the winter snow regime (Sakai and Fujita, 2017; Thayyen and Gergan, 2010).

Continentality: Shi and Liu (2000) classified glaciers from the Tibetan Plateau and its surroundings into three categories based on temperature and precipitation: maritime (temperate), subcontinental, and continental. Maritime glaciers are mainly located in the central and eastern Himalayas and ISM dominates the total precipitation of these glaciers. The mean summer temperature at the equilibrium line altitude (ELA in m) of these glaciers is high and ranges from 1 to 5 °C. Subcontinental glaciers are mostly located in the eastern Kunlun, eastern Tibetan Plateau, and western Himalaya. The mean summer temperature at the ELA of these glaciers is between 0 to 3 °C. Continental glaciers are mostly located in the Karakoram, western Kunlun, and western Tibetan Plateau. The summer mean temperature at the ELA of these types of glaciers is estimated to be less than -1 °C. Continental and subcontinental glaciers are located in dry areas than their maritime counterparts.

2.3 Climate trends and projections across the region

Temperature changes have been observed since 1850 at the rate of + 0.06 °C per decade, with accelerated increase since 1982 (+ 0.20 °C per decade) (Lindsey and Dahlman, 2020). These temperature changes have been the largest in the last two decades (IPCC, 2021). This warming trend is closely linked to human activities, and the temperature is likely to increase rapidly in the future (IPCC, 2021).

2.3.1 Observed temperature changes

Over the past 120 years (1901 to 2020), there has been a notable increase in the annual mean surface air temperature across Asia, with rates of change averaging at 0.13 ± 0.1 °C decade⁻¹ (Ren et al., 2023). This warming trend has been particularly pronounced since the mid-20th century, with significant temperature increases predominantly observed in mountainous areas, and particularly on the southern slope of the Himalayas (Figure 2.2; Azam et al., 2021; Thakuri et al., 2019). These trends vary in magnitude across the region (Figure 2.2), and for some specific sites, observed trends are also available. For example, in the Western Himalaya,

analysis of meteorological data from 1955 to 2016 from the Upper Indus Basin revealed an annual increase of $0.14\text{ }^{\circ}\text{C decade}^{-1}$ in maximum temperatures, with a significant decrease of $-0.08\text{ }^{\circ}\text{C decade}^{-1}$ in minimum temperatures. These warming trends in maximum temperatures have been particularly pronounced in winter and spring, while cooling trends in minimum temperatures are more evident in summer and autumn (Hussain et al., 2021). Similarly, Moazzam et al. (2024) highlighted the symmetrical pattern of the rising trend of maximum and minimum temperatures in the Indus basin. However, there is no clear relationship between annual temperature trends and altitude.

In the central Himalaya (Nepal), analyses of in-situ temperature data for the period 1976-2015 (Thakuri et al., 2019) reveal warming trends ranging from $+0.09$ to $+0.45\text{ }^{\circ}\text{C per decade}$. The mean temperature trend of $+0.027\text{ }^{\circ}\text{C a}^{-1}$ is observed, which is consistent with the previous findings from Shrestha et al. (1999). Salerno et al. (2015) reported variability in temperature change with altitude based on data from different stations in the Koshi basin in Nepal, with mean temperature trends at the Pyramid (5035 m a.s.l.) in the upper Koshi basin being $+0.44\text{ }^{\circ}\text{C decade}^{-1}$ (1994-2013), which is $\sim 30\%$ higher than at lower elevations (850-2480 m a.s.l.: $+0.29\text{ }^{\circ}\text{C decade}^{-1}$). Over the same period, the maximum and minimum temperature change rates are $+0.09$ and $+0.72\text{ }^{\circ}\text{C decade}^{-1}$ at the Pyramid AWS.

The question of understanding the spatial pattern of temperature trends remain largely unanswered, and in particular the role of elevation remain unclear. Despite some contradictory results in Indus basin, there is growing evidence of increased temperature change rates at high-altitude areas, a phenomenon referred to as "elevation-dependent warming" (Pepin et al., 2015; Zhang et al., 2023). Thakuri et al. (2019) found an increasing trend of warming with elevation in the southern slope of the central Himalaya, but their study is restricted to stations below 3000 m a.s.l., and thus does not allow to firmly conclude on the existence of an elevation-dependant warming.

2.3.2 Observed precipitation changes

The increase in land and ocean temperature causes increases in evaporation rates from land and water surfaces, which in turns alters atmospheric circulation patterns, significantly impacting the amount, timing and precipitation phase (Wester et al., 2019). The rapid warming of the Indian Ocean and the transition of the Pacific oscillation play a crucial role in the monsoon circulation and rainfall (Huang et al., 2020; Roxy et al., 2015). For instance, due to the transition of the interdecadal Pacific oscillation, the trend of ISM precipitation intensity in north-central India has changed from $-0.16\text{ mm day}^{-1}\text{ decade}^{-1}$ (1950-1999) to $0.68\text{ mm day}^{-1}\text{ decade}^{-1}$ (2000-2016) (Huang et al., 2020). For the different areas in the Himalaya Karakoram region, precipitation trends are found to be a mixture of drying and wetting from different observations and grided/reanalysis data sets (Palazzi et al., 2013; Talchabhadel and Karki, 2019). Overall, the physical processes influencing precipitation are much more complex than for temperature changes, resulting in large variability in precipitation trends across sub-regions (Figure 2.2). In particular, from the Asian Precipitation Highly-Resolved Observational Data Integration Towards Evaluation (APHRODITE) data set between 1951 and 2007, summer precipitation significantly decreased in the Himalayan region. This trend was not significant for the winter months (Palazzi et al., 2013). However, in the western Himalaya, Shekhar et al.

(2017) reported a strong negative trend in precipitation rates between 1971 and 2013, primarily due to changes in winter precipitation (Shekhar et al., 2017). In the central Himalaya, the data recorded at stations from below 3500 m a.s.l. over the period 1971 to 2014 show decreasing precipitation trends throughout the year (DHM, 2017). These consistent but insignificant patterns across the regions patterns might be associated with short-term variability in atmospheric phenomena. In the Khumbu area (Pyramid 5035 m a.s.l.), the precipitation trend was negative ($-13.7 \pm 2.4 \text{ mm a}^{-1}$) between 1993 and 2013, and the negative trend is significant in all months of recent years (Salerno et al., 2015).

2.3.3 Temperature and precipitation trends in the Himalaya-Karakoram

Average global surface air temperature over the period 2081-2100 is projected to be 0.2 °C to 1.0 °C higher in the low emissions scenario and 2.4 °C to 4.8 °C higher in the high emissions scenario compared to the last three decades (Lee et al., 2021). In the case of the Himalaya region, even if efforts are made to limit global warming to 1.5 °C by 2100, temperatures are still expected to rise by at least +0.3 °C compared to global average. The changes are expected to be even larger (+ 0.5 °C) in specific areas such as the northwestern Himalaya and the Karakoram (Wester et al., 2019).

2.4 Glacier mass balance (theoretical concepts)

Glaciers gain mass primarily from snowfall and lose mass from melt, sublimation, and calving, which is only relevant for lake-terminating glaciers. In the Himalaya Karakoram, most of the glaciers are land-terminating, and thus calving is not a dominant process. Glacier mass balance represents the cumulative process of all mass exchanges occurring across its boundaries i.e., the sum of surface mass balance (\dot{b}_s), englacial mass balance (\dot{b}_e), basal mass balance (\dot{b}_b) and calving. If the glacier is land-terminating, then the change in mass ($\frac{dM}{dt}$, in kg a^{-1} or $\text{m}^3 \text{ w.e. a}^{-1}$) can be expressed as (Cuffey and Paterson, 2010);

$$\frac{dM}{dt} = \int_A [\dot{b}_s + \dot{b}_e + \dot{b}_b] dA \quad (2.1)$$

where A (in m^2) is the plan-view area of the glacier and \dot{b}_s , \dot{b}_e , and \dot{b}_b are expressed in $\text{kg m}^{-2} \text{ a}^{-1}$ or m w.e. a^{-1} . However, most of the time, surface mass balance dominates the overall glacier mass balance, and other mass balances are usually neglected.

Accumulation and ablation

The process by which snow and ice are added to the glacier is known as glacier accumulation, and the area where accumulation is larger than ablation at the annual scale is called the accumulation area/zone. Snowfall is the major accumulation process. However, other processes, such as avalanches, re-sublimation, refreezing of rain or percolated meltwater, and snow redistribution, may also contribute to glacier accumulation depending on the geomorphological and climatic conditions. The mass loss from the glacier surface is called ablation, and the area where ablation is larger than accumulation at the annual scale is called the ablation area or zone. For land-terminating glaciers, ablation is primarily caused by snow

and ice melt and, to a lesser extent, by sublimation. Additionally, the equilibrium-line altitude (ELA) is a crucial concept in glaciology. The ELA is the average altitude of the glacier where the annual net balance is zero (the accumulation = ablation) (Braithwaite and Raper, 2009)

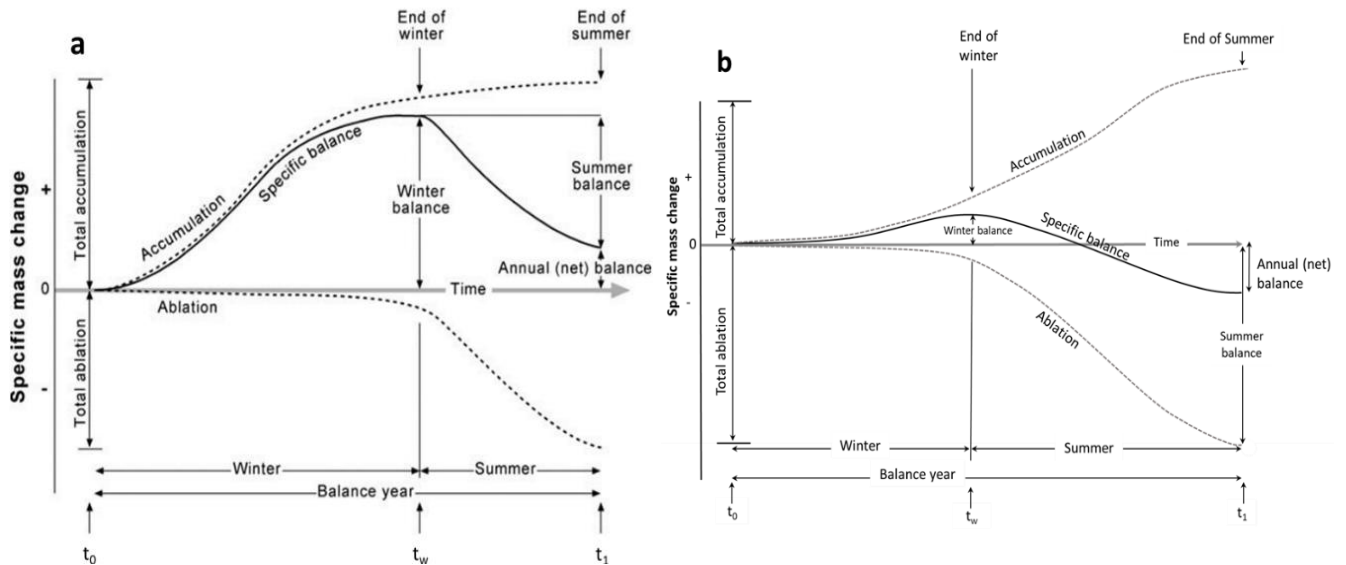


Figure 2.4. Definitions of terms in the seasonal progression of specific surface balance. "Annual" or "net" balance is the "specific balance" cumulated over one year: a) winter accumulation type glacier and b) summer accumulation type glacier. Note that a positive annual balance is represented for the winter accumulation type glacier, and a negative one is represented for the summer accumulation type glacier. Figure adapted from Cuffey & Paterson (2010).

2.4.1 Glaciological mass balance

Glacier mass balance is estimated by either the glaciological method (Cuffey and Patterson, 2010) and/or the geodetic methods (Bolch et al., 2012). Here we first discuss the glaciological method, which is the direct method of measuring the surface mass balance of a glacier. It is a field-based approach that allows gathering information from the field to calculate point surface mass balance (Figure 2.4). This method involves the annual or seasonal measurements of the glacier surface height relative to stakes inserted at multiple points on the glacier. The mass balance in the accumulation area is measured through snow pit/core measurements to find the previous year horizon and snow density. For the specific case of Mera Glacier (explained in section 3.1.1), where the previous year horizon can be difficult to identify without ambiguity and where the annual surface mass balance in the accumulation area is relatively small, we additionally mark the horizon with a stake and/or blue powder. In the ablation area, changes in glacier surface height relative to the ablation stakes are measured, and the point mass balances are obtained directly for each stake based on the density of snow/ice. For the whole glacier, the vertical mass balance gradients can be calculated using the different point mass balance data from different elevation stakes. The gradient is then linearly extrapolated to the whole glacier from the mass balance at different elevations (Figure 2.5). Then, the annual glacier-wide mass balance (B_n in $\text{kg m}^{-2} \text{a}^{-1}$ or m w.e. a^{-1}) is calculated as the area-weighted sum of altitudinal surface mass balances (Eq 2.2)

$$B_n = \frac{1}{S} \int b_i \cdot s_i \quad (2.2)$$

where b_i ($\text{kg m}^{-2} \text{a}^{-1}$ or m w.e. a^{-1}) is the altitudinal mass balance, s_i (m^2) is the altitudinal surface area at different elevations of the glacier, and s (m^2) is the total glacier area, respectively.

The glacier-wide mass balance from this method is highly sensitive to systematic errors that accumulate linearly with the number of measurement years. These errors arise from errors in density, snow depth, stake length measurements, combined with the number of samples and sampling area (Thibert et al., 2008). Also, non-negligible basal and englacial processes may not be captured by the glaciological method, inducing further uncertainties. Therefore, the glaciological mass balance needs to be reanalyzed using the geodetic method (Thibert et al., 2008; Wagnon et al., 2021; Zemp et al., 2013). Still, when the measurements are carried out at high frequency (monthly, seasonal, annual), glaciological measurements give detailed glacier-wide information such as snow depth and density at a different area, surface condition, as well as the spatial distribution of surface mass balance for different time scales.

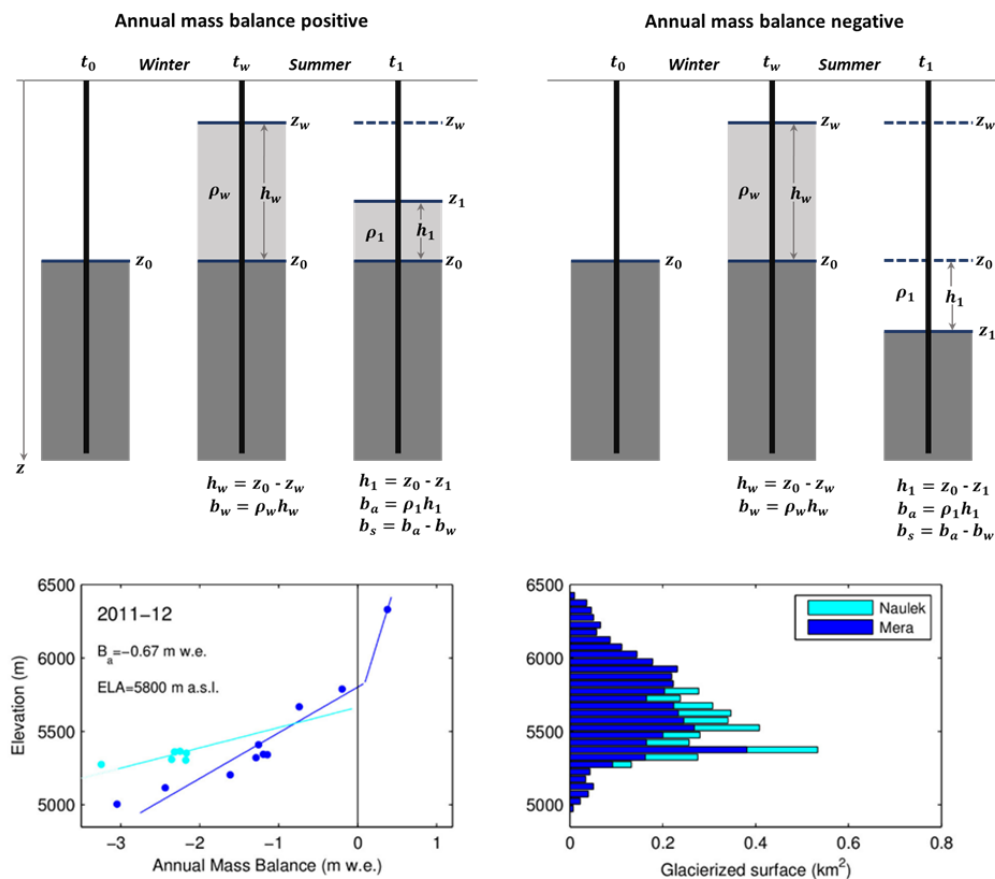


Figure 2.5. Top panels (adapted from Cogley et al. (2011)): Stake measurements of seasonal mass balances in a year of positive (left) and a year of negative (right) surface mass balance, with no superimposed ice for a winter accumulation type glacier. Bottom left panel (adapted from Wagnon et al. (2013)): 2011-2012 annual point mass balance (dots) as a function of altitude derived from field measurements (stakes or pits), and the linear line represents the vertical mass balance gradients on Mera Glacier. The bottom right panel shows the hypsometry of Mera Glacier, showing the respective areas of Naulek (light blue) and Mera (dark blue) branches.

2.4.2 Geodetic mass balance

Field-based study of glaciers is intensive and expensive, and due to the geographical and climatic extremities, it is not possible to cover all glaciers, even from the same region. (Bamber and Rivera, 2007). Only one percent of the world glacier has observational data from the

glaciological method (WGMS, 2024) and most of the regional mass balances were represented by the extrapolation of these measurements (Zemp et al., 2019). The 21st century has led to significant advances in remote sensing data (for example, ASTER, Pleiades) and methods for measuring glacier mass changes. The availability of new spaceborne sensors (stereo-images, laser, radar etc.) and large computational and storage capacities significantly accelerated the development the methodologies to calculate at local, regional, and global scales mass balance with lower uncertainties (Figure 2.6, Bamber & Rivera, 2007; Berthier et al., 2023; Hugonnet et al., 2021; Marzeion et al., 2017).

The geodetic method, also known as the photogrammetric or volumetric method, determines the volume change over a given time interval (usually one to several years) at various spatial scales (glacier to regional or even global scale). This methods estimates the glacier thickness change resulting from ice flow dynamics and mass balance processes. Compared to the glaciological method, this method estimates the total mass balance (including basal, internal, and surface mass balance) and glacier-wide mass balance, not the spatial distribution of surface mass balance (Berthier et al., 2023).

Geodetic mass balance is most commonly estimated by differencing of digital elevation models (DEMs) (Thibert et al., 2008). The geodetic method allows determining the glacier volume change (ΔV in m^3) from DEMs representing the elevation of the glacier surface at two different dates. The volume change over the entire area is calculated as the product of the glacier-wide mean elevation change (dh in m) and glacier area (s), i.e. $\Delta V = dh \times s$. The geodetic mass change (B_g in $kg\ m^{-2}\ a^{-1}$) is then calculated by using the changes in volume, in m^3 , and area of the glacier (s), in m^2 , with the assumption of a volume to mass conversion factor ($f_{\Delta V} = 850 \pm 60\ kg\ m^{-3}$, Huss, 2013) (Eq 2.3)

$$B_g = f_{\Delta V} \frac{\Delta V}{s} \quad (2.3)$$

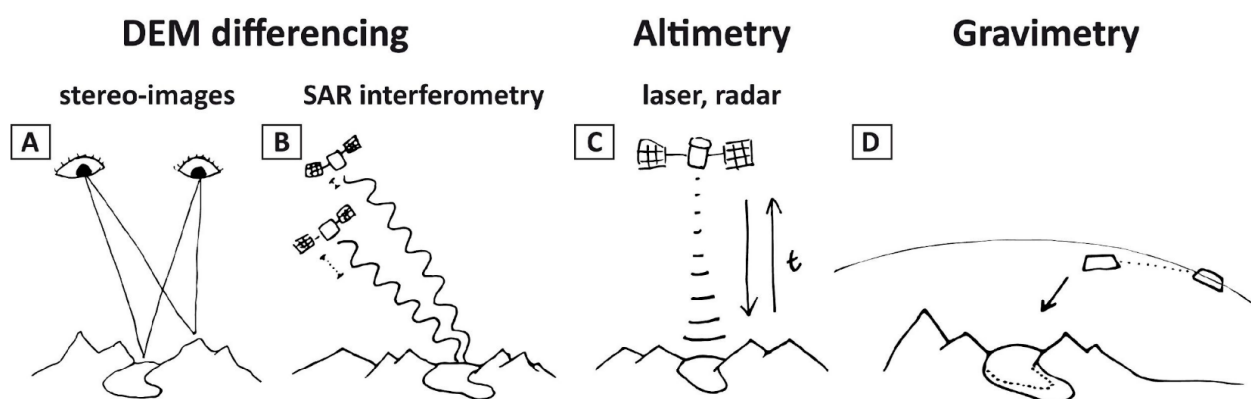


Figure 2.6. Sketch of the main techniques used to estimate glacier mass change from space. DEM differencing and altimetry (A-C) first determine glacier volume changes through repeat measurement of the glacier elevations. (D) Satellite gravimetry is used to detect mass changes directly: two satellites on the same orbit are connected with a ranging system that detects acceleration/deceleration of the satellites relative to each other caused by changes in the gravimetric force. These changes include, among others, glacier mass change between different satellite overpasses. Figure adapted from Berthier et al. (2023) and Treichler (2017).

This method is a valuable tool to calculate the glacier-wide mass balance of glaciers with no field measurements. The geodetic method are indirect method of calculating mass balance which are valuable for reanalyzing mass balance from glaciological methods (Thibert et al.,

2008; Wagnon et al., 2021; Zemp et al., 2013). However, to calculate short-period (seasonal to a few years) geodetic mass balance, the spatial DEM resolution should be higher (i.e., the order of 2 to 10 m Beraud et al., 2023), but for long-term mass balance, 30 to 100 m resolution DEM would be fine (example: Hugonnet et al., 2021; Brun et al., 2017; Shean et al., 2020).

2.5 Glacier energy balance

Assessing snow and glacier melt is essential in the glacierized mountain to predict the discharge and the changes in snow and glaciers in different climatic conditions. Glacier ice melt is generally estimated using the temperature index models or the energy balance models (Hock, 2005). The temperature-index model assumes a direct relationship between the amount of melting and the cumulative positive air temperatures (Hock, 1999). However, glacier ablates from sublimation too, and many variables like radiation, wind speed, and specific humidity are linked with the ablation processes. These processes of ablation, whether through melting or sublimation, are determined by the energy balance at the interface between the glacier and the atmosphere. This balance is influenced by both the climatic conditions above the glacier and the physical features of the glacier itself (Hock, 2005; Cuffey and Paterson, 2010). In particular, a wealth of theoretical and experimental work was devoted to investigating energy fluxes responsible for the ice and snow melt (Oerlemans and Knap, 1998). Here, we highlight the basic energy exchange processes and their importance.

The surface of the glacier exchanges energy with both the atmosphere and the subsurface. The difference in energy exchange is primarily due to the advection/conduction of heat and absorption/emission of radiation, resulting in temperature or phase changes. These phase changes include melting, refreezing, sublimation, and re-sublimation (Figure 2.7). These critical glaciological concepts are a fundamental metric to understanding how glaciers evolve and respond to different climatic conditions (Hock and Holmgren, 2005). Figure 2.7 highlights the different processes of energy exchanges between the glacier surface, subsurface, and atmosphere, which can be expressed as the total of all energy fluxes at the surface (Cuffey and Paterson, 2010).

$$QM = SW_{net} + LW_{net} + QS + QL + QC + QR \quad (2.4)$$

where SW_{net} (in Wm^{-2}) is the sum of incoming solar radiation and the reflected solar radiation ($SW_{net} = SW_{in} + SW_{out}$). SW_{in} is a function of the solar constant ($1368 Wm^{-2}$) that varies over the year and time of the day because of solar geometry, topography, cloud, and atmospheric conditions. SW_{out} is a function of SW_{in} and surface albedo (SW_{in}/SW_{out}), that depends upon surface conditions (snow or ice). The net incoming solar radiation (SW_{net}) penetrates the surface of snow/ice (QPS in Figure 2.7) and is absorbed at different depths, where it provides heat to the subsurface. LW_{net} is the sum of incoming (LW_{in}) and outgoing (LW_{out}) longwave radiation. LW_{in} is a function of cloud cover and air temperature and is emitted by atmospheric components such as water vapor, carbon dioxide, and ozone. LW_{out} is the longwave radiation emitted by the glacier surface, which depends on snow/ice emissivity and surface temperature. Sensible heat flux (QS) and latent heat flux (QL) are the turbulent fluxes that exchange the energy between the surface and atmosphere. The

turbulent heat fluxes are functions of the temperature/vapour pressure gradients, roughness length, wind speed, and air density. QS is the heat transfer between the surface and atmosphere without phase change. It depends on the temperature difference between the surface and the air above it and the wind speed. QL refers to the exchange of heat energy between a glacier surface and the surrounding atmosphere due to sublimation, evaporation or condensation. QL is directly proportional to the gradient of specific humidity, which is effectively dependent also on the air temperature. The subsurface heat flux (QC) depends on the temperature gradient between the surface and the subsurface. QC is often considered as a minor flux compared with the other ones. QR is the heat transported by the rain, which directly depends on the rainfall intensity and temperature. Rain has a minor impact on the energy of the glacier surface, but it significantly affects the surface albedo of snow. Therefore, rain plays an indirect role in bringing energy to the surface. All the energy fluxes towards the surface are positive and negative when away. When the sum of all these fluxes (QM) is positive at the surface, and the surface temperature reaches the melting point ($0\text{ }^{\circ}\text{C}$), melting begins (Hock and Holmgren, 2005; Cuffey and Paterson, 2010). More details about the specific parametrizations of each flux are provided in Chapter 5.6.

The various computed energy fluxes are converted to water equivalent mass changes (expressed in m w. e.) using the latent heat of fusion/sublimation. Then, the mass balance (b_{clim}) is determined by summing all mass fluxes derived from energy fluxes and snowfall (Eq 2.5).

$$b_{clim} = b_{sfc} + b_i = c_{sfc} + a_{sfc} + c_i + a_i \quad (2.5)$$

Where b_{sfc} is the surface mass balance, b_i is the internal mass balance, c_{sfc} is surface accumulation, a_{sfc} is surface ablation, c_i is internal accumulation, and a_i internal ablation.

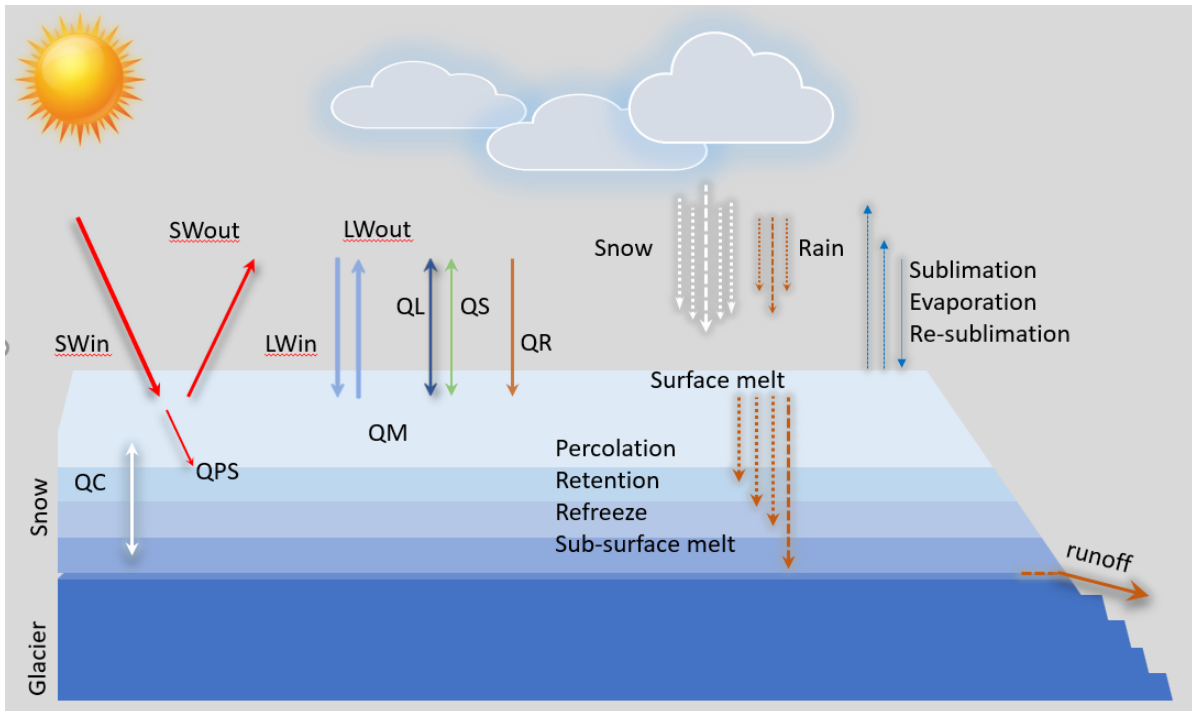


Figure 2.7. Schematic picture of the major energy and mass fluxes at the glacier surface. Symbols are explained in the section 2.5

2.6 Mass balance sensitivity

The glacier mass balance sensitivity (MBS in m w.e.) is defined as the amount of change in mass balance when changing the climatic variables such as temperature, precipitation, relative humidity, by certain values or percentages (Oerlemans, 1989; Oerlemans and Reichert, 2000). For example, the change in mass balance (ΔM) when the temperature (ΔT) is increased by $+1\text{ }^{\circ}\text{C}$ is called MBS (m w.e. $^{\circ}\text{C}^{-1}$) to $+1\text{ }^{\circ}\text{C}$ temperature.

$$MBS = \frac{\Delta M}{\Delta T} \quad (2.6)$$

The change in temperature or precipitation is expressed as climate change, which is crucial for understanding how glaciers mass balance changes to future climate change scenarios. In 1992, Oerlemans (1992) introduced the mass balance sensitivity analysis using the energy balance method. This was initiated to comprehend the correlation between glacier melt and sea level rise (Oerlemans and Fortuin, 1992; Zuo and Oerlemans, 1997; Gregory and Oerlemans, 1998). The sensitivity of glacier mass balances to climate has also been widely used to assess and understand the variability of the melt contribution to streamflow (Immerzeel et al., 2010; Lutz et al., 2014), to understand the variation in glacier volume (Rounce et al., 2020; Miles et al., 2021) and to predict future changes in streamflow (Immerzeel et al., 2010; Khanal et al., 2021). However, all the previously mentioned hydrological models use temperature index models instead of energy balance models for the sensitivity analysis.

2.7 Present knowledge of Himalaya Karakoram glaciers

Geodetic mass balance revealed that glaciers are experiencing mass loss globally, with varying rates in different regions of the world (Hugonnet et al., 2021). The mass balance calculated between 2000 and 2018 using high-resolution digital elevation models from stereo imagery and ASTER shows that the mean mass balance loss for HMA is -0.19 ± 0.03 m w.e. a^{-1} (Shean et al., 2020). This mass balance is highly variable in different areas, which is more negative in the eastern part of Himalaya-Karakoram and less negative westward (Figure 2.8). The mass loss in the eastern Himalaya is -0.52 ± 0.15 m w. e. a^{-1} , and in the central Himalaya, it is -0.37 ± 0.08 m w.e. a^{-1} . The mass balance in the western Himalaya (-0.32 ± 0.08 m w.e. a^{-1}) is slightly less negative than central Himalaya, whereas the Karakoram has the least negative mass balance (-0.04 ± 0.04 m w. e. a^{-1} ; Shean et al., 2020). Overall, this regional glacier mass loss has been larger during the last decade (2010–2020) compared to the previous decades (2000–2010) and before (Jackson et al., 2023).

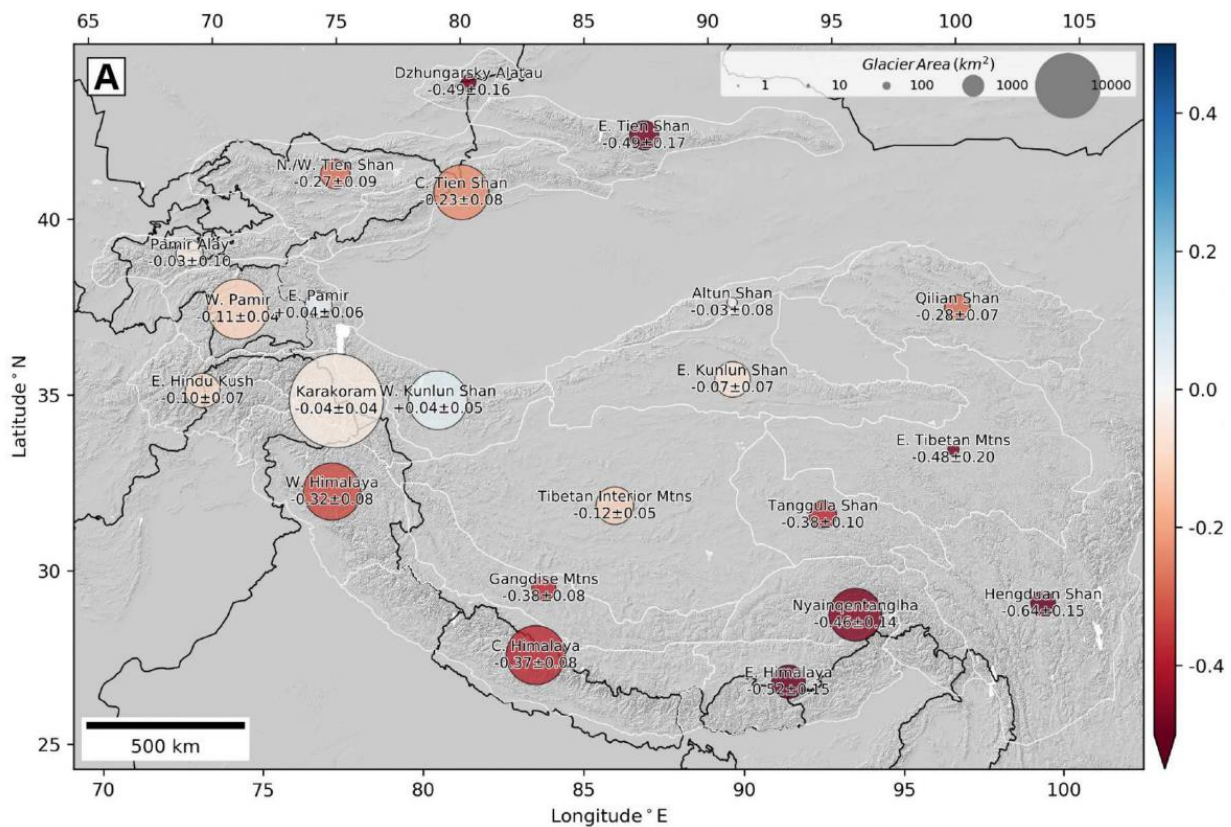


Figure 2.8. Specific glacier mass balance (m w.e. a^{-1}) for the period from 2000 to 2018 in HMA, aggregated over glacierized sub-regions from Bolch et al. (2019). Figure adapted from Shean et al. (2020).

Regarding glaciological mass balances in the Himalaya Karakoram region, several glaciers have been measured for the past years, but only two have more than 15 years of continuous mass balance data (Figure 2.1, Table 2.1, Srivastava & Azam, 2022; Wagnon et al., 2021). The following sections highlight the glaciological work on the central Himalaya, focusing on Nepal.

2.7.1 Glacier mass balance studies in central Himalaya

Table 2.1 presents the details of all field-based glaciological work in the Himalaya-Karakoram region since the 1970s. Most of this work has been conducted in the western and central

Himalayas. The first glaciological fieldwork in Nepal was carried out in 1974 on Rikha Samba Glacier by Japanese researchers as part of the Glaciological Expedition of Nepal (Fujii et al., 1976). Later, the first glaciological annual mass balance measurement was conducted on the AX01 Glacier (0.5 km²) in 1978/79. Subsequently, mass balance measurements were conducted between 1995 and 1999 on the AX01 glacier, revealing a mass balance of -0.69 m w.e. a⁻¹ (Jackson et al., 2023; Fujita et al., 2001). Currently, several groups of scientists are involved in glaciological surveys, and Nepal is now home to seven monitored glaciers (Figure 2.9). The mass balance of AX01 has not been measured since 1999. Most of Nepal's glacier mass balance studies have been conducted around 2010 (Table 2.1, Figure 2.9, Azam et al., 2018; Jackson et al., 2023; Wagnon et al., 2021). The mass balance monitoring at Mera Glacier (5.1 km² in 2012) began in 2007, and now it is the longest continuously measured glacier in Nepal. The mean mass balance for this glacier between 2007 and 2023 was -0.42 m w.e. a⁻¹ with only four positive annual mass balance. In 2009 and 2010, monitoring began for two small glaciers in Khumbu, Pokalde (0.1 km² in 2011) and West Changri-Nup (0.9 km² in 2013). Additionally, Yala Glacier (1.6 km² in 2012) in Langtang and Rikha Samba Glacier (5.74 km² in 2010) in Hidden Valley have been continuously measured since 2011. Both of these glaciers have recorded one positive annual mass balance out of twelve and eleven, respectively.

The available measurements in Nepal indicate a large inter-annual variability in mass balance, with the last two years being particularly negative (< -0.8 m w.e.; Figure 2.9). This is primarily due to climatic variability, as well as the mean elevation and the ratio of accumulation area to total area (Sherpa et al., 2017).

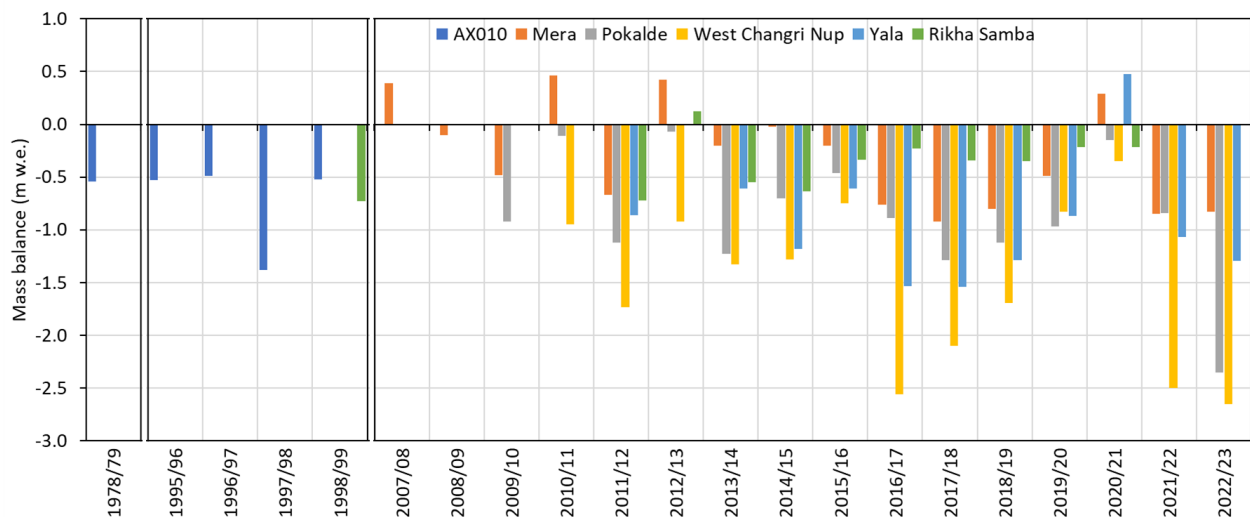


Figure 2.9. Glaciological mass balance observations in Nepal. The mass balance data from 1978 to 1979 and 1995 to 1999 are separated with the gap in figure as the time series is too far from the rest of the data series. The data are from WGMS (2024). Note the broken axis that highlights the time separation between different measurement periods.

Table 2.1. Glaciological mass balance observations in the Himalayan range. The error estimations in mass balances were given when calculated in the original source (Reproduced from (Azam et al., 2018; Jackson et al., 2023)).

SN	Glacier name	Region	Latitud	Longitud	Area	Debris cover	Aspect	MB Period	MB (m w.e. a ⁻¹)	Reference
1	Changmekhangu (CG)	Eastern Himalaya	27.57	88.41	5.6	50	S	1979-1986	-0.26	(Raina, 2009)
2	Gangju La (GL)	Eastern Himalaya	27.94	89.95	0.3	clean	NE	2003-2004;	-1.38±0.18	(Tshering and Fujita, 2016)
3	AX010 (AX)	Central Himalaya	27.72	86.55	0.6	clean	SE	1995-1999	-0.69	(Fujita et al., 2001)
4	Chorabari (CB)	Central Himalaya	30.74	79.09	6.7	53	S	2003-2010	-0.77	(Dobhal et al., 2013)
5	Dokriani (DR)	Central Himalaya	30.83	78.83	7	6	NW	1992-1995; 2007-2013	0.32	(Dobhal et al., 2021)
6	Dunagiri (DG)	Central Himalaya	30.55	79.9	2.6	~80	N	1984-1990	-1.04	(GSI, 2011)
7	Kangwure (KW)	Central Himalaya	28.46	85.82	1.9	clean	NE	1991-1993;	-0.57	(Liu et al., 1996; Yao et al., 2012)
8	Miera (MR)	Central Himalaya	27.72	86.88	5.1	clean	N	2007-2023	-0.42	(Wagnon et al., 2021)
9	Naimona'nyi (NN)	Central Himalaya	30.45	81.33	7.8	clean	N	2005-2010	-0.56	(Yao et al., 2012)
10	Pokalde (PK)	Central Himalaya	27.93	86.83	0.1	clean	NW	2009-2023	-0.87	(Wagnon et al., 2013; Sherpa et al., 2017)
11	Rikha Samba (RS)	Central Himalaya	28.83	83.5	4.6	clean	S	2011-2021	-0.39±0.32	(Gurung et al., 2022)
12	Satopanth (SP)	Central Himalaya	30.73	79.32	19	58	NE	2014-2015	-2	(Laha et al., 2017)
13	Tipra Bank (TB)	Central Himalaya	30.73	79.7	7	15	NW	1981-1988	-0.14	(Gautam and Mukherjee, 1992)
14	Trambau (TB)	Central Himalaya	27.9	86.5	31.7	clean	S	2016-2018	-0.74 ± 0.44	(Sunako et al., 2019)
15	West Changri Nup (CN)	Central Himalaya	27.98	86.77	0.9	clean	NE	2010-2023	-1.51	(Sherpa et al., 2017)
16	Yala (YL)	Central Himalaya	28.23	85.6	1.6	clean	S	2011-2023	-0.86	(Stumm et al., 2021; WGMS, 2024)
17	Chhota Shigri (CS)	Western Himalaya	32.23	77.51	15.5	3.4	N	2002-2022	-0.53	(Azam et al., 2018; Srivastava & Azam, 2022;
18	Hamtah (HT)	Western Himalaya	32.57	77.62	3.2	~70	N	2000-2009;	-1.43	(GSI, 2011; Mishra et al., 2014)
19	Gara (GR)	Western Himalaya	31.47	78.42	5.2	17	NE	1974-1983	-0.27	(Raina et al., 1977; Sangewar and Siddiqui, 2007)
20	Gor Garang (GG)	Western Himalaya	31.62	78.82	2	~60	S	1976-1985	-0.38	(Sangewar and Siddiqui, 2007)
21	Kolahoi (KH)	Western Himalaya	34.33	75.78	11.9	clean	N	1983-1984;	-0.27; -0.84±0.34	(Kaul, 1986; Romshoo et al., 2023)
22	Naradu (ND)	Western Himalaya	31.33	78.45	4.6	~60	N	2000-2003;	-0.72	(Koul and Ganjoo, 2010)
23	Neh Nar (NN)	Western Himalaya	34.15	75.52	1.3	clean	N	1975-1984	-0.43	(GSI, 2011)
24	Patsio (PT)	Western Himalaya	32.73	77.3	2.25	12	N	2010-2017	-0.34	(Angchuk et al., 2021)
25	Rulung (RL)	Western Himalaya	33.12	78.26	1.1	clean	NE	1979-1981	-0.11	(Sangewar & Siddiqui, 2007; Srivastava et al., 2001)
26	Shaune Garang (SG)	Western Himalaya	31.28	78.33	4.9	24	N	1981-1991	-0.42	(GSI, 2011; Sangewar and Siddiqui, 2007)
27	Shishram (SR)	Western Himalaya	34.33	75.72	9.9	clean	N	1983-1984	-0.29	(Kaul, 1986)
28	Stok (ST)	Western Himalaya	33.98	77.45	0.74	5	N	2014-2019	-0.39	(Soheb et al., 2020)

2.7.2 Glacier surface energy balance studies in Himalaya-Karakoram

Figure 2.1 and Table A1 highlight various studies on the surface energy balance of Himalaya-Karakoram glaciers. The first study on energy balance in central Himalaya was conducted by Kayastha et al. (1999) on AX010 Glacier. These studies found that the net radiation dominated by solar radiation is the main source for snow and ice melt, with a relatively small contribution of sensible and latent heat flux (Kayastha et al., 1999; Acharya and Kayastha, 2019). Since then, several studies have been published on the surface energy balance and mass balance of different glaciers in Nepal.

The following sections present the main findings of glacier surface energy balance and mass studies in the Himalaya-Karakoram.

i) Contribution of different energy fluxes to melt

Kayastha et al. (1999) analyzed the in-situ data recorded during the monsoon of 1978 on the AX010 glacier to determine its mass balance and sensitivity to meteorological variables. An energy balance study was conducted at multiple points on the AX010 glacier to calculate the mass balance based on one season of data from 25 May to 25 September 1978. Acharya & Kayastha (2019) also employed the Kayastha et al. (1999) model to examine the energy and mass balance of Yala Glacier. Both studies highlighted that SW_{net} is the main energy source on the glacier surface and that the majority of this energy is lost, mainly by LW_{net} . Acharya & Kayastha (2019) found that the mean contribution of net radiation to the total melting energy on Yala Glacier (up to 5358 m a.s.l.) is in the 61-66 % range, whereas Kayastha et al. (1999) found it was 85 % during the monsoon 1978 at AX010. Small fluctuations in SW_{in} , LW_{in} , and surface albedo can significantly alter the net radiation, thereby influencing the total available energy for melting on the glacier surface.

ii) Importance of sublimation

At Mera Glacier, Litt et al. (2019) highlighted the relevance of the energy balance model in the accumulation zone for computing sublimation, which cannot be achieved with the temperature index model. They found that higher albedo and lower cloud cover in the accumulation area, compared with the ablation area, explain the difference between available energy at the accumulation and ablation area of Mera Glacier. Sublimation is contributing 100 % and 93 % of mass loss during pre-monsoon and monsoon at the accumulation zone of Mera Glacier (Litt et al., 2019). Matthews et al. (2020) conducted a simulation of the point energy balance at Camp 2 (6464 m a.s.l.) and South Col (7945 m a.s.l.) on Everest during the 2019 monsoon to analyze the different energy balance components and suggest the occurrence of melt at very high elevation during monsoon. Similarly, at the South Col of Everest Sherpa et al. (2023) found that sublimation ($2.5 \text{ mm w.e. day}^{-1}$) is a major component of energy and mass balance processes due to high winds and low relative humidity in winter. Similarly, from the eddy covariance measurement at Yala (5,350 m a.s.l.), cumulative sublimation is 1 mm day^{-1} for 32 days period from October to November 2016 (Stigter et al., 2018).

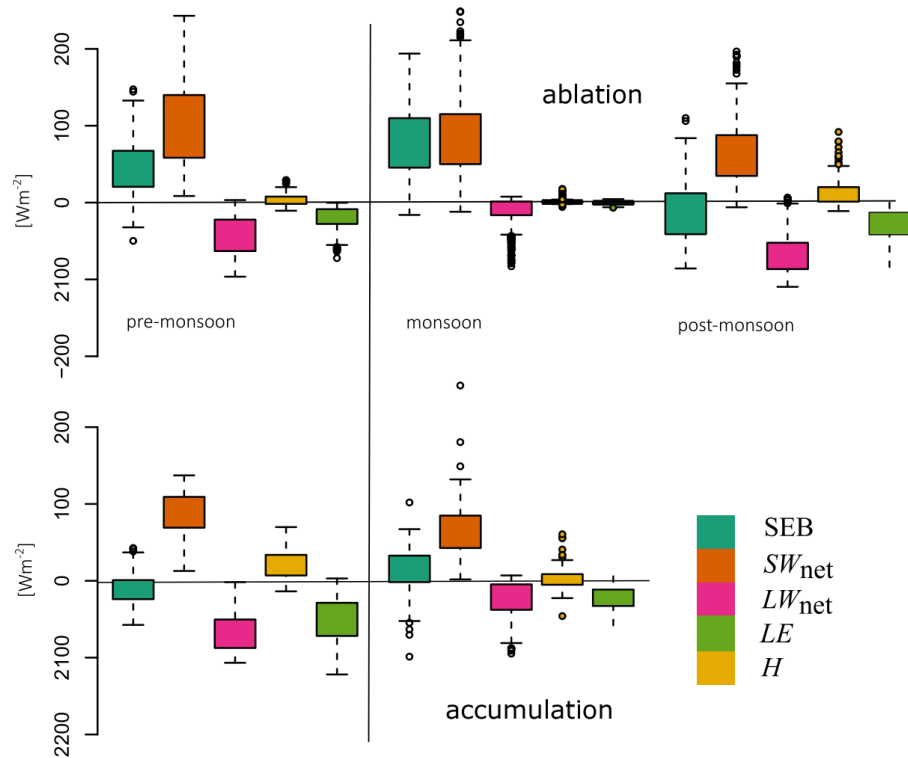


Figure 2.10. Boxplot summaries of mean daily surface energy balance (SEB) components calculated from all the available data between 2013 and 2017, classified by season and grouped into ablation (upper panel) and accumulation (lower panel) sites. Each box upper (resp. lower) edge is drawn at the third quartile (resp. first) of the variable distribution, and whiskers provide the same value plus (resp. minus) the interquartile range. Values outside the whiskers are provided by the dots. Figure adopted from Litt et al. (2019)

iii) Importance of monsoon for mass balance processes

The atmospheric components, such as cloud cover fraction and water vapour have a direct relationship with the surface mass balance of glaciers. Conway et al. (2022) implemented an energy balance model forced with in-situ data to investigate the relationship between cloudiness, near-surface meteorology, radiation, and energy balance for mountain glaciers located in different regions worldwide. The study found that surface melt is more frequent in cloudy conditions compared to clear-sky conditions due to the higher contribution of temperature-dependent fluxes. Especially at Mera Glacier (5360 m a.s.l.), the melting frequency sharply increased with the higher cloudiness. However, the cloud cover does not affect the total daily melt compared to clear-sky conditions. Albedo and cloud cover likely have equal and opposite effects on substantial seasonal variations in net radiations. Additionally, Shaw et al. (2022) used in-situ data for the bias correction of Weather Research and Forecasting (WRF) model to run an energy balance in three different sites of HKH. The study simulated the effect of ISM on Himalayan glaciers for 40 years. The results showed complex and contrasting responses of glacier energy and mass balance to the patterns of the ISM. These responses were largely driven by the timing, amount, and phase of snowfall. Overall the findings underscore the critical importance of understanding of ISM shaping surface melt patterns and the overall energy balance at glacier surface.

iv) Mass balance reconstruction

Due to the lack of long-term in-situ data, some energy balance studies and mass balance reconstructions were conducted using reanalyzed meteorological data. In the western part of central Himalaya, the mass balance of Halji Glacier for the period 1982-2019 was calculated using bias-corrected ERA5 Land data (Arndt et al., 2021). However, as there were no radiation measurements available, the incoming radiation were used in the same form as the reanalysis dataset without downscaling. The reconstructed mass balance of Halji glacier from 2000 to 2018 was $-0.53 \text{ m w.e. a}^{-1}$, which is slightly less negative than the regional mass balance result ($-0.70 \text{ m w.e. a}^{-1}$) from Shean et al. (2020). Similarly, Arndt and Schneider (2023) reconstructed the mass balance of several glaciers in HKH (including Yala and Hanji) using ERA5 land data and highlighted that the summer accumulation type glacier has highest mass turnover. Simulations were re-executed by scaling the precipitation until the mass balance results were similar between the output and Shean et al. (2020). They also highlighted the lack of in-situ data, which prevented proper calibration and validation of the different inputs and outputs of the model. Gurung et al. (2022) reconstructed the climatic mass balance of the Rikha Samba Glacier (1974–2021) and compared it with the glaciological mass balance using bias-corrected ERA5 land data. The study shows that the Rikha Samba Glacier has experienced less negative mass loss in recent decades ($-0.47 \text{ w.e. a}^{-1}$) compared to before 2000 ($-0.65 \text{ m w.e. a}^{-1}$). Additionally, the overall mass balance of Rikha Samba Glacier ($-0.56 \text{ m w.e. a}^{-1}$, 1974-2020) is less negative than the 39-year reconstructed mass balance of Trambau Glacier ($-0.65 \pm 0.39 \text{ m w.e. a}^{-1}$; Sunako et al., 2019).

2.7.3 Glacier mass balance sensitivity studies in Himalaya-Karakoram

In HMA, the mass balance is highly heterogeneous across regions (explained in 2.7: Shean et al., 2020), and the glacier melt contribution in the HMA rivers is spatially variable with the changing climate (Khanal et al., 2021). The heterogeneity of glacier behavior is a consequence of local/regional climate change and its response to meteorological variables. However, the spatial variability of mass balance sensitivity is dependent on each climate and glacier regime (Figure 2.3, Oerlemans and Fortuin, 1992; Fujita and Ageta, 2000; Fujita, 2008; Sakai and Fujita, 2017). Three main studies investigated the regional pattern of mass balance sensitivity to temperature in HMA (Sakai and Fujita, 2017; Wang et al., 2019b; Arndt and Schneider, 2023). Sakai and Fujita (2017) found that the maritime glaciers are more sensitive to temperature changes compared to continental glaciers (Figure 2.3, 2.11). Sakai and Fujita (2017) also found that the mass balance sensitivity of winter accumulation glaciers in the Karakoram and western Himalaya is less than that of summer accumulation glaciers in the central, eastern Himalaya and Tibetan Plateau, where summer precipitation dominates annual precipitation (Figure 2.3, 2.11. and 2.12), even though they do not provide definitive explanations for this phenomenon.

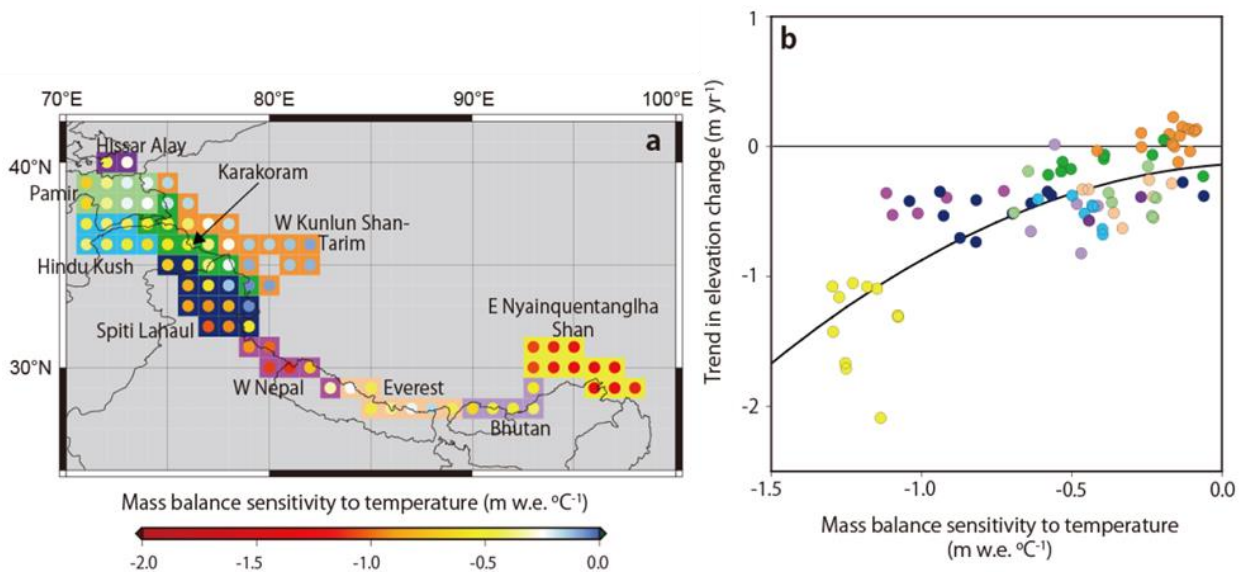


Figure 2.11. a) Mass balance sensitivity for Himalaya-Karakoram region. b) Relationship between the mass balance sensitivity and trend in elevation change, coloured by sub-regions depicted in a. Figure adopted from Sakai and Fujita (2017)

The regional pattern of mass balance sensitivity from Wang et al. (2019), using a temperature index model and 45 glaciers from the different regions of HMA, is somewhat similar to that from Sakai and Fujita (2017). The mass balance sensitivity calculated from the energy balance model (Arndt and Schneider, 2023) on the 16 glaciers from different regions found that the 15 glaciers are sensitive to summer precipitation. Arndt and Schneider (2023) found that glaciers with higher mass turnover per year (higher accumulation and ablation) are more sensitive to temperature. However, the pattern is similar to the regional mass balance sensitivity analysis of Sakai and Fujita (2017). Furthermore, this mass balance sensitivity is usually non-linear, with variations in the climatic variables (Vincent, 2002; Arndt and Schneider, 2023). This means that perturbing one variable positively or negatively by a certain amount will not result in the same mass balance change, i.e., changing temperature by +1 °C or -1 °C will not result in the same mass balance change. The non-linearity likely arises from albedo feedbacks (Arndt and Schneider, 2023), and hence the results from a temperature index model, that does not account very well for these feedbacks, show that the mass balance sensitivity is linear with precipitation (Wang et al., 2019).

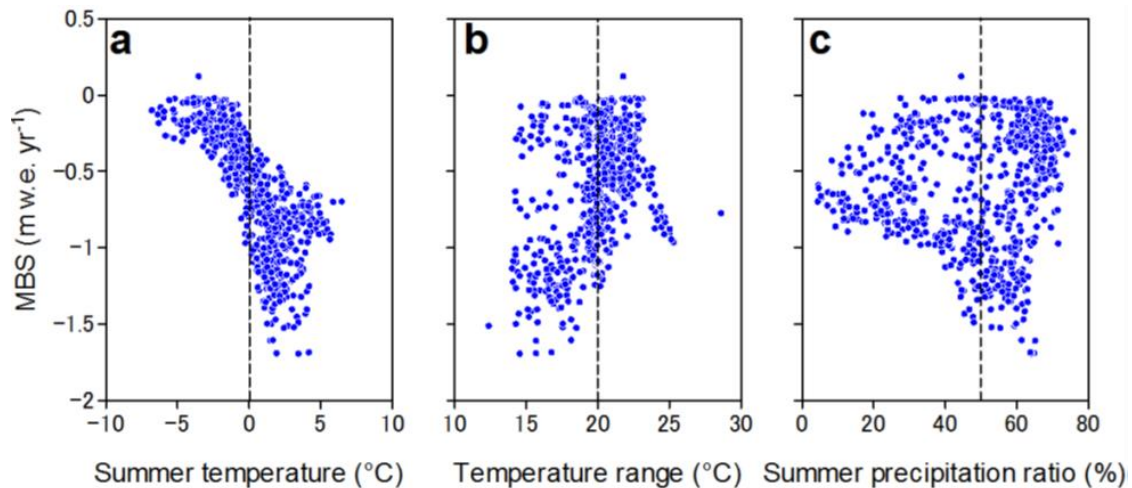


Figure 2.12. Relationship between mass balance sensitivity (MBS) and explanatory factors, a. summer temperature, b. annual range in monthly temperature (temperature range), and c. summer precipitation ratio in HMA. Dashed vertical lines indicate the threshold values used in Figure 2.3. Figure adapted from the supplementary material of Sakai and Fujita (2017).

All mass balance sensitivity studies using the energy balance method (Figure 2.1) in the HMA are highlighted in Table A1. These studies use different data (reanalysis, in-situ), different time periods (seasonal, annual), and different meteorological variables for the mass balance sensitivity. The main findings and different results from the studies are highlighted below;

i) ± 1 °C temperature vs ± 20 % of precipitation variation

The mass balance sensitivity is not linear with temperature and precipitation; however, the mass balance sensitivity by an increase in temperature can be compensated by the increase in precipitation (Vincent, 2002). In the central Himalaya, the mass balance sensitivity of the AX010 glacier was calculated by perturbing meteorological variables for only one season (25 March to 25 September 1978), and the glacier mass balance was found to be strongly sensitive to changes in summer temperature and precipitation but less sensitive to relative humidity (Kayastha et al., 1999). Sunako et al. (2019) analyzed the sensitivity of Trambau Glacier (27 km west of Mera Glacier) in the eastern part of the central Himalaya. They found that a temperature increase of +1 °C resulted in greater mass loss than the mass gain by + 20 % increase in precipitation.

ii) maritime and (sub-)continental glacier mass balance sensitivity

Most of maritime glaciers like Parlung no 4, 94, Yala, and Halji are more sensitive to both changes in temperature and precipitation (Arndt and Schneider, 2023). Naimona'nyi glacier is more sensitive to warmer and drier conditions than colder and wetter conditions (Arndt and Schneider, 2023). In contrast, Trambau and Rikha Samba glaciers have lower mass balance sensitivity than other maritime glaciers (Sunako et al., 2019; Gurung et al., 2022). The lower mass balance sensitivity of Rikha Samba and Trambau might be because of the higher elevation range (Arndt and Schneider, 2023), or maybe they are continental glaciers. Compared to the studies mentioned, the glacier in the subcontinental region (the western Himalayan glacier: Chhota Shigri, Shruti Dhaka, and Dokriani Glaciers) exhibits lower mass balance sensitivity for both temperature and precipitation (Srivastava and Azam, 2022; Oulkar et al., 2022; Arndt and Schneider, 2023)

iii) Sensitivity studies that used in-situ and reanalysis data sets

The mass balance sensitivity of the Parlung No 4 Glacier in the southeastern Tibetan Plateau and the Zhadang Glacier in the south-central Tibetan Plateau by in-situ data (Zhu et al., 2018) and the reanalysis data (Arndt and Schneider, 2023) are not similar. Arndt and Schneider (2023) found that the mass balance sensitivity of Parlung no 4 is less sensitive to temperature than the result obtained by Zhu et al. (2018) but more sensitive to precipitation. In Zhadang Glacier, Arndt & Schneider (2023) found that the mass balance is more sensitive to both temperature and precipitation than the result from Zhu et al. (2018).

Overall, the variation in seasonal climates may lead to variations in the timing and intensity of snowfall and glacier melting in HKH, which can directly impact glacier mass balance (Shaw et al., 2022; Fugger et al., 2022; Sakai and Fujita, 2017). Furthermore, it is important to note that significant variation in mass balance sensitivity results has been found even among glaciers within the same region (Zhu et al., 2018; Arndt and Schneider, 2023; Yang et al., 2017; Sakai and Fujita, 2017). This discrepancy highlights that the variability of results of the mass balance analysis and sensitivities are influenced by the calculation method, the calibration process, the quality of the data, and the distribution of meteorological variables (Zolles et al., 2019; Sunako et al., 2019). Therefore, it is important to improve data quality and the methodologies used to obtain more accurate results.

2.8 Summary and objectives

Glaciers cover a significant area of the Himalaya-Karakoram and are important sources of fresh water in the region. These glaciers are in different climatic regimes, dominated by different circulation systems. Regional mass balance estimates from the geodetic method found that glaciers have been losing mass rapidly in recent years. The mass loss rate is contrasted at the scale of Himalaya-Karakoram, with the highest rates of mass loss on the eastern side of Himalaya-Karakoram. Different mass balance sensitivities to temperature changes could be one of the main factor to explain this spatial variability (Sakai and Fujita, 2017). From the literature, it is clear that the mass balance sensitivity varies significantly from east to west, and it is also evident that the sensitivity of glaciers varies with climate and geography (Arndt and Schneider, 2023; Sakai and Fujita, 2017). The field-based studies of glaciers in this region began five decades ago, but only a few glaciers have been measured, resulting in limited data and knowledge. Studies based on available in-situ data are short, while those based on reanalysis data are more extensive in the whole Himalaya-Karakoram region, leading to different mass balance sensitivities depending on the data and study periods (Zhu et al., 2022, 2018; Arndt and Schneider, 2023). However, even the quantification of glacier mass balance sensitivity to meteorological variables in most HKH glacierized areas is unclear.

Therefore, the main objective of this thesis is to fill the gap in the knowledge of glacier mass balance sensitivity to climate in the eastern part of the central Himalayas, with the aim of advancing the knowledge of future glacier evolution. In this thesis, we have compared reanalysis to in-situ meteorological data, as the ultimate goal is to reconstruct the mass balance of Mera Glacier using downscaled meteorological data. We have also analyzed the

sensitivity of Mera Glacier surface mass balance to in-situ meteorological variables, primarily temperature and precipitation.

The overview of the key questions addressed in this thesis are:

- ❖ What are the current meteorological conditions in the upper Dudh Koshi basin?
- ❖ What are the performances of different high-resolution reanalysis meteorological data in the upper Dudh Koshi basin?
- ❖ What are the major physical processes governing the seasonal and spatial variability of the glacier mass balance at the Mera Glacier?
- ❖ What is the relationship between the meteorological variables and glacier surface mass balance, and which meteorological variables drive the surface mass balance in this region?

Chapter 3

3 Study area and data

This chapter presents the different study sites investigated. They are all located in the upper Dudh Koshi basin in Nepal. The automatic weather stations (AWS) used in this study and the mass balance data of Mera Glacier are also described. It is important to note that other AWSs in Khumbu, installed by different groups of researchers (Matthews et al., 2020; Salerno et al., 2015), are not discussed. Additionally, two reanalysis data sets used in this thesis are also introduced at the end.

3.1 Dudh Koshi basin and Mera Glacier

The Dudh Koshi basin is located about 200 km east of Kathmandu in the central Himalayas (eastern Nepal). The basin is home to several large glaciers, including the Khumbu and Ngozumpa glaciers. Approximately 410 km² (10 %) of the basin area is covered by glaciers, and about one-fourth (110 km²) of the glacierized area is covered by supraglacial debris (Figure 3.1, Shea et al., 2015). The basin includes some of the world's highest mountains, such as Mount Everest, Lhotse, Cho Oyu, and Nuptse. Furthermore, the basin contains several glacier lakes, including Imja and Hunku North, which are susceptible to glacial lake outburst floods (Shrestha et al., 2023).

Mera Glacier (27.72 N, 86.88 E) is located in the upper Dudh Koshi basin (Figure 3.2). It is a clean plateau-type glacier covering an area of 4.84 km² in 2018 (Wagnon et al., 2021). The glacier flows from an altitude of 6390 m a.s.l. to a minimum of 4910 m a.s.l. and has a gentle slope averaging around 16 degrees. It is a popular destination for trekkers and novice mountaineers due to its gentle slopes, moderate elevation in the Himalayas, and accessibility from Lukla airport (Sherpa et al., 2017; Wagnon et al., 2021).

At approximately 5900 m a.s.l., the glacier splits into two branches: the Mera branch and the Naulek branch. The Mera branch, the largest of the two, heads north before curving westward, while the Naulek branch extends about 2 km to the northeast. The Mera branch is larger, accounting for about 80 % of the glacier's total area (Wagnon et al., 2021).

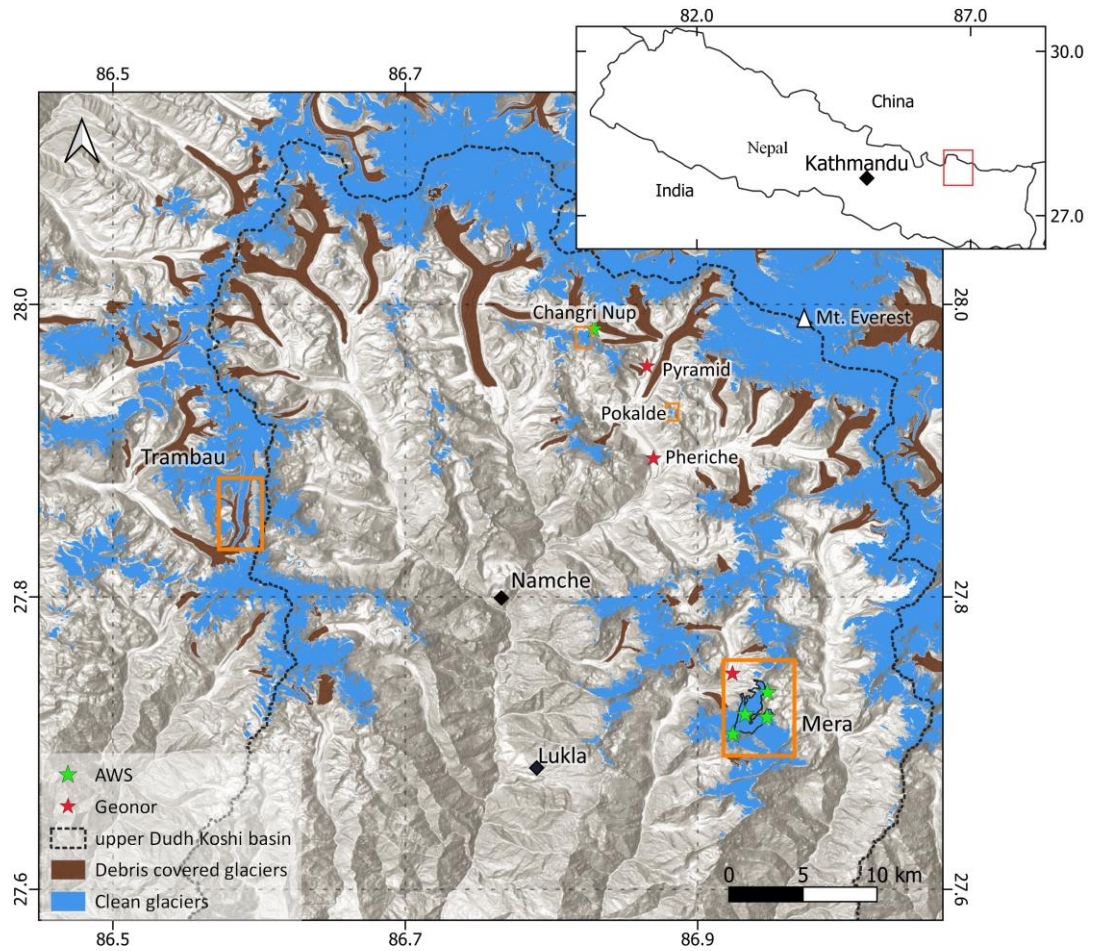


Figure 3.1. Upper Dudh Koshi basin, eastern Nepal, with clean and debris covered glacier extent, different Automatic Weather Stations (AWSs: green stars), and precipitation measurement sites (red stars). The different orange rectangles represent the glacier measurement sites: Mera Pokalde, west Changri Nup, and Trambau. The Mera Glacier outlines are from Wagnon et al. (2021), the basin boundary is same as Shea et al. (2015b), and the base layer is an open hillshade tile by ESRI.

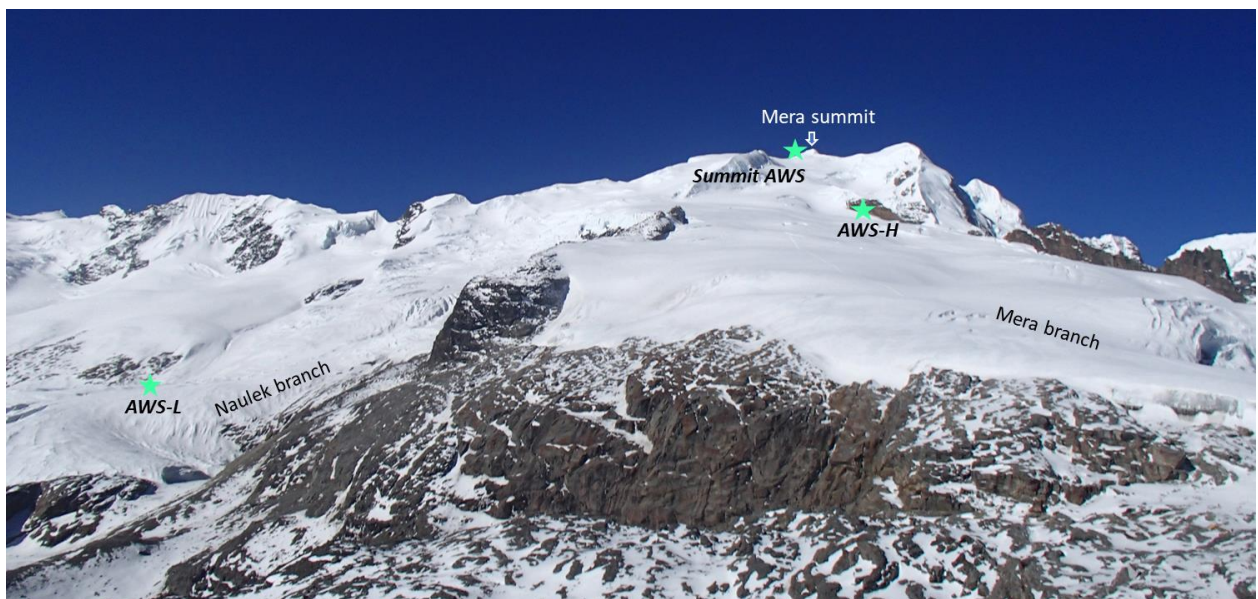


Figure 3.2. View of Mera Glacier from Mera La AWS, photo taken during April 2019 fieldwork. Photo by A. Khadka.

3.1.1 Mass balance data of Mera Glacier

The mass balance of Mera Glacier has been continuously monitored since 2007, at least once a year in the fall, yielding one of the longest mass balance continuous field-based series in the Nepal Himalayas (Wagnon et al., 2021). Glaciological mass balance measurements are obtained based on a network of ~16 stakes installed in the ablation area and five accumulation sites. This glacier-wide mass balance series has been calibrated with the 2012-2018 geodetic mass balance (Figure 3.3). From 2007 to 2023, the mean corrected glacier-wide mass balance was -0.42 ± 0.22 m w.e. a^{-1} , with only four positive mass balance years out of sixteen. During our study period of 2016-2020, mass balance years were consistently negative, with a mean glacier-wide value of -0.74 ± 0.18 m w.e. a^{-1} . The most negative year was 2017/18 (-0.92 ± 0.16 m w.e.) and the least negative was 2019/20 (-0.49 ± 0.22 m w.e.; Table 3.1, Figure 3.3). Between 2007 and 2021, the glacier lost approximately 10 % of its surface area (Wagnon et al., 2021).

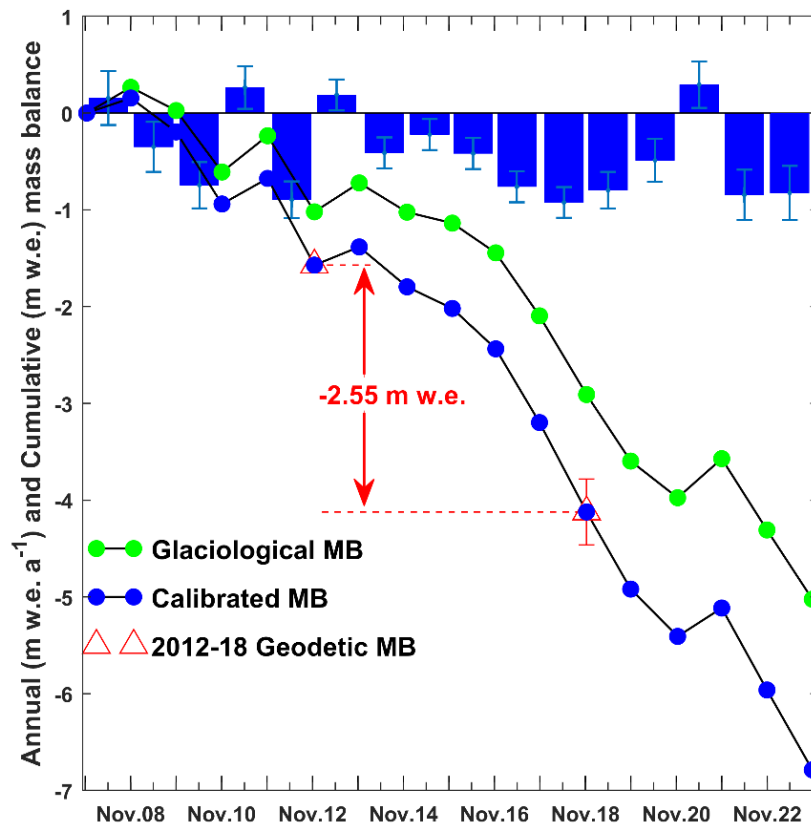


Figure 3.3. Annual and Cumulative mass balance of Mera Glacier since 2007 (adapted from Fig. 5 of Wagnon et al. (2021), credit: P. Wagnon)

Table 3.1 presents the calibrated annual and mean mass balances ($B_{a,cal}$ in m w.e. a^{-1}) from 2007 to 2023, along with ELA, accumulation area ratio (AAR), and mass balance gradients (db/dz in m w.e. $(100\text{ m})^{-1}a^{-1}$) in both Naulek and Mera branches.

Table 3.1. Glacier-wide annual mass balance (calibrated with the 2012-18 geodetic mass balance) along with equilibrium line altitude (ELA), accumulation area ratio (AAR), and mass balance gradients (db/dz) in both Naulek and Mera branches of Mera Glacier since 2007 (adapted from table 1 from Wagnon et al. 2021)

Years	07/08	08/09	09/10	10/11	11/12	12/13	13/14	14/15	15/16	16/17	17/18	18/19	19/20	20/21	21/22	22/23	Mean	SD
B_{total} (m w.e. a ⁻¹)	0.15	-0.35	-0.75	0.26	-0.9	0.19	-0.41	-0.22	-0.42	-0.76	-0.92	-0.8	-0.49	0.29	-0.85	-0.83	-0.42	0.44
ELA (m)	5450	5611	5704	5356	5836	5492	5581	5453	5607	5748	5796	5782	5684	5330	5817	5728	5623	165
AAR	0.67	0.44	0.35	0.81	0.23	0.62	0.50	0.69	0.48	0.33	0.28	0.29	0.40	0.86	0.27	0.35	0.47	0.20
db/dz_{Mera} (m w.e.(100 m) ⁻¹ a ⁻¹)	0.48	0.41	0.46	0.58	0.32	0.45 ^a	0.45 ^a	0.53	0.51	0.4	0.4	0.4	0.39	0.70	0.35	0.53	0.46	0.10
db/dz_{Naulek} (m w.e.(100 m) ⁻¹ a ⁻¹)	0.97	0.74	0.97	0.87 ^a	0.72	0.87 ^a	0.87 ^a	0.95	0.87 ^a	0.87	0.13							

^a Applying a mean gradient because not enough stakes were visible

3.1.2 Meteorological data

AWS data

Various AWSs have been installed in different locations in the upper Dudh Koshi basin since 2010 as part of the GLACIOCLIM monitoring network (Figure 3.1, Figure 3.4, and Figure 3.5). Most of them are still operational, but one from the Mera Summit was removed in 2016 due to technical issues. These stations measure meteorological data every 30 to 60 seconds, which is then averaged and/or recorded every 30 minutes using Campbell Scientific dataloggers. The AWSs are inspected and serviced once or twice a year during fieldwork in the region. However, the station sometimes fails due to issues such as battery failure caused by snow covering solar panels, AWS tilting or collapsing on glaciers, or snow or water entering sensors, resulting in several data gaps.



Figure 3.4. Photos of Pheriche, Pyramid, and Khare precipitation gauges (Geonor), along with the date of the photo taken.

When collecting field data, it is important to ensure that it undergoes careful checking and quality control. Procedures for identifying gaps, correcting raw data, and quality control are described in the supplementary section of Khadka et al. (2022).

Two precipitation gauges (**Pyramid Geonor**, at 5035 m a.s.l. and **Pheriche Geonor** at 4260 m a.s.l.) were installed in December 2012 in the Khumbu valley. **Khare Geonor** (4888 m a.s.l.) is the only precipitation measurement near Mera Glacier, and was installed in November 2016 (Figure 3.1 and 3.4). These gauges have been providing continuous data since installation and

are regularly maintained once or twice a year. The data are corrected for undercatch based on methods by Førlund et al. (1996) and Lejeune et al. (2007) depending on wind speed and precipitation phase. The correction procedure is described in the supplementary section of Khadka et al. (2022).

Changri Nup AWS (5360 m a.s.l.) was installed in the debris-covered ablation zone of the west Changri Nup Glacier in November 2010 (Figure 3.5). Four AWSs have been installed around Mera Glacier since 2012. **AWS-L (Naulek; 5360 m a.s.l.,** named AWS-L in Chapter 5) was the first AWS installed on Mera Glacier, on the flat, clean ice surface of the Naulek branch. **Mera La AWS** (5350 m a.s.l.) is located near Mera base camp on a rocky ridge. **AWS-H** (high camp AWS: 5770 m a.s.l.) and **Mera Summit AWS** (6352 m a.s.l.) are located in the accumulation zone of Mera Glacier. Mera La has high-quality data with no gaps, but Mera Summit and AWS-H have many gaps, especially after heavy snowfalls, mostly during the monsoon. This station has been collecting data but has several data gaps (5-15%) due to occasional battery and sensor failures. The details of each AWS, including sensors and data period, are in chapters 4 and 5 and supplementary sections.

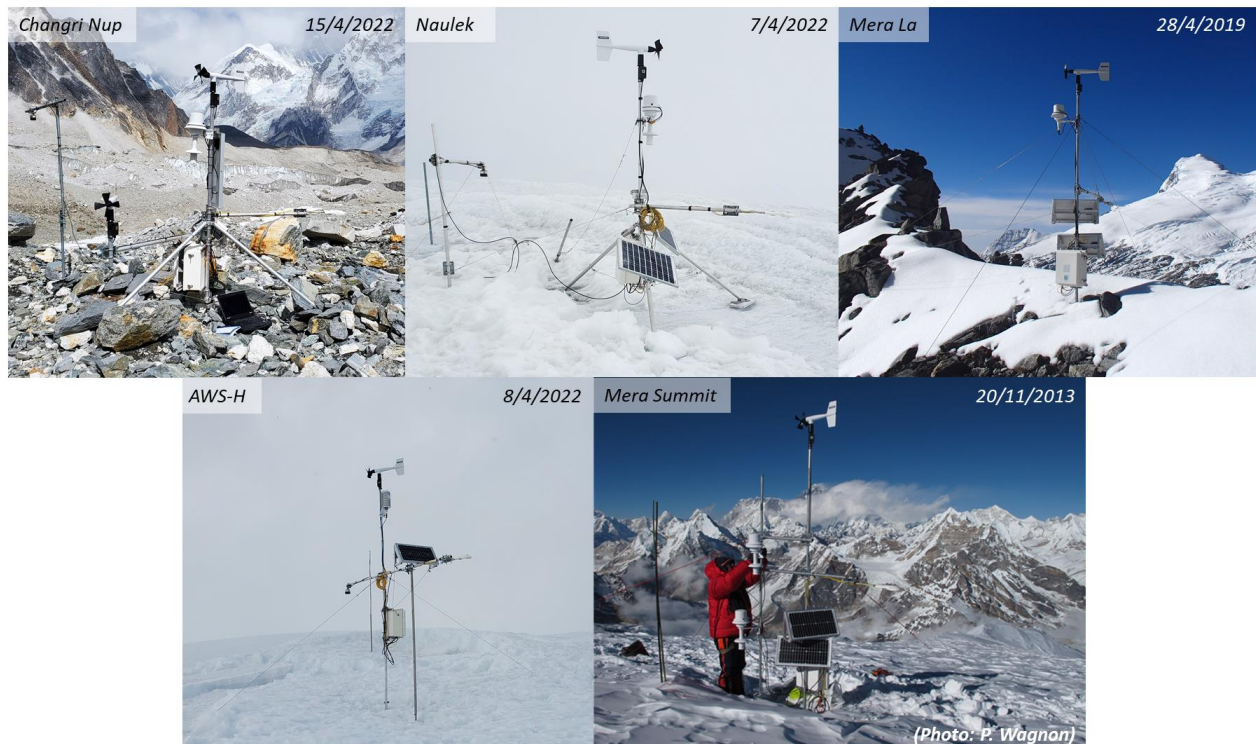


Figure 3.5. Photos of different AWSs installed on different surfaces on the upper Dudh Koshi basin.

Reanalysis data

In this study, we evaluated the different meteorological variables from two reanalysis data sets, **ERA5 Land** and **HARv2** (High Asia Refined Reanalysis volume 2), developed using in-situ measurements. ERA5 Land is a fifth-generation higher-resolution (~ 9 km) data set that includes the land component of the ECMWF ERA5 climate reanalysis. It provides comprehensive information on various land surface parameters, such as soil moisture, temperature, radiations, and many meteorological variables with global coverage (Muñoz-Sabater et al., 2021). The HARv2 dataset is a significant advancement in understanding the atmospheric dynamics and climate characteristics of the High Asia region. It is a product of ECMWF ERA5 downscaled using WRF at a 10 km resolution (Wang et al., 2020). These two are the higher-resolution datasets, which include many atmospheric variables besides temperature and precipitation. They provide valuable insights into land processes and climate, climate trends, and are very useful for regional cryospheric studies (Muñoz-Sabater et al., 2021; Maussion et al., 2014).

This thesis utilizes data from three precipitation gauges (Geonor) and five meteorological stations described above. All data, except for AWS-H, were used to analyze the meteorological conditions of the region and to evaluate reanalysis data in Chapter 4. Additionally, data from AWS-L, Mera La AWS, AWS-H, Khare Geonor, and mass balance data of Mera Glacier were used for the sensitivity analysis of the glacier.

Chapter 4

4 Evaluation of ERA5-Land and HARv2 reanalysis data at high elevation in the upper Dudh Koshi basin (Everest region, Nepal)

After

Khadka, A., Wagon, P., Brun, F., Shrestha, D., Lejeune, Y., & Arnaud, Y. (2022). Evaluation of ERA5-Land and HARv2 reanalysis data at high elevation in the upper Dudh Koshi basin (Everest region, Nepal). Journal of Applied Meteorology and Climatology, 61(8), 931–954. <https://doi.org/10.1175/jamc-d-21-0091.1>

4.1 A short introduction

The ultimate goal of this PhD was to conduct mass balance sensitivity analysis of the Mera glacier and reconstruct the mass balance using the energy balance model. For the energy balance model, high-quality meteorological data sets are required to understand the physical processes on the glacier surface and subsurfaces. In the Himalayas, in-situ data collection is challenging due to the complex topography and remoteness. There are gaps in the data collected due to infrequent maintenance and failure of the AWS. The alternative to this problem is the high-resolution reanalysis data sets. However, the reanalysis data sets in the Himalayas are rarely evaluated with observations, which is very important for sensitive studies like glacier surface energy and mass balance calculations. Taking advantage of data recorded at the two precipitation gauges and five AWSs installed in the upper Dudh Koshi basin by IRD and partners since 2010, this chapter highlights the

- meteorological condition in the upper Dudh Koshi basin, and
- comparison of two high-quality reanalysis data sets and in-situ measurements.

Six different meteorological variables are evaluated with three different classical metrics. The evaluation is carried out on mean daily, seasonal, and annual scales. Overall, temperature is found to be in very good agreement with observations, whereas precipitation from both data sets has high difference with the observations. Also, the HARv2 data sets are better for wind speed than those of the ERA5 Land. Overall, it is very important to know this type of information before using the reanalysis data in very specific studies related to glaciers.

4.2 Abstract

We present a multi-site evaluation of meteorological variables in the Everest region (Nepal) from ERA5-Land and High Asian Refined Analysis, version 2 (HARv2), reanalyses in comparison with in-situ observations, using classical statistical metrics. Observation data have been collected since 2010 by seven meteorological stations located on or off glacier between 4260 and 6352 m MSL in the upper Dudh Koshi basin; 2-m air temperature, specific and relative humidities, wind speed, incoming shortwave and longwave radiations, and precipitation are considered successively. Overall, both gridded datasets are able to resolve the mesoscale atmospheric processes, with a slightly better performance for HARv2 than that for ERA5-Land, especially for wind speed. Because of the complex topography, they fail to reproduce local- to microscale processes captured at individual meteorological stations, especially for variables that have a large spatial variability, such as precipitation or wind speed. Air temperature is the variable that is best captured by reanalyses, as long as an appropriate elevational gradient of air temperature above ground, spatiotemporally variable and preferentially assessed by local observations, is used to extrapolate it vertically. A cold bias is still observed but attenuated over clean-ice glaciers. The atmospheric water content is well represented by both gridded datasets even though we observe a small humid bias, slightly more important for ERA5-Land than for HARv2, and a spectacular overestimation of precipitation during the monsoon. The agreement between reanalyzed and observed shortwave and longwave incoming radiations depends on the elevation difference between the station site and the reanalysis grid cell. The seasonality of wind speed is only captured by HARv2. The two gridded datasets ERA5-Land and HARv2 are applicable for glacier mass and energy balance studies, as long as either statistical or dynamical downscaling techniques are used to resolve the scale mismatch between coarse mesoscale grids and fine-scale grids or individual sites.

keywords: Asia; Complex terrain; Glaciers; Automatic weather stations; Surface observations; Statistics; Reanalysis data; Mountain meteorology

4.3 Introduction

High-Mountain Asia (HMA), which comprises the Tibetan Plateau and its surrounding mountain ranges is referred to as the water tower of Asia. Cryosphere, i.e. snow, ice and permafrost, contributes to water storage in this region (Immerzeel et al., 2010). Observed and projected changes in the cryosphere will affect the magnitude and timing of streamflow, more sensitively upstream with large socio-economic impacts (Lutz et al., 2014; Pritchard, 2019; Bolch et al., 2019; Immerzeel et al., 2020).

HMA contains the largest concentration of glacier ice outside of the polar regions, with nearly 100,000 km² of glacierized area (Pfeffer et al. 2014). Glaciers have been shrinking at least since the 1970s except for parts of Karakoram, eastern Pamir and western Kunlun (e.g., Bolch et al., 2019; Berthier and Brun, 2019). The sea level rise contribution from High-Mountain Asia glacier mass loss since 2000 is up to $\sim 0.05 \pm 0.01$ mm sea level equivalent yr⁻¹ (Brun et al., 2017; Shean et al., 2020). The ice loss rates are the greatest across Nyainqentanglha, the Himalayas, and Tien Shan (Shean et al., 2020). Even if global warming is constrained to the most ambitious target of 1.5°C (2015 Paris agreement), more than 30% of HMA glacier ice will likely disappear by the end of this century (Kraaijenbrink et al. 2017; Bolch et al. 2019).

In the central Himalaya, the rate of mass loss is proportionally high (Shean et al., 2020). Several field-based glaciological studies in Nepal show negative mass balance years, especially during the last 5-10 years (e.g., Sherpa et al., 2017; Sunako et al., 2019; Stumm et al., 2021). Glacier mass changes result from climatic forcing and from the mass-balance sensitivity to meteorological variables such as air temperature or precipitation (Sakai and Fujita, 2017). To examine the relationship between mass balance and climate, long-term high-quality meteorological datasets are required. In the upper Dudh Koshi basin, our region of interest, the first meteorological data ever recorded come from the historical mountaineering expeditions to Everest, back in the 1950s (Pugh 1954), but continuous and systematic records were not initiated before the installation of Pyramid, at the beginning of the 1990s (Salerno et al., 2015). Since 2010, a network of Automatic Weather Stations (AWSs) was installed and has been operating in the upper Dudh Koshi basin, with a focus on glacier areas and high elevation (>4260 m a.s.l.) (Shea et al., 2015a; Sherpa et al., 2017). The data from these AWSs contributed to better understand the glacier behavior locally (Sherpa et al., 2017), but they provide very local information and consequently cannot be used to analyze regional glacier evolution.

Climate reanalyses provide alternative data for climate and glacier studies, especially in regions where in-situ data are scarce and discontinuous. The European Centre For Medium-range Weather Forecasts (ECMWF) reanalysis product, ERA-Interim (Dee et al., 2011) has been used, for instance to reconstruct mass balance data in Nepal (Sunako et al., 2019). In 2017, ECMWF released a fifth generation of reanalysis product, ERA5 (Hersbach et al., 2020) with a higher spatial and temporal resolution than ERA-Interim. ERA5 reanalyses perform well in the Antarctic and Arctic regions (Wang et al., 2019a; Tetzner et al., 2019). The performance of ERA5 temperature and wind data has been significantly improved in comparison with ERA-Interim in the Antarctic Peninsula, where ERA5 data have been used to calibrate proxy records from ice cores (Tetzner et al., 2019). Similarly, in the Indus basin, ERA5 precipitation data are

highly correlated with APHRODITE (Highly-Resolved Observational Data Integration Towards Evaluation of the Water Resources) data (Baudouin et al., 2020). However, ERA5-Land (ERA5L), which is a reanalysis product derived by running the land component of ERA5 at increased resolution, is not well suited for permafrost studies because it overestimates soil temperature in high latitudes, and underestimates it in mid-low latitudes (Cao et al., 2020). Also, the High Asian Refined analysis version 2 (HARv2) is another recently published high-resolution dataset generated by dynamical downscaling of ERA5 reanalysis data (Wang et al., 2020b). Maussion et al. (2011, 2014) provided a first generation of HAR data and analyzed the precipitation seasonality and variability over the Tibetan Plateau and surrounding regions. They validated HAR precipitation data with both rain gauge observations unevenly distributed over the Tibetan Plateau, and satellite-based precipitation estimates from the Tropical Rainfall Measuring Mission. Based on their regional dataset, they proposed a classification of glaciers according to their accumulation regimes. Mölg et al. (2012, 2014) used this dataset and showed that the timing and amount of snowfall in the early ablation season (May-June) is a key process controlling the annual mass balance of glaciers on the southern Tibetan Plateau.

Because of the lack of long-term observation data, the use of high-resolution reanalysis data is promising in the Nepalese Himalayas, where in-situ data collection is challenging given the complex topography, remoteness, and data gaps caused by infrequent maintenance and failure of AWSs. Nevertheless, even though those reanalysis products have the best spatiotemporal resolution in the central Himalayas, ERA5L and HARv2 data have not been validated yet using available in-situ data from high-elevation AWSs located on and off glaciers although such products often need calibration.

In this study, we compare ERA5L and HARv2 reanalysis data with in-situ data from seven AWSs from different glacierized and unglacierized areas since 2010 in the upper Dudh Koshi basin, which are not assimilated in the reanalysis process of ERA5L and HARv2. The main focus of this study is to assess the performance of ERA5L and HARv2 reanalysis data at glacier elevations in the central Himalaya. We qualitatively discuss whether such data are reliable for glacier mass and energy balance studies and we discuss the relevance of substituting in-situ data, if not available, with reanalysis data for glaciological or hydrological modelling purposes.

4.4 Study site and climatology

The Nepalese Himalaya is under the influence of the Indian monsoon originating from the Bay of Bengal. In summer, large amounts of humid air travel north to northwest and trigger orographic precipitation (e.g., Bookhagen and Burbank, 2010; Perry et al., 2020). In the upper Dudh Koshi basin (Figure 4.1), approximately three quarters of the annual precipitation fall between June and September (Shea et al., 2015a; Sherpa et al., 2017; Perry et al., 2020). Following previous studies (e.g., Bonasoni et al., 2010), we divide the year into four seasons: winter (December-February), pre-monsoon (March-May), monsoon (June-September) and post-monsoon (October-November).

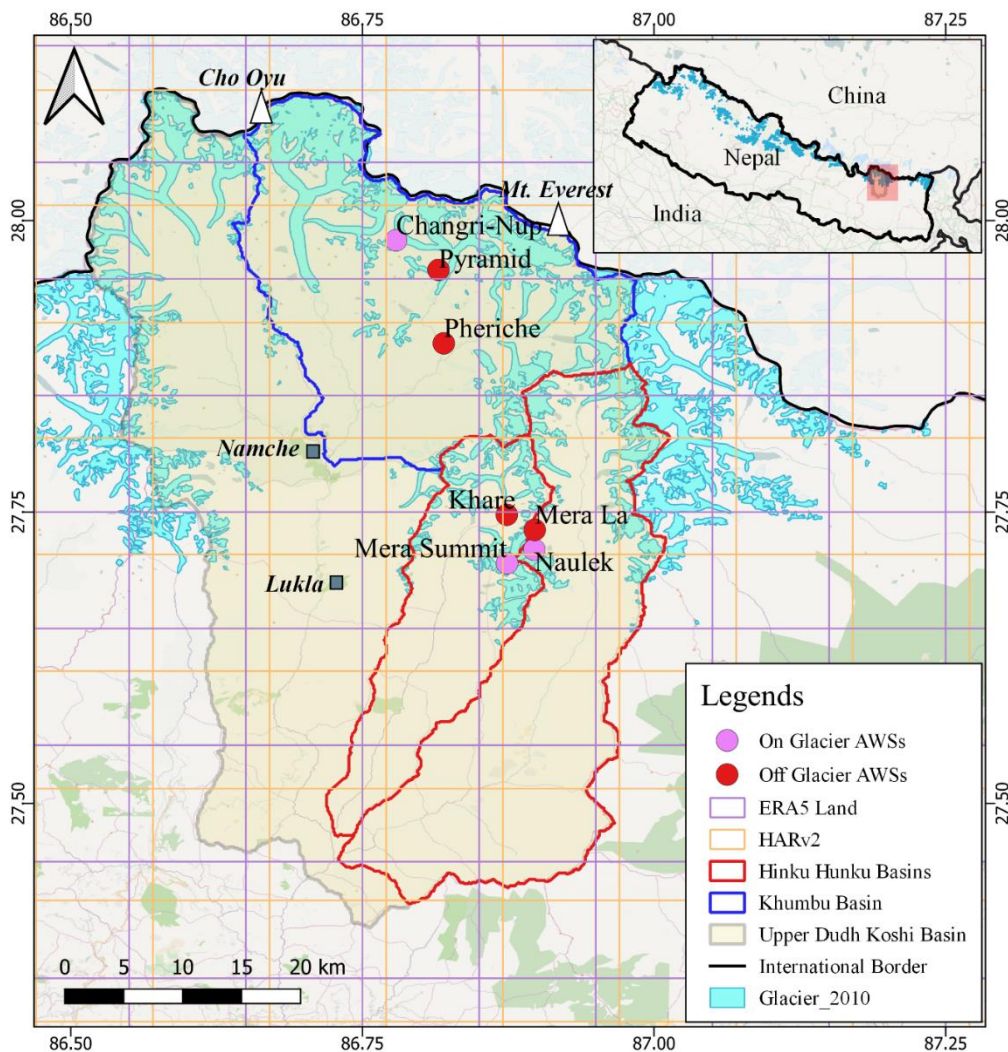


Figure 4.1. Map of the study area with the AWSs located on-glacier (pink dots) and off-glacier (red dots). The glaciers are represented in blue (ICIMOD inventory 2010), and the grids represent the reanalysis grid cells (ERA5L in purple, HARv2 in orange). The Dudh Koshi basin is also delineated (yellow shading and grey line) in the main map as well as in the inset.

4.5 Data and methods

4.5.1 Data

4.5.1.1 AWS data

Meteorological observations are collected at various AWSs off and on glaciers in the upper Dudh Koshi basin at elevations ranging from 4260 to 6352 m a.s.l. Precipitation data have been collected by all-weather raingauges (Geonor T-200B) at only three sites (Pyramid and Pheriche since December 2012; Khare since November 2016). They have been corrected for undercatch following the method by Førlund et al. (1996) and Lejeune et al. (2007) as a function of wind speed and precipitation phase (liquid or solid) depending on air temperature (section 4.10). This correction results in an approximately 20 % increase of the amount of precipitation originally measured by the gauge, and the error range is estimated to be $\pm 15\%$ (Sherpa et al., 2017). Records go back to October 2010 at Changri Nup site, which makes this dataset one of the longest at high elevation (5350 m a.s.l.) in Nepal (Figure 4.1, Table 4.1). Table 4.1 provides the range of accuracy of every sensor used on those AWSs, as specified by the manufacturer.

However, in such harsh environment, measurement errors may sometimes exceed this error range, even though all datasets have been quality controlled (cf. section 4.10, and AWS photos on Chapter 3). Temperature/humidity sensors are artificially ventilated (with an aspirated Atmos radiation shield, model 43502, maintaining a 5 m/s ventilation during daytime when clear sky), when installed over glacierized surfaces, except at Mera Summit. At this extremely high site, it is not possible to maintain artificial ventilation and the sensor is thus prone to over-heating when shortwave radiation is large and natural ventilation low. Consequently, observed air temperature at 6352 m a.s.l. is likely to be over-estimated when wind speed is low, mainly during the monsoon. There is no data at Mera Summit during the post-monsoon, because the AWS has been systematically buried by monsoonal snowfalls.

Table 4.1. AWS locations, measurements, data gaps, sensor types, heights and accuracy, data periods and morphological settings (T = air temperature, RH = relative humidity, u = wind speed, $SWin$ = shortwave incoming radiation, $LWin$ = longwave incoming radiation, P = total precipitation, P_a = atmospheric pressure).

	Elev (m MSL) AWS/ERA5L/HARv2	Lat; Lon (°)	Variables (% missing data)	Sensors (height; error range)	Data period	Morphological setting
Changri Nup	5360/5579 ^a /5217	27.983; 86.783	T and RH (5.9) $SWin$ (9.3) and $LWin$ (15.5) u (15.5)	Vaisala-HMP45C ^b (2 m; $\pm 0.2^\circ C$ and $\pm 2\%$) Kipp and Zonen CNR4 (1.2 m; $\pm 3\%$) Young 05103-5 (2.5 m; $\pm 0.3 \text{ m s}^{-1}$)	Nov 2010–Nov 2020 ^d	Flat debris-covered surface of the ablation zone of West Changri Nup Glacier
Mera La	5350/4662 ^a /5342	27.735; 86.898	T and RH (0) $SWin$ and $LWin$ (0) u (0) P_a (0)	Vaisala-HMP45C ^b (2.4 m; $\pm 0.2^\circ C$ and $\pm 2\%$) Kipp and Zonen CNR4 (1.2 m; $\pm 3\%$) Young 05103-5 (2.8 m; $\pm 0.3 \text{ m s}^{-1}$) CS100 (0.8 m; $\pm 1.5 \text{ hPa}$)	Nov 2013–Nov 2020	Rough rocky surface off glacier, near Mera Pass
Mera Summit	6352/4662 ^a /4637	27.706; 86.874	T and RH (10.9) $SWin$ (22.5) and $LWin$ (18.3) u (12.2) P_a (10.9)	Vaisala-HMP45C (1.6 m; $\pm 0.2^\circ C$ and $\pm 2\%$) Kipp and Zonen CNR4 (1.3 m; $\pm 3\%$) Young 05103-5 (3.2 m; $\pm 0.3 \text{ m s}^{-1}$) CS100 (0.8 m; $\pm 1.5 \text{ hPa}$)	Nov 2013–Jul 2016	5° north-facing sloppy surface of the accumulation zone of Mera Glacier, near the south summit
Naulek	5360/4662 ^a /5342	27.718; 86.897	T and RH (12.7) $SWin$ (19.3) and $LWin$ (19.4) u (20.2)	Vaisala-HMP45C ^b (1.5 m; $\pm 0.2^\circ C$ and $\pm 2\%$) Kipp and Zonen CNR4 (0.8 m; $\pm 3\%$) Young 05103-5 (2 m; $\pm 0.3 \text{ m s}^{-1}$)	Dec 2012–Nov 2020 ^d	Flat clean-ice surface of the ablation zone of Mera Glacier, on Naulek Branch
Pyramid	5035/5579 ^a /5217	27.958; 86.815	P (0)	GEONOR T-200BM (1.8 m; $\pm 15\%$) (shielded and corrected ^c)	Dec 2012–Nov 2019	Flat grassy surface, off glacier
Pheriche	4260/4922 ^a /4723	27.895; 86.820	P (0)	GEONOR T-200BM (1.8 m; $\pm 15\%$) (shielded and corrected ^c)	Dec 2012–Nov 2019	Flat grassy surface, off glacier
Khare	4888/4662 ^a /5342	27.748; 86.874	P (0)	GEONOR T-200BM (1.8 m; $\pm 15\%$) (shielded and corrected ^c)	Nov 2016–Dec 2020	Flat grassy surface, off glacier

^a Calculated by dividing the geopotential height by the standard acceleration due to gravity $g_0 = 9.81 \text{ m s}^{-2}$.

^b Artificially ventilated during daytime.

^c Precipitation data have been corrected for noise and undercatch (section 1 in the online supplemental material; Førlund et al. 1996).

^d For specific humidity q , the period is restricted to November 2013–November 2020, because P_a (Mera La) is used to compute q .

4.5.1.2 Reanalysis data

ERA5L (1981–2020) is an ECMWF reanalysis dataset providing a consistent view of the evolution of land variables at a higher resolution ($0.1^\circ \times 0.1^\circ$) than that of ERA5 ($0.25^\circ \times 0.25^\circ$). ERA5L has been produced by replaying the land component of the ECMWF ERA5 climate reanalysis (Hersbach et al., 2020). The High Asia Refined analysis (HAR, Maussion et al., 2011, 2014) is a regional atmospheric data set generated by dynamical downscaling using the Weather Research and Forecasting (WRF) model as regional climate model. HARv2 (1991–2020) is a refined version of HAR data with extended temporal and spatial coverage, using ERA5 as input data. It will be extended back to 1979 and continuously updated in the future. It provides gridded meteorological fields at 10-km resolution for the Tibetan Plateau and surroundings (Wang et al., 2020b).

4.5.2 Methods of evaluation

The two reanalyses (ERA5L and HARv2) provided from the nearest grid points to each AWS site are compared to AWS data to evaluate their performance. In the Khumbu area (Changri Nup, Pyramid and Pheriche sites), AWSs are located on two distinct cells of ERA5L and HARv2, whereas Mera AWSs are located on one single cell of ERA5L and two neighboring cells of HARv2 (Figure 4.1, Table 4.1). We compare the temporal variability of two-meter air temperature (T), relative humidity (RH), specific humidity (q), wind speed (u), shortwave ($SWin$) and longwave incoming radiations ($LWin$) and total precipitation (P) recorded at the different AWSs to that of ERA5L and HARv2 reanalysis data. We evaluate the performance of HARv2 and ERA5L reanalysis datasets until November 2020, over the exact same periods corresponding to the periods when in-situ data are available (Table 4.1). Consistently, the reanalysis data are converted into Nepal Standard time (+5:45 GMT) to match the observed data and are removed when there is a gap in the measurements (section 4.10).

Table 4.2. Statistical metrics used to compare ERA5L and HARv2 reanalysis variables with observed meteorological variables.

Statistical metrics	Formula ^a	Perfect value
Correlation coef (r)	$\frac{\sum_{i=1}^n (x_i - \bar{x})(y_i - \bar{y})}{\sqrt{\sum_{i=1}^n (x_i - \bar{x})^2} \sqrt{\sum_{i=1}^n (y_i - \bar{y})^2}}$	-1; 1
Bias	$(1/N) \sum_{i=1}^N (y_i - x_i)$	0
SD	$\sqrt{(1/N) \sum_{i=1}^N [(x_i - \bar{x}) - (y_i - \bar{y})]^2}$	0
RMSE	$\sqrt{(1/N) \sum_{i=1}^N (y_i - x_i)^2}$	0

Four different performance indicators are used to evaluate daily mean values, of the different reanalysis variables listed above: Pearson Correlation Coefficient (r), Bias (bias), Standard Deviation (SD), and Root Mean Square Error (RMSE) (Table 4.2). r is a measure of linear correlation between reanalysed and observed data, BIAS is the mean value of the difference between those two sets of data and is also called systematic error, SD is the dispersion of the error and RMSE is the standard deviation of the error (Tetzner et al. 2019; Rodrigo et al. 2013). Also, the sub-daily bias for different seasons and the mean seasonal bias are calculated using hourly data and daily data, respectively. In order to mitigate the artificial increase in r when comparing two series with a strong seasonal cycle, we also calculate series of anomalies defined in Suppl. Material (section 4.10).

To account for the elevation difference between reanalysis grid cells and AWS sites (Table 4.1), we apply various elevational gradients of air temperature above ground from Kattel et al. (2013) and Immerzeel et al. (2014). They are always shallower than the standard environmental lapse rate ($-6.5 \cdot 10^{-3} \text{ }^\circ\text{C m}^{-1}$). The mean seasonal elevational gradients, derived by Kattel et al. (2013) provide the best match with measurements at each AWS and are considered in this study. Reanalysed air temperature T_R at the elevation of the grid point z_{gp} is shifted to the elevation of the AWS, z_{AWS} , as:

$$T_R(z_{AWS}) = T_R(z_{gp}) + LR \times (z_{AWS} - z_{gp}) \quad (\text{in } ^\circ\text{C}) \quad (4.1)$$

Where LR is the elevational gradient of air temperature above ground from Table 3 of Kattel et al. (2013). LR varies between minimal values of $-5.9 \cdot 10^{-3} \text{ }^\circ\text{C m}^{-1}$ and $-5.3 \cdot 10^{-3} \text{ }^\circ\text{C m}^{-1}$ during the pre-monsoon and the post-monsoon, respectively and maximal values of $-4.7 \cdot 10^{-3} \text{ }^\circ\text{C m}^{-1}$ and $-5.1 \cdot 10^{-3} \text{ }^\circ\text{C m}^{-1}$ in winter and monsoon, respectively.

Table 4.3. Seasonal and annual mean values of meteorological variables observed at different AWS sites, except precipitation where seasonal or annual totals are reported.

	AWS site	Seasonal ^a				Annual mean ^a /total
		DJF	MAM	JJAS	ON	
T ($^\circ\text{C}$)	Changri Nup	-10.1	-5.5	2.0	-5.0	-3.9
	Mera La	-8.9	-5.3	1.8	-3.6	-3.5
	Mera Summit	-18.3	-12.8	-2.5	—	-11.2
	Naulek	-10.4	-6.8	0.3	-6.7	-5.4
RH (%)	Changri Nup	25	52	85	39	55
	Mera La	30	60	91	42	60
	Mera Summit	39	55	76	—	56
	Naulek	33	56	92	42	61
q (g kg^{-1})	Changri Nup	0.8	2.6	7.0	2.1	3.6
	Mera La	1.0	3.1	7.5	2.4	3.9
	Mera Summit	0.8	1.8	5.1	—	2.5
	Naulek	1.0	2.7	6.8	2.3	3.6
u (m s^{-1})	Changri Nup	2.9	2.1	1.2	2.3	2.1
	Mera La	3.0	2.0	1.1	1.9	2.0
	Mera Summit	6.5	4.8	2.5	—	4.6
	Naulek	4.6	3.0	1.4	3.3	2.6
SWin (W m^{-2})	Changri Nup	205	296	212	230	236
	Mera La	223	254	162	234	212
	Mera Summit	212	331	315	—	283
	Naulek	216	304	222	224	234
LWin (W m^{-2})	Changri Nup	173	223	303	199	233
	Mera La	182	234	308	209	243
	Mera Summit	148	191	272	—	203
	Naulek	175	219	300	197	240
P (mm w.e.)	Pyramid	39	108	413	32	591
	Pheriche	49	115	337	39	540
	Khare	78	142	570	28	818

^a Seasonal or annual mean values are discarded when data gaps exceed 33% of the time.

We calculate specific humidity both for the observation and reanalysis datasets. For the AWS measurements, air temperature (T , in $^\circ\text{C}$), relative humidity (RH , in %) and atmospheric pressure (P_a , in hPa) are used to calculate specific humidity (q , in g kg^{-1}) for Mera La and Mera Summit sites. At Naulek and Changri Nup AWSs where there is no barometer, we use the atmospheric pressure recorded at Mera La as all three sites are almost at the same elevation (less than 10 m of difference; Table 4.1), and horizontal gradients of atmospheric pressure are small over a few kilometers (Naulek and Changri Nup are 1.5 km and 30 km away from Mera La, respectively). At each AWS site, q is calculated as:

$$q = \frac{\varepsilon * e}{P_a - (1 - \varepsilon)e} * 10^{-3} \text{ (in g kg}^{-1}\text{)} \quad (4.2)$$

where ε , the ratio of molar mass of water to that of dry air, equals to 0.622. The actual vapour pressure (e , in hPa) is calculated from saturation vapour pressure (e_s , in hPa) and RH (in %) as:

$$e = \frac{RH * e_s}{100} \quad (\text{in hPa}) \quad (4.3)$$

$$\text{with } e_s = 6.1094 * \exp\left(\frac{17.625 * T}{243.04 + T}\right) \quad (\text{in hPa}) \quad (4.4)$$

For ERA5L, q is calculated from equations 4.2 to 4.4, with relative humidity (RH , in %) obtained following Alduchov and Eskridge (1996) using air temperature (T , in °C) and dew point temperature (T_d , in °C) from ERA5L:

$$RH = 100 * \left\{ \frac{\exp\left(\frac{17.625 * T_d}{243.04 + T_d}\right)}{\exp\left(\frac{17.625 * T}{243.04 + T}\right)} \right\} \quad (\text{in \%}) \quad (4.5)$$

For HARv2, q is obtained from the mixing ratio (r_h , in g kg⁻¹) as:

$$q = \frac{r_h}{(1+r_h)} \approx r_h \quad (\text{in g kg}^{-1}) \quad (4.6)$$

To convert the wind fields obtained from the reanalyses to those comparable to in-situ measurements, we use the following equation providing the total wind speed, u as a function of the zonal (U) and meridional (V) wind velocities:

$$u = \sqrt{U^2 + V^2} \quad (\text{in m s}^{-1}) \quad (4.7)$$

Additionally, to directly compare both datasets, a height adjustment is applied to convert the 10-m reanalysed total wind speed to the AWS measurement height, assuming neutral atmospheric conditions (e.g., Oke, 2002):

$$u_h = u_{10} \frac{\ln(z_h) - \ln(z_0)}{\ln(z_{10}) - \ln(z_0)} \quad (\text{in m}) \quad (4.8)$$

where u_{10} is the reanalysed wind speed at $z_{10} = 10$ m, u_h is the wind speed at height z_h and z_0 is the aerodynamic roughness length [assumed to be 10⁻³ m above snow/ice surfaces, 10⁻² m elsewhere i.e. debris cover or bare rocky ground (e.g., Miles et al., 2017)]. The assumptions of considering neutral conditions or using usual roughness lengths over AWS surfaces are questionable in mountain environment because such conditions are seldom encountered or roughness lengths may vary in space and time. Nevertheless, that is the best compromise we can find to adjust the reanalyzed wind speed to AWS heights. The resulting decrease in wind speed is weak (<23 % of the 10-m wind speed).

4.6 Results

4.6.1 Meteorology of the upper Dudh Koshi basin

Our dataset corroborates the course of the seasons already observed previously (Shea et al., 2015a; Sherpa et al., 2017). The winter is cold ($T < -8^{\circ}\text{C}$, above 5350 m a.s.l.) (Figure 4.2 and 4.3), very dry ($q < 1.0 \text{ g kg}^{-1}$ and $\text{RH} < 40\%$ at all sites) (Figure 4.4,4.5,S4.2,S4.3) and windy especially at high elevation ($u = 6.5 \text{ m s}^{-1}$ at 6352 m a.s.l.) (Figure 4.6 and 4.7). SWin and LWin have their minimum annual values (205 to 223 W m^{-2} and 148 to 182 W m^{-2} , respectively) (Figure 4.8 and 4.11), in relation with low solar angle and the low cloudiness of this high-altitude dry and cold atmosphere, respectively (Table 4.3). At all AWS sites, less than 10% of precipitation fall during this season (Table 4.3, Figure 4.12). At the beginning of March, as the atmosphere starts to slowly warm up, the moisture content increases, leading to progressively cloudier conditions and more frequent precipitation events until the monsoon starts in June. During the pre-monsoon, wind speed gradually decreases, and SWin is maximal (254 to 331 W m^{-2}), due to high solar angle and still frequently clear atmosphere, at least in the morning. The monsoon is warm (93% of the days have a positive daily air temperature at 5350 m a.s.l.), constantly humid ($q > 6.8 \text{ g kg}^{-1}$ and $\text{RH} > 85\%$ at 5350 m a.s.l.) and the wind speed remains low (u is close to 1 m s^{-1} at 5350 m a.s.l.). Permanently overcast conditions prevail reducing SWin to the benefit of LWin which reaches its maximal values ($\text{LWin} > 300 \text{ W m}^{-2}$ at 5350 m a.s.l.). It rains or snows 4 days out of 5. Daily precipitation exceeds 1 mm water equivalent (w.e.) approximately 2 days out of 3. It is noteworthy to mention that precipitation occurs mostly during the late afternoon and night (Perry et al. 2020). Suddenly, in less than one week usually at the end of September, the monsoon stops and conditions switch to the post-monsoon, warmer and slightly less dry but otherwise similar to winter, i.e., quasi-absence of precipitation and strengthening of western winds.

Table 4.4. Monsoonal/annual mean meteorological variables at Mera La and total precipitation at Pyramid, Pheriche and Khare. The annual values are calculated from 1st December of one year to 30th November of the following year. The mean value over the entire measurement period and the SD are also shown.

Year	2012–13	2013–14	2014–15	2015–16	2016–17	2017–18	2018–19	2019–20	Mean	SD
T ($^{\circ}\text{C}$)	—	1.4/–4.1	1.5/–3.8	1.7/–3.0	1.8/–3.3	2.0/–3.1	1.9/–3.9	2.3/–3.9	1.8/–3.5	0.3/0.5
RH (%)	—	91/59	89/60	93/59	92/61	92/60	90/61	93/63	91/60	1.4/1.6
q (g kg^{-1})	—	7.3/3.8	7.2/3.8	7.5/4.0	7.5/4.0	7.6/3.9	7.4/3.9	7.9/4.2	7.5/3.9	0.2/0.2
u (m s^{-1})	—	1.0/2.0	1.1/1.9	1.0/1.9	1.0/1.8	1.0/1.9	1.1/2.1	1.2/2.1	1.1/2.0	0.1/0.1
SWin (W m^{-2})	—	160/214	171/220	152/205	159/212	156/205	172/213	162/213	162/212	7.4/5.1
LWin (W m^{-2})	—	305/243	302/239	312/242	309/242	308/242	306/240	311/247	308/243	3.5/2.6
P_{Pyramid} (mm)	387/619	397/595	332/585	491/633	416/549	435/539	430/620	—	413/591	49/36
P_{Pheriche} (mm)	331/692	334/539	286/611	407/615	351/454	288/361	364/504	—	337/540	43/111
P_{Khare} (mm)	—	—	—	—	522/753	542/668	582/862	635/987	570/818	50/138

The meteorology at Changri Nup AWS located over the debris covered part of West Changri Nup Glacier, in the upper Khumbu valley is very similar to that of Mera La or Naulek AWSs, located over bare ground or over the debris-free ablation zone of Mera Glacier, respectively, in Hinku/Hunku valleys at the same elevation (~ 5350 m a.s.l.) (Figure 4.2 to 4.13; Table 4.3, and 4.4). This means that meteorological conditions are homogeneous in both valleys at glacier elevations, more than 30 km apart. The main difference comes from the total amount of precipitation, $\sim 30\%$ higher in upper Hinku than in upper Khumbu due to the orographic effect leading to a strong negative horizontal gradient of annual precipitation in south-to-north direction across the range (Sherpa et al., 2017)(Table 4.4). However, it is noteworthy to mention that at similar elevations, air temperature is on average 1.5°C lower and wind speed is 0.5 m s^{-1} higher over clean-ice glaciers (Naulek) than over debris covered glaciers (Changri Nup) or bare rocky ground (Mera La) (Table 4.3).

Over the seven-year (2012-2019) period, annual precipitation is 591 mm w.e. and 540 mm w.e. at Pyramid and Pheriche, respectively, with 70% and 62% of precipitation occurring during the monsoon (Table 4). Between 2016 and 2020, precipitation is higher at Khare with a mean annual total of 818 mm w.e., 70% of which falling during the monsoon (Table 4.4). Pheriche always receives less precipitation than Pyramid, during the monsoon, as well as during the year except for 2012-13 and 2014-15, two exceptional years, the former impacted by typhoon Phailin in mid-October 2013 (Shea et al., 2015a), and the latter with exceptional precipitation events in winter and pre-monsoon 2014-15 like ~ 120 km further West in the Langtang valley as already noticed by Fujita et al. (2017). If we discard the three years 2012-15 (characterized by exceptional non-monsoonal precipitation events in October 2013 and 2014 due to typhoons Phailin and Hudhud, respectively or in winter and spring 2015), three quarters of annual precipitation fall during the monsoon at Pyramid and Pheriche. The depletion in precipitation between the upper Hinku valley and the upper Khumbu valley at similar elevations i.e. Khare (4888 m a.s.l.) and Pyramid (5035 m a.s.l.) sites, respectively, is 28% at annual scale as well as during the monsoon (Table 4.4).

The continuous record of data at Mera La, Pyramid, Pheriche and Khare without any gaps since November 2013 (November 2016 for Khare) allows for a year-by-year comparison. 2015-16 and 2013-14 are the warmest ($T = -3.0^{\circ}\text{C}$) and coldest years ($T = -4.1^{\circ}\text{C}$), with 123 and 115 days of daily temperature above the freezing point at 5350 m a.s.l., respectively (Table 4.4). The 2020 monsoon is the warmest, with a mean temperature of 2.3°C , half a degree above the 2013-20 mean. During the warmest year 2015-16, SWin is the lowest at annual and

monsoon time scale (205 and 152 W m⁻², respectively) of the seven-year studied period, and the annual and monsoonal precipitation is the highest (633 and 491 mm w.e. at Pyramid, respectively). The other variables are not significantly different than those of the other years. 2017-18 is the driest year of the series with only 539 mm w.e at Pyramid (Table 4.4). Nevertheless, the 2015 monsoon is the driest of our seven-year studied period, with only 332 mm w.e. at Pyramid. 2014-15 is an unusual year with only 57% of the annual precipitation during the monsoon, due to exceptional events in winter and pre-monsoon 2014-15 (Fujita et al., 2017).

4.7 Comparison between reanalysis and observed data in the upper Dudh Koshi basin

Figure 4.2, 4.4, 4.6, 4.8, 4.10 and 4.12 show the mean annual cycle of daily in-situ and reanalysis data of air temperature, specific humidity, wind speed, incoming shortwave and longwave radiations, and precipitation (at monthly scale for this latter variable), respectively. The mean annual cycle is obtained by averaging, for each date of the year, the daily values of this given date of each year of the complete measurement period. Figure 4.3, 4.5, 4.7, 4.9, 4.11, and 4.13 show the mean daily cycle during each season. Table 4.5 provides the values of each statistical metrics, *r*, bias, SD and RMSE obtained by comparing in-situ and reanalysis data at daily time scale, over the total measuring period for each AWS. Table S4.1 is the counterpart of Table 4.5 for the series of anomalies. Table 4.6 gives the seasonal bias between reanalysis and observed data of those six meteorological variables.

4.7.1.1 Air temperature

Over the whole measuring period, reanalysed and observed daily temperatures are highly correlated ($r > 0.95$, $p < 0.001$; $r > 0.72$ for the anomalies, see section 4.10.3.b.i, Table S4.1) whichever sites or reanalysed data are considered (Table 4.5, Figure 4.2). Seasonal and daily cycles of temperature are well reproduced in both reanalysis datasets (Figure 4.3). Reanalysed temperatures are usually lower than in-situ data during non-monsoonal season (except Mera Summit). This cold bias is less important over debris-free glacier areas (Naulek and Mera Summit) than over debris-covered or rocky surfaces (Changri Nup and Mera La, respectively).

For the four seasons, the reanalyzed data are the closest to observations in monsoon and the farthest in winter, except at Naulek for ERA5L, where the reanalyzed data are the closest to observations during intermediate seasons (Table 4.6). Like for annual values, the differences between reanalysed and in-situ temperatures are larger over rocky surfaces (debris-covered glacier or bare ground), with a negative bias always exceeding 3.2°C in winter for ERA5L or HARv2, than over clean glacier surfaces. The bias over clean ice surfaces is mostly negative but does not exceed 1.8°C except for HARv2 in winter where it is positive (3.1°C at Mera Summit).

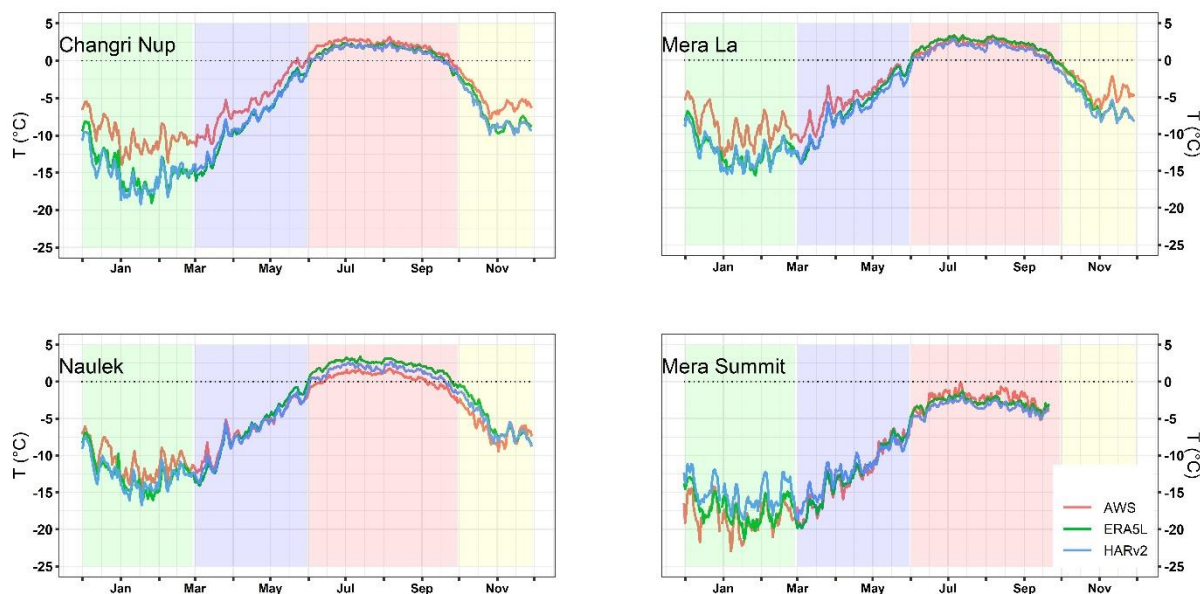


Figure 4.2. Mean annual cycle of daily air temperature from ERA5L, HARv2 and AWS at different sites. The referred periods used to calculate the mean annual cycle are reported with the AWS site name in Table 4.1. Shaded areas correspond to seasons: winter (green), pre-monsoon (blue), monsoon (red) and post-monsoon (yellow).

At sub-daily time scale (Figure 4.3), the differences between reanalysed and observed temperatures are very dependent on whether it is night or daytime. The bias is usually slightly lower at night than during the day (i.e., monsoon for both reanalysed data) but large biases, often negative, can still be observed at night like in winter for ERA5L and HARv2. It is noteworthy to mention that at night, the bias may be positive for HARv2 and at the same time negative for ERA5L like in winter at Mera Summit (Figure 4.3). We usually observe a mean daily cycle of the bias, with a minimum at midday especially for HARv2 data. When this bias is close to zero or negative at night, which is often observed, it is strongly negative at daytime. However, such mean daily cycle of the bias is not always observed, like for ERA5L in winter or pre-monsoon, where the bias passes through a maximum at daytime.

Considering all statistical metrics (Figure 4.2, 4.3, Table 4.5, 4.6, and S4.1), the performances of ERA5L and HARv2 reanalysis datasets are not significantly different, but large biases exceeding 4°C, mostly negative, are only encountered for HARv2 at any season and at all sites except Naulek. Both reanalysed datasets still tend to under-estimate air temperature at high elevation in the upper Dudh Koshi basin, especially over rocky surfaces.

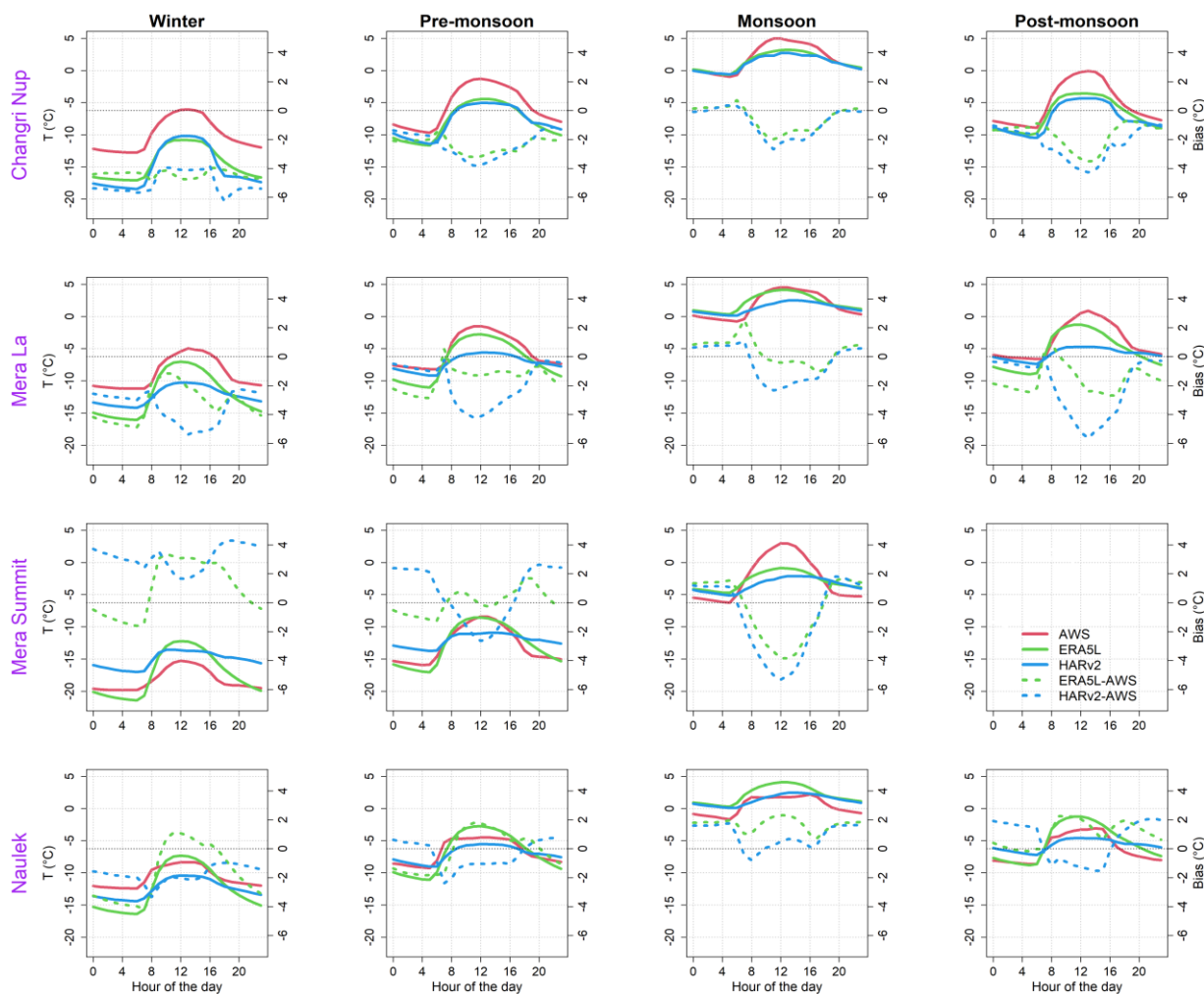


Figure 4.3. Mean diurnal cycle of 2-m reanalysed and observed air temperature (plain lines) and biases (dotted lines) at different AWS sites for different seasons.

4.7.1.2 Specific and relative Humidities

At annual time scale, both reanalysed and observed daily specific humidities are very well correlated ($r > 0.97$, $p < 0.001$; $r > 0.62$ for the anomalies) except at Mera Summit where the correlation is lower especially for the anomalies ($r = 0.92$ and 0.93 for ERA5L and HARv2, respectively, $p < 0.001$; $r = 0.27$ and 0.42 for the anomalies for ERA5L and HARv2, respectively) and the bias is large (bias $> 2.1 \text{ g kg}^{-1}$ for both reanalyses) (Table 4.5 and S4.1). The seasonal cycle of specific humidity is well reproduced by both reanalyses, with an almost perfect match at Changri Nup for both reanalyses and at Mera La for HARv2 (Figure 4.4, Table 4.5 and 4.6). Looking at the anomalies (section 4.10 3.b.ii. and 3.b.iii.), HARv2 performs slightly better than ERA5L, but both reanalysis products are not very good at Mera Summit, where they predict saturation during the monsoon, although this is not the case in reality (Figure S4.2), leading to an over-estimation of specific humidity (Figure 4.4). The bias, SD, and RMSE are higher at Mera Summit than at lower elevation AWSs mainly because of the difference in elevation and in turn in atmospheric pressure between the AWS and the grid cells of the respective reanalysis datasets. To a lesser extent, this is also the case at Mera La and Naulek sites for ERA5L data, because the grid cell altitude is approximately 700 m below that of the AWSs (Table 4.1), inducing a higher surface atmospheric pressure, and as a consequence higher reanalysed specific humidity compared to in-situ values.

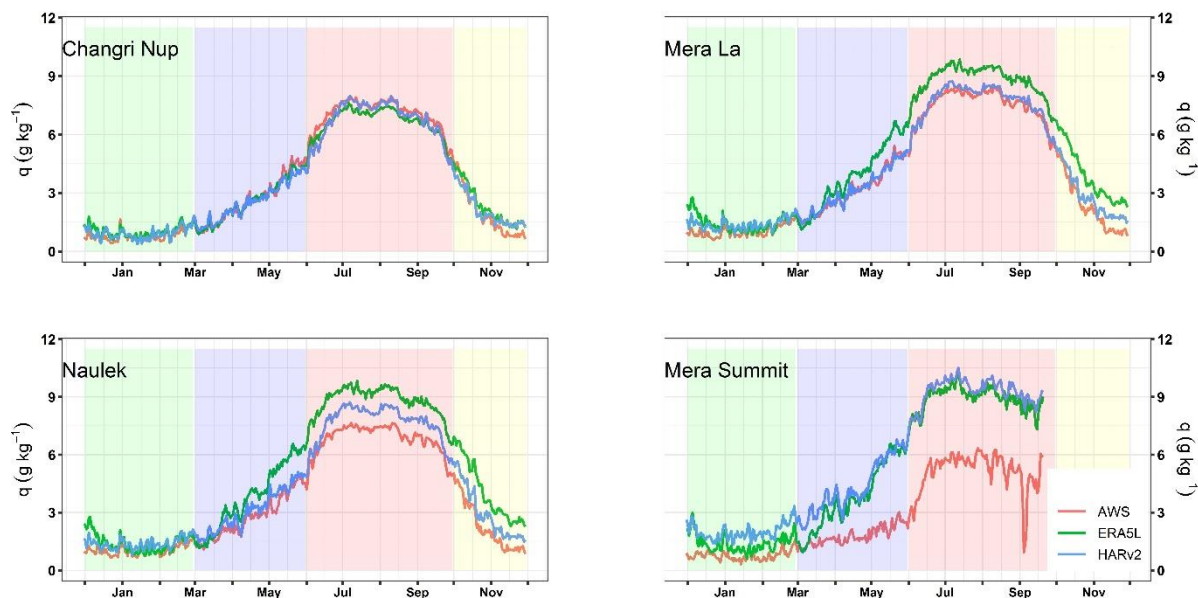


Figure 4.4. Mean annual cycle of daily specific humidity from ERA5L, HARv2 and AWS at different sites. The referred periods used to calculate the mean annual cycle are reported with the AWS site name in Table 4.1. Shaded areas correspond to seasons: winter (green), pre-monsoon (blue), monsoon (red) and post-monsoon (yellow).

At the sub-daily time scale, we observe a daily cycle of specific humidity, with most of the time a minimum value in the early morning, and a maximum in the early afternoon (Figure 4.5). This cycle is well reproduced by the two gridded datasets, sometimes almost perfectly like during pre-monsoon at Changri Nup. We often observe a slight positive humid bias usually a little more important in the afternoon, especially for ERA5L (Figure 4.5).

Considering all statistical metrics (Figure 4.4, 4.5, Table 4.5, and S4.1), we can conclude that the seasonal and the daily cycles of specific humidity are well represented by both gridded datasets, with still a large humid bias at Mera Summit. Overall, for specific humidity, HARv2 is slightly closer to the observations than ERA5L.

We performed a similar analysis for relative humidity (section 4.10.2). Relative humidity is slightly systematically over-estimated by reanalysis data, and better represented by HARv2 than ERA5L when considering the seasonal cycle of RH, and *vice versa* when looking at its daily cycle. Nevertheless, the agreement between observed and reanalysed relative humidity is still not very good at high elevation (Mera Summit), except in winter.

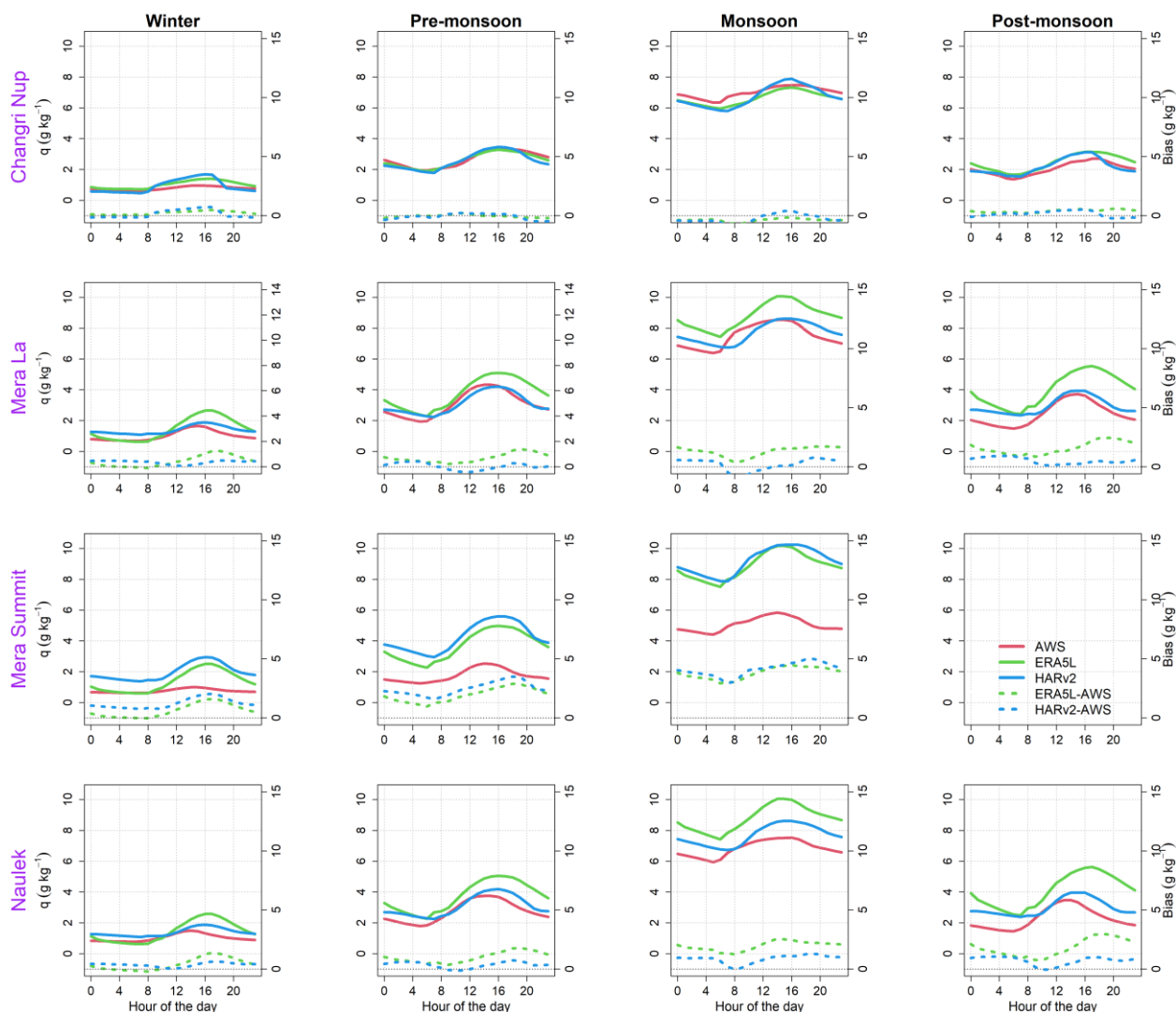


Figure 4.5. Mean diurnal cycle of reanalysed and observed specific humidity (plain lines) and biases (dotted lines) at different AWS sites for different seasons.

4.7.1.3 Wind Speed

Over the entire measuring period, the correlation between reanalysed and observed daily wind speed is very variable, from low to high ($r = 0.15$ to 0.82 , $p < 0.001$; $r = 0.13$ to 0.66 for the anomalies, see section 4.10.3.b.iv.) (Table 4.5 and S4.1). However, those correlations do not reflect the fact that both reanalyses do not represent well the local wind speed at all sites, because the wind speed is mainly controlled by local topography and surface conditions that cannot be accounted for correctly in reanalysis products.

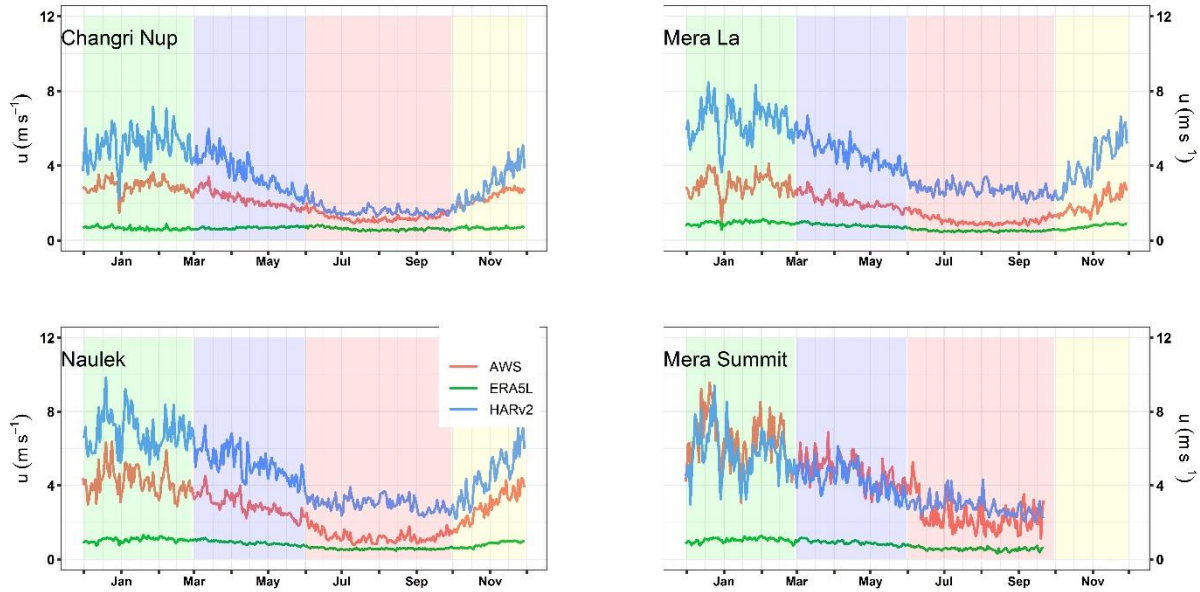


Figure 4.6. Mean annual cycle of daily wind speed from ERA5L, HARv2 and AWS at different sites. The referred periods used to calculate the mean annual cycle are reported with the AWS site name in Table 4.1.

Overall, HARv2 over-estimates wind speed by a factor of 1.5 to 3 for all sites located at ~5350 m a.s.l., but is really close to the AWS measurements at Mera Summit, a high-altitude open site where conditions are likely close to the free atmosphere. However, even at this very high site, the wind speed is a little over-estimated during the monsoon (bias = 0.5 m s^{-1}), and slightly under-estimated the rest of the year (Table 4.5 and 4.6, Figure 4.6).

On the other hand, ERA5L strongly under-estimates wind speed at all sites, except during the monsoon (bias ranging from -4.0 to -1.2 m s^{-1} ; Table 4.5). Moreover, ERA5L shows neither any pronounced seasonality like at Changri Nup, where wind velocity is almost the same year-round, nor any day-to-day variability, although this is often observed especially in winter at all sites (Figure 4.6). The only season when ERA5L performs fairly well is the monsoon, at all sites except Mera Summit, even though it still fails to reproduce the day-to-day variability (Table 4.6, Figure 4.6).

Both reanalysis datasets fail to reproduce the sub-daily cycle of wind speed. We usually do not observe any clear daily cycle of wind speed, except a slight decrease of wind speed in the morning or during the daytime, over clean-ice areas, more pronounced at very high elevation (Mera Summit). This daily cycle is not reproduced by reanalysis data at all, and HARv2 data even show an opposite cycle, with increasing wind velocity during the day (Figure 4.7).

In conclusion, none of the reanalysis datasets reproduce observed wind speed at high elevation in this region, partly because local wind speed is very dependent on local topography and surface conditions, but not only because the performance is barely enhanced on high altitude open sites. HARv2 reproduces well the seasonality of wind speed observed at AWSs but tends to over-estimate it, and completely fails to reproduce its observed daily cycle. ERA5L systematically under-estimates the wind speed at all elevations and does not even show any seasonality.

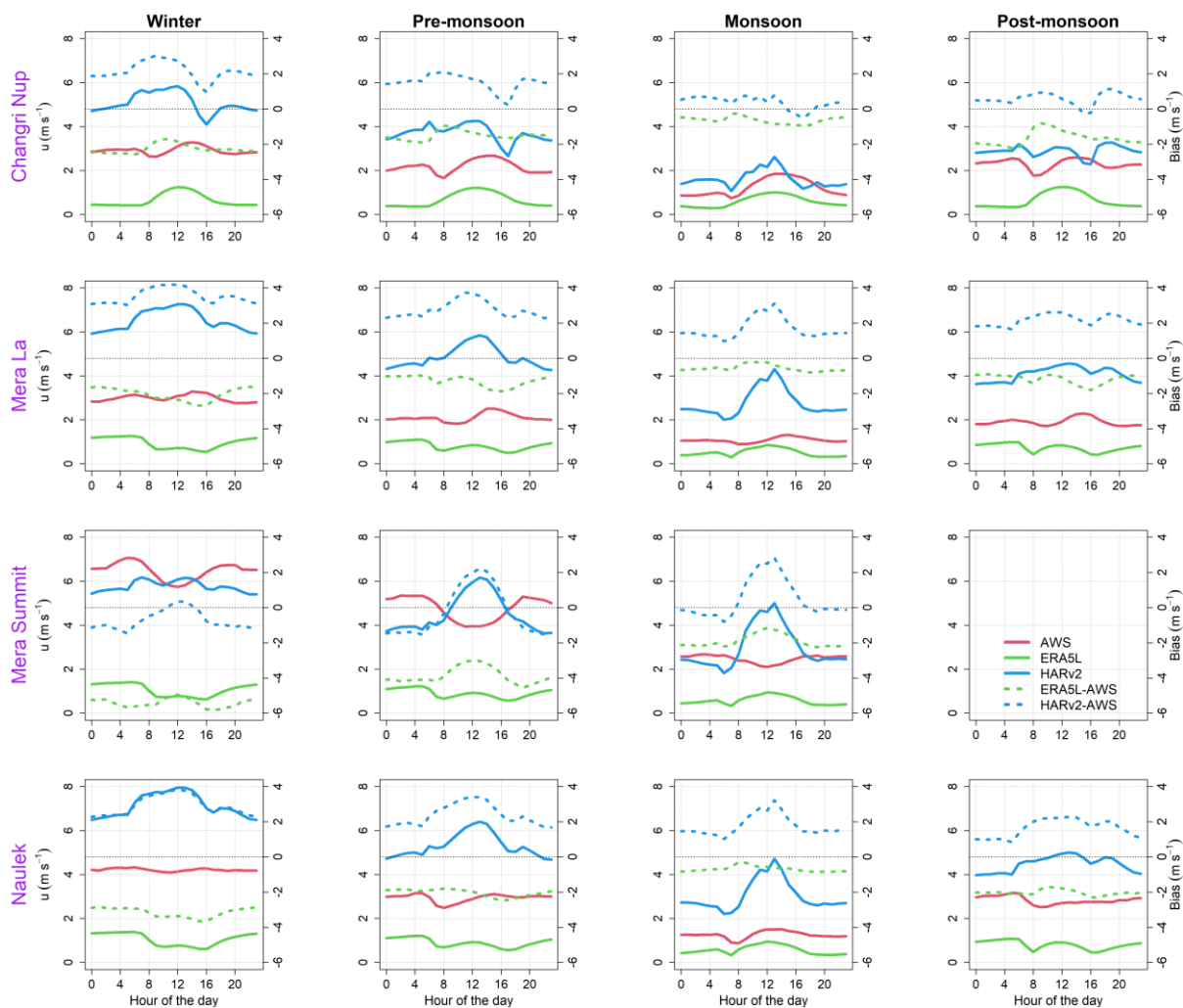


Figure 4.7. Mean diurnal cycle of reanalysed and observed wind speed (plain lines) and biases (dotted lines) at AWS sites for different seasons.

4.7.1.4 Incoming shortwave radiation

At annual time scale, reanalysed and observed daily values are fairly or well correlated, with r values higher than 0.62 and even often close to 0.77 (Table 4.5, except Mera Summit). Even when removing the seasonal cycle, r values stay high and close to 0.60 (section 4.10.3.b.v. and Table S4.1). However, these relatively high correlations should not hide the fact that the reanalyses do not represent the cloudiness very well, and, as a consequence, have degraded evaluation metrics during the monsoon. More precisely, during the winter and the post-monsoon, both reanalyzed incoming radiation have a negative bias not exceeding 16 W m^{-2} (winter) or 30 W m^{-2} (post-monsoon), for ERA5L at all sites (Table 4.5). However, as soon as it starts to be cloudy during the pre-monsoon and the monsoon, this bias tremendously increases especially for HARv2 data (Table 4.6, Figure 4.8). This bias is most of the time negative and exceeds sometimes 100 W m^{-2} during the monsoon.

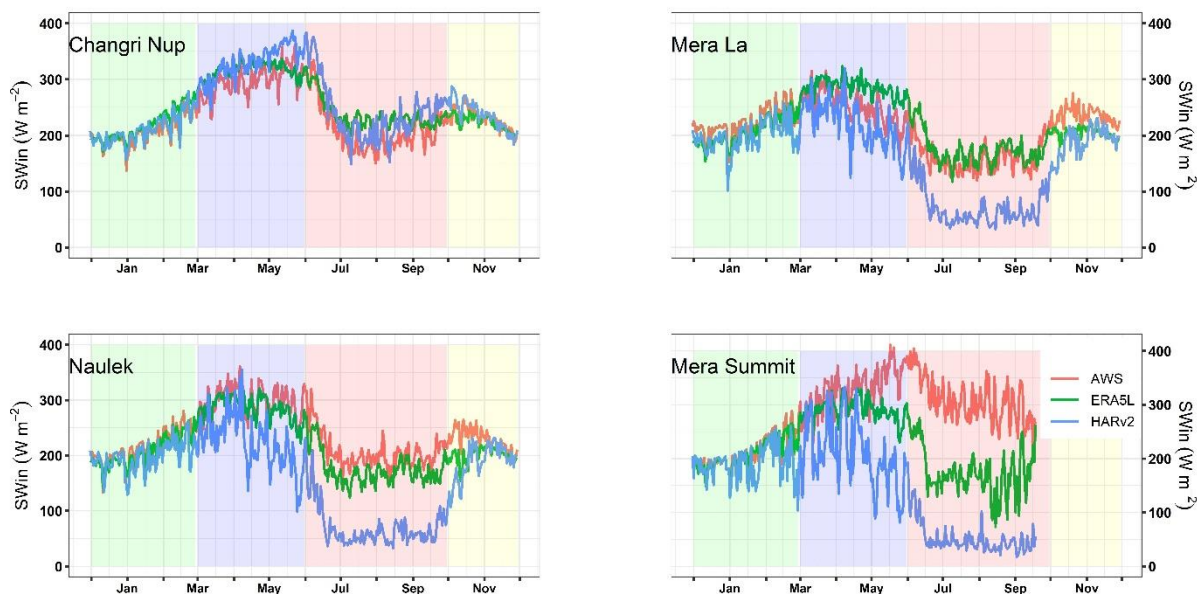


Figure 4.8. Mean annual cycle of daily SWin from ERA5L, HARv2 and AWS at different sites. The referred periods used to calculate the mean annual cycle are reported with the AWS site name in Table 4.1. Shaded areas correspond to seasons: winter (green), pre-monsoon (blue), monsoon (red) and post-monsoon (yellow).

Both reanalyses fail to reproduce incoming shortwave radiation at Mera Summit except in winter, although this site receives the highest solar radiation of all, due to its very high altitude and large sky view factor. During the monsoon, HARv2 and ERA5L under-estimate SWin by a factor of 6 and 2, respectively. This under-estimation is also mainly due to atmosphere attenuation given that the elevations of the reanalysis grid cells (4662 m a.s.l. for ERA5L, and 4637 m a.s.l. for HARv2) are much lower than the AWS site elevation (6352 m a.s.l. for Mera Summit) (Table 4.1). The only site where both reanalyses are close to the observations is Changri Nup, although HARv2 is less good than ERA5L, and this time over-estimates SWin during the pre-monsoon and monsoon (Table 4.5, 4.6, and Figure 4.8). Overall, the performance of ERA5L is slightly better than HARv2 at all sites, but still poor at very high altitude when there are clouds (pre-monsoon and monsoon). This performance strongly depends on the elevation difference between the observed site and the corresponding reanalysis grid cell.

The mean daily cycle of the bias is sometimes asymmetrical, negative in the morning and positive in the afternoon like in winter at all sites, or on Changri Nup, and Naulek, because those sites are oriented east, and in the shade early in the afternoon (14:00 to 15:00 local time) (Figure 4.9). The surrounding complex topography is responsible for some shading effects blocking direct sunlight at AWS sites, which explains why the bias between reanalysed and observed data can be variable during the day.

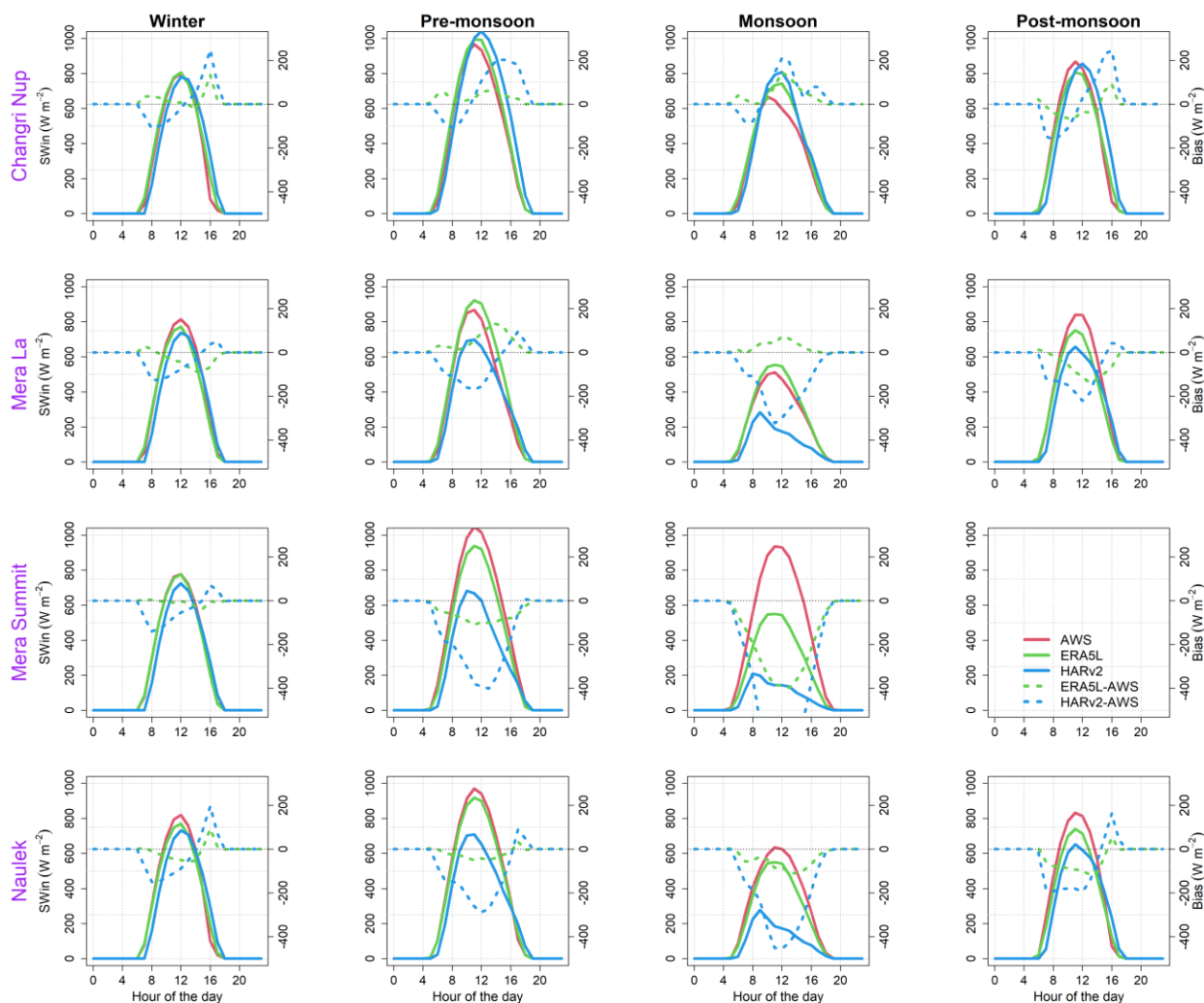


Figure 4.9. Mean diurnal cycle of reanalysed and observed incoming shortwave radiation (plain lines) and biases (dotted lines) at AWS sites for different seasons.

4.7.1.5 Incoming longwave radiation

Over the whole measuring period, daily reanalysed and observed values are extremely well correlated, with r higher than 0.89 ($p < 0.001$) for all sites (Table 4.5). When removing the seasonal cycle, this correlation stays high, with r values higher than 0.70 except at Mera Summit where r drops to 0.55 for ERA5L data (section 4.10.3.b.vi and Table S4.1). This is somehow expected because correlations for T and q are also high. Overall, ERA5L performs very well at all sites, as shown by the good performance of all statistical metrics (Table 4.5), with a mean bias usually not exceeding 16.1 W m^{-2} (except Mera Summit where the bias is as high as 40 W m^{-2}), negative at Changri Nup, positive elsewhere (Table 4.6, Figure 4.10). As for HARv2 data, the bias is most of the time more important, usually exceeding 20 W m^{-2} , positive at Mera Summit, negative elsewhere. Like for SWin, this bias strongly depends on the elevation difference between the observation site and the reanalysis grid cell. For instance, the positive bias at Mera Summit is mainly explained by elevation difference between the HARv2 or ERA5L grid point and the observation site located $\sim 1700 \text{ m}$ higher (Table 4.1).

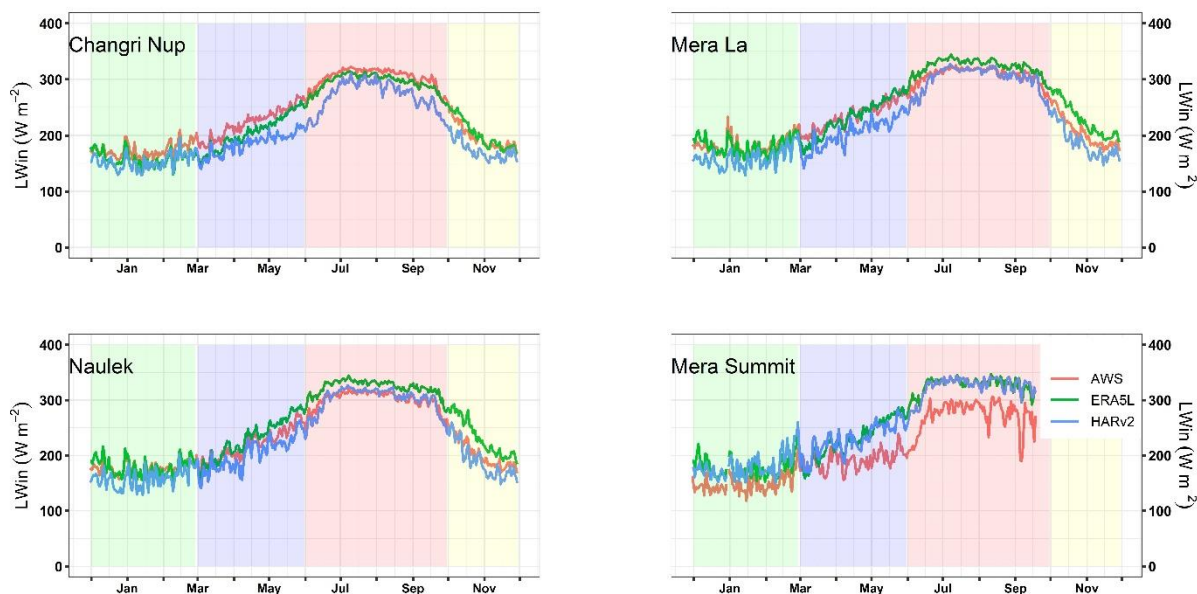


Figure 4.10. Mean annual cycle of daily LWin from ERA5L, HARv2 and AWS at different sites. The referred periods used to calculate the mean annual cycle are reported with the AWS site name in Table 4.1. Shaded areas correspond to seasons: winter (green), pre-monsoon (blue), monsoon (red) and post-monsoon (yellow).

The seasonality is also very well reproduced. The seasonal bias between ERA5L and observed LWin is reasonable, and in worst cases reaches 20 to 50 $W m^{-2}$, sometimes positive, sometimes negative, depending on the site and season, as well as the elevation difference between AWS and grid cell (Table 4.6, Figure 4.10). For HARv2 data, the bias is usually higher, positive at Mera Summit mainly due to this elevation difference, and negative elsewhere.

The daily cycle of reanalysed data agrees usually well with the observed daily cycle, still with a slight shift of the daily maximum observed at 13:00 LT, but occurring later for ERA5L, and earlier for HARv2 (Figure 4.11).

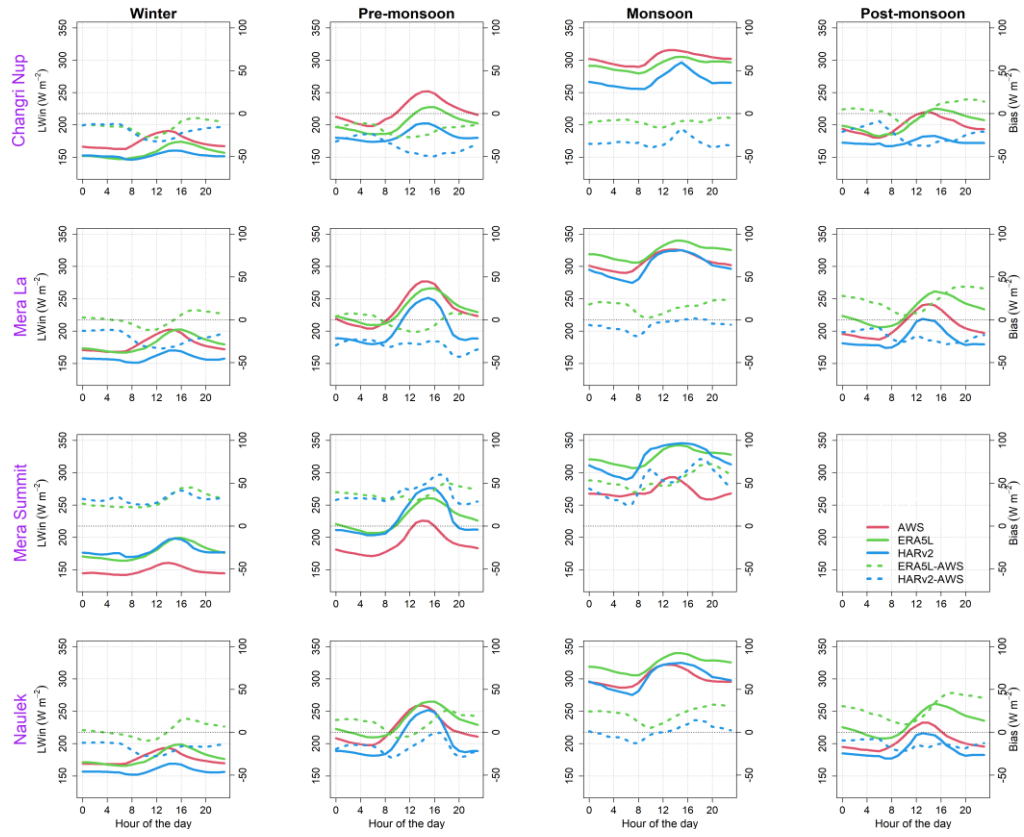


Figure 4.11. Mean diurnal cycle of reanalysed and observed incoming longwave radiation (plain lines) and biases (dotted lines) at AWS sites for different seasons.

Table 4.5. Values of each statistical metrics, r , Bias, SD, and RMSE obtained by comparing in-situ and reanalysed data at a daily time scale, over the total measuring period for each AWS. Measuring periods at each site are reported in Table 1.

Metric	ERA5L vs AWS				HARv2 vs AWS			
	r	Bias	SD	RMSE	r	Bias	SD	RMSE
Changri Nup								
T ($^{\circ}\text{C}$)	0.97	-2.2	2.2	3.1	0.96	-2.4	2.3	3.3
RH (%)	0.90	12.2	13.2	18.0	0.90	4.2	12.8	13.6
q (g kg^{-1})	0.98	0	0.4	0.6	0.98	-0.1	0.4	0.5
u (m s^{-1})	0.15	-1.4	0.9	1.7	0.64	1.1	1.6	2.0
SWin (W m^{-2})	0.76	15.9	46.9	49.6	0.78	21.1	51.1	55.3
LWin (W m^{-2})	0.95	-10.7	19.0	21.8	0.93	-30.1	22.9	37.8
Mera La								
T ($^{\circ}\text{C}$)	0.95	-1.3	2.1	2.4	0.97	-1.8	2.1	2.4
RH (%)	0.86	6.4	15.2	16.5	0.93	10.8	11.8	16.0
q (g kg^{-1})	0.97	1.0	0.8	1.3	0.99	0.2	0.5	0.5
u (m s^{-1})	0.69	-1.2	0.9	1.5	0.82	2.4	1.4	2.8
SWin (W m^{-2})	0.71	4.0	49.4	49.6	0.77	-52.3	63.6	82.3
LWin (W m^{-2})	0.94	7.9	22.1	23.3	0.94	-19.0	23.8	30.5
Mera Summit								
T ($^{\circ}\text{C}$)	0.97	0.3	1.8	1.8	0.97	1.0	2.5	2.5
RH (%)	0.59	7.7	22.1	23.4	0.69	15.2	18.3	23.6
q (g kg^{-1})	0.92	2.1	1.7	2.7	0.93	2.6	1.4	3.0
u (m s^{-1})	0.68	-4.0	2.3	4.6	0.80	-0.3	1.5	1.5
SWin (W m^{-2})	0.47	-59.8	72.7	94.1	-0.01	-134.6	123.7	182.8
LWin (W m^{-2})	0.89	40.5	30.5	50.7	0.92	39.6	26.8	47.9
Naulek								
T ($^{\circ}\text{C}$)	0.95	0.3	2.1	2.1	0.97	-0.2	1.7	1.7
RH (%)	0.87	5.0	14.4	15.0	0.91	10.3	12.1	15.9
q (g kg^{-1})	0.97	1.3	0.9	1.6	0.99	0.6	0.5	0.8
u (m s^{-1})	0.71	-1.8	1.4	2.3	0.81	2.1	1.3	2.5
SWin (W m^{-2})	0.73	-22.2	49.3	54.0	0.62	-79.3	77.6	110.9
LWin (W m^{-2})	0.95	16.1	19.9	25.6	0.96	-10.4	21.5	23.8
Pyramid								
P (mm day^{-1})	0.63	0.5	3.7	3.7	0.60	0.9	5.2	5.3
Pheriche								
P (mm day^{-1})	0.62	1.4	4.6	4.8	0.67	1.1	5.4	5.5
Khare								
P (mm day^{-1})	0.68	1.8	6.0	6.3	0.66	2.8	8.8	9.2

4.7.1.6 Precipitation

Over the 2012-19 measuring period, daily reanalysed and observed precipitation are well correlated ($r > 0.60$, $p < 0.001$) (Table 4.5). The seasonal distribution of precipitation is well reproduced. Indeed, observations show that over this 7-year period, 70 % of annual precipitation fall during the monsoon at Pyramid (62% at Pheriche), while ERA5L and HARv2 give 74 % and 65 %, respectively (76 % and 72 %, respectively, at Pheriche). Similarly, between 2016 and 2020, Khare AWS collected 28 % more precipitation than at Pyramid, 70% of which falling during the monsoon, while ERA5L and HARv2 give 63 % and 66 % more precipitation than at Pyramid, with 79 % and 75 % falling during the monsoon, respectively. However, both reanalyses strongly over-estimate precipitation at all sites, with a mean positive bias of 0.5 to 0.9 mm w.e. day^{-1} at Pyramid for ERA5L and HARv2, respectively, and twice to three times higher at Pheriche and Khare, respectively (Table 4.5). Overall, the annual totals of precipitation estimated by both reanalysis products exceed by a factor of 2 to 3.5 the observed precipitation, except for ERA5L at Pyramid where the over-estimation is only 30 %. Those biases are even more important during the monsoon and exceed 1.1 mm day^{-1} at Pyramid or are even larger at Pheriche or Khare with values reaching 6.5 mm day^{-1} for HARv2 (Table 4.6).

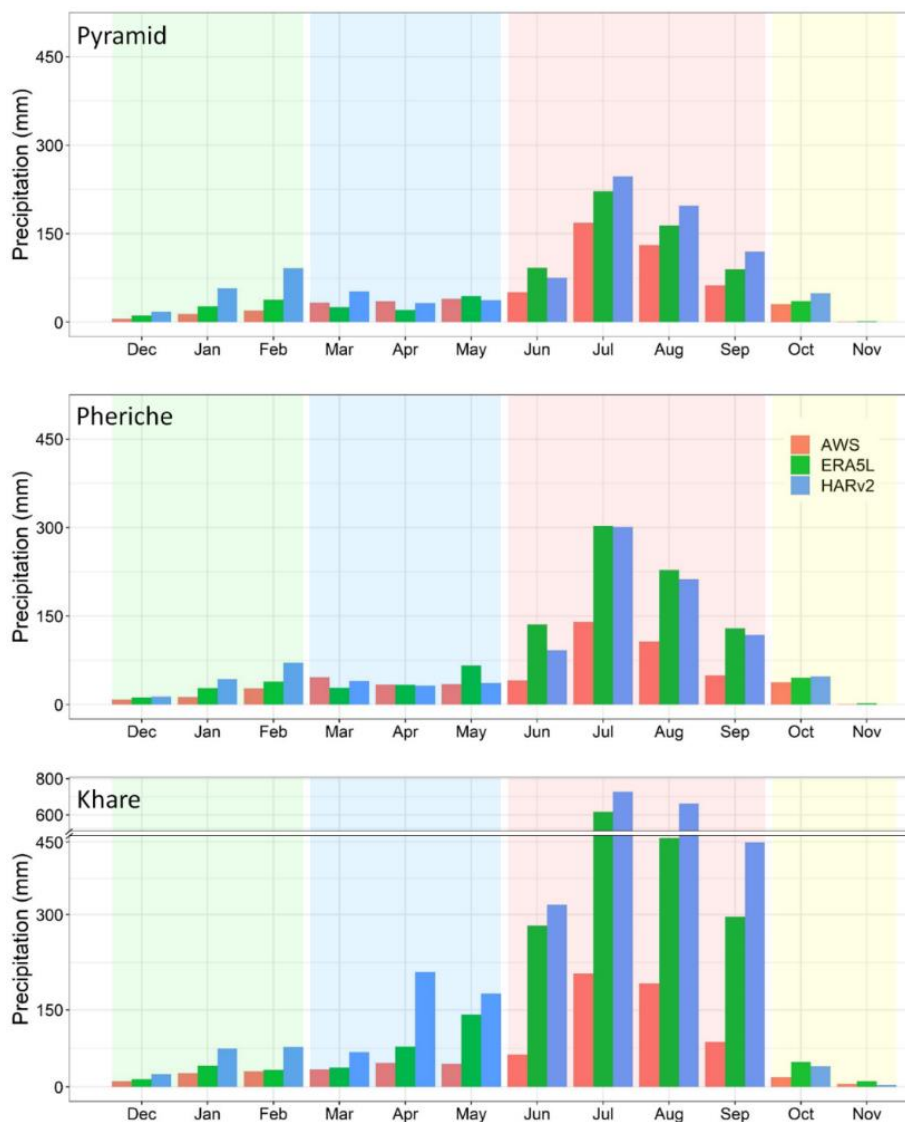


Figure 4.12. Mean monthly precipitation (mm w.e./month) at Pyramid, Pheriche and Khare sites. Monthly precipitation has been calculated over the period 2012-19 for Pyramid and Pheriche and 2016-20 for Khare. Note the broken scale of the y-axis in the lower panel, materialized by the double horizontal line.

The comparison at monthly time scale (Figure 4.12) confirms that reanalysis products tend to systematically over-estimate observed precipitation, but the pattern is very dependent on the site and on the season. At all sites, the agreement is good during the driest months, i.e. during the post-monsoon and in winter, with still an over-estimation of precipitation in January-February for HARv2 data (Table 4.6). During the pre-monsoon, in the driest part of our studied area (i.e. Pheriche and Pyramid), precipitation is well represented by both reanalysis products. At Khare, precipitation is over-estimated by both reanalyses, more importantly by HARv2, when the monsoon gets closer (April and May). Monsoon is the season when the positive bias is systematic and the highest, with monthly precipitation being often over-estimated by a factor of 1.6 to 3.8, especially in the wettest part of our studied area (Khare). Only ERA5L data represent fairly well precipitation recorded at Pyramid, with an over-estimation of only 37 % during the monsoon.

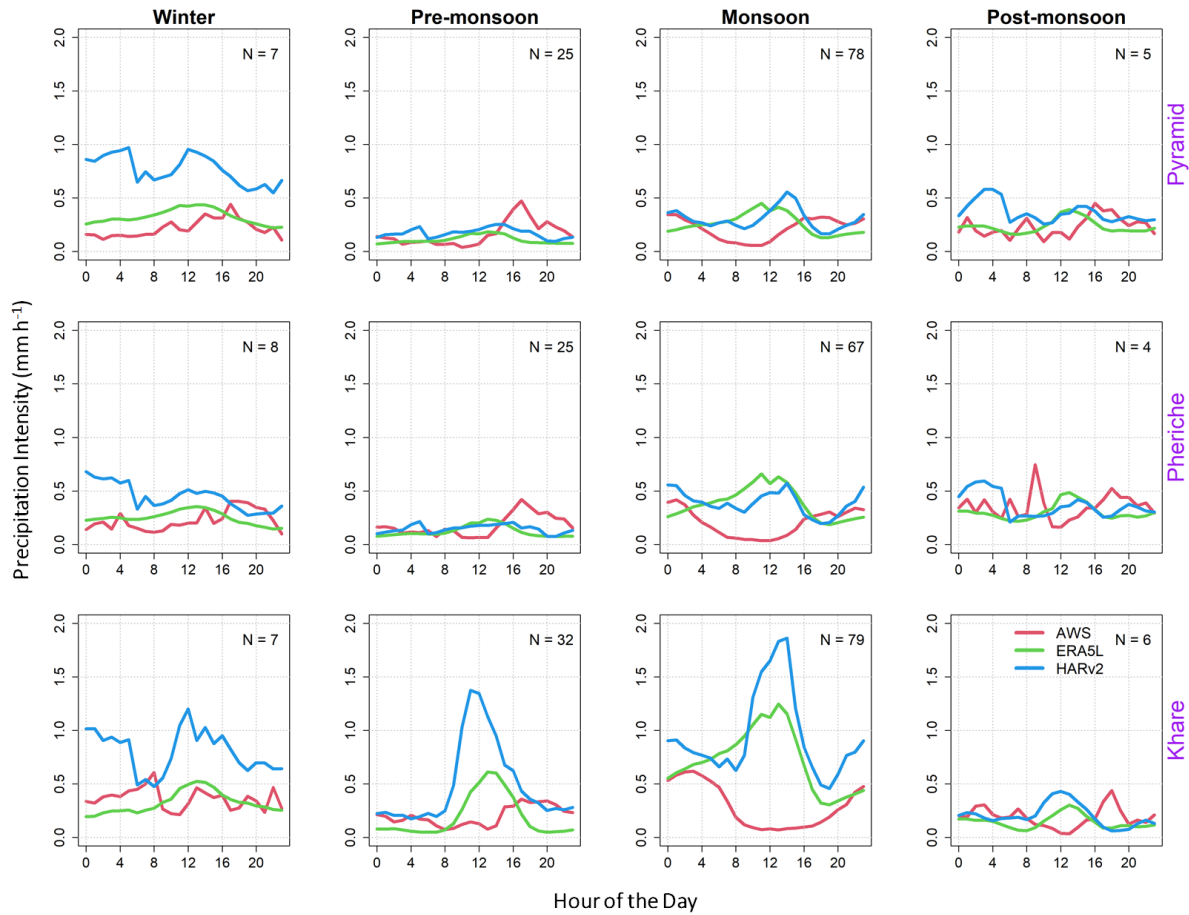


Figure 4.13. Mean diurnal cycle of reanalysed and observed total precipitation at AWS sites for different seasons. Only days with observed daily precipitation exceeding 1 mm w.e. day⁻¹ are used in those plots. The mean number of days with daily precipitation exceeding 1 mm day⁻¹ w.e. for each season, N, at each site is reported in each panel.

Figure 4.13 compares the mean daily cycle of observed precipitation to that of reanalysed data, for each season. Days with less than 1 mm w.e. of observed daily precipitation are discarded in these daily cycles. As already observed in other studies (e.r., Ueno et al., 2008; Yamamoto et al., 2011; Perry et al., 2020), during the monsoon, precipitation is more intense at night than during daytime, with a peak of precipitation at sunset at Pyramid or later during the night at the other sites. The pattern is similar during the pre-monsoon, but less clear. During the other seasons, given that there are only a few days with precipitation exceeding 1 mm w.e. day⁻¹, we cannot extract any clear and representative pattern of daily distribution of precipitation. Focusing on the two most humid seasons (i.e., monsoon and pre-monsoon), both reanalyses are unable to reproduce the daily cycle of precipitation, and are most of the time out-of-phase with maximum precipitation intensity at daytime. This is especially true at Khare where strong precipitation maxima at noon, concomitant to the observed precipitation minimum, are responsible for large precipitation over-estimations already reported.

Table 4.6. Mean seasonal bias between reanalysed daily data (ERA5L and HARv2) and observed data (T = Air Temperature, RH = Relative Humidity, u = Wind Speed, $SWin$ = Shortwave incoming radiation, $LWin$ = Longwave incoming radiation, and P = total Precipitation) over different seasons (DJF = Winter, MAM = Pre-monsoon, JJAS = Monsoon and ON = Post-monsoon).

	AWS site	Seasonal ^a				Annual mean ^a /total
		DJF	MAM	JJAS	ON	
T (°C)	Changri Nup	-10.1	-5.5	2.0	-5.0	-3.9
	Mera La	-8.9	-5.3	1.8	-3.6	-3.5
	Mera Summit	-18.3	-12.8	-2.5	—	-11.2
	Naulek	-10.4	-6.8	0.3	-6.7	-5.4
RH (%)	Changri Nup	25	52	85	39	55
	Mera La	30	60	91	42	60
	Mera Summit	39	55	76	—	56
	Naulek	33	56	92	42	61
q (g kg ⁻¹)	Changri Nup	0.8	2.6	7.0	2.1	3.6
	Mera La	1.0	3.1	7.5	2.4	3.9
	Mera Summit	0.8	1.8	5.1	—	2.5
	Naulek	1.0	2.7	6.8	2.3	3.6
u (m s ⁻¹)	Changri Nup	2.9	2.1	1.2	2.3	2.1
	Mera La	3.0	2.0	1.1	1.9	2.0
	Mera Summit	6.5	4.8	2.5	—	4.6
	Naulek	4.6	3.0	1.4	3.3	2.6
$SWin$ (W m ⁻²)	Changri Nup	205	296	212	230	236
	Mera La	223	254	162	234	212
	Mera Summit	212	331	315	—	283
	Naulek	216	304	222	224	234
$LWin$ (W m ⁻²)	Changri Nup	173	223	303	199	233
	Mera La	182	234	308	209	243
	Mera Summit	148	191	272	—	203
	Naulek	175	219	300	197	240
P (mm w.e.)	Pyramid	39	108	413	32	591
	Pheriche	49	115	337	39	540
	Khare	78	142	570	28	818

Table 4.7 and Table 4.8 compare the occurrence of precipitation at AWS sites with that of reanalysis products, at hourly and daily time scales, respectively over the entire measuring period and over the monsoons only. Overall, the agreement between observed and reanalysed precipitation occurrences is reasonable, slightly better for HARv2. Still, 13 to 36 % of the time (sum of the false counts in Tables 7 and 8, 13 % being for HARv2 data at Pheriche at hourly time step for the entire measuring period (Table 4.7) and 36 % being for ERA5L data at Khare at hourly time step for the monsoons only (Table 4.7)), depending on the site and on ERA5L or HARv2, reanalysis data fail to reproduce precipitation mostly simulating precipitation while there is not in reality (False positive in Table 4.7 and Table 4.8), but *vice versa* also, not only at hourly time scale but also at daily time scale. Looking only at the monsoons, the days with precipitation are fairly well reproduced with a percentage of total false values not exceeding 25 % (Table 4.8). But the agreement is less good while considering the occurrences of precipitation at hourly time scale when the total percentage of false values is comprised between 13 % and 36 % (Table 4.7).

Table 4.7. Comparison between the occurrence of precipitation observed at AWS and in reanalysis datasets at hourly time scale. True positive (negative) means that there is (is no) precipitation at AWS and in reanalysis dataset. False positive

(negative) means that reanalysis dataset simulates (does not simulate) precipitation, although precipitation is not (is) observed at AWS. Values are percentages of hours as a function of the total number of hours. On the one hand, we consider the entire measuring periods (see Table 1 for those periods) and on the other hand, only the monsoons. To discriminate hours with or without precipitation, a threshold of 0.1 mm w.e. hr⁻¹ is used for AWS data, below which we consider that there is no precipitation. The thresholds for reanalysis data are 1.3 to 3.5 higher than that of AWS based on the overall over-estimation of the precipitation by reanalysis.

	True positive	True negative	False positive	False negative
Pyramid				
AWS vs ERA5L	5/9	79/65	11/19	5/7
AWS vs HARv2	4/6	83/72	7/11	6/10
Pheriche				
AWS vs ERA5L	4/8	79/64	12/22	5/7
AWS vs HARv2	3/5	84/73	7/12	6/9
Khare				
AWS vs ERA5L	7/12	71/52	15/25	7/11
AWS vs HARv2	7/11	74/57	12/20	8/12

Table 4.8. Comparison between the occurrence of precipitation observed at AWS and in reanalysis datasets, at daily time scale. True positive (negative) means that there is (is no) precipitation at AWS and in reanalysis dataset. False positive (negative) means that reanalysis dataset simulates (does not simulate) precipitation although precipitation is not (is) observed at AWS. Values are percentages of days as a function of the total number of days. On the one hand, we consider the entire measuring periods (see Table 1 for those periods) and on the other hand, only the monsoons. To discriminate days with or without precipitation, a threshold of 0.5 mm w.e. d⁻¹ is used for AWS data, below which we consider that there is no precipitation. The thresholds for reanalysis data are 1.3 to 3.5 higher than that of AWS based on the overall over-estimation of the precipitation by reanalysis.

	True positive	True negative	False positive	False negative
Pyramid				
AWS vs ERA5L	30/53	53/30	10/13	7/4
AWS vs HARv2	23/39	57/37	5/6	15/18
Pheriche				
AWS vs ERA5L	28/49	50/26	15/22	7/2
AWS vs HARv2	22/37	60/41	6/7	13/15
Khare				
AWS vs ERA5L	35/57	40/17	22/24	3/1
AWS vs HARv2	32/53	52/29	10/12	6/5

We also look at the two most important events of our precipitation record, i.e. typhoons Phailin and Hudhud which both occurred mid-October, in 2013 and 2014, respectively (Shea et al., 2015a; Sherpa et al., 2017). Even though both reanalysed datasets tend to over-estimate precipitation during those extreme events, especially for HARv2 data, the daily precipitation distribution is fairly well reproduced over the three days of each event. For both typhoons, October 14 was the wettest day, receiving 55 to 70 % of the total precipitation of each event (Table 4.9).

Table 4.9. Two three-day precipitation events captured at Pyramid and Pheriche AWSs during Typhoon Phailin in October 2013 and Typhoon Hudhud in October 2014, and compared with reanalysis data (in mm w.e.).

Date	Pyramid AWS	Pheriche AWS	Pyramid ERA5L	Pheriche ERA5L	Pyramid HARv2	Pheriche HARv2
Typhoon Phailin						
13 Oct 2013	13.7	21.4	13.1	13.7	31.1	30.3
14 Oct 2013	58.2	91.1	54.5	57.8	95.1	96.4
15 Oct 2013	14.7	24.4	28.0	32.8	8.8	6.8
Total	86.6	136.9	95.7	104.3	135	133.5
Typhoon Hudhud						
13 Oct 2014	5.8	5.9	9.3	9.0	16.4	10.5
14 Oct 2014	27.9	21.9	18.1	19.0	44.9	25.6
15 Oct 2014	5.7	14.7	3.1	3.5	1.2	0.5
Total	39.4	42.5	30.5	31.5	62.5	36.5

4.8 Discussion

4.8.1 Performances of ERA5L and HARv2 reanalyses in the central Himalaya

We present here a multi-site evaluation of meteorological variables using ERA5L and HARv2 reanalyses compared to *in-situ* observations from seven meteorological stations located in the upper Dudh Koshi basin, Nepal. It is noteworthy to mention that reanalysis data are spatially resolved data ($0.1^\circ \times 0.1^\circ$ for ERA5L and $10 \text{ km} \times 10 \text{ km}$ for HARv2) whereas *in-situ* observations are point-scale data at AWS sites. Due to this scale difference, we cannot expect a perfect match between datasets, especially when the topography is complex. The performance of reanalysis data depends on the meteorological variables, on the geographical context (Tetzner et al., 2019) and on the surface state. In the upper Dudh Koshi basin, the 2-m air temperature is the best captured ($r = 0.95 - 0.97$; $p < 0.001$; RMSE of 2 to 3 °C; $r = 0.72$ to 0.91 for the anomalies) among all variables by both reanalyses (ERA5L and HARv2), which are nevertheless usually cold biased especially over rocky surfaces (bias of -2.2 to -2.4°C at Changri Nup) (Table 4.5 and 4.6). This cold bias, typical of most reanalysis products in this region (Orsolini et al., 2019), is attenuated over glacierized surfaces because they are themselves colder than the average surfaces. The variations between AWS and reanalysis data are likely to be attributed to the elevation difference between the AWS site and the grid point of the reanalysis (Tetzner et al., 2019). Even though both reanalysis temperature data are corrected using a seasonal elevational gradient of air temperature above ground (Kattel et al., 2013), the bias is stronger during the cold seasons of the year (winter and post-monsoon) than during the humid season, and is also more important at daytime than during the night. During these cold seasons in this mountainous environment, an inversion layer may occur. In this case, the use of a vertical gradient of air temperature is inappropriate and may be responsible for this cold bias, especially when the altitude difference between the reanalysis grid cell and the AWS exceeds a few hundreds of meters. As already pointed out by Immerzeel et al. (2014) and Steiner and Pellicciotti (2016) in the nearby Langtang valley, there is a great spatio-temporal variability of temperature lapse rates in Himalayan valleys due to extreme topography and the type of glaciers. Instead of a standard environmental lapse rate, it is strongly recommended to use observed lapse rates usually shallower, at high temporal resolution i.e. hourly time scale for instance (Ragetti et al., 2015; Mimeau et al., 2019a). A standard correction method based on spatially and temporally variable lapse rates should be developed to correct surface temperature reanalysis data for the central Himalaya, accounting for not only the season and

the hour of the day (Steiner and Pellicciotti, 2016), but also the surface state and the location of the measurement site as a function of topography (leeward vs windward for instance).

Specific humidity is directly related to local convection of the region as well as the monsoonal activity. In the upper Dudh Koshi basin, the Indian summer monsoon has a significant effect from June to September, but local convection already increases regularly during the pre-monsoon, leading to a gradual increase of specific humidity, less pronounced at very high elevation though (Mera Summit) (Figure 4.4). At 5350 m a.s.l., q is very well represented by both reanalyses, although the difference in altitude and thus atmospheric pressure between the reanalysis grid and the AWS induces a wet bias as for both gridded datasets at Mera Summit, or for ERA5L at Naulek and Mera La (Figure 4.4, Table 4.5, and 4.6). The seasonality of q at Mera Summit is significantly different from what we observe at lower elevations. Indeed, at high elevation, the only humid season is the monsoon even though the atmosphere is far from being permanently saturated (Figure S4.9), the day-to-day variability is higher than at lower altitude, and the atmospheric water content slowly increases during the pre-monsoon (Figure 4.4). It seems that there is a decoupling of the atmosphere at around 6000 m a.s.l. during the pre-monsoon and the monsoon, the lower layers being much more affected by convection than the higher layers, more occasionally reached by convective clouds and in turn much drier. As a consequence, since the reanalysis grid points for ERA5L and HARv2 are located ~ 1700 m lower in elevation, they cannot reproduce the water content of the atmosphere at Mera Summit.

ERA5L completely fails to reproduce observed wind velocities at any elevation or over any surfaces. In addition to the large systematic under-estimation of the wind velocity, this reanalysis product is not able to reproduce its large seasonal variability, characteristic of high elevation areas of the central Himalaya. Probably due to the fact that this product is obtained by dynamical downscaling of ERA5, HARv2 reanalysis performs better, but tends to systematically over-estimate wind speed at lower elevations all year round (Figure 4.6). The only site where HARv2 wind speed agrees well with observations is Mera Summit, even though wind speed is over-estimated during the monsoon, under-estimated the rest of the year and the daily cycle is out-of-phase (Figure 4.7). In mountain areas, wind results from the interplay of synoptic scale circulations like strong westerly winds in winter or during the post-monsoon, and local circulation like katabatic winds over glaciers or valley breeze circulation systems (Bollasina et al. 2002). Consequently, 2-m wind speed is highly heterogeneous in the central Himalaya at small spatial scale, due to the extreme topography, a competition between local and general circulation systems, and variable land covered patterns. In such conditions, the poor performance of reanalysis products is expected, except at very high elevation open sites like Mera Summit, where conditions are closer to the free atmosphere, i.e. less affected by local circulation systems or surface types. In this study region, only HARv2 reanalysis is able to represent meso-scale wind speed, but downscaling techniques are necessary to resolve local-scale wind regimes like anabatic or catabatic winds. It is also noteworthy to mention that applying a logarithmic profile to compute reanalysis wind speed at AWS measurement level from 10-m wind is likely to add further errors. Indeed, a stable stratification is common over glacier surfaces, which can result in a vertical wind gradient that is much steeper than a simple logarithmic profile, and in turn in a more pronounced reduction of wind speed. This could explain why HARv2 wind speed is often over-estimated.

We observe a strong seasonality of incoming shortwave and longwave radiations, with maximal values of *SWin* during the pre-monsoon, and of *LWin* during the monsoon because of the presence of warm air and thick convective clouds. The seasonality of both incoming radiations is well captured by ERA5L and HARv2 reanalysis datasets (Figure 4.8 and 4.10). However, there are sometimes large biases for some sites, mainly due to the elevation difference between the AWS and the reanalysis grid point. For some sites like Mera Summit, this elevation difference is as high as ~1700 m, explaining why reanalysed *SWin* is negatively biased, especially during the pre-monsoon and monsoon when a large part of *SWin* is reflected by an extra 1700 m of cloud thickness, and why *LWin* is systematically positively biased, due to an additional longwave emission of this extra 1700 m thick layer of atmosphere. When the reanalysis grid point elevation is close to that of the AWS, the agreement between reanalysed and observed radiations is very good like at Naulek for HARv2 data. Nevertheless, on each site, ERA5L performs much better than HARv2. Indeed, HARv2 incoming shortwave radiation is abnormally depleted during the monsoon at all sites except Changri Nup, likely due to an over-estimation or an exaggerated reflection of the cloud cover. In mountain areas with extreme topography, *SWin* and *LWin* are also strongly influenced by local conditions such as slope or aspect which contribute to enhance biases. As a consequence, incoming shortwave and longwave radiations can be reconstructed from ERA5L reanalysis (and to a lesser extent also from HARv2 data but with a lower accuracy) as long as a correction method accounting for the elevation difference between the reanalysis grid point and the studied site and the local topography is considered.

Both reanalysis datasets are able to reproduce precipitation during the dry seasons (post-monsoon and winter, even though HARv2 precipitation is over-estimated in January-February) but strongly over-estimate precipitation when it starts to rain or snow, in pre-monsoon, and more evidently during the monsoon. Additionally, reanalysis products predict maximum precipitation intensity at daytime although it occurs at night. The performance of ERA5L is better than HARv2, but an over-estimation by a factor of 2 to 3 is still usual, between June and September (Figure 4.12 and 4.13). This is all the more problematic as more than 70% of the annual precipitation is concentrated in those 4 months. It is interesting to note that a recent study found different results when comparing HARv2 (at 10 and 2 km resolutions) and ERA5L with three stations located on the Tibetan Plateau (Hamm et al., 2020). They concluded that HARv2 had a better ability to represent the orographic effect on precipitation, and was in better agreement with station measurements than ERA5L. Multiple reasons could explain these differences: i) there is a strong annual variability in precipitation, which might hinder systematic biases, ii) the stations they investigate are located on the northern flank (leeward side) of the central Himalaya, and consequently the influence of topography is expected to be different, and iii) the stations investigated in this present study are located at higher elevations than those in Hamm et al. (2020). The comparison with this study shows that it is difficult to draw general conclusions from site specific studies, and some conclusions apply only to specific settings.

It is well known that solid precipitation measurements are beset with significant inaccuracies, depending on the gauge catch efficiency (e.g., Kochendorfer et al., 2017). Nevertheless, our dataset has been corrected for undercatch (Førland et al. 1996 and 4.10.1.d) and the bias is strongest during the monsoon when conditions i.e, light winds and mostly rain below 5000 m

a.s.l., are favorable for an efficient gauge catch. Consequently, we expect our precipitation measurements not to be under-estimated. Anyway, with such a complex topography, the spatial variability of precipitation is extreme (Eeckman et al., 2017; Mimeau et al., 2019a) and the spatial resolution of reanalysis products, as good as it is, is still not sufficient to reproduce the observations. The occurrence of precipitation is reasonably reproduced at least at daily time scale, but reanalysis products have still a tendency to simulate precipitation when there is not, mainly at hourly time scale (Table 4.7 and 4.8). Promisingly, both reanalysis datasets have well captured the extreme precipitation events due to typhoons Phailin and Hudhud, mid-October 2013 and 2014, respectively with a moderate over-estimation especially for HARv2 (Table 4.9).

In general, both gridded datasets are able to well represent the seasonal cycle of all meteorological variables, except ERA5L for wind speed. This means that they are able to resolve the meso-scale atmospheric processes but they cannot be directly used as surrogates for AWS based observations due to the scale mismatch. For instance, for most of the analyzed variables, the agreement between reanalysis data and in-situ data decreases when the altitude difference between the reanalysis grid point and that of the AWS increases. It is thus impossible to use the same grid point for different AWSs concurrently, without applying either dynamical or statistical techniques to downscale the gridded data to local scale or individual sites.

4.8.2 Qualitative relevance for mass and energy balance studies over glaciers

Regarding energy and mass balance studies over glaciers in the central Himalaya, several point-scale surface energy balance studies, mostly conducted in the ablation area, have revealed that net all-wave radiation is the main energy flux controlling the melt of clean-ice glaciers (e.g., Kayastha et al., 1999; Litt et al., 2019) while turbulent fluxes play a secondary role, still relatively important in the accumulation zone (e.g., Stigter et al., 2018) or over debris-covered areas (e.g., Stigter et al., 2018; Giese et al., 2020). Solid precipitation with its impact on albedo and air temperature, with its control on the rain-snow limit, are therefore very important meteorological variables influencing the glacier mass balance in the ablation area, while wind speed, which governs sublimation, is more important in the accumulation area. When in-situ measurements are not available close to glaciers, SWin and LWin from ERA5L data should be preferred to those from HARv2, as long as the elevation difference between the reanalysis grid point and the studied point is accounted for. Reanalysed air temperature, from ERA5L or HARv2, are both suited to control the elevation of the rain-snow limit when using adequate elevational gradients of air temperature above ground, preferentially calibrated with observed records at different elevations in the studied area. However, both reanalysis datasets largely over-estimate precipitation records at high elevation and should be bias corrected, also using in-situ measurements. Additionally, a special attention should be paid for the occurrence of precipitation, not always in phase with observations at high temporal resolution i.e., hourly time scale. Finally, ERA5L wind speed totally fails to capture wind speed at high elevation, and HARv2 wind velocity, even though it is slightly over-estimated, should be considered preferentially to assess sublimation over glaciers, especially at high elevation where sublimation is an important component of glacier mass balances. Litt et al. (2019) have shown that temperature index models, including or not

a shortwave radiation scheme, are suitable to assess melt in the ablation zone of glaciers in the central Himalaya, during the monsoon, but are unable to quantify ablation higher in altitude or during the other seasons, because sublimation prevails and is unresolved by such models. In turn, air temperature, from both reanalysis datasets, can be used as input variables for those models to assess melt in the ablation area of glaciers in the monsoon, as long as site- and season-specific ablation factors are considered (Litt et al. 2019). For physically-based surface energy balance modelling, we suggest to pay more attention to the non-stationary biases in all variables.

In conclusion, the two gridded datasets ERA5L and HARv2 are applicable for glacier mass and energy balance studies, as long as either statistical or dynamical downscaling techniques are used to resolve the scale mismatch between coarse meso-scale grids to fine-scale grids or individual sites. We found biases for some variables like temperature and precipitation, and these biases may be non-stationary and vary in the different seasons. If no AWS measurements are available in the neighborhood of the studied glacier, the temperature and precipitation biases can still be corrected by indirect methods (i.e., Immerzeel et al., 2015; Kraaijenbrink et al., 2017). However, the indirect bias corrections remain less accurate than direct comparisons with AWS, due to equifinality in the glacier mass and energy balance models.

4.9 Conclusion

Due to the scarcity and discontinuity of long-term observational data at high elevation in the Himalaya, the main sources of data for studying climate-glacier relationship at regional scale are the reanalysis datasets. Here, ERA5L and HARv2 reanalyses, having the best spatial and temporal resolution available, are compared to in-situ meteorological data to evaluate their performance based on classical statistical metrics. Observation data have been collected since 2010 by seven AWSs located on or off glaciers above 4260 m a.s.l. in the upper Dudh Koshi basin (Everest region, Nepal). 2-m air temperature, specific and relative humidities, wind speed, incoming shortwave and longwave radiations as well as precipitation are considered in this study. Climate reanalyses show different levels of performance depending on the meteorological variables, the geographical context and the surface state. Due to the complex topography of this high-altitude basin, the spatial resolution of reanalysis products is still a strong limitation to reproduce the observations, especially for highly spatially variables such as precipitation or wind speed which need local-scale spatial resolution obtained by further downscaling (e.g., Mölg et al., 2012). Air temperature is the best captured by reanalyses, as long as an appropriate elevational gradient of air temperature above ground, spatio-temporally variable and preferentially assessed by local observations, is used to extrapolate it vertically. A cold bias is still observed but less important over clean-ice glaciers than over rocky surfaces. Regarding relative and specific humidities, both reanalysis products perform well except at Mera Summit, but still have a moderate humid bias, especially during the driest months, i.e. in winter and post-monsoon. ERA5L totally fails to reproduce wind speed, with a systematic under-estimation and an absence of seasonality. HARv2 performance is better, with high wind speeds in winter and post-monsoon, and calm conditions during the monsoon in agreement with observations. Nevertheless, HARv2 wind speed is systematically over-estimated and its daily cycle is out-of-phase with the observed one. The performance of

reanalysis datasets for shortwave and longwave incoming radiations is highly dependent on the elevation difference between the reanalysis grid point and the observation site. When the elevation of the grid point is lower than that of the observation site, the discrepancy between reanalysed and observed incoming radiation (under-estimation for shortwave radiation and over-estimation for longwave radiation) increases as the additional layer of atmosphere to be crossed is thicker. A correction procedure to account for the elevation difference between the reanalysis grid point and the observation site should be considered to properly reproduce incoming shortwave and longwave radiations. The seasonality and the horizontal south-to-north gradient of precipitation are reasonably captured by these two reanalyses. Nevertheless, they tend to highly over-estimate precipitation up to a factor three during the monsoon, ERA5L performing better than HARv2. The occurrence of precipitation is reasonably reproduced at daily time scale but less well at hourly time scale. In conclusion, the two gridded datasets ERA5L and HARv2 cannot be directly used as surrogates for AWS based observations. Nevertheless, they are applicable for glacier mass and energy balance studies, as long as either statistical or dynamical downscaling techniques are used to resolve the scale mismatch between coarse meso-scale grids to fine-scale grids or individual sites.

As long as high-quality long-term meteorological records are not available at high elevation in the Himalayas, reanalysis datasets will not be able to do otherwise than assimilate data only at lower altitudes. This is problematic for any studies focusing on climate at high elevation such as glacier studies. In that case, assessing the performance and adequately correcting the used reanalysis datasets is a prerequisite, and implies having a weather station running at glacier elevations for at least one year. In remote mountain areas like the Himalayas, due to access difficulties, extreme weather, and complex topography, maintaining continuous high-quality meteorological records over a long-term is almost impossible, and therefore combining in-situ data and various high resolution reanalyses is highly recommended.

4.10 Supplementary material

1. *Data treatment and quality control procedure (except precipitation)*

Meteorological observations at different stations are sampled at a frequency between 30 and 60 seconds, and recorded as 30-minute averages by Campbell Scientific dataloggers. All the procedure to identify gaps, correct the raw data and control them is partially described in Shea et al. (2015). Precipitation data are subject to a specific procedure, described in the following section 1.c

a) Data gaps

Most of the gaps are due to either i.) power failure (solar panel buried by snow for instance, or battery failure) or ii.) tilting or collapse of the on-glacier AWSs. As a consequence, in the first case, all half-hourly values are missing, and in the second case, most of the half-hourly values are removed, except air temperature and relative humidity. Occasional problems were also identified such as: i) water ingress into the CNR4 housing, leading to discard shortwave and longwave radiation data, ii) snow ingress into the radiation shield of Vaisala T/RH sensors (at Mera Summit only) leading to discard the data or iii) blockage of the Young sensor, during the monsoon, when wind speed is low and humidity high, leading to abnormal half-hourly null values of wind speed, then discarded. Once this first step is done, hourly values are calculated from half-hourly values, and discarded if at least one half-hourly value is missing. Then daily values are computed from hourly values and discarded if more than 33% of the hourly values are missing.

b) Data treatments

Half-hourly values of SW_{in} lower than 7 W m^{-2} are set to zero and the maximum albedo α is assumed to be 0.95. When albedo exceeds 0.95, SW_{in} is recalculated as $SW_{in} = SW_{out}/0.95$. RH sometimes slightly exceeds 100% and is then fixed to 100%.

c) Quality control procedure

Every year, after the data have been collected in the field, all data are quality controlled. Once the obvious gaps have been removed (see sub-section a) above), all data are plotted at half-hourly and daily time scales, over the whole year. They are then 1. visually inspected to identify obvious sensor malfunction and 2. compared to previous year records to identify potential calibration problems or malfunction not detected during the visual inspection. All sensors are changed when they are damaged (when a station collapses for instance) and anyway changed every 2 to 4 years. CNR4 sensors are recalibrated at least every 4 years and often more frequently when there is humidity inside their housing or when a malfunction of one sensor is detected.

d) data availability and accuracy

All those data are publicly available (<https://glacioclim.osug.fr/Donnees-himalaya>) on the GLACIOCLIM website and are extensively used by the scientific community (e.g., by the IACS working group on debris covered glaciers (<https://cryosphericsscience.org/activities/wgdebris/>) and many other scientists). As a

consequence, we regularly receive some feedbacks concerning some errors about this dataset, allowing us to identify problems not detected initially and then to correct (or discard) the corresponding data. Nevertheless, despite all these precautions and systematic control of data quality, we cannot completely rule out the possibility to have missed some sensor malfunctions or problems. For instance, detecting over heating of the T-RH sensor housing due to intense radiation of those glacier environments is extremely difficult. We maintain an artificial ventilation of 5 m s^{-1} at daytime when clear sky (Atmos shield, model 43502) of all T-RH sensors of our AWSs except at Mera Summit, where air temperature may thus sometimes be over-estimated when wind speed is low (which happens mainly during monsoon). In short, we think that the accuracy of each dataset is close to that announced by the manufacturer (Table 4.1).

d) *Precipitation data treatment*

The data treatment is done in two steps:

i. NOISE AND EVAPORATION CORRECTION

Precipitation at the Pyramid, Pheriche and Khare sites are extracted from the bucket weight, which is recorded with a Geonor T-200BM at 30-minute intervals. To extract the precipitation at each time step, we first calculate the change in bucket content, which is supposed to be always positive given that evaporation is blocked by a layer of oil spread out over the water. However, the vibrating device used to weigh the bucket is sensitive to external perturbations such as wind or temperature fluctuations, which results in a background noise, i.e., small positive or negative changes every 30-minute time step. To smooth the signal and avoid any negative precipitation, we compensate each negative change recorded over a 30-minute time step by summing it with the neighboring positive changes. In this way, the accumulated precipitation recorded over the entire period remains unchanged. In November 2013, and between November 2015 and April 2016, we have experienced prolonged few-day periods of evaporation at Pyramid and Pheriche (repeated negative values), due to the use of poor quality oil. Consequently, we set the precipitation values to zero during these periods.

ii. CORRECTION RECOMMENDED BY WORLD METEOROLOGICAL ORGANISATION (WMO)

Raingauge devices including Geonor sensors are known to undercatch precipitation in case of snowfall (we assume there is no undercatch in case of rain). A second treatment is thus done using air temperature (for phase discretization i.e. rain vs snow: below 0°C , only snow; above 2°C , only rain; in between 0 and 2°C , a mixture of rain and snow with the ratio between both phases being linearly interpolated from 0 to 2°C) and wind speed (the correction is largely dependent on wind speed). This correction ratio *kneige* is shown in Figure S8, in case of solid precipitation, with *corrected precipitation* = *kneige* × *recorded precipitation*. This correction following Forland et al. (1996) is recommended by WMO and was applied in tropical environments (Lejeune et al., 2007a, b; Wagnon et al., 2009). The accuracy is estimated at +/- 15 %.

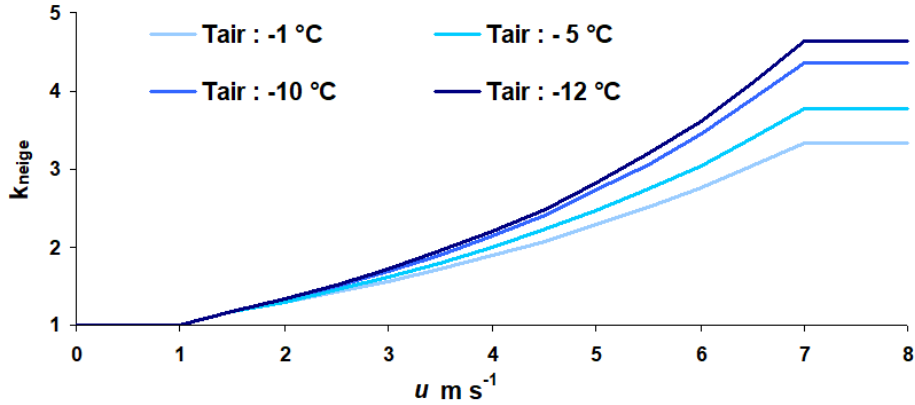


Figure S4.1. Correction factor for solid precipitation (*kneige*) as a function of air temperature (*Tair*) and wind speed (*u*); for liquid precipitation, no correction factor is applied.

2. Comparison between reanalysis and observed specific humidity in the upper Dudh Koshi basin

a) Methods

We calculate the specific humidity (q) both for the observation and reanalysis datasets. Measured air temperature, relative humidity and atmospheric pressure are used to calculate the specific humidity for Mera La and Mera Summit sites. At Naulek AWS where there is no barometer, we use atmospheric pressure recorded at Mera La AWS as both sites are approximately 1.5 km from each other and almost at the same elevation.

As no specific humidity data are directly available in the ERA5L and HARv2 datasets, we calculate the specific humidity for both reanalyses. For ERA5L, 2-m air temperature and 2-m dew point temperature of the grid cell corresponding to the AWS are used to compute relative humidity (RH) (equation 4.2 of the manuscript). Then, the saturation vapour pressure, e_s , is calculated from equation 4.5 of the manuscript, using 2-m ERA5L air temperature. Knowing RH and e_s , the vapour pressure, e , is obtained from equation 4.3 of the manuscript. And finally, using the surface atmospheric pressure P_a of the ERA5L grid cell, specific humidity (q) is calculated as:

$$q = \frac{0.622 * e}{P_a - (1 - 0.622)e} \quad (S4.1)$$

For HARv2, e is calculated from the equation 4.4 of the manuscript using the HARv2 mixing ratio, r_h . Then q is calculated from eq. (S4.1) by using e and the surface atmospheric pressure of the HARv2 grid cell.

b) Results

Over the comparison period, both reanalysed specific humidity are highly correlated with in-situ daily data ($r > 0.92$, $p < 0.001$) (Table S4.1, Figure S4.1). Reanalysed specific humidity is higher than the AWS data, except for exceptional days during the pre-monsoon at Mera La. The bias, SD, and RMSE are higher at Mera Summit than at lower elevation AWSs mainly because of the difference in elevation and in turn in atmospheric pressure between the AWS

and the grid cells of the respective reanalysis datasets. To a lesser extent, this is also the case at the two other AWSs for ERA5L data, because the grid cell altitude is approximately 700 m below that of the AWSs, inducing a higher surface atmospheric pressure, and as a consequence higher reanalysed specific humidity compared to in-situ values. At Mera La HARv2 and in-situ specific humidities agree very well all year round. For the other cases, the agreement between reanalysed and observed specific humidity is excellent in winter, and not so good in monsoon where we observe the highest biases (Table S4.2, Figure S4.2, and S4.3). During the intermediate seasons, the bias is usually slightly lower during the pre-monsoon (Table S4.2). The diurnal cycle of the observed specific humidity is fairly well reproduced by reanalysed data, with a peak in the early afternoon, but slightly shifted toward the middle of the afternoon for reanalysed data compared to observed specific humidity (Figure S4.3).

Table S4.1. Values of each statistical metrics, r , bias, SD, and RMSE obtained by comparing in-situ and reanalysed specific humidity (in g kg^{-1}) at a daily time scale over the total measuring period for each AWS. Measuring periods at each site are reported in Table 1.

	Mera La								Mera Summit								Naulek							
	ERA5L vs. AWS				HARv2 vs. AWS				ERA5L vs. AWS				HARv2 vs. AWS				ERA5L vs. AWS				HARv2 vs. AWS			
	r^*	bias	SD	RMSE																				
q	0.97	1.0	0.8	1.3	0.99	0.2	0.5	0.5	0.92	2.1	1.7	2.7	0.93	2.6	1.4	3.0	0.97	1.3	0.9	1.6	0.99	0.6	0.5	0.8

* $p < 0.001$ for all values reported in this table

Table S4.2. Mean seasonal bias between reanalysed daily specific humidity (ERA5L and HARv2) and observed specific humidity q over different seasons (DJF = Winter, MAM = Pre-monsoon, JJAS = Monsoon and ON = Post-monsoon).

	AWS site	ERA5L vs. AWS				HARv2 vs. AWS			
		DJF	MAM	JJAS	ON	DJF	MAM	JJAS	ON
q (g kg^{-1})	Mera La	0.4	0.7	1.3	1.6	0.4	0	0.2	0.5
	Mera Summit	0.6	1.9	3.8	--	1.2	2.5	4.1	--
	Naulek	0.4	1.0	2.0	1.8	0.4	0.4	0.9	0.7

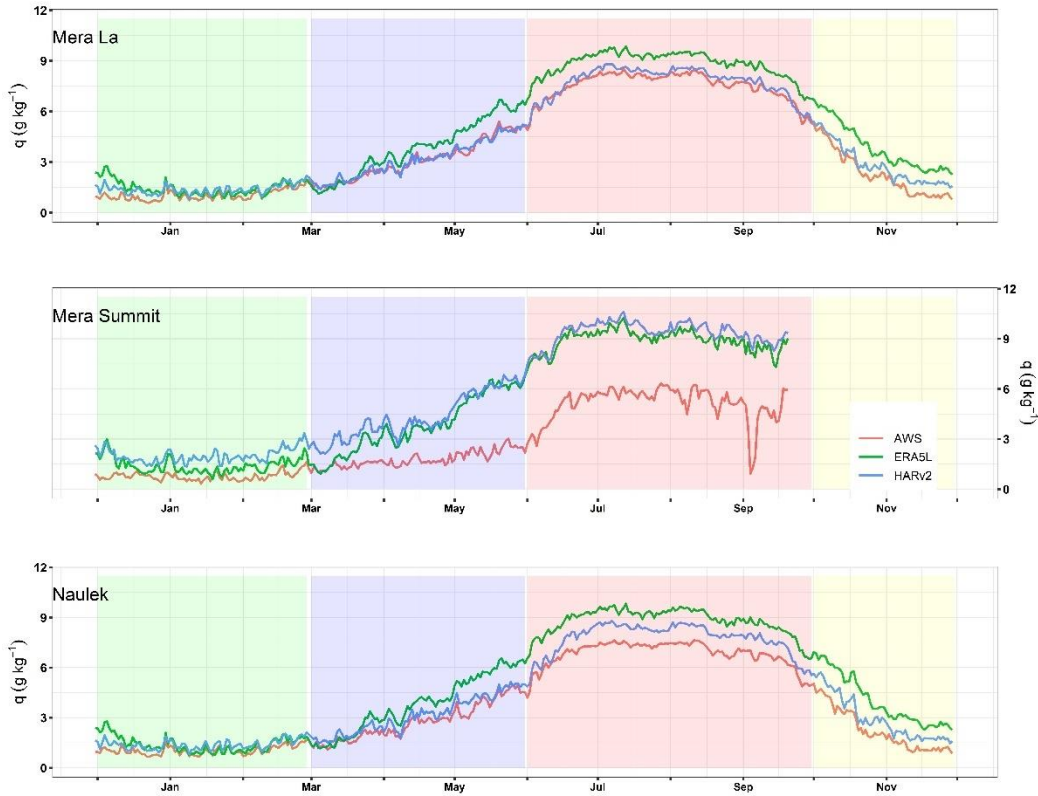


Figure S4.2. Mean annual cycle of daily specific humidity (q) from ERA5L, HARv2, and AWS at different sites. The referred periods used to calculate the mean annual cycle are reported with the AWS site name in Table 1 of the manuscript. Shaded areas correspond to seasons: winter (green), pre-monsoon (blue), monsoon (red), and post-monsoon (yellow).

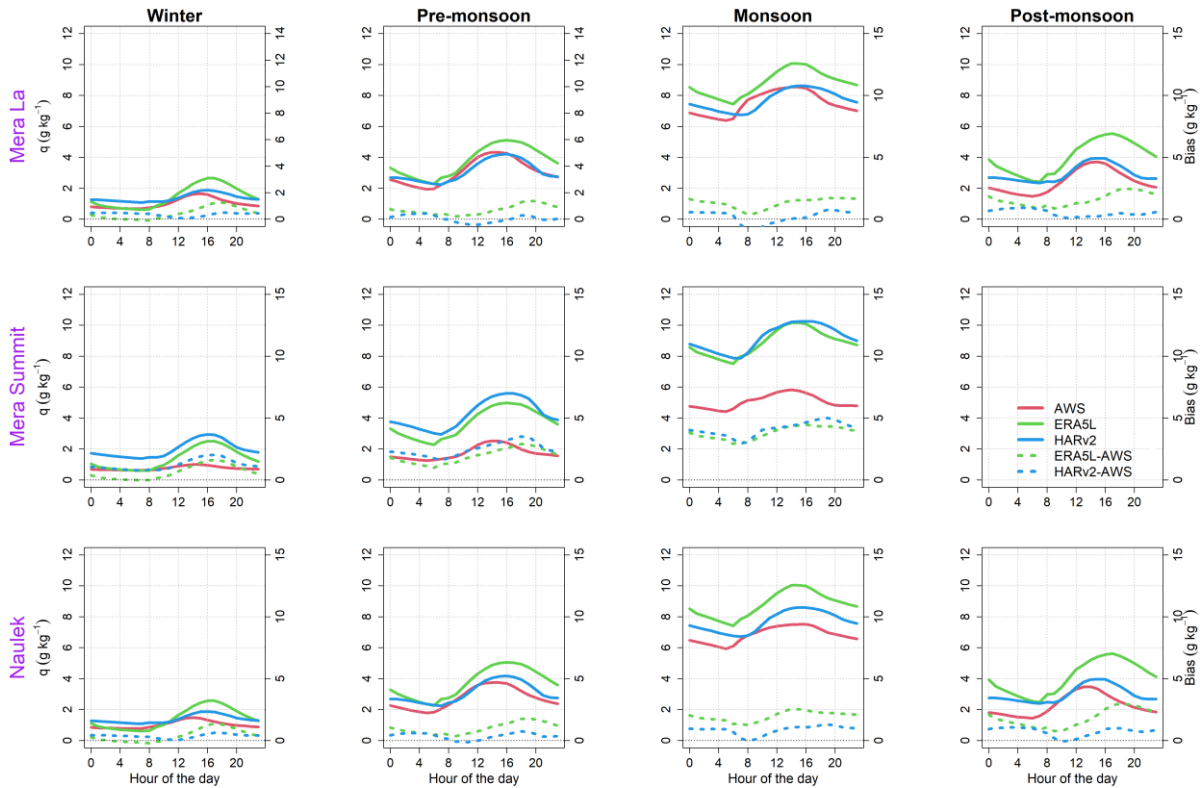


Figure S4.3. Mean diurnal cycle of reanalysed and observed specific humidity (plain lines) and biases (dotted lines) at different AWS sites for different seasons.

3. Calculation and analysis of anomalies

a) Methods

As the correlation between reanalysis and AWS data may be artificially increased by the seasonal cycle, we provide additional analysis where we remove the seasonal cycle to the daily series. We calculate the mean daily values of anomalies of all variables: T , RH , u , $SWin$, $LWin$, and q . The mean annual cycle is calculated by averaging the day-of-year values for each year and smoothing with a 7-day running average. The anomalies are calculated by subtracting the mean annual cycle to the daily values. All the data are filtered in the same way as the data presented in the main manuscript.

The correlation coefficient (r), Bias (bias), Standard Deviation (SD) and Root Mean Square Error (RMSE) are calculated between the anomalies following the method section described in section 4.5.2. of the manuscript. Those metrics are displayed on the scatter plots of Figure S4.4, S4.9 and repeated again in Table S4.3. By construction, the bias is always zero between the series, and consequently the RMSE and SD are equal.

a) Results

i. TEMPERATURE ANOMALIES

As expected the correlation coefficients between observed and reanalysed anomalies are lower than those of the raw series (Table 4.5) but they are still high (r varying from 0.72 to 0.91 and SD or RSME $< 1.6^{\circ}\text{C}$; Table S4.3). This means that both reanalysis products capture well the day-to-day variability in air temperature. The performances of HARv2 and ERA5L are rather similar even though both reanalyses do not perform very well at Mera Summit (Table S4.3, Figure S4.4).

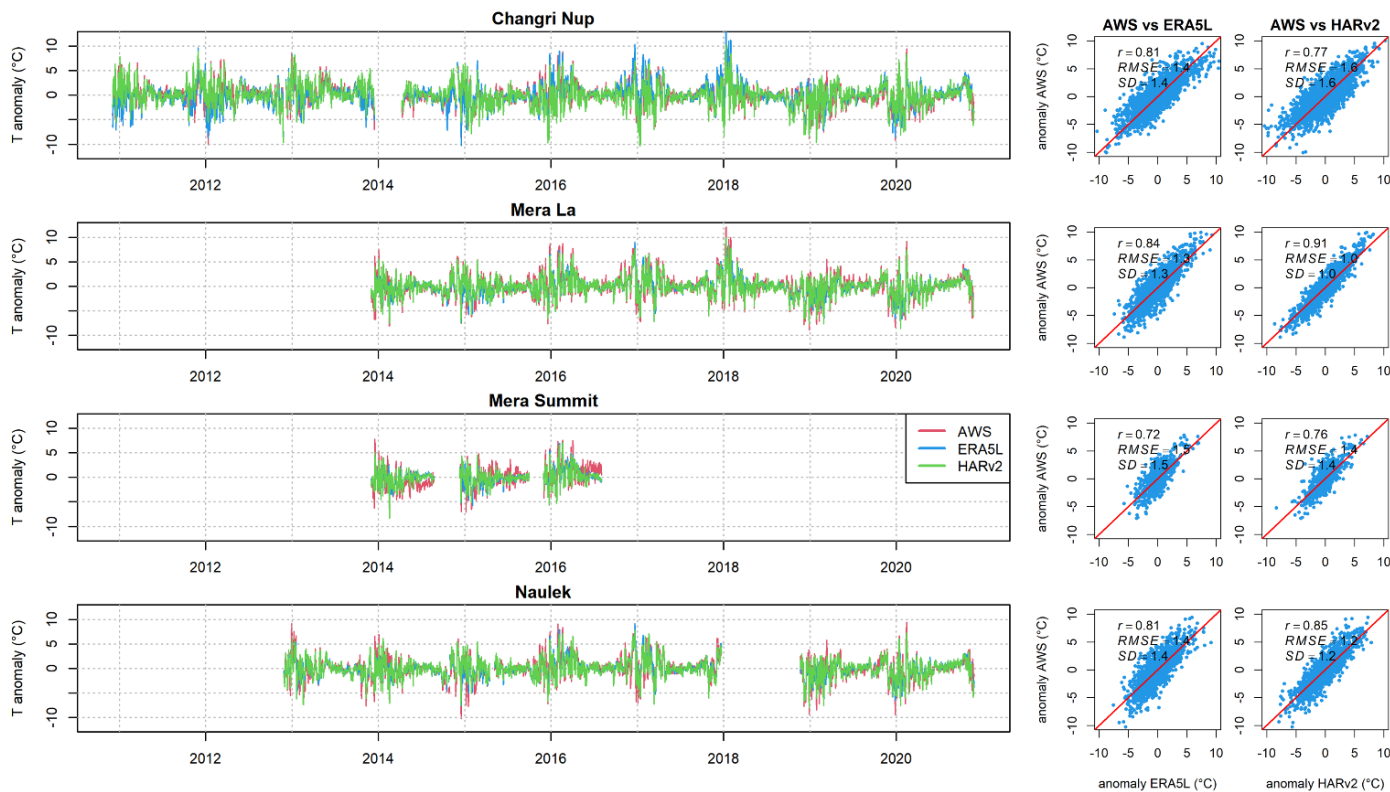


Figure S4.4. Time series of the daily temperature anomalies. On the right are displayed the scatter plots between T anomalies of HARv2 and ERA5L data vs. AWS T anomalies with a 1:1 line. The referred period to calculate the anomalies is reported in Table 4.1 of the chapter 4.

Table S4.3. Values of each statistical metrics, *r*, bias, SD, and RMSE obtained by comparing in-situ and reanalysed anomalies at a daily time scale over the total measuring period for each AWS. Measuring periods at each site are reported in Table 4.1.

	Changri Nup			Mera La			Mera Summit			Naulek																							
	ERA5L vs. AWS	HARv2 vs. AWS																															
T (°C)	r* 0.8	bias 0	SD 1.4	r* 0.8	bias 0	SD 2	r* 0.84	bias 0	SD 1	r* 1.3	bias 0.9	SD 0	r* 1	bias 0.7	SD 2	r* 1.5	bias 0.8	SD 1	r* 1.4	bias 0.8	SD 1	r* 1.4	bias 0.9	SD 1	r* 1.2	bias 0.8	SD 1						
RH (%)	r* 0.6	bias 0	SD 11	r* 0.7	bias 0	SD 11	r* 0.58	bias 0	SD 11	r* 0.8	bias 0	SD 9	r* 0.9	bias 0	SD 9	r* 0.2	bias 0	SD 17	r* 0.4	bias 0	SD 15	r* 0.6	bias 0	SD 11	r* 0.7	bias 0	SD 10	r* 0.7	bias 0	SD 10			
u (m s ⁻¹)	r* 0.1	bias 0	SD 1	r* 0.6	bias 0	SD 0.3	r* 0.1	bias 1.4	SD 0.24	r* 0.1	bias 0.7	SD 0.6	r* 0.1	bias 1.1	SD 0.2	r* 0.2	bias 0	SD 2	r* 1.5	bias 0.7	SD 0	r* 1	bias 1.2	SD 0.2	r* 0	bias 1	SD 1	r* 0.6	bias 0	SD 1	r* 1.2	bias 0	SD 1
SWIn (W m ⁻²)	r* 0.6	bias 0	SD 43	r* 0.6	bias 0	SD 43	r* 0.58	bias 0	SD 49	r* 0.58	bias 0	SD 42	r* 0.6	bias 0	SD 56	r* 0.5	bias 0	SD 39	r* 0.3	bias 0	SD 65	r* 0.6	bias 0	SD 41	r* 0.6	bias 0	SD 41	r* 0.6	bias 0	SD 56	r* 0.6	bias 0	SD 56
LWin (W m ⁻²)	r* 0.7	bias 0	SD 16	r* 0.7	bias 0	SD 16	r* 0.69	bias 0	SD 20	r* 0.69	bias 0	SD 17	r* 0.8	bias 0	SD 20	r* 0.6	bias 0	SD 23	r* 0.6	bias 0	SD 22	r* 0.7	bias 0	SD 16	r* 0.8	bias 0	SD 16	r* 0.8	bias 0	SD 19	r* 0.7	bias 0	SD 19
q (g kg ⁻¹)	r* 0.62	bias 0	SD 1	r* 0.6	bias 0	SD 0.8	r* 0.8	bias 0	SD 0	r* 0.4	bias 0.3	SD 0	r* 1	bias 0.7	SD 0.4	r* 0	bias 1	SD 0.6	r* 0.7	bias 0	SD 1	r* 0.6	bias 0.7	SD 0	r* 1	bias 0.5	SD 0.8	r* 0	bias 0	SD 0	r* 0.4	bias 0	SD 0.4

*p<0.001 for all values reported in this table

ii. ANOMALIES OF RELATIVE HUMIDITY

When removing the seasonal cycle, the performance of reanalysed products drops with correlation coefficients varying between 0.18 and 0.77 (Table S4.3), compared to r values varying from 0.59 to 0.93 for the raw values (Table 4.5). Overall, HARv2 performs better than ERA5L with systematically higher r values and lower SD or RMSE, even though both products fail to reproduce relative humidity at Mera Summit (Table S4.3, Figure S4.5).

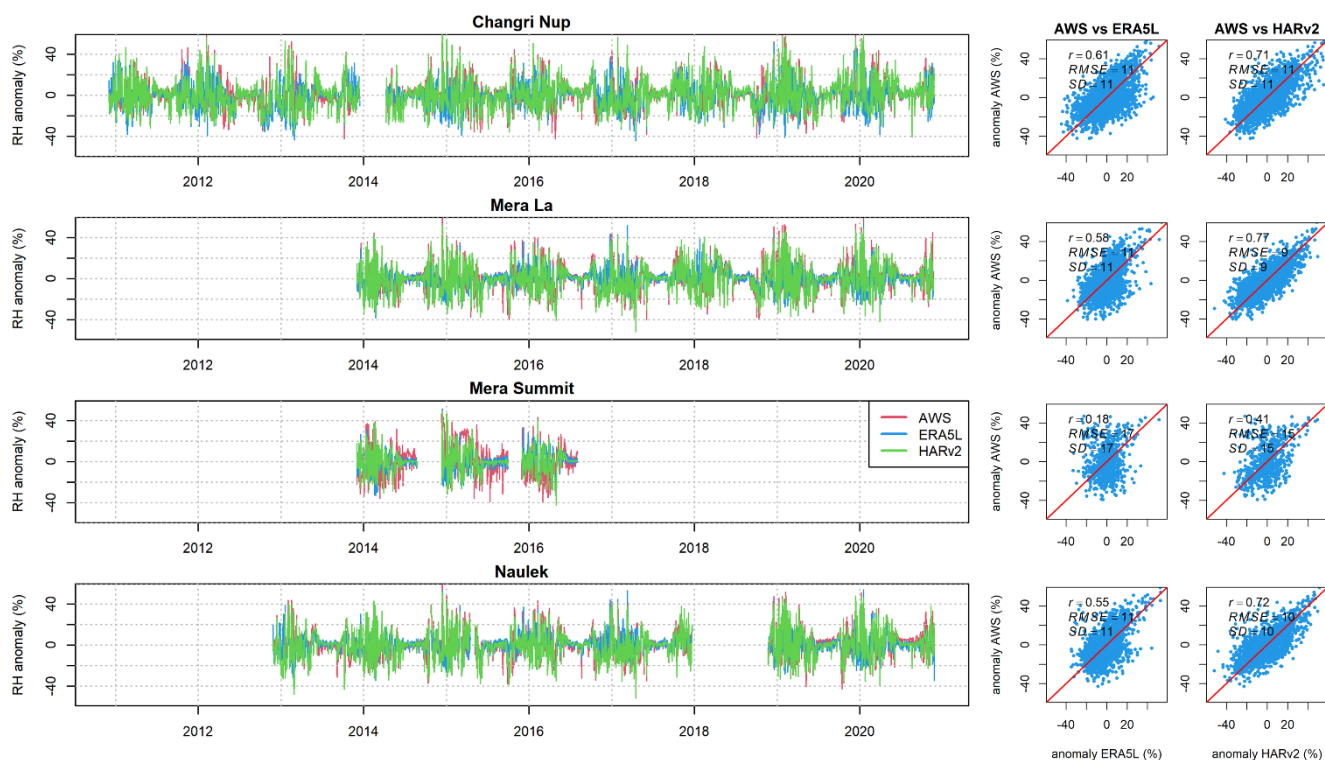


Figure S4.5. Time series of the daily relative humidity anomalies. On the right are displayed the scatter plots between RH anomalies of HARv2 and ERA5L data vs. AWS RH anomalies with a 1:1 line. The referred period to calculate the anomalies is reported in Table 4.1 of the chapter 4.

iii. ANOMALIES OF WIND SPEED

Like for raw data, wind speed anomalies show that ERA5L completely fails to reproduce observed wind speed at any sites, while HARv2 wind speed agrees better with AWS measurements, especially at Mera Summit which is a high-altitude open site ($r = 0.66$, SD and RMSE = 1.2 m s^{-1}) (Table S4.3, Figure S4.6).

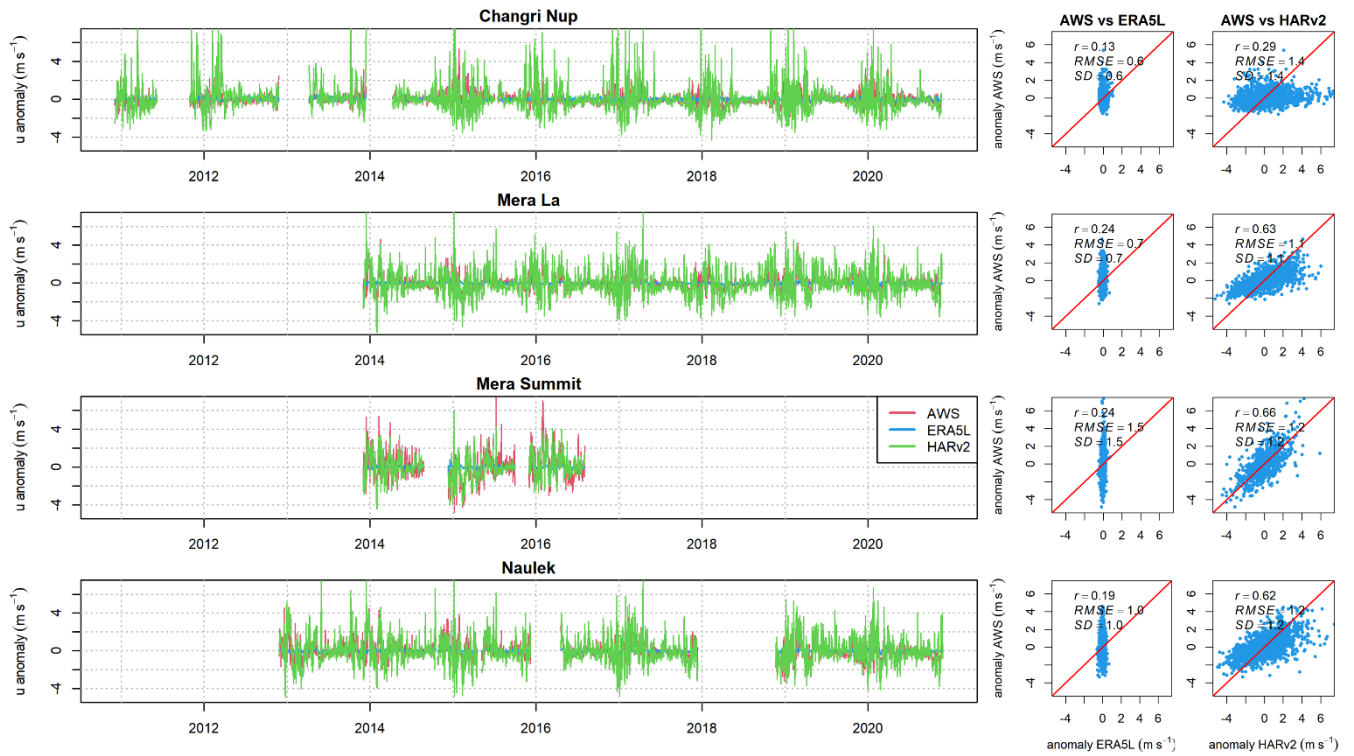


Figure S4.6. Time series of the daily wind speed anomalies. On the right are displayed the scatter plots between u anomalies of HARv2 and ERA5L data vs. AWS u anomalies with a 1:1 line. The referred period to calculate the anomalies is reported in Table 4.1 of chapter 4.

iv. ANOMALIES OF INCOMING SHORTWAVE RADIATION

As expected for a variable with a marked seasonal cycle, the performance of both reanalysis products is lower for the incoming shortwave radiation, when looking at the anomalies. It is still acceptable, with r ranging from 0.31 to 0.62, except at Mera Summit, where it is bad especially for HARv2 (Table S4.3, Figure S4.7).

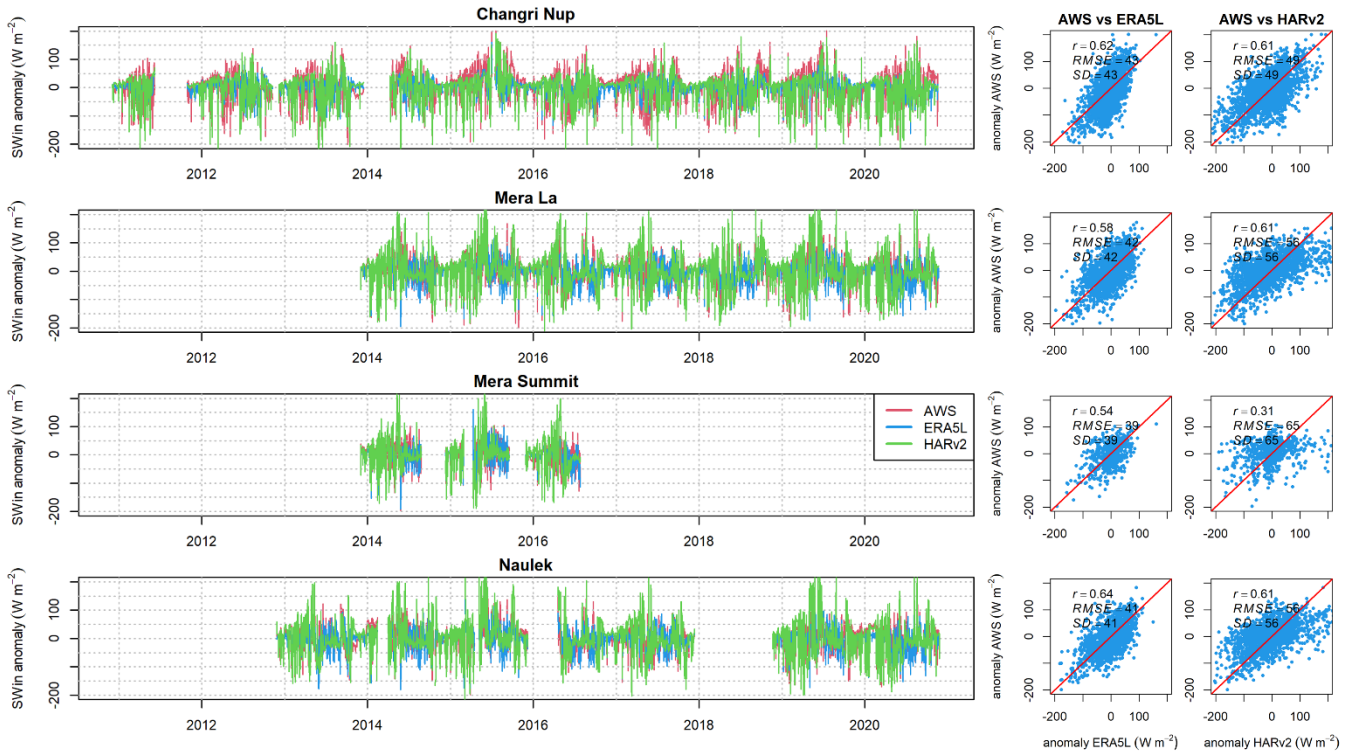


Figure S4.7. Time series of the daily incoming shortwave radiation anomalies. On the right are displayed the scatter plots between SWin anomalies of HARv2 and ERA5L data vs. AWS SWin anomalies with a 1:1 line. The referred period to calculate the anomalies is reported in Table 4.1 of the chapter 4.

V. ANOMALIES OF INCOMING LONGWAVE RADIATION

The performance of reanalysed products after removal of the seasonal cycle is good, with r values ranging between 0.55 and 0.79 (Table S4.3). Incoming longwave radiation is thus one of the best reproduced variable by reanalysis products, at any elevation, even though the performance is the worst at Mera Summit (Figure S4.8). Both reanalysis products have a similar performance.

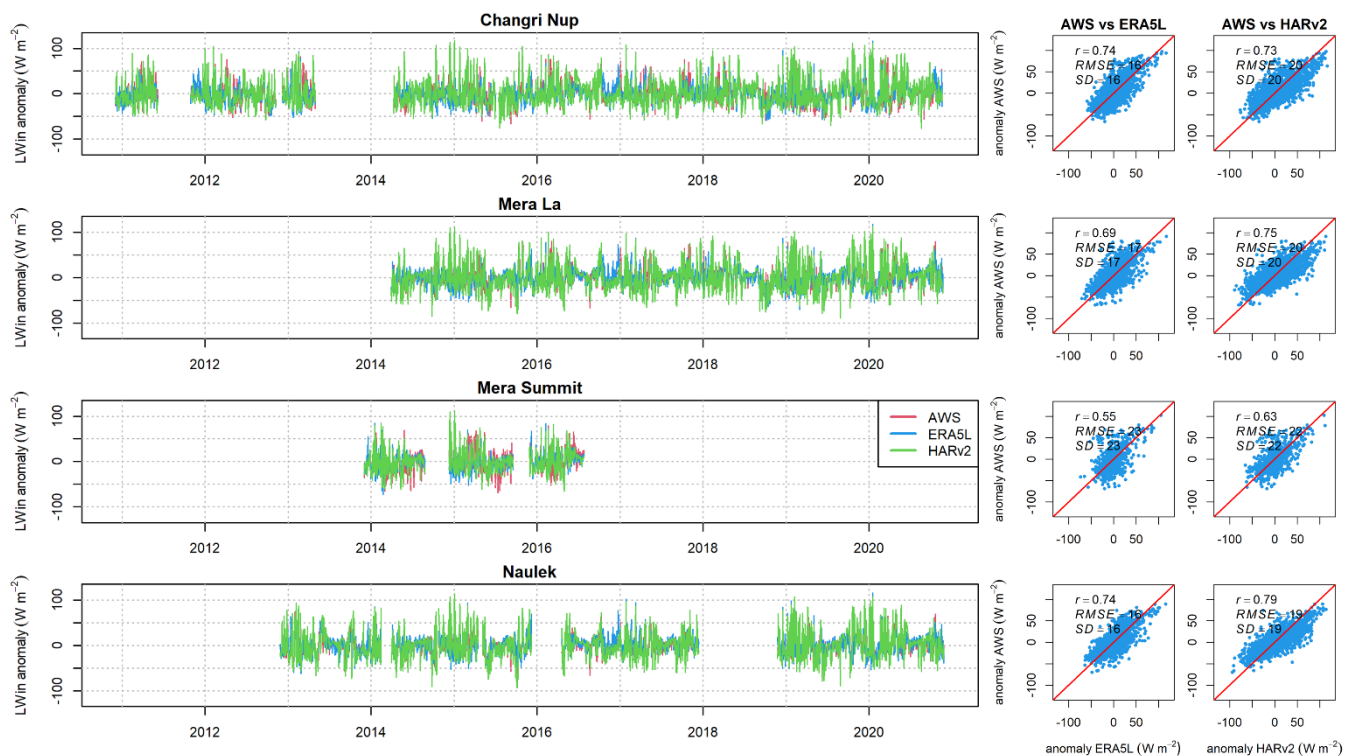


Figure S4.8. Time series of the daily incoming longwave radiation anomalies. On the right are displayed the scatter plots between LWin anomalies of HARv2 and ERA5L data vs. AWS LWin anomalies with a 1:1 line. The referred period to calculate the anomalies is reported in Table 4.1 of the chapter 4.

vi. ANOMALIES OF SPECIFIC HUMIDITY

Like for relative humidity, specific humidity is badly reproduced at Mera Summit, but fairly well retrieved by both reanalysis products at Naulek and Mera La sites ($r > 0.62$ at those sites), with slightly better performance for HARv2 (Table S4.3; Figure S4.9).

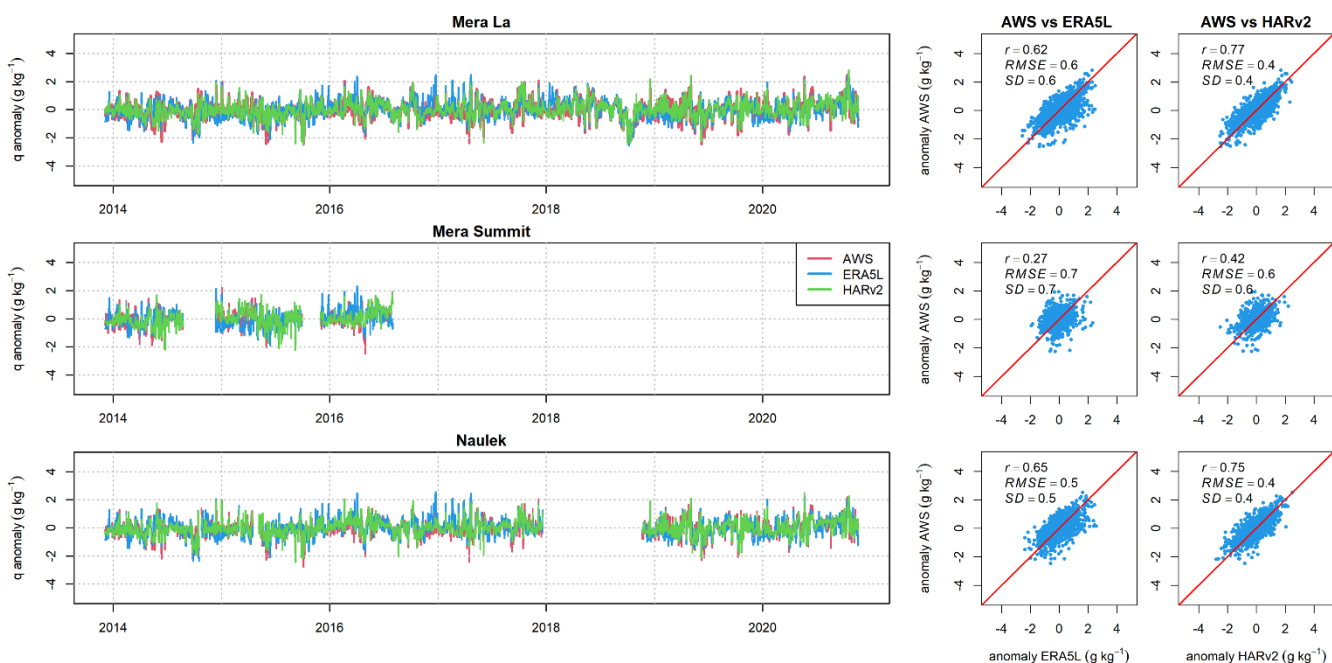


Figure S4.9. Time series of the daily specific humidity anomalies. On the right are displayed the scatter plots between q anomalies of HARv2 and ERA5L data vs. AWS q anomalies with a 1:1 line. The referred period to calculate the anomalies is reported in Table 4.1 of chapter 4.

Chapter 5

5 Surface energy and mass balance of Mera Glacier (Nepal, Central Himalaya) and their sensitivity to temperature and precipitation

After

Khadka, A., Brun, F., Wagnon, P., Shrestha, D., & Sherpa, T. (under revision). Surface energy and mass balance of Mera Glacier (Nepal, Central Himalaya) and their sensitivity to temperature and precipitation. Journal of Glaciology

5.1 A short introduction

Mera Glacier on the eastern side of the central Himalaya is now one of the benchmark glaciers for the region (Wagnon et al., 2021). Therefore, taking advantage of the data collected over the upper Dudh Koshi basin around the Mera Glacier (explained in the previous chapter), this chapter highlights the energy/mass balance components and sensitivity of Mera Glacier to precipitation and temperature. As usual, there were several data gaps in the AWS data; nearby stations filled the gaps, and the COSIPY model is used to simulate the energy and mass balance over Mera Glacier.

The most interesting work in this chapter is the sensitivity analysis, which is done by making synthetic scenarios. As Nicholson et al. (2013) and Prinz et al. (2016) highlight, the perturbing of some meteorological variables changes the relationship between them. Therefore, we wanted to develop some scenarios by taking advantage of good datasets. Then, the discussion with Philémon Autin about the methods used by Autin et al. (2022) helped to develop the synthetic scenarios based on observations. We followed somewhat similar methods developed by Autin et al. (2022) and Prinz et al. (2016) to develop synthetic scenarios. A total of 180 scenarios were developed, but the problem was the notation of the scenarios. After a round of discussions with Fanny and Patrick, we finally managed to make it more understandable.

5.2 Abstract

The sensitivity of glacier mass balance to temperature and precipitation variations is crucial for informing models that simulate glaciers' response to climate change. In this study, we simulate the glacier-wide mass balance of Mera Glacier with a surface energy balance model, driven by in-situ meteorological data, from 2016 to 2020. The analysis of the share of the energy fluxes of the glacier shows the radiative fluxes account for almost all the energy available during the melt season (May to October). However, turbulent fluxes are significant outside the monsoon (June to September). On an annual scale, melt is the dominant mass flux at all elevations, but 44 % of the melt refreezes across the glacier. By reshuffling the available observations, we create 180 synthetic series of hourly meteorological forcings to force the model over a wide range of plausible climate conditions. A +1 (-1)°C change in temperature results in a -0.75 ± 0.17 ($+0.93 \pm 0.18$) m w.e. change in glacier-wide mass balance and a +20 (-20)% change in precipitation results in a $+0.52 \pm 0.10$ (-0.60 ± 0.11) m w.e. change. Our study highlights the need for physically based approaches to produce consistent forcing datasets, and calls for more meteorological and glaciological measurements in High Mountain Asia.

5.3 Introduction

The pace of climate warming in HMA is accelerating (Pepin et al., 2015) and precipitation in these regions exhibits significant heterogeneity and remains insufficiently comprehended (Lutz et al., 2014). Furthermore, the intricate relationship between precipitation and temperature variations proves to be a formidable puzzle. This connection, intricately intertwined with glacier mass balance, poses a challenge for understanding the recent evolution of glaciers in HMA (Oerlemans and Reichert, 2000). While multi-year satellite-based estimates of mass changes allow to map the heterogeneity of glacier mass balance across large scales (e.g., Hugonnet et al., 2021), they need to be complemented by other approaches to further elucidate these patterns of contrasted mass losses. One possible approach is to consider that glacier mass changes are the combination of a change in climate conditions modulated by a glacier sensitivity to these changes (e.g., Oerlemans and Reichert, 2000; Marzeion et al., 2012). Following this approach, Sakai and Fujita (2017) demonstrated that regionally different sensitivity to temperature changes could be the main driver of observed mass losses across Asia. They found that the glacier mass balance sensitivity to temperature was determined by the general climatology, and in particular, by the summer temperature, the annual range of temperature and the ratio between summer and annual precipitation. However, their approach relies on a number of simplifying assumptions that consider only the climate at the ELA (Ohmura et al., 1992) and the climate data they used has a coarse spatial resolution. There is thus room to improve the methodology they applied, in particular through a better representation of processes responsible for glacier mass losses and gains.

These processes controlling the glacier mass are determined by the surface energy balance (SEB), which is commonly modelled to investigate how glacial mass balance is governed and how sensitive it is to climatic variables (Fujita, 2008b; Azam et al., 2014a; Fugger et al., 2022). There is a long history of studies that investigated the glacier SEB at various locations and at various temporal and spatial scales to relate atmospheric variables to glacier mass changes (e.g., Oerlemans and Knap, 1998; Favier et al., 2004). Specifically, in Hindu Kush Himalaya

(HKH), a number of studies investigated the SEB of glaciers in different climate contexts (Mölg et al., 2012; Zhu et al., 2015, 2018, 2020, 2021; Huintjes et al., 2015; Fugger et al., 2022; Arndt and Schneider, 2023). They highlight the different sensitivities to temperature and precipitation in different climate conditions, with the dry and cold (continental) climate that prevails in the north west margin of HKH being associated to low sensitivities of glacier mass balance to temperature, and the warmer and wetter (oceanic) climate of south east HKH corresponding to larger sensitivities (e.g., Arndt and Schneider 2023). The larger sensitivities are associated to the prevalence of surface melt in the surface mass balance. Surface energy based studies find highly non linear sensitivity of the mass balance to precipitation, unlike studies based on empirical approaches, such as degree-day modeling (e.g., Wang et al., 2019). This is due to the highly non linear response of glacier surface mass balance to the albedo effect (e.g., Arndt and Schneider, 2023).

However, in HKH most of the SEB studies have two main limitations: either they were done at point scale (Kayastha et al., 1999; Azam et al., 2014; Acharya and Kayastha, 2019; Litt et al., 2019; Mandal et al., 2022), or they used meteorological data from reanalysis products (Arndt and Schneider, 2023). The point-scale modelling of the SEB is limited because the SEB is very sensitive to the surface state of the glacier (ice, snow or debris), and to the distribution of meteorological variables (precipitation, temperature, radiative fluxes...) that vary across the glacier area (Oerlemans et al., 1999). Modelling the SEB of a glacier across its entire area requires distributed measurements of meteorological variables, and measurements of the glacier surface mass balance at multiple locations, including the accumulation area. Unfortunately, such data are seldom available in HKH (Huintjes et al., 2015; Arndt et al., 2021; Srivastava and Azam, 2022; Oulkar et al., 2022). Meteorological variables obtained from reanalysis can be heavily biased, especially if they are not downscaled with local measurements (e.g., Hamm et al., 2020; Khadka et al., 2022). When meteorological variables from reanalysis are used to force a glacier mass balance model, they first need to be debiased, which is often done by tuning a precipitation correction factor until the glacier mass balance matches observations. While there is usually no alternative, this method is known to be subject of equifinality (e.g., Rounce et al., 2020).

This article presents a glacier-wide SEB analysis of Mera Glacier in the eastern part of Central Himalaya. We applied the 'COupled Snowpack and Ice surface energy and mass balance model in PYthon' (COSIPY: Sauter et al., 2020) which has been optimised and evaluated using site specific measurements (Figure S5.1 in supplementary material). Among Nepal's monitored glaciers, Mera Glacier stands out for its extensive and continuous meteorological and mass balance data, making it one of the most comprehensively observed glaciers in the region (Wagnon et al., 2021; Khadka et al., 2022). By integrating field measurements, in-situ meteorological data, and the SEB model, we aim to enhance our understanding of (1) the physical processes governing the seasonal and spatial variability of the glacier mass balance, and (2) the sensitivity of the mass balance to meteorological variables. The findings from this comprehensive study will give us a better understanding of the impact of the on-going climate change on Himalayan glaciers.

5.4 Study area and climate

5.4.1 Mera Glacier

Mera Glacier, situated in the eastern part of the Central Himalaya within the Upper Dudh Koshi basin, is a plateau-type debris free glacier. Encompassing an area of 4.84 km² in 2018, the glacier stretches from an altitude of 6390 m a.s.l. to a minimum of 4910 m a.s.l. (Figure 5.1). This north-facing glacier features a gentle slope with a mean inclination of around 16 degrees. At an elevation of approximately 5900 m a.s.l., the glacier separates into two distinct branches, the Mera branch and the Naulek branch. The Mera branch initially heads north and then curves westward, while the Naulek branch extends ~2 km towards the northeast. The Mera branch is the largest of the two branches and accounts for about 80 % of the glacier's total area.

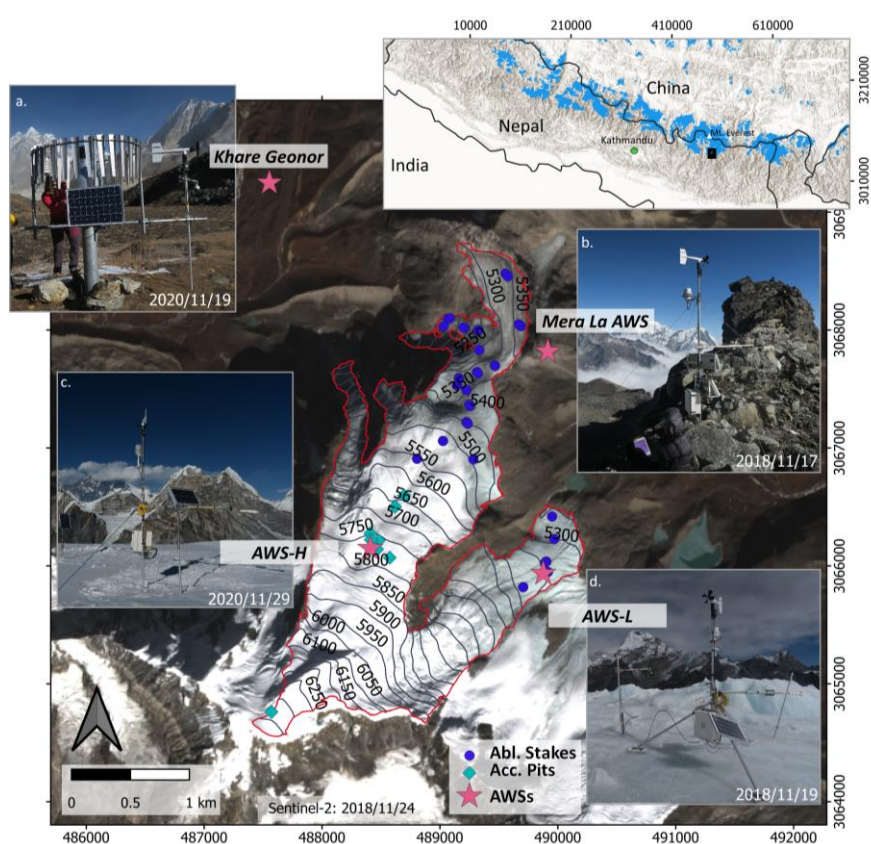


Figure 5.1. Map of Mera Glacier showing the network of ablation stakes (blue dots) and accumulation pits (cyan diamonds). The stake location and number are taken from November 2020. The number of stakes vary from year to year, due to total excavation, reinstallation at the original location, snow burial or destruction. The pink stars represent the locations of different AWSs with their respective photos and dates (a. Khare Geonor, b. Mera La AWS, c. AWS-H, and d. AWS-L). The outline of Mera Glacier is from 2018 with a total area of 4.84 km², and the background image was acquired by Sentinel-2 on 24 November 2018. Elevation lines are extracted from the 2012 Pléiades DEM (Wagnon et al., 2021). The inset map gives the location of Mera Glacier in Nepal (black square) and the glacierized areas from RGI6 (shaded blue areas).

5.4.2 Climate

Like other glaciers in Nepal, Mera Glacier is a summer accumulation type glacier, gaining mass mainly from the summer monsoon (June to September) snowfalls brought by the South Asian monsoon system (Wagnon et al., 2013; Thakuri et al., 2014; Shea et al., 2015). The glacier experiences most of its accumulation and ablation during the monsoon, which makes it a key

season to understand the climatic regime of the glacier (Ageta and Higuchi, 1984). From June to September, the average air temperature measured between 2012 and 2020 at 5360 m a.s.l. on Naulek branch is 0.3 °C, and the average precipitation recorded at 4888 m a.s.l. is equal to 570 mm, with an annual precipitation of 818 mm (Khadka et al., 2022). During this season, warm air masses flow from the Bay of Bengal and bring moisture and precipitation in the Himalayas (Perry et al., 2020). In just a few days, marking the start of the post-monsoon (October-November), generally at the beginning of October, meteorological conditions change abruptly to become dry, sunny and increasingly cold and windy. Very occasionally, this season is marked by the intrusion of typhoons in the Himalayas, which bring large amounts of snowfalls above ~4000 m a.s.l. in just a few days, like in October 2013 and 2014 (Shea et al., 2015). The winter (December-February) is similar but harsher than the post-monsoon with constantly cold, dry, and very windy conditions. At Naulek (5360 m a.s.l.), the average air temperature during this season is -10.4 °C. The pre-monsoon starts in March and is characterized by progressively warmer, wetter and less windy conditions until the monsoon is totally installed at the beginning of June. The pre-monsoon is then the second wettest season after the monsoon with approximately one quarter of the annual precipitation on the glacier (Khadka et al., 2022).

5.5 Data

5.5.1 Meteorological data

A network of automatic weather stations (AWSs) has been installed and gradually expanded since 2012 in Mera Glacier catchment at different elevations and on various surfaces (Figure 5.1). In this present study, we mainly use data from two on-glacier AWSs, one located in the ablation area on Naulek branch at 5360 m a.s.l., AWS-Low (hereafter referred as AWS-L; 4 years of data between November 2016 and October 2020), and one located in the accumulation area at 5770 m a.s.l., AWS-High (hereafter referred as AWS-H; 3 years of data between November 2017 and November 2020; Figure S5.2). Both AWSs record air temperature (T), relative humidity (RH), wind speed (u), incoming and outgoing longwave (LWin and LWout, respectively) and shortwave (SWin and SWout, respectively) radiation (Table 5.1). There are numerous data gaps in both records, due to AWS failure, power shortage during occasional abundant snowfalls covering the solar panels for instance or sensor breakdowns (Table 5.1, Figure 5.1, and see <https://glacioclim.osug.fr/>). The largest data gap occurred at AWS-L, when the station fell down from 12 December 2017 to 24 November 2018. To fill these gaps, data from the off-glacier Mera La AWS was used. Linear correlation relationships were established each month between the same variables from the two stations from November 2016 to October 2020, at an hourly time step (Figure S5.3 and Table S5.1). The atmospheric pressure (Pa) measured at Mera La AWS is used at AWS-L without any interpolation, as both AWSs are located less than 2 km apart at almost the same elevation (Table 5.1, Figure 5.2).

The Khare Geonor station (4888 m a.s.l.) has been installed on 24-25 November 2016, 472 m lower in elevation and ~3 km northwest of AWS-L. In Mera catchment, this is the only station of the network recording all-weather precipitation, thanks to a weighing device. The precipitation data have been corrected for undercatch following the method by Førland et al.

(1996) as a function of wind speed and precipitation phase (liquid or solid) depending on air temperature (See the details in the supplement of Khadka et al., 2022).

Table 5.1. List of the different AWSs operating on Mera Glacier, or in its vicinity, with their elevations, operating periods, list of sensors and associated meteorological variables used as forcing, optimisation or validation data of the SEB model. T = air temperature, RH = relative humidity, u = wind speed, SWin = incoming shortwave radiation, SWout = outgoing shortwave radiation, LWin = incoming longwave radiation, LWout = outgoing longwave radiation, P_a = atmospheric pressure and P = precipitation). The numbers in brackets indicate the data gap of the variables (second column) or the uncertainty of each sensor provided by the manufacturer (third column).

Station	Variables (gap % during the study period)	Sensors (uncertainty)
Khare Geonor 4888 m a.s.l. 25 Nov 2016 – 18 Nov 2020 Off-glacier, on a grassy surface	P (0)	GEONOR T-200BM (±15%)
Mera La AWS 5350 m a.s.l. 01 Nov 2016 – 31 Oct 2020 Off-glacier, on a rocky surface	T (0), RH (0) u (1) SWin (0) LWin (0) P _a (0)	Vaisala-HMP45C* (±0.2°C; ±2%) Young 05103-5 (±0.3 m/s) Kipp&Zonen CNR4 (±3%) CS100 (±2.0 hPa)
AWS-L 5360 m a.s.l. 01 Nov 2016 – 31 Oct 2020 On-glacier (ablation area)	T (23.2), RH (23.2) u (25.8) SWin (23.8), SWout (24.0) LWin (24.0), LWout (24.0)	Vaisala-HMP45C* (±0.2°C; ±2%) Young 05103-5 (±0.3 m/s) Kipp&Zonen CNR4 (±3%)
AWS-H 5770 m a.s.l. 11 Nov 2017 – 18 Nov 2020 On-glacier (accumulation area)	T (17.1), RH (17.1) u (17.1) SWin (17.2), SWout (17.2) LWin (17.1), LWout (27.8)	Vaisala-HMP45C (±0.2°C; ±2%) Young 05103-5 (±0.3 m/s) Kipp&Zonen CNR4 (±3%)

* artificially aspired during daytime

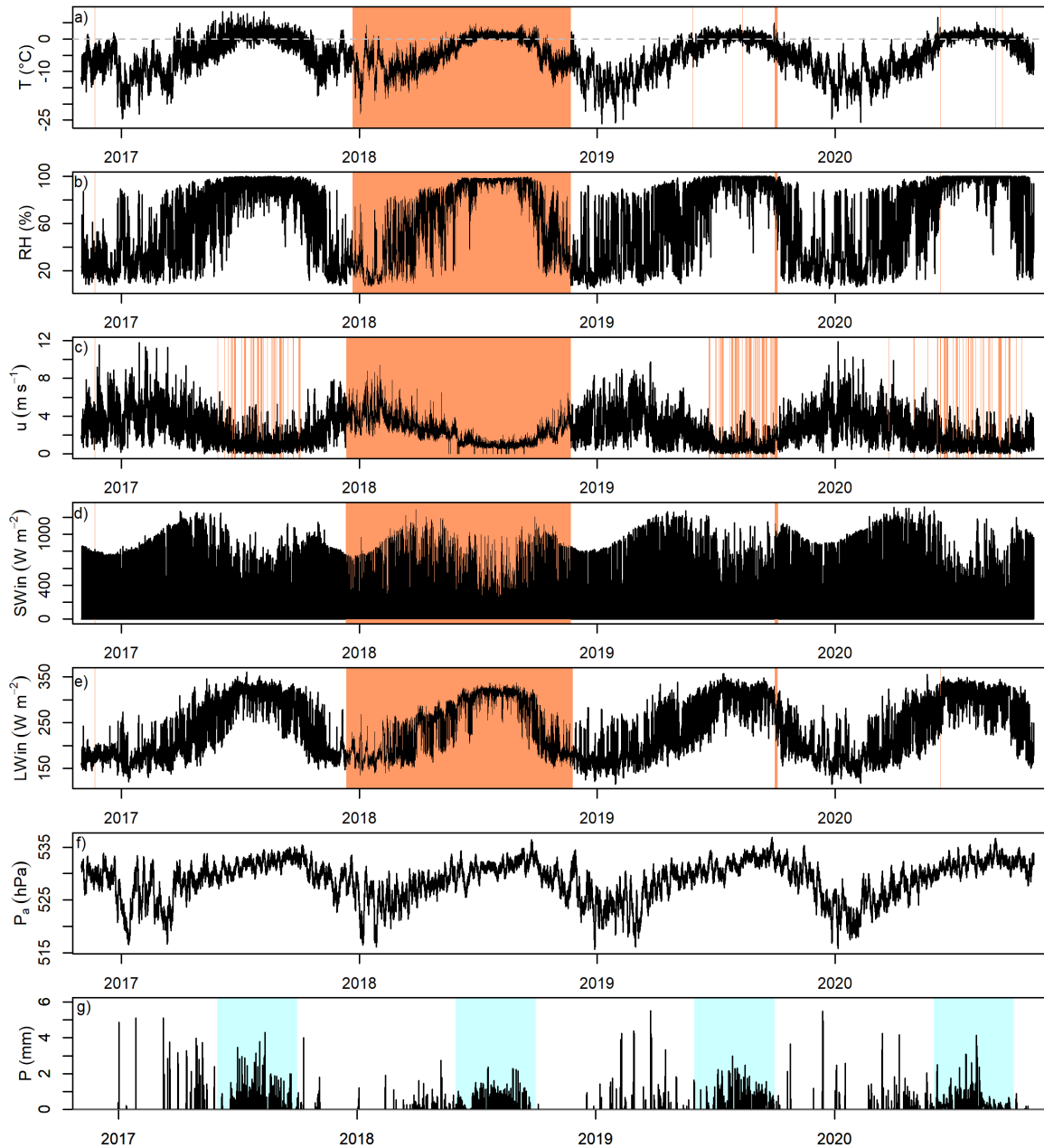


Figure 5.2. Hourly data from 1 November 2016 to 31 October 2020 of (a) air temperature (T), (b) relative humidity (RH), (c) wind speed (u), (d) incoming shortwave radiation (SW_{in}), (e) incoming longwave radiation (LW_{in}) at AWS-L, (f) atmospheric pressure (P_a) at Mera La AWS and (g) precipitation (P) at Khare Geonor. Orange shaded areas indicate data gaps at AWS-L, which have been filled by Mera La AWS data using linear interpolation, and the light blue shaded areas in panel (g) visualise the monsoons.

5.5.2 Spatial distribution of meteorological forcings

Given the complexity and heterogeneity of the local climate and terrain, it is a challenging task to distribute point data spatially. For air temperature, relative humidity and incoming longwave radiation, we derived empirical linear relationships from the respective measurements of the two on-glacier AWSs installed with a 410 m difference in altitude. To take advantage of the longest data series without gaps at AWS-H, we calculate the gradients between 01 March 2018 and 28 February 2019, even though a major part of the data from AWS-L is reconstructed over this period. Since AWS-L has a relatively longer and more consistent dataset than AWS-H, we distribute meteorological data from this lower station

across the glacier using observed altitudinal gradients of air temperature, relative humidity, and incoming longwave radiation (Table S5.2; Figure S5.4). In meteorology, the dew-point temperature gradient is more commonly encountered than the relative humidity gradient. However, in this particular study, the relative humidity gradient is utilised because the COSIPY model is developed based on relative humidity input data. For completeness, we also compute the dew-point temperature gradient from data collected at both stations, which we subsequently convert into a relative humidity gradient. This converted gradient is comparable to the one directly obtained from relative humidity measurements at AWS-L and AWS-H, that we use in our study (Figure S5.5 and corresponding supplementary text).

The incoming solar radiation has been distributed for each grid following the methods of Sauter et al. (2020), already tested and applied on Himalayan glaciers (e.g., Arndt and Schneider, 2023). First the fraction of diffuse radiation (F_{diff}) is calculated based on Wohlfahrt et al. (2016):

$$F_{diff} = e^{-e^{p1 - (p2 - p3CI)}} * (1 - p4) * p4 \quad (5.1)$$

Where $p1 = 0.1001$, $p2 = 4.7930$, $p3 = 9.4758$, $p4 = 0.2465$ are parameters from Wohlfahrt et al. (2016) and CI , for clearness index, is the ratio of incoming solar radiation to maximum incoming solar radiation. F_{diff} may vary from 0 to 1. Second, the measured incoming shortwave radiation is splitted into beam ($R_b = SW_{in} * (1 - F_{diff})$) and diffuse ($R_d = SW_{in} * F_{diff}$) radiation. Then, the corrected solar radiation (R_c) is calculated on each grid based on Ham (2005).

$$R_c = R_b * cf + R_d \quad (5.2)$$

Where cf is the correction factor calculated based on the azimuth and the slope of each grid following Ham (2005).

As our network does not allow to assess precipitation variations with elevation over Mera Glacier catchment, precipitation amounts are assumed constant all over the catchment and equal to Khare Geonor records. Similarly, wind speed is likely spatially variable due to terrain aspect, roughness and heterogeneity but in first approximation, we had no choice but to consider the wind as constant over Mera Glacier and equal to that at AWS-L. These first-order approximations are discussed in section 5.6.3.

5.5.3 Mass balance data

Mera Glacier has been monitored since 2007 at least once a year in November and its mass balance series is one of the longest continuous field-based series of the Himalayas. Its glacier-wide mass balance is obtained annually using the glaciological method based on a network of 16 ablation stakes and five accumulation sites on average (Figure 5.1). This glacier-wide mass balance series has been calibrated with the 2012-2018 geodetic mass balance (Wagnon et al.,

2021). Over the period 2007-2023, the mean corrected glacier-wide mass balance is equal to -0.42 ± 0.23 m w.e. a^{-1} , with only four positive mass balance years out of 16. Our study period 2016-20 was characterized by constantly negative mass balance years with a mean glacier-wide value of -0.74 ± 0.18 m w.e. a^{-1} , 2017-2018 being the most negative year (-0.92 ± 0.16 m w.e. a^{-1}) and 2019-2020 being the least negative (-0.49 ± 0.22 m w.e. a^{-1}) (Table 5.2). Between 2007 and 2023, the glacier has lost around 10 % of its surface area.

Point mass balances measured at each stake or at each accumulation site can exhibit significant spatial variability depending on factors such as elevation, slope, aspect, and wind redistribution. Table 5.2 provides the annual and mean values of point mass balances over the study period 2016-20 at the two on-glacier AWSs. For AWS-L, it is computed by using all stake measurements available on Naulek branch between 5300 and 5380 m a.s.l., using a mean measured snow density of 370 kg m^{-3} and an ice density of 900 kg m^{-3} . For AWS-H, point mass balances measured at sites located between 5750 and 5790 m a.s.l. in the vicinity of the station are averaged, using depth averaged snow densities measured during each field campaign (from 380 to 430 kg m^{-3}).

Table 5.2. Glacier-wide mass balance for Mera Glacier, point mass balance at AWS-L (obtained by averaging all stake measurements on Naulek branch between 5300 and 5380 m a.s.l.) and at AWS-H (obtained by averaging stake measurements close to AWS-H, from 5750 to 5790 m a.s. l.), as well as snow depths in the ablation area (annually measured during field campaigns in November) and in the accumulation area (assumed for the model). An ice density of 900 kg m^{-3} and measured snow densities were used to compute point mass balances (370 kg m^{-3} for Naulek, and 380 to 430 kg m^{-3} for the accumulation area). The error range for point mass balances is the standard deviation of all measurements.

Glaciological mass balance of Mera Glacier					
	2016/17	2017/18	2018/19	2019/20	2016-20
Glacier-wide mass balance* (m w.e. a^{-1})	-0.76 ± 0.16	-0.92 ± 0.16	-0.80 ± 0.19	-0.49 ± 0.22	-0.74 ± 0.18
Mean point mass balance around AWS-L (m w.e. a^{-1})	-2.26 ± 0.12	-2.34 ± 0.19	-2.27 ± 0.10	-2.10 ± 0.24	-2.24 ± 0.09
Mean point mass balance around AWS-H (m w.e. a^{-1})	0.16 ± 0.01	-0.08 ± 0.07	0.12 ± 0.13	0.35 ± 0.12	0.14 ± 0.15
Snow depth in the ablation zone (< 5750 m a.s.l.) used for the model initialisation (m)	0.50	0.12	0	0.20	
Snow depth in the accumulation zone (> 5750 m a.s.l.) used for the model initialisation (m)	0.50 m at 5750 m a.s.l. and an additional 0.20 m for each 100 m increase in altitude				

* updated from Wagnon et al. (2021)

5.6 Methods

5.6.1 Model description (COSIPY)

In this study, we use COSIPY model, which is a python-based coupled snowpack and ice SEB model (Sauter et al., 2020). The model is a one-dimensional multi-layer discretisation of the snowpack/ice column that resolves the energy and mass conservation, and calculates the surface energy fluxes using input meteorological variables as forcings. For spatially distributed simulations, the point model is run independently at each point of the glacier domain, neglecting the lateral mass and energy fluxes. The model's reliability has been validated across distinct contexts and geographical regions (Sauter et al., 2020; Blau et al., 2021; Arndt et al.,

2021). COSIPY model calculates the energy available for melt (QM) for each time step and is expressed as:

$$QM = SW_{net} + LW_{net} + QS + QL + QC + QR \quad (5.3)$$

where SW_{net} is the remaining net shortwave radiation at the surface after penetration inside the snow/ice surface, LW_{net} is net longwave radiation and Q denotes the other heat fluxes of different subsequent scripts S: sensible, L: latent, C: sub-surface (called ground-heat flux in Sauter et al., 2020), and R: rain in $W m^{-2}$. All the fluxes are positive when directed towards the surface and negative away from the surface. When the surface temperature is at the melting point and $QM > 0$, the excess energy is used to melt. Additionally, COSIPY calculates a subsurface melt, that is calculated from the penetration of the incoming shortwave radiation (Sauter et al., 2020). For the rest of the analysis, we refer to total melt as the sum of surface and subsurface melt.

5.6.1.1 Model settings

The COSIPY model is used in its default configuration. The turbulent fluxes, QS and QL , are calculated as:

$$QS = \rho_{air} C_p C_s u (T - T_s) \quad (5.4)$$

$$QL = \rho_{air} L_v C_l u (q - q_s) \quad (5.5)$$

where ρ_{air} is air density (in $kg m^{-3}$); C_p is the specific heat of air at constant pressure (in $J kg^{-1} K^{-1}$) and L_v is the latent heat of sublimation/vaporization (in $J kg^{-1}$). C_s and C_l are the dimensionless transport coefficients calculated using the bulk method with initial roughness lengths taken from Mölg et al. (2012) and further calibrated (see section 5.6.2), q is the specific humidity of air (in $g kg^{-1}$), T_s and q_s are the temperature (in $^{\circ}C$) and specific humidity at the surface, respectively. The bulk Richardson number has been used to assess the stability correction.

The snowfall is distinguished from liquid precipitation using a logistic transfer function based on Hantel et al. (2000) (Figure S5.6):

$$n = \frac{1}{2} \{ \tanh [((T - T_0) - T_{00}) s_0] + 1 \} \quad (5.6)$$

where n is the fraction of snowfall (1 when it is only snow, 0 if only rain and in between 0 and 1 if this is mixed rain and snow), T_0 is the melting point ($0^{\circ}C$), T_{00} is the center for snow transfer function (in $^{\circ}C$) and s_0 is spread snow transfer function. The aging/decay of the

snowpack's albedo is then based on Oerlemans and Knap (1998), where it depends on the number of days after the last snowfall. Snow density is another important property of snow, particularly for its liquid water content or thermal conductivity. It is obtained by following Essery et al. (2013). The default albedo and densification parameterizations used in this study are described in the supplementary material (see additional text related to the method section p. 9-10).

5.6.1.2 Model description and initialisation

We run COSIPY at point scale at AWS-L and in a distributed way over 51 glacierized grid points of $0.003^\circ \times 0.003^\circ$ (0.0984 km^2) resolution (corresponding to a total glacier-covered area of 5.01 km^2), resampled from Copernicus GLO-30 DEM (<https://doi.org/10.5270/ESA-c5d3d65>) using the glacier outlines in 2012 (5.10 km^2) from Wagnon et al. (2021). Additionally, the grid elevations were adjusted downward by 19 meters to align with the elevation of AWS-L. The selection of this particular resolution is a compromise between the computational time and a reasonable representation of the topography. The model is run at an hourly time scale, independently for the four years of data, from 1 November of one year until 31 October of the following year over 2016-20, without spin-up time. We impose a temperature of 265.16 K at the glacier sole because the glacier is cold-based (Wagnon et al., 2021). The model is initialised with 600 layers of glacier ice topped by a snowpack whose profile is specified by the user. In our case, this profile is determined by the snow depth (Table 5.2), with each layer having an optimal snow layer height of 0.1 m. The initial snow depth in the ablation zone is kept closest to the observations made every November, corresponding to the snow depth measurement at AWS-L. Above 5750 m a.s.l., the model is initialised with a snow depth that increases by 20 cm per 100 m with altitude, starting at 50 cm on 1 November at 5750 m a.s.l. (Table 5.2). This assumption is essential because it ensures that there is always snow in the accumulation zone for the simulations. Even though annual observations in November show that the snow line is always lower than 5750 m a.s.l., which is in line with this assumption, the altitudinal gradient is not verifiable in the field. The snow depth in the accumulation zone is probably greater than that used for the initialisation, as the firn-ice interface is several metres below the glacier surface. However, for modelling purposes, the initial snow depth within this zone is of minimal concern as accumulation consistently outweighs ablation, and the snow depth gradually synchronises with the ongoing snowfall.

5.6.2 Optimisation

SEB models are sensitive to the choice of parameter sets (e.g., Zolles et al., 2019). Consequently, model parameters need to be calibrated, and the model's ability to reproduce the glacier surface mass balance needs to be evaluated. We optimise the model following a multi-objective optimisation procedure using forcing data measured at AWS-L between 1 November 2018 and 31 October 2019, the mass balance year with the least gaps and the most reliable dataset. The optimisation is performed based on the maximum amount of data available i.e., observed albedo, surface temperature calculated from LWout using the Stefan-Boltzmann equation with a surface emissivity of 0.99 (Blau et al., 2021), and point mass balance at AWS-L (Table 5.2).

5.6.2.1 Parameters

There are many parameters in COSIPY and the eight important ones are listed in Table 5.3. To identify the most sensitive ones among this set, we conducted 108 manual model runs at a point-scale, specifically at AWS-L. In these runs, we alternatively and randomly explored various values for selected sensitive parameters, focusing on five parameters related to albedo and three associated with roughness lengths. This rigorous testing encompassed a plausible range of values, allowing us to qualitatively assess their impact on the model's outcomes. These ranges of albedo parameters and roughness lengths are taken from Mölg et al. (2012). As we only have one level of wind speed measurement at AWS-L, roughness lengths cannot be directly calculated at this site. Notably, the roughness lengths exhibited lower sensitivity compared to the albedo parameters, which were identified as the most sensitive (in bold in Table 5.3). These albedo parameters are known sensitive parameters for energy balance studies (e.g., Zolles et al., 2019). We then optimise these five parameters following the procedure described in section 5.6.2.2 starting from a plausible range of values taken from the literature (Mölg et al., 2012; Zolles et al., 2019). All other parameters are taken from the default settings, except those listed in bold in Table 5.3, that are optimised.

Table 5.3. List of selected parameters used in COSIPY, and manually tested before running our optimisation procedure. In bold are the 5 most sensitive parameters that are optimised from a plausible range of values (Min-Max range, taken from the Mölg et al. (2012) and used in this present study). The investigated range of max-min values for the roughness lengths is also shown.

Parameters	Min	Max	Optimised/default
Fresh snow albedo	0.82	0.88	0.85
Firn Albedo	0.50	0.60	0.55
Ice albedo	0.25	0.35	0.30
Albedo time scaling factor (days)	3	9	3
Albedo depth scaling factor (cm)	2	14	4
Roughness length for fresh snow (mm)	0.19	0.29	0.24
Roughness length for firn (mm)	1.5	6.5	4
Roughness length for ice (mm)	0.7	2.7	1.7

5.6.2.2 Multi-objective optimisation

Multi-objective optimisation is a calibration method that enables the possibility of more than one optimal solution and provides a way to evaluate a variety of parameter sets (Yapo et al., 1998; Rye et al., 2012; Zolles et al., 2019). The multi-objective approach can be expressed as:

$$\text{minimise } \{f_1(\theta), f_2(\theta), \dots, f_n(\theta)\} \quad (5.7)$$

where $f_1(\theta), f_2(\theta), \dots, f_n(\theta)$ are n objective functions of model realisations of parameter sets θ . The optimisation process combines multiple objectives into a single ideal through scalar aggregation. For this, a weighted sum ($f_{agg}(\theta)$) is applied to find the minimum aggregate of different single objectives (Rye et al., 2012):

$$\text{minimise } f_{agg}(\theta) = \{w_1 f_1(\theta), w_2 f_2(\theta), \dots, w_n f_n(\theta)\} \quad (5.8)$$

where w is the weight applied to all single objectives based on their performance and the arguments of the aggregating functions to obtain the Pareto solution (Pareto, 1971). With the

multiple single objective, the selection of Pareto solution and multi-objective is more precise. Here, the multi-optimisation is done based on three objective metrics that compare the observation at AWS-L and model outputs:

$$f_1(\theta) = \left[\frac{\sum_{i=1}^n (x_i - \bar{x})(y_i - \bar{y})}{\sqrt{\sum_{i=1}^n (x_i - \bar{x})^2} \sqrt{\sum_{i=1}^n (y_i - \bar{y})^2}} \right]^2 \quad (5.9)$$

$$f_2(\theta) = \frac{1}{N} \left| \sum_{i=1}^N (y_i - x_i) \right| \quad (5.10)$$

$$f_3(\theta) = |(MB_{obs} - MB_{mod})| \quad (5.11)$$

where f_1 is the coefficient of determination (r^2) between the observed (x_i) and modelled (y_i) values of albedo and surface temperature (T_s), f_2 is the mean absolute error (MAE) between the observed (x_i) and modelled (y_i) values of both variables and f_3 is the absolute error (AE) between observed (MB_{obs}) and modelled (MB_{mod}) point mass balances.

The simplest way to calibrate the model is to optimise the different objective functions for four study periods (4 years x 3 objective functions = 12 performances). This approach results in a large range of uncertainty with many sensitive parameters for different mass balance years. Similarly, the set of parameters optimised for one period may not perform better in another period, resulting in higher uncertainty (Soon and Madsen, 2005). However, by simulating Pareto solutions for individual mass balance years and evaluating the objective functions over the other years, it is possible to select the best set of parameters.

5.6.3 Evaluation of the model at point and distributed scale

First, we optimise the five sensitive model parameters highlighted in Table 5.3 at AWS-L for the 2018/19 period. Second, we evaluate the model performance at point scale at AWS-L site for the other three mass balance years, systematically comparing measured and simulated albedo, surface temperature and point mass balance. Third, we run the model in a spatially distributed way and similarly evaluate it at point scale at AWS-H site, over the three years of available data (2017-20). Finally, we also compare simulated mass balance to measured surface mass balance at glacier-wide scale for each year between 2016 and 2020. This allows us to test both the spatial and the temporal transferability of the model optimised parameters.

5.6.4 Sensitivity analysis

Our study aims to evaluate the sensitivity of the surface mass balance to changes in meteorological forcings. In previous studies, the sensitivity to temperature or precipitation is usually assessed by a constant change in temperature (e.g., $\pm 1-2$ °C) or a relative change in precipitation (e.g., $\pm 10-30$ %), keeping all other meteorological variables unchanged at the same time (Kayastha et al., 1999; Mölg et al., 2012; Azam et al., 2014; Sunako et al., 2019; Arndt et al., 2021; Gurung et al., 2022; Arndt and Schneider, 2023). The main disadvantage of this method, hereafter referred to as the classical method, is that perturbing a single meteorological variable breaks the physical links between the meteorological variables, which

is detrimental to the simulation of surface mass balance (e.g., Prinz et al., 2016; Clauzel et al., 2023). To overcome this issue, a number of methods were developed to perturb meteorological data while preserving the link between variables (Sicart et al., 2010; Prinz et al., 2016; Autin et al., 2022). Here we both perturb the meteorological forcings in a classical way and we produce synthetic scenarios, described below (see also Figure S5.7 for a flow chart explaining how scenarios are obtained).

5.6.4.1 *Classical scenarios*

For the classical sensitivity analysis method, the scenarios are developed by varying temperature by $\pm 1^\circ\text{C}$ and precipitation amount by $\pm 20\%$ for four mass balance years without changing the other meteorological variables. In total, we produce 16 runs ($+ 1^\circ\text{C}$, $- 1^\circ\text{C}$, $+ 20\%$ and $- 20\%$ for each of the four years) between 2016 and 2020. In order to determine the sensitivity of the mass balance to temperature or precipitation, it is then simply necessary to calculate the average anomaly in the mass balance over the four-year period for each corresponding perturbation.

5.6.4.2 *Synthetic scenarios*

Utilising the initial four-year dataset, we performed a cyclic selection process, systematically considering each month of the year commencing with November and concluding in October of the subsequent year. During each cycle, we alternately chose data from the unaltered original dataset and data from the warmest, coldest, wettest, or driest month within the four-year period (2016-20). This process allowed us to generate synthetic annual datasets at an hourly resolution. By this way, we create 180 one-year-long synthetic meteorological series, exploring a wide range of climatic variability from very warm to very cold conditions, and from very dry to very wet conditions (see details below). For each scenario, for each month, we keep original hourly data and we only shuffle the months from different years with each other. In this way, both the physical integrity between meteorological variables and the weather conditions with respect to the time of the year are preserved.

First, the four most extreme synthetic scenarios are developed by making one-year long series of hourly forcing data that contain the most extreme months among the four years of data. For instance, the wet scenario (hereafter referred as We_We) is obtained by combining the wettest (We) months: if November 2017 is the month with the maximum monthly amount of precipitation among the four months of November of the 2016-20 series, all hourly forcing data from November 2017 are selected in scenario We_We; then if December 2019 is the wettest of the four December months, then hourly data from December 2019 will be selected as the second month of scenario We_We; etc. until October. In this way the wet scenario We_We combining the hourly data of all meteorological variables from the 12 months with the maximum monthly amount of precipitation is created. Similarly, we combine the hourly data of all meteorological variables from the 12 driest months to create the dry scenario (D_D), or from the 12 warmest months to create the warm scenario (Wa_Wa), or from the 12 coldest months to create the cold scenario (C_C).

Second, starting from these four extreme scenarios referred hereafter as baseline conditions, we also create 48 additional scenarios by modifying some specific seasons. For instance, we

keep the conditions of the wet scenario W_e , except during one season, let's say the monsoon, where we decide to take the conditions of the warm scenario W_a . The four considered seasons are winter (win), pre-monsoon (pre), monsoon (mon), and melting season (melt). We decide not to consider the post-monsoon which is not critical for the glacier mass balance because there is usually neither any large precipitation nor any large melt but we prefer to introduce a six-month long melting season which we suspect to be more critical to control the glacier mass balance. This melting season covers half of the year from May to October, the only months where significant melt is observed in the field. The synthetic scenarios follow the naming convention AB_x , where A is the climate baseline coming from the four extreme scenarios, so A is either W_e , D, C, or W_a , B characterizes the conditions of the modified season i.e., B is also either W_e , D, C, or W_a and X refers to the season that has been modified to create the additional scenario, so X is either win, pre, mon, or melt. In case of the specific example described above, the scenario is named $W_e_W_a_{mon}$ which means that the dataset is one year long, using hourly forcing data from the wet scenario except during the monsoon where the warmest months are selected. A can take 4 values, B can take 3 values and X can take 4 values (the number of values for B cannot be similar to that of A, otherwise we define one of the extreme scenario), resulting in a total of $4 \times 3 \times 4 = 48$ scenarios.

Similarly, we also mix the original unshuffled data (U) from each year of the study period with extreme months. U can be alternatively 2016/17, 2017/18, 2018/19 or 2019/20 respectively referred as 2017, 2018, 2019 or 2020. These scenarios follow the same naming convention, with U being an additional value for A and B. For example, the scenario $2018_W_a_{mon}$ corresponds to the unchanged original data of the year 2017/18, except during the monsoon where data from the warmest months are selected. We obtain here $4 \times 4 \times 4 = 64$ scenarios. Similarly, D_2020_{melt} corresponds to the driest months, where months of the melting season have been replaced by the original 2019/20 data. Again, we obtain here $4 \times 4 \times 4 = 64$ scenarios. In total, we have $4 + 48 + 64 + 64 = 180$ scenarios.

For each of these 180 synthetic annual datasets, we calculate the glacier-wide annual mass balance of Mera Glacier using COSIPY and calculate the difference from the mean annual glacier-wide mass balance simulated by COSIPY using the original 2016-20 dataset. We call this difference the mass balance anomaly. Similarly, we have an anomaly for each forcing meteorological variable. We can now derive the mass balance sensitivity to each meteorological variable by fitting a linear regression between the mass balance anomaly and the anomaly of the variable under consideration. The slope of this linear relationship gives the mass balance sensitivity to the given variable. The error bars on these sensitivities for ± 1 °C temperature and ± 20 % precipitation variation have been calculated using the 99 % confidence interval, given by three standard deviations, of this linear regression.

5.7 Results

5.7.1.1 *Optimisation and evaluation*

The point-scale optimisation strategy at AWS-L results in a well identified group of parameter sets (Pareto solutions) that minimise multiple objective functions simultaneously (Figure 5.3). The objective functions of each set of original parameters are largely scattered with the range

of r^2 and MAE of albedo being 0.06-0.54 and 0.11-0.25, respectively (Figure 5.3a). Similarly for surface temperature, r^2 and MAE are in-between 0.81-0.92, and 1.37-3.24 °C, respectively (Figure 5.3d). The range of AE is 0-3.92 m w.e. for the point mass balance at AWS-L (Figure 5.3b,c,e,f). The 200 solutions closest to the utopia point in terms of how well they perform across all objective functions represent the Pareto solutions (Figure 5.3: bold black dots). All these multiple Pareto solutions are almost equally good and plausible. The metrics of the Pareto solutions are less scattered than the original ensemble, with the range of r^2 and MAE of albedo being 0.31-0.54 and 0.11-0.15 (Figure 5.3a), and the range of r^2 and MAE of surface temperature being 0.87-0.92 and 1.58-2.33 °C (Table 5.4). The range AE is 0-1.28 m w.e. for the point mass balance at AWS-L (Table 5.4).

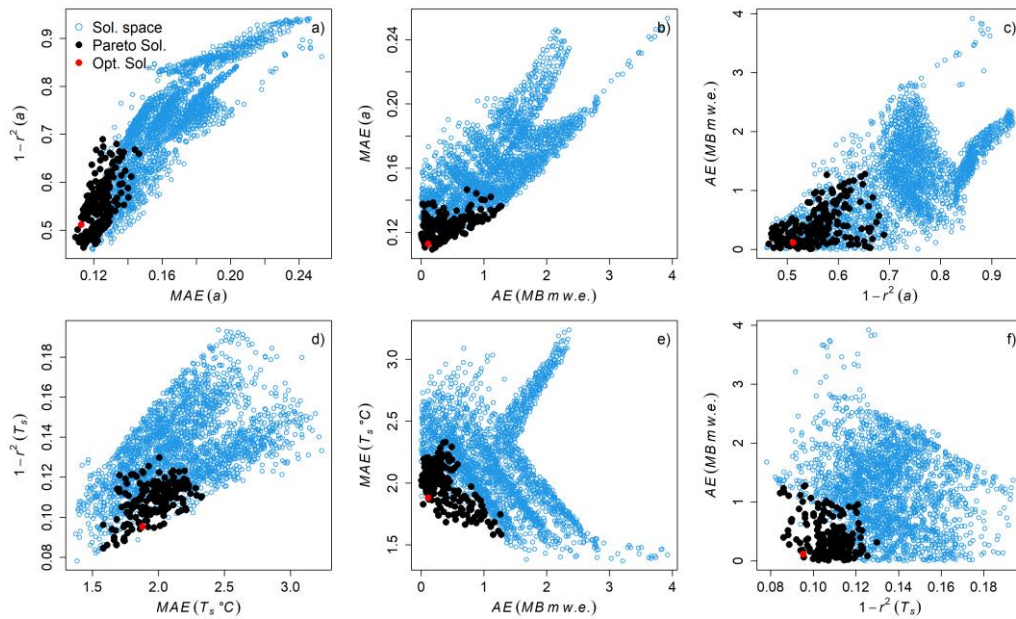


Figure 5.3. Solution space for the multi-objective optimisation for the period 1 November 2018 – 31 October 2019. One dot represents results obtained with one set of parameters, and bold black and red dots define the Pareto solution space and optimised solution, respectively. Plots show the scatter plot between a) $1-r^2$ and MAE from albedo comparison, b) MAE from albedo comparison and AE from mass balance comparison, c) AE of mass balance comparison vs $1-r^2$ from albedo, d) $1-r^2$ and MAE from surface temperature comparison, e) MAE from surface temperature comparison and AE from mass balance and f) AE of mass balance vs $1-r^2$ from surface temperature comparison.

Table 5.4. The range of different objective function values in the first 200 Pareto solution space for 2018/19 period at AWS-L.

Objective function	Albedo	Surface temperature	Mass balance
$f_1(\theta)$	0.31-0.54	0.87-0.92	
$f_2(\theta)$	0.11-0.15	1.58-2.33 °C	
$f_3(\theta)$			0-1.28 m w.e.

Since Pareto solutions perform well over all time and space ranges, the best parameter set among these Pareto solutions is then chosen as the optimised set (Table 5.3). The r^2 and MAE between the observed albedo and that resulting from the selected optimised parameter set are 0.48 and 0.12, respectively; similarly, for surface temperature r^2 and MAE are 0.91 and 1.92 °C, respectively (Figure 5.4), and AE for the point mass balance is 0.17 m w.e. This final optimised set of parameters corresponds to a time scaling factor of three days and a depth scaling factor of four centimetres for the albedo model (Oerlemans and Knap, 1998) as well as values of albedo of snow (0.85), firn (0.55) and ice (0.30) similar to the default values used in COSIPY (Table 5.3).

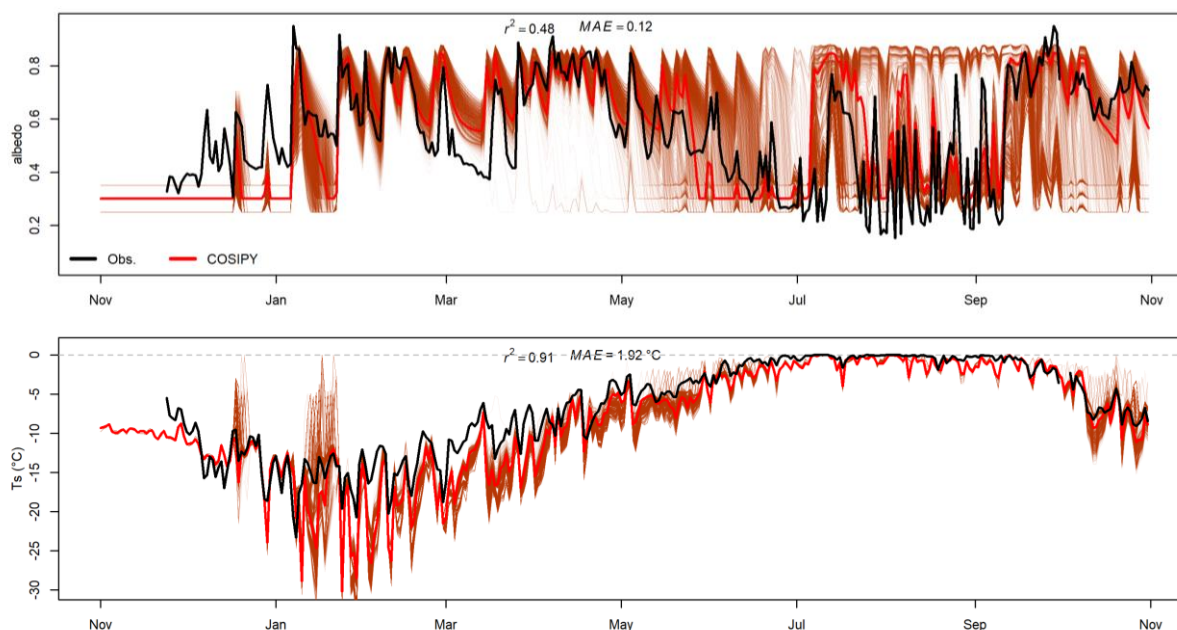


Figure 5.4. Mean daily snow albedo (top) and surface temperature (bottom) from observation (Obs., black line) and simulated with COSIPY between 1 November 2018 and 31 October 2019 at AWS-L. r^2 and MAE represent the correlation coefficient and mean absolute error between the observed and simulated variables, respectively. The red thick line and the brown thin lines represent the simulated variables using the final optimised parameter set and using all other solution spaces, respectively.

5.7.1.2 Glacier-wide simulation of COSIPY

The good performance of COSIPY simulations at point scale with the optimal set of parameters does not guarantee the good performance of the distributed simulations that rely on additional hypotheses, such as the meteorological forcing distribution that changes the meteorological forcings even at the AWS-L location, because for instance SWin is re-computed at AWS-L based on the slope and the aspect of the considered grid cell. We thus evaluate the distributed COSIPY simulations over the period 2016-20 with the albedo and surface temperature at AWS-L and AWS-H, and with the glacier-wide mass balance. r^2 (MAE) for albedo is 0.32 (0.15) and 0.16 (0.14) for the 2016/17 and 2019/20 years at AWS-L, respectively (Figure S5.8). At AWS-H, over the three-year period 2017-20, r^2 for albedo and surface temperature are 0.50 and 0.92 respectively, and the mean AE for 2016-20 at AWS-H is only 0.15 ± 0.14 m w.e. The surface temperature is always highly correlated with a low bias in both sites (Figure S5.8). These metrics are close to the ones from point-scale simulations.

Additionally, we compare the observed and simulated surface point and glacier-wide mass balances. The simulated point surface mass balances match well with the in-situ measurements obtained at stakes for all the four years (Figure 5.5Figure 5.6). The location of the ELA is well represented in COSIPY simulations and the general shape of the dependency of the surface point mass balance on elevation is satisfyingly reproduced. The glacier-wide mass balance from the model is the mean value from all 51 individual grid cells and it is compared to the in-situ glacier-wide mass balance taken from Wagnon et al. (2021). Over the four year period, the mean observed glacier-wide in-situ mass balance is -0.74 ± 0.18 m w.e. a^{-1} (Table 5.1) and the simulated mass balance is -0.66 m w.e. a^{-1} with a standard deviation of ± 0.26 m w.e. a^{-1} . The largest difference between the observed and modelled glacier-wide mass balance happens in 2019/20, with the simulated mass balance being 0.22 m w.e. less negative than the observed one (Figure 5.5).

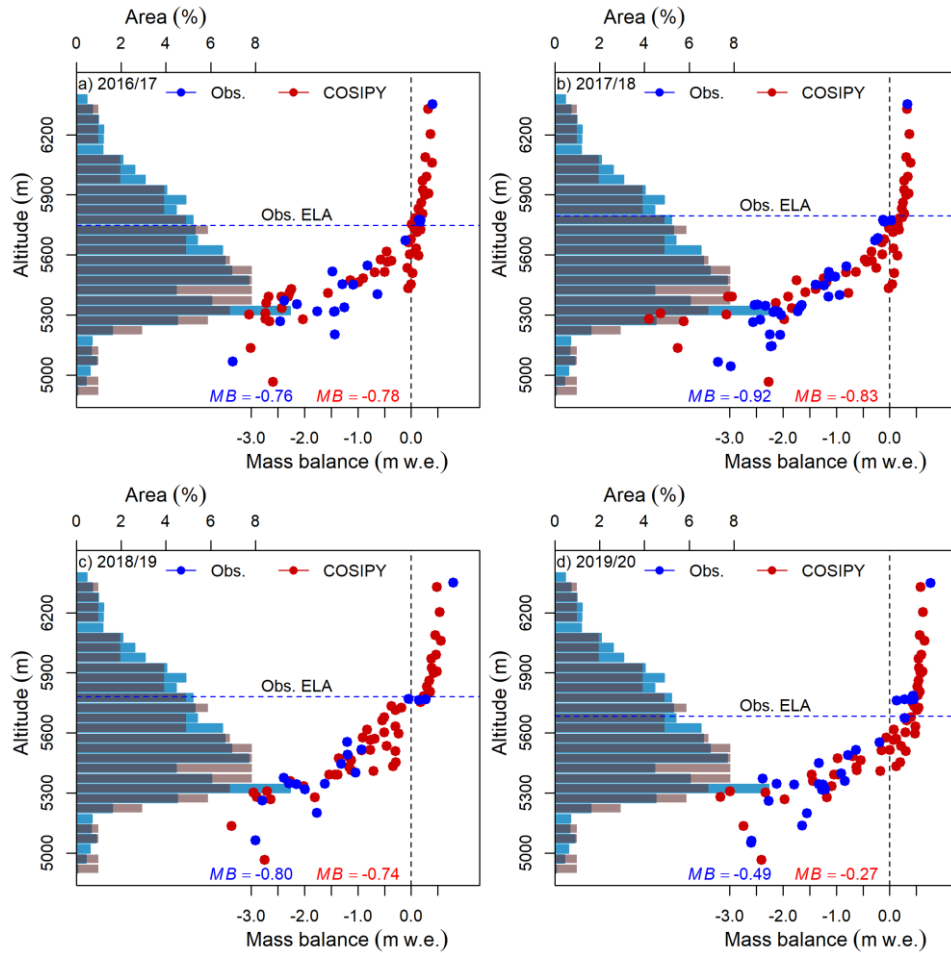


Figure 5.5. In-situ (blue dots) and simulated at each grid cell (red dots) point mass balances as a function of elevation on Mera Glacier for each year of the 2016-20 period. MB is the glacier-wide mass balance obtained from field measurements (blue text) (Wagnon et al., 2021) and simulated with COSIPY (red text). Also shown are the hypsometries of Mera Glacier used for in-situ glacier-wide mass balance calculations (light blue histograms) and for COSIPY (light brown histograms).

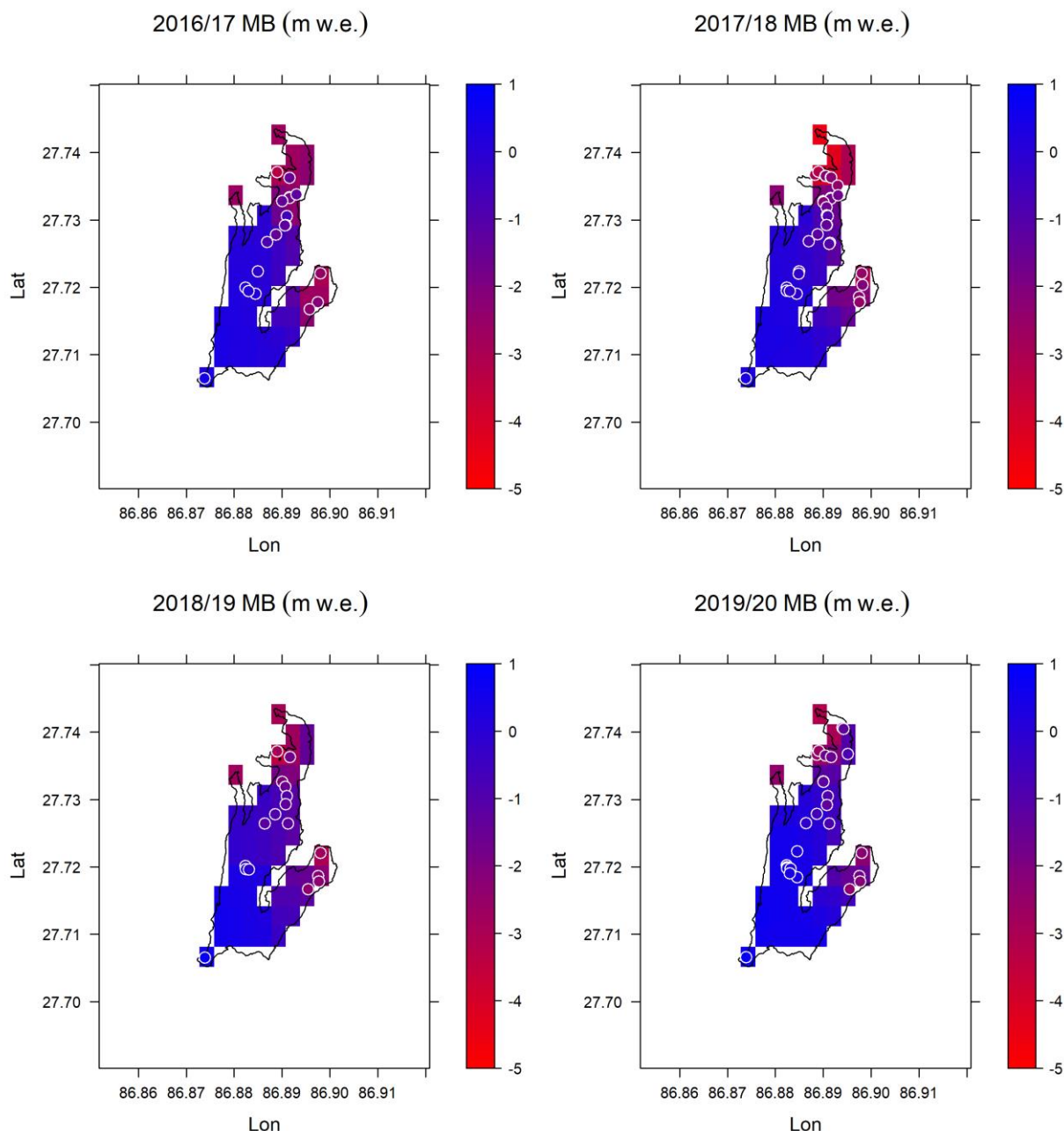


Figure 5.6. Distributed simulated annual mass balance (MB, in m w.e.) for each year of the study period. Also shown as white circles are the point mass balance observations (ablation stakes and accumulation pits) with the inside colour corresponding to the respective annual measurement.

5.7.2 SEB and mass balance components

5.7.2.1 Seasonal and annual energy balance components

Figure 5.7 shows the monthly glacier-wide surface energy and mass balance components at Mera Glacier for the period 2016-20, and Figure S5.9-S16 are maps of the glacier, showing the distributed annual energy and mass fluxes for each year of the study period. Net shortwave radiation (SWnet) is the primary energy source available at the surface throughout the year, the second energy source being the sensible heat (QS), that is significant only between November and March. Along the year, incoming shortwave radiation (SWin) is controlled by the position of the sun responsible for the potential SWin and also by cloudiness, explaining why it decreases from 274 W m^{-2} in the pre-monsoon to 195 W m^{-2} during the monsoon

(Annual and seasonal surface energy fluxes (W m^{-2}) and their contribution to the total energy intake (Q_{in}) and outtake (Q_{out}) over the whole Mera Glacier area, at AWS-L and at AWS-H. The annual values are calculated between 1 November to 31 October of the following year, using all data over the study period. The negative (-) sign indicates the energy loss from the surface. Winter = Dec-Feb, Pre-monsoon = Mar-May, Monsoon = Jun-Sep, Post-monsoon = Oct-Nov.). Similarly, SW_{net} decreases from 83 W m^{-2} during the pre-monsoon to 61 W m^{-2} during the monsoon because of SW_{in} reduction rather than change in albedo (glacier-wide values of 0.71 during the pre-monsoon and 0.70 during the monsoon). The change in air temperature and water vapour (moisture) is responsible for a strong increase of incoming longwave radiation (LW_{in}) from the pre-monsoon (217 W m^{-2}) to the monsoon (296 W m^{-2}), the only season when LW_{in} nearly counterbalances the outgoing longwave radiation (LW_{out}).

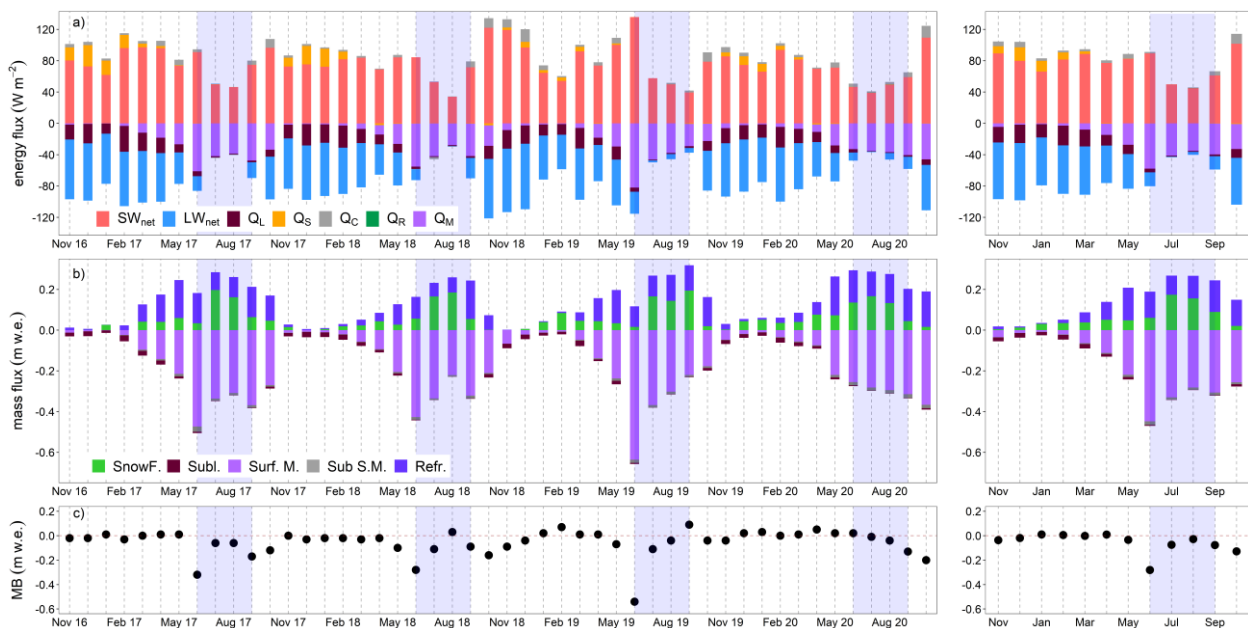


Figure 5.7. Glacier-wide monthly (a) energy fluxes, (b) mass fluxes and (c) mass balance from November 2016 to October 2020 on Mera Glacier (left panels) and mean monthly annual cycle (right panels). SW_{net} = net shortwave radiation, LW_{net} = net longwave radiation, Q_L = latent heat flux, Q_S = sensible heat flux, Q_C = subsurface heat flux, Q_R = rain heat flux, Q_M = available melt energy at the surface, SnowF. = solid precipitation, Subl. = sublimation, Surf. M. = melt at surface, Sub S. M. = subsurface melt and Refr. = refreezing. Blue shaded areas visualise the monsoons.

The total energy intake at the surface is highest and almost similar during the pre-monsoon (496 W m^{-2}) and the monsoon (491 W m^{-2}) (Table 5.5). However, the net all-wave radiation, calculated as the sum of SW_{net} and LW_{net} , is 32 W m^{-2} during the pre-monsoon and 20 W m^{-2} higher during the monsoon. This indicates that the change in cloud cover and atmospheric condition has a relatively minor effect on the total energy intake at the glacier surface, but does impact the net all-wave radiation. In the pre-monsoon, this net all-wave radiation is equally compensated by latent heat (Q_L) and melting energy (Q_M) ($\sim -16 \text{ W m}^{-2}$ each). During the monsoon, LW_{net} and Q_L are both reduced or close to zero leaving all the energy available for melt with an average energy value of -43 W m^{-2} . The contributions of sensible heat (Q_S) and ground heat flux (Q_C) are always low during the pre-monsoon and the monsoon, while the rain heat flux (Q_R) is negligible all the time.

The energy balance components vary across different glacier areas; they are analysed in the ablation area at AWS-L and in the accumulation area at AWS-H. When considering the annual

means, the magnitudes of SWnet and QM are higher at AWS-L (93 and -34 W m⁻², respectively) than at AWS-H (61 and -15 W m⁻², respectively). LWnet, QL, and QS exhibit similar annual means throughout the year at both sites. At AWS-L, SWnet remains similar during the pre-monsoon (87 W m⁻²) and the monsoon (88 W m⁻²) because the decrease in SWin (287 W m⁻² in the pre-monsoon and 201 W m⁻² in the monsoon) is compensated by a decrease in albedo (0.70 in the pre-monsoon and 0.56 in the monsoon). The albedo remains high at AWS-H during the whole year, and there is thus a decrease of SWnet in the monsoon (43 W m⁻²) compared to the pre-monsoon (76 W m⁻²). The variation of LWnet at AWS-L and AWS-H is rather small as the difference between LWin and LWout remains similar. Comparing both sites, QL remains rather similar during all seasons. QM dominates QL all year round except during the winter at AWS-L, but at AWS-H, QL always dominates QM, except during the monsoon. QS is significant only during the cold months of the winter and the post-monsoon, with a similar magnitude whichever the location. QC is positive and rather small (<5 W m⁻², slightly higher during the post-monsoon) all year round except during the monsoon at AWS-L where it is slightly negative (Table 5.5).

Table 5.5. Annual and seasonal surface energy fluxes (W m⁻²) and their contribution to the total energy intake (Qin) and outtake (Qout) over the whole Mera Glacier area, at AWS-L and at AWS-H. The annual values are calculated between 1 November to 31 October of the following year, using all data over the study period. The negative (-) sign indicates the energy loss from the surface. Winter = Dec-Feb, Pre-monsoon = Mar-May, Monsoon = Jun-Sep, Post-monsoon = Oct-Nov.

	SWin	SWout	SWnet	albedo	LWin	LWout	LWnet	QL	QS	QC	QR	QM	Qin	Qout
Annual values (W m⁻²)														
Glacier-wide mean	215	-139	76	0.65	229	-273	-43	-13	4	4	0	-22	453	-447
AWS-L	227	-134	93	0.59	235	-278	-43	-14	4	3	0	-34	470	-460
AWS-H	218	-157	61	0.72	225	-269	-44	-13	4	5	0	-15	453	-454
Seasonal Glacier-wide (W m⁻²)														
Winter	183	-107	76	0.59	172	-237	-66	-22	13	4	0	-2	372	-368
Pre-monsoon	274	-191	83	0.71	217	-268	-51	-16	1	4	0	-17	496	-491
Monsoon	195	-133	61	0.70	296	-306	-10	-2	0	2	0	-43	491	-485
Post-monsoon	217	-121	96	0.56	199	-265	-66	-15	4	9	0	-18	429	-420
Seasonal AWS-L (W m⁻²)														
Winter	196	-113	83	0.58	178	-247	-69	-26	13	5	0	-2	392	-388
Pre-monsoon	287	-200	87	0.70	223	-275	-52	-16	1	5	0	-22	517	-513
Monsoon	201	-113	88	0.56	302	-307	-5	-1	1	-3	0	-66	504	-490
Post-monsoon	235	-108	127	0.46	205	-273	-68	-18	4	6	0	-33	450	-432
Seasonal AWS-H (W m⁻²)														
Winter	183	-120	63	0.66	167	-231	-63	-19	15	3	0	0	368	-369
Pre-monsoon	280	-204	76	0.73	212	-265	-52	-17	1	4	0	-13	496	-498
Monsoon	198	-155	43	0.78	291	-305	-13	-4	-1	5	0	-29	494	-493
Post-monsoon	221	-146	75	0.66	195	-261	-66	-15	4	10	0	-12	430	-433

5.7.2.2 Seasonal and annual mass balance components

Table 5.6 lists the annual and seasonal mass balance components of Mera Glacier. After the direct accumulation (through snowfalls) and surface melt on Mera Glacier, annual refreezing and sublimation are two major mass balance components, refreezing being even higher than

snowfalls. Indeed, at glacier scale, 44 % of the total (surface + sub-surface) melt refreezes annually. The glacier-wide sublimation is -0.15 m w.e. and therefore contributes 23 % of the total mass balance or 6 % of the ablation terms (total melt + sublimation).

Looking at seasonal scale, pre-monsoon and monsoon are important seasons in terms of mass balance processes, as more than 86 % of solid precipitation falls and 84 % of annual melt happens from March to September. However, post-monsoon is not completely negligible in terms of melt (-0.30 m w.e. or 14 % of the annual melt). This melt is almost equal to the surface mass balance (-0.17 m w.e.) due to the limited magnitude of the other processes, and in particular the limited refreezing in the snow free areas of the glacier. The winter is characterized by limited mass balance processes, with approximately 11 % of the annual solid precipitation and 2 % of the annual total melt (Table 5.6).

At glacier scale, the total melt (-0.42 m w.e.) and sublimation (-0.05 m w.e.) during the pre-monsoon are balanced by the refreezing (0.30 m w.e.) and snowfall (0.14 m w.e.), leading to a near zero surface mass balance (Table 5.6). The glacier-wide total melt during the monsoon is -1.42 m w.e., which is higher at AWS-L (-2.15 m w.e.) and lower at AWS-H (-0.99 m w.e.). Depending on the presence and the state of a snowpack (snow depth, density and temperature), melt water refreezes below the surface. Glacier-wide refreezing is 0.49 m w.e. during the monsoon, it is lower at AWS-L (0.19 m w.e.) where ice is often exposed at the surface, and higher at AWS-H (0.70 m w.e.) where there is always a snowpack with negative temperature. The refreezing preserves 35 % (0.49 m w.e) of the total glacier-wide melt during the monsoon; its relative contribution is higher at AWS-H (71 %) than at AWS-L (9 %).

The annual glacier-wide sublimation is -0.15 m w.e. and is nearly identical at both AWSs (-0.16 and -0.15 mm w.e. at AWS-L and AWS-H, respectively; Figure S5.6). Most of the sublimation (93 % glacier-wide) happens outside the monsoon, when cold, dry and windy conditions prevail. Wind is not spatially distributed in our simulations, leading to rather homogeneous sublimation across the glacier. There are few exceptions, like a slightly higher sublimation in winter at AWS-L (-0.07 m w.e.) than at AWS-H (-0.05 m w.e.) due to higher roughness length linked to the surface state (exposed ice at AWS-L versus snow at AWS-H) and to the mixing ratio that depends on the air temperature. Due to the absence of wind, sublimation is insignificant at both AWS sites during the monsoon (Table 5.6).

Table 5.6. Glacier-wide annual and seasonal mass balance components (mm w.e.) over the total glacier area and at point scale at AWS-L and AWS-H using all data over the study period 2016-20. The negative (-) sign indicates a mass loss from the surface.

	Snowfall	Sublimation	Surface melt	Subsurface melt	Total melt	Refreezing	Mass balance
Annual means (mm w.e.)							
Glacier-wide mean	718	-150	-2095	-88	-2183	956	-656
AWS-L	641	-164	-3194	-88	-3282	659	-2144
AWS-H	792	-149	-1434	-88	-1522	1174	297
Seasonal Glacier-wide (mm w.e.)							
Winter	77	-62	-43	-4	-47	27	-4
Pre-monsoon	137	-48	-395	-20	-415	298	-27

Monsoon	479	-10	-1366	-53	-1419	489	-461
Post-monsoon	25	-30	-291	-11	-302	142	-165
Seasonal AWS-L (mm w.e.)							
Winter	77	-74	-51	-6	-57	41	-12
Pre-monsoon	136	-50	-519	-29	-548	368	-94
Monsoon	403	-4	-2098	-47	-2145	191	-1554
Post-monsoon	25	-36	-526	-6	-532	58	-485
Seasonal AWS-H (mm w.e.)							
Winter	77	-54	-11	-1	-12	11	22
Pre-monsoon	138	-51	-309	-17	-326	275	37
Monsoon	551	-15	-929	-57	-986	701	251
Post-monsoon	26	-29	-185	-12	-197	187	-13

5.7.3 Mass balance sensitivity to meteorological forcings

5.7.3.1 Link between meteorological forcing anomalies and mass balance anomalies

In order to analyse the link between the different input meteorological variables and the outputs from the simulations, we calculate anomalies of each variable from the 180 scenarios by subtracting the mean of the original unshuffled 2016-20 simulations (Figure 5.8). From all synthetic scenarios, the magnitude of variation of air temperature is nearly ± 1 °C, whereas for precipitation, it varies from -35 to +55 % annually. The anomalies of relative humidity (± 5 %) and incoming radiations (± 10 W m⁻²) are rather narrow. There are many significant correlations ($p < 0.001$) between the anomalies of the different variables, suggesting that they are likely to be physically related to each other. On an annual scale, the anomaly of air temperature correlates significantly and positively with the wind speed and the air pressure anomalies, and negatively with the precipitation and relative humidity anomalies. Regarding radiations that are expected to have an impact on the mass balance, the SWin anomaly correlates significantly and negatively with the relative humidity, the precipitation and the LWin anomalies. The LWin anomaly correlates significantly and positively with the relative humidity and the precipitation anomalies, and negatively with the SWin and wind speed anomalies.

The mass balance anomaly correlates significantly with the anomalies of every meteorological variables except SWin (Figure 5.8). The correlations between mass balance anomalies and those of LWin, atmospheric pressure, or wind speed are moderate but significant, positive in case of LWin, and negative for the other variables. The correlation between mass balance anomalies and air temperature is significant and highly negative ($r = -0.79$). Mass balance anomalies are highly and positively correlated with those of precipitation ($r = 0.87$) and relative humidity ($r = 0.84$; Figure 5.8).

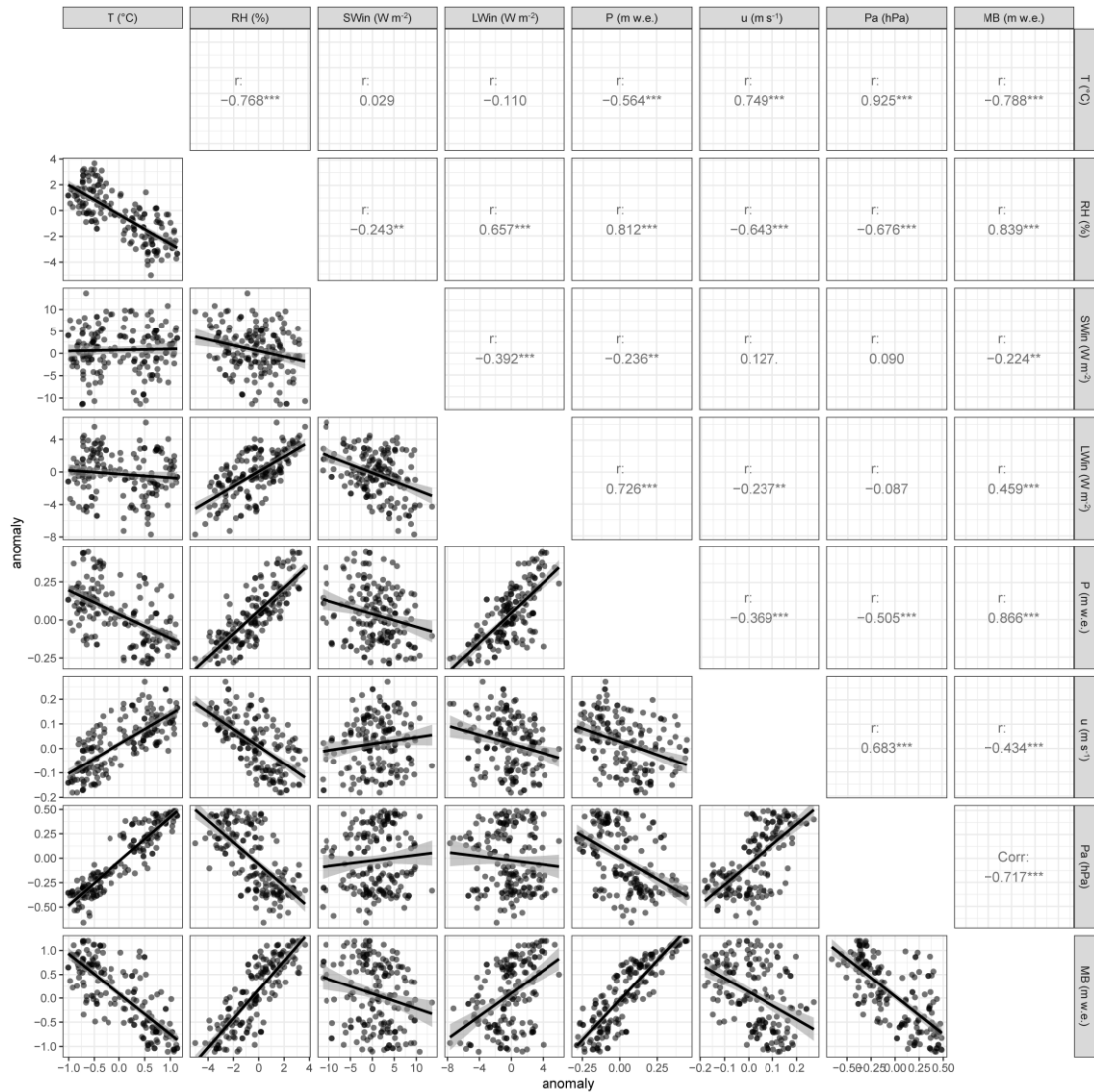


Figure 5.8. Scatter plot between anomalies of different input variables and glacier-wide mass balance anomalies for the 180 synthetic runs. Also shown are the Pearson correlation coefficients between the series of annual anomalies. The black lines represent the linear regressions and the grey shaded areas indicate the standard error. The anomalies of each variable are calculated by subtracting the mean of the original unshuffled 2016-20 simulation. (stars represent significance levels, accordingly: * = 0.05, ** = 0.01, *** = 0.001).

5.7.3.2 Mass balance sensitivity to air temperature and precipitation

From the classical method, we find that perturbing the temperature by +1 (-1) °C leads to a change in glacier-wide mass balance of -0.61 (+0.41) m w.e. (Table 5.7). A -20 (+20) % change in precipitation leads to a -0.79 (+0.48) m w.e change in glacier-wide mass balance (Table 5.7). With the synthetic scenario method, we find that a temperature change of +1 (-1) °C leads to a glacier-wide mass balance change of -0.75 ± 0.17 ($+0.93 \pm 0.18$) m w.e., and a -20 (+20) % change in precipitation results in a mass balance change of -0.60 ± 0.11 ($+0.52 \pm 0.10$) m w.e. Due to the physical link between variables, and in particular the negative correlation between temperature and precipitation, we find that the sensitivity of mass balance to temperature is significantly higher when calculated from synthetic scenarios than from the classical method, especially in case of cooling. For precipitation, it is significantly reduced in case of a precipitation deficit but almost unchanged in case of an increase.

This synthetic scenario approach allows to derive mass balance sensitivities to any meteorological variable, as long as a significant correlation exists between the anomalies of mass balance and the variable under consideration. In particular, as we find a high correlation between mass balance and relative humidity anomalies, we can assess also the mass balance sensitivity to this variable: a -4 (+4) % change in RH corresponds to a -1.02 (+1.38) m w.e. change in mass balance. However, we caution on the interpretation of these correlations, as most of the input meteorological variables covary, the correlations may be significant, but they do not show a causal relationship, that needs to be discussed in the light of the knowledge of the processes (see discussion section).

Table 5.7. Mass balance anomalies as compared to the mean of the four 2016-20 years from the classical and synthetic scenarios' methods.

Sensitivity	Classical method (m w.e.)	Synthetic scenarios (m w.e.)
-1 °C T	+0.41	+0.93 ± 0.18
+1 °C T	-0.61	-0.75 ± 0.17
+20 % P	+0.48	+0.52 ± 0.10
-20 % P	-0.79	-0.60 ± 0.11

5.7.3.3 Specific meteorological conditions leading to the most positive/negative mass balances

From the synthetic scenarios, the annual glacier-wide mass balances range from -1.76 to 0.54 m w.e. (Figure 5.9 and Figure S5.17), which is a wider range than the historically measured glaciological mass balance since 2007 (min = -0.92 m w.e. in 2017/18 and max = 0.26 m w.e. in 2010/11; Wagnon et al., 2021). The simulated annual mass balances are compared with the original mean annual glacier-wide mass balance of -0.66 m w.e. (Table 5.6) over the 2016-20 study period, referred hereafter as the reference year. Most of scenarios that have warm or dry conditions as a baseline correspond to the first category of scenarios characterised with negative mass balances ranging from -1.76 to -0.81 m w.e. They have a positive SWnet anomaly compared to the reference year (+2 to +17 W m⁻²), associated either with a change in air temperature toward a warming (-0.71 to +1.13 °C) or to a decrease in snowfall (0 to -0.29 m w.e.) or to both, resulting in a low glacier-wide albedo (0.53 to 0.64). With more energy intake, melting is enhanced, and due to the reduced snowfalls, ice is more exposed at the glacier surface favoring runoff, and in turn less than 46 % of this meltwater refreezes, ultimately leading to the most negative glacier-wide mass balances (Figure S5.17).

The second category of scenarios corresponds to glacier-wide mass balances from -0.80 to -0.25 m w.e. close to that of the reference year. Here, we find scenarios combining a baseline and a seasonal component that would normally lead to opposite mass balance responses such as dry with wet conditions or warm with cold conditions (e.g., Wa_We_{mon}, D_We_{mon}, Wa_We_{win}, D_C_{win}). We also find the majority of scenarios that have the unperturbed data as baseline (Figure 5.9 and Figure S5.17). The mass balance is affected equally but in an opposite direction by the temperature anomalies (-0.97 and +1.02 °C) and the precipitation anomalies (-0.16 to +0.23 m w.e.). In this category, the refreezing ranges from 37 to 56 % of total melt, which is close to that of the reference year (44 %), and the ranges of SWnet (-8 to +6 W m⁻²) and LWnet (-4 to +3 W m⁻²) anomalies are small (Figure 5.8).

The third category corresponds to positive or near-balanced glacier-wide mass balances (> -0.25 m w.e.) mostly produced by scenarios with wet or cold baselines. They have temperature

anomalies between -1.00 and $+0.52^{\circ}\text{C}$ and precipitation anomalies between -0.04 and $+0.45$ m w.e. (Figure 5.9 and Figure S5.17). The higher amount of snowfall increases the accumulation, increases the albedo, and in turn decreases the SWnet (-19 to -4 W m^{-2}). In addition, the refreezing is high (46-71 % of total melt). Overall, the scenarios with a wet year baseline always create a mass balance that is close to balance, and specifically, the highest positive mass balance is produced by the wettest conditions all year round (scenario We_We) (Figure 5.9 and Figure S5.17).

For all scenarios, we find that the mass balance is primarily influenced by the baseline conditions, and not by the seasonal variation. We do not find any season that has an influence larger than the other ones (Figure S5.17). In particular, when we look at the scenarios of unperturbed data with seasonal variations, we find that winter seems to have as much influence, if not even more influence, than the other seasons on the mass balance (Figure S5.17). This result is rather counter intuitive, as most of the mass balance processes happen in monsoon and pre-monsoon (e.g., Figure 5.9).

Regarding the classical scenarios, as expected, both -20 % and $+1^{\circ}\text{C}$ scenarios produce negative mass balances, but less extreme than the dry and warm synthetic scenarios. In contrast, both $+20$ % and -1°C classical scenarios are characterised by near-balanced mass balances, far from the positive glacier-wide mass balances obtained with the wet and cold scenarios. The energy and mass fluxes in the classical scenarios are also comparable to those of the synthetic scenarios. The LWnet is similar in all classical scenarios. However, SWnet is 13 W m^{-2} higher and refreezing is 25 % lower in the -20 % precipitation and $+1^{\circ}\text{C}$ scenarios than those in the $+20$ % and -1°C scenarios.

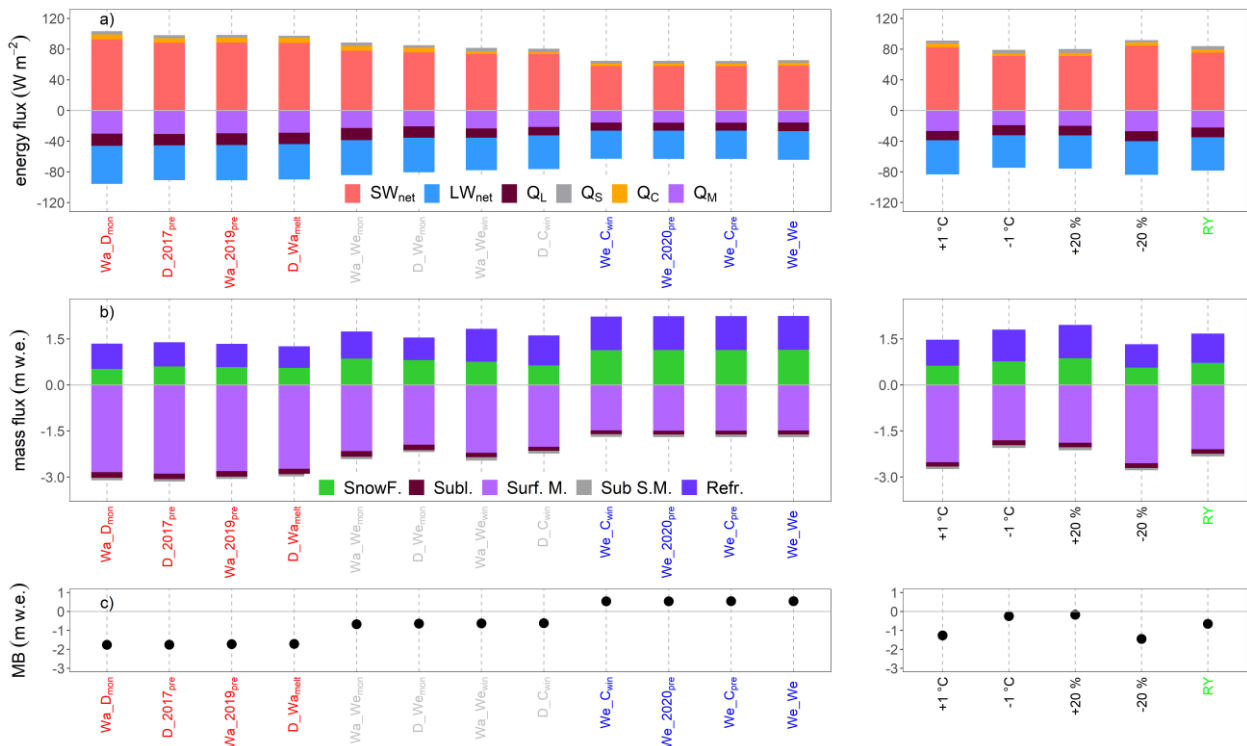


Figure 5.9. Glacier-wide (a) energy fluxes, (b) mass flux components, and (c) mass balance (MB) from (left panels) 12 selected synthetic scenarios (in red, grey, and blue, on the x-axis), as well as (right panels) from the four mean classical scenarios (in black) and the reference year (RY, in green, on the x-axis). The results from the classical scenarios or the reference year have

been averaged over the four years 2016-20. Based on the MB results, 12 synthetic scenarios are selected (four corresponding to the most negative MBs, four from the middle of the MB set with moderately negative MBs, and four most positive MBs) out of the 180 scenarios (all visible in Figure S5.17). The colour code of synthetic scenarios visualises the MB range, from the most negative (red), to the most positive (blue), grey being intermediate and moderately negative. 2019 and 2020 represent the 2018/19 and 2019/20 mass balance years, respectively. SW_{net} = net shortwave radiation, LW_{net} = net longwave radiation, QL = latent heat flux, QS = sensible heat flux, QC = subsurface heat flux, QR = rain heat flux, QM = available melt energy at the surface, $SnowF.$ = solid precipitation, $Subl.$ = sublimation, $Surf. M.$ = melt at surface $Sub S. M.$ = subsurface melt and $Refr.$ = refreezing.

5.8 Discussion

5.8.1 Surface energy and mass balance components of Mera Glacier, and comparison with other similar studies in HKH

It is difficult to compare different glacier surface energy and mass balance analyses rigorously across the same region because study periods are never similar. Moreover, temporal (multi-annual, annual, or seasonal) and spatial (point scale or glacier-wide) resolutions are often different and not comparable (Table 5.8). In HKH region, the seasonality of precipitation has a strong impact on the energy and mass balance components. In the western Himalaya, the winter precipitation dominates the annual accumulation, and sublimation strongly contributes to the ablation processes (Oulkar et al., 2022; Srivastava and Azam, 2022; Mandal et al., 2022). In the Central Himalaya, the glaciers are summer accumulation type with significant longitudinal variability in mean summer temperature, which has the strongest impact on mass balance sensitivity (Sakai and Fujita, 2017). Still, precipitation, which depends on the monsoon intensity and duration, is a key variable governing the energy and mass balance of glaciers through the albedo effect and its control on the refreezing (Shaw et al., 2022).

The pattern of surface energy and mass balance over the whole Mera Glacier confirms what has already been observed on other glaciers of HKH (Table 5.8, which is an update of Table 4 of Azam et al., 2014). Overall, the radiative fluxes strongly dominate the SEB, and control the amount of energy available for melt (Figure 5.7). Between the pre-monsoon and the monsoon, with the gradual establishment of the dense cloud cover typical of this latter wet and warm season, incoming shortwave radiation gradually loses intensity, replaced at the same time by increasing incoming longwave radiation, resulting in a constantly high amount of radiative energy available for the glacier. This amount of energy decreases with elevation mainly because albedo is higher in the accumulation zone, where ice is never exposed at the surface. Turbulent fluxes are only significant out of the monsoon, contributing to bring additional energy toward the surface by sensible heat flux (Figure 5.7). Contrary to glaciers in the western Himalaya where resublimation occasionally occurs during the monsoon (Azam et al., 2014), on Mera Glacier, the latent heat flux is always negative which means that sublimation is a non-negligible process of mass loss, especially during seasons with strong wind (winter and post-monsoon), like on Zhadang and Parlung No 4 glaciers on the southeast Tibetan Plateau (Mölg et al., 2012; Sun et al., 2014; Zhu et al., 2018). On Mera Glacier, glacier-wide sublimation accounts for 23 % of the glacier-wide mass balance (Table 5.6), in agreement with previously published values in the Himalayas (e.g., Gurung et al., 2022; Srivastava and Azam, 2022) or lower than that of Shruti Dhaka Glacier in the western Himalaya (55 %; Oulkar et al. 2022). However, this value on Mera Glacier is under-estimated because wind speed strongly increases with elevation (Khadka et al., 2022), an effect that has not been taken into account in our study. Refreezing is also an important process, because at annual and glacier-wide

scales, as much as 44 % of meltwater refreezes on Mera Glacier, with a clear increase of this percentage with elevation (Table 5.6). This finding is again in agreement with other studies in the region (Stigter et al., 2018; Kirkham et al., 2019; Bonekamp et al., 2019; Veldhuijsen et al., 2022; Arndt and Schneider, 2023). It is noteworthy mentioning that sublimation and refreezing are two important processes for glaciers in this region but they are not included in empirical degree-day models (Litt et al., 2019). Moreover, refreezing is always parameterised in a more or less sophisticated way in physical snowpack models, but field experiments are crucially missing to evaluate the accuracy of such parameterisations.

Table 5.8. Comparison of SEB components on different glaciers in HMA, whose location is visible in Figure S5.18. The various studies already included in Azam et al. (2014) are not reported in this table. (All the fluxes are in $W m^{-2}$)

Glacier Name	Study type	Altitude (m a.s.l.)	Region (ISM dominated, Y or N)	Study Period	SWnet	LWnet	QS	QL	QC	QM	Reference
Parlung No. 4	Point/annual	4657-5937	southeast Tibetan Plateau, China (N)	1 Oct 2008 to 21 Sept 2013	77	-46	11	-21	1	-22	Zhu et al. (2018)
Zhandang	Point/annual	5515-5947	Nyainqentanglha Range, China (Y)	1 Oct 2008 to 21 Sept 2013	69	-49	14	-13	-1	-20	Zhu et al. (2018)
Purogangri ice cap	Glacier-wide/annual	5350-6370	Tibetan Plateau, China (Y)	Oct 2000 to Oct 2011	36	-39	28	-22	-1.3	-2	Huintjes et al. (2015)
Qiangtang No.1	Point/annual	5882	inland Tibetan Plateau, China (Y)	Oct 2012 to Oct 2016	49	-56	26	-15	2	-6	Li et al. (2018)
Rikha Samba	Glacier-wide/annual	5427-6515	Central Himalaya, Nepal (Y)	Oct 1974 to Sept 2021	105	-74	-20*		NA	-12	Gurung et al. (2022)
Naimona'nyi	Glacier-wide/annual	5545-7262	western Himalaya, China (Y)	Oct 2010 to Sept 2018	77	-69	12	-16	2	6	Zhu et al. (2021)
Dokriani	Glacier-wide/annual	4050-6632	western Himalaya, India (Y)	1979 to 2020	68	-35	9	-32	NA	-10	Srivastava and Azam (2022)
Chhota Shigri	Point/monsoon	4670	western Himalaya, India (Y)	8 Jul to 5 Sept 2013	202	-14	31	11	4	-233	Azam, et al. (2014)
Chhota Shigri	Glacier-wide/annual	4070-5850	western Himalaya, India (Y)	1979 to 2020	77	-57	15	-25	NA	-10	Srivastava and Azam (2022)
Srutri Dhaka	Glacier-wide/annual	4500-6000	western Himalaya, India (Y)	Oct 2015 to Sept 2017	157	-85	7	-5	-3	-71	Oulkar et al. (2022)
Muztag Ata No. 15	Point/annual	5237-5935	eastern Pamir, China (N)	1 Oct 2008 to 21 Sept 2013	69	-61	18	-24	0	-2	Zhu et al. (2018)

* corresponding to QS+QL here

5.8.2 Mass balance sensitivity to different meteorological variables and comparison with other studies in HKH

5.8.2.1 Mass balance sensitivity of Mera Glacier to meteorological variables

Estimating the sensitivity of glacier mass balance to a change in temperature and/or precipitation is a classical problem in glaciology (e.g., Ohmura et al., 1992). Different approaches have been implemented in HKH to assess the glacier mass balance sensitivity at different scales (e.g., Sakai and Fujita, 2017; Wang et al., 2019; Arndt et al., 2021; Gurung et al., 2022). However, the classical approach (perturbing temperature and precipitation by certain values or percentages), which involves perturbing individual meteorological variables while keeping others unchanged, has been criticised due to the interconnectedness of these variables (Nicholson et al., 2013; Prinz et al., 2016). For example, changing air temperature directly impacts the water vapor ratio of the atmosphere, which can ultimately affect the turbulent heat fluxes.

For Mera Glacier, we find strong correlations among the meteorological variables, which makes difficult to decipher their individual effects on mass balance. Notably, the negative correlation between temperature and precipitation anomalies ($r = -0.56$; slope of the linear relationship: $-0.16 \text{ m w.e. } ^\circ\text{C}^{-1}$) leads to larger mass balance sensitivities to temperature when this relationship is preserved (Table 5.7). The mass balance sensitivity to SWin is unexpectedly limited ($-0.06 \text{ m w.e. a}^{-1} (\text{W m}^{-2})^{-1}$; $r = -0.22$) due to the role of albedo. Indeed, the correlation between albedo anomalies and mass balance anomalies is very high ($r = 0.97$) showing that the surface state, that depends primarily from the amount of snowfalls, is more important than the actual incoming shortwave radiative flux. Despite its direct contribution to the SEB, LWin correlates positively with mass balance due to its strong correlation with precipitation. One limitation of our approach is that we can virtually find sensitivities of the mass balance to any input variable, as long as a correlation exists. For instance, the strong sensitivity to the relative humidity shown in Figure 5.8 should not be interpreted as an expected change in mass balance due to a change in relative humidity. Instead it shows that the relative humidity is closely tied to the other meteorological variables, and that meteorological conditions that favor high relative humidity also favor positive mass balances.

Another interesting feature is the asymmetry towards negative values in the sensitivities to temperature with the classical method (Table 5.7). While continental and sub-continental glaciers typically exhibit less sensitivity to negative temperature changes (e.g., Arndt and Schneider, 2023; Wang et al., 2019), maritime glaciers tend to have symmetrical sensitivity, especially when estimated with degree-day models (Wang et al., 2019b). However, with the synthetic scenario approach, we find the opposite asymmetry for temperature sensitivity (Table 5.7), likely due to the correlations between precipitation and temperature. This leads to higher negative mass balances than the simple $+1 \text{ } ^\circ\text{C}$ perturbation (Figure 5.8), indicative of the maritime climate setting for Mera Glacier. Regarding precipitation, its sensitivity is asymmetric towards negative values with both methods (Table 5.7). It is clearly due to albedo feedback effects in the model, which are poorly represented in degree-day models that predict a symmetric sensitivity to precipitation (e.g., Wang et al., 2019).

5.8.2.2 Mass balance sensitivity comparison with other studies in HKH

The impact of temperature and precipitation changes on mass balance depends on the climate of the region, but it can be attenuated or exacerbated depending on the glacier's morphology and topography (Brun et al., 2019). Contrary to glaciers located in arid cold climates less sensitive to temperature changes (Ohmura et al., 1992), those affected by the Indian summer monsoon, such as Mera Glacier, are sensitive to both temperature and precipitation (Fujita, 2008a; Johnson and Rupper, 2020; Arndt et al., 2021). With higher temperature, first less precipitation falls as snow and in turn accumulation is reduced, and second and more important, more shortwave radiation is absorbed through lower albedo leading to enhanced melt (Fujita, 2008a). Still the mass balance sensitivity to temperature and precipitation varies among different glaciers. The glacier-wide sensitivity of Mera Glacier to changes in temperature and precipitation is of the same order of magnitude as other glaciers in HKH, even though it is noteworthy to mention that these glacier sensitivities have been assessed through the classical method and in turn are not directly comparable (Figure 5.10, Table S5.3).

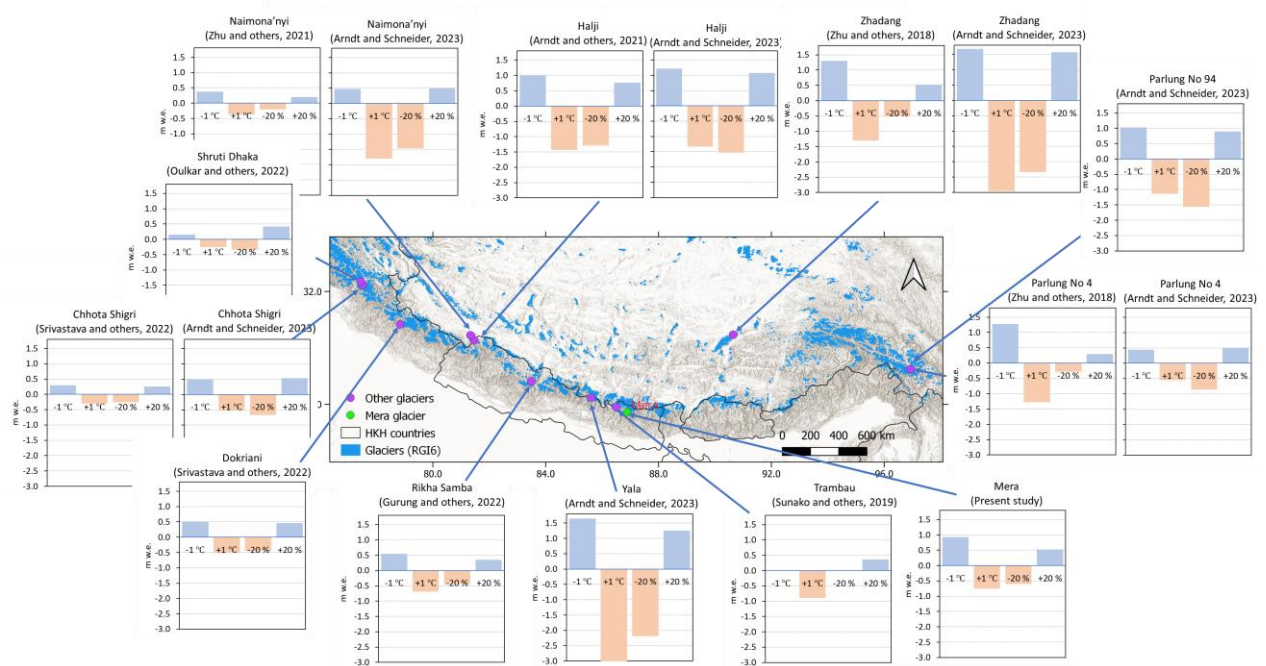


Figure 5.10. Location of glaciers where studies of mass balance sensitivities have been conducted in the Himalaya and Tibetan Plateau regions. Each panel gives the mass balance sensitivity to temperature and precipitation of each glacier, with the associated reference. Table S5.3 lists all these glaciers, and provides additional information.

For instance, on Mera Glacier, with the synthetic scenarios approach, a ± 1 °C temperature perturbation has greater impact than that of a ± 20 % precipitation change, which is mostly the case for glaciers on Figure 5.10, especially those located in Nepal. However, this pattern differs for glaciers in the Indian western Himalaya, which mostly exhibit lower sensitivities, sometimes higher for precipitation than for temperature like Shrutu Dhaka Glacier (Oulkar et al., 2022). Surprisingly, Arndt and Schneider (2023) find extreme sensitivities of glacier-wide mass balances to warming or to increase in precipitation for glaciers in the Central Himalaya (Yala and Halji glaciers) or Nyainqentanghla Range (Zhadang Glacier) compared to what we observe on Mera Glacier, although all these glaciers are submitted to rather humid monsoon dominated conditions.

Our approach with the synthetic scenarios does not allow to investigate whether the sensitivity changes linearly. It is well established that the sensitivity to temperature is nonlinear and much higher for larger temperature changes (e.g., Arndt and Schneider, 2023). As we rely only on existing observations, we cannot assess what would be the other meteorological variables in a +2 or +3 °C climate setting. Directions to overcome this issue could be to investigate the links between glaciers' response to synoptic variables (e.g., Mölg et al., 2012; Zhu et al., 2022), to investigate specific monsoon characteristics and their impacts on the mass balance (e.g., Shaw et al., 2022), or to force glacier mass balance models with downscaled global circulation model outputs that preserve the physical relationships between variables (e.g., Bonekamp et al., 2019; Clauzel et al., 2023). Furthermore, the size of the glacier plays a role on its mass balance sensitivity. Glaciers with a higher accumulation area, such as Shrutu Dhaka, Trambau, and Mera glaciers, exhibit a lower sensitivity than glaciers whose accumulation zone is strongly reduced, such as Zhadang and Halji glaciers (Zhu et al., 2018; Sunako et al., 2019; Arndt et al., 2021; Srivastava and Azam, 2022).

5.8.3 Limitations of our approach

Simulating the distributed surface energy and mass balance of a glacier presents numerous challenges and limitations. Uncertainties arise primarily from (i) the model's process representation, (ii) in-situ data, (iii) their spatial distribution over the glacier area, and (iv) the model's initial conditions.

One crucial process in snowpack modelling is the decay of snow albedo over time. COSIPY implements the Oerlemans parameterisation (Oerlemans and Knap, 1998), which has known limitations in certain climate contexts (e.g. Voordendag et al., 2021; Wang et al., 2022). Typically, albedo parameters are fixed or adopted from previous studies using COSIPY or any other energy balance model. However, here, we optimised these parameters at AWS-L before distributing the meteorological forcings. The snow aging and depth scaling factors used in this study fall within the range of commonly used factors (Sauter et al., 2020; Arndt et al., 2021; Wang et al., 2022; Sherpa et al., 2023), but differ slightly from those used in other studies (Sauter et al., 2020; Arndt et al., 2021; Potocki et al., 2022). Although the model can accurately predict albedo at a point scale, it is sometimes misrepresented (Figure S5.8). The lack of robust parameterisation and uncertainties surrounding the amount of snow deposited on the glacier surface and its redistribution by the wind contribute to this issue.

Additionally, refreezing is another poorly constrained process. In the HKH region, refreezing has primarily been assessed using models (Steiner et al., 2018; Kirkham et al., 2019; Saloranta et al., 2019; Veldhuijsen et al., 2022), rather than snowpack temperature and density measurements, as is done in the seasonal snowpack (e.g. Pfeffer and Humphrey, 1996). Specific experiments should be conducted to evaluate the effects of refreezing on glaciers, particularly to determine whether meltwater percolates below the previous year's horizon and contributes to internal accumulation. Additionally, COSIPY lacks certain processes, such as wind erosion and wind-driven snow densification. These processes can be very important, particularly during the post-monsoon and winter seasons due to the strong winds at high elevations (Litt et al., 2019; Brun et al., 2023; Sherpa et al., 2023). During November field campaigns, wind erosion features such as sastrugis are frequently observed.

Distributing meteorological data over a rough terrain is one of the most challenging task. The spatial distribution of the meteorological data based on a single vertical gradient throughout the year is somehow questionable. Additionally, applying a vertical gradient to distribute meteorological variables weakens the physical links between them, as already discussed in the sensitivity analysis. For the study period and the range of elevation of Mera Glacier, the vertical gradients for temperature, relative humidity, and LWin exhibit high variability (Figure S5.3). To derive the gradients, we selected the year with the minimum gaps at AWS-H despite a large portion of the data at AWS-L being reconstructed at that time. Additionally, the T/RH sensor was not artificially ventilated at AWS-H, which introduces some measurement uncertainty. Therefore, we tested a range of gradients to distribute T $[-6.5$ to -4.2 °C km⁻¹] and RH $[-25$ to 0 % km⁻¹]. In alpine environments, LWin provides large amounts of melt energy and can dominate the energy balance of snow or glacier surfaces. LWin is highly sensitive to surface melt when the atmosphere is saturated, particularly during the monsoon (Sicart et al., 2010). On Mera Glacier, the daily LWin gradient as a function of elevation varies greatly from day to day and season to season, with a minimum of -41 W m⁻² km⁻¹ observed during the monsoon. Various LWin gradients have been tested within the $[-40$ to 0 W m⁻² km⁻¹] range and optimised to -25 W m⁻² km⁻¹ (Table S5.2). In conclusion, there is no ideal method for spatially distributing meteorological variables on a complex glacier surface that extends over a large altitudinal range. On Mera Glacier, two on-glacier AWSs enable us to provide reasonable vertical gradients of temperature, relative humidity, and longwave incoming radiation. These gradients are highly variable in time and likely in space as well. To maintain simplicity in our modelling approach, we prefer to use a single gradient for these variables instead of using temporally or spatially variable gradients. The use of variable gradients would require a denser observation network than the two AWSs we currently have. Additionally, using different gradients would alter the set of optimised parameters without necessarily affecting the final results.

The depletion of precipitation as a function of elevation in the upper Khumbu region is still a matter of debate due to the lack of reliable data at high elevations, difficulties in correcting the undercatch of snow, and comparing precipitation records obtained with different devices (Salerno et al., 2015; Perry et al., 2020). On the Mera catchment, there is only one all-weather rain gauge located at 4888 m a.s.l., just below the glacier. The precipitation recorded at this station is considered constant across the glacier surface. The distribution of precipitation is clearly more complex due to the rough topography (Immerzeel et al., 2014) and snow redistribution by wind. We prefer not to apply any vertical precipitation gradient, as it would complicate the modelling and increase equifinality issues, as with other meteorological variables. Similarly, applying a vertical gradient of wind speed based on records at AWS-L and AWS-H is not recommended due to the site-specific nature of the records (Shea et al., 2015). Therefore, like precipitation, wind speed is assumed to be constant and equal to the wind velocity at AWS-L across the glacier. Given that wind speed mainly affects turbulent fluxes, which are of secondary importance compared to radiative fluxes, any assumptions made only impact the total sublimation and its spatial distribution.

To initialise the model, the snow depth on each grid cell at the start of the simulation, specifically on 1 November, must be known. As field trips typically occur around mid-November each year, and November is a relatively dry month with minimal melting, snow

depth initialisation is based on direct observations performed around 15 days later than the initialisation date. However, this method is not entirely error-free as not all grid cells are surveyed and precipitation or wind drift may have occurred between 1 November and the survey date. Such error may have large impacts over the entire simulation period when a surface is initially recognized snow free although it is not, or vice versa.

In COSIPY, between 10 and 20 % of SWnet penetrates below the surface and is partly reflected at different depths within the snowpack or the ice (van den Broeke and Bintanja, 1995). This amount of shortwave radiation is not accounted for in the outtake term Q_{out} of Table 5.5, which explains why Q_{in} and Q_{out} do not exactly compensate each other. Therefore, the energy balance is not perfectly closed in the COSIPY model (e.g., Arndt et al., 2021).

5.9 Conclusion

The COSIPY energy and mass balance model was applied to Mera Glacier in the Central Himalaya, Nepal. In-situ meteorological datasets were used, recorded both on and off the glacier at different elevations ranging from 4888 m a.s.l. (for precipitation) to 5770 m a.s.l. The data was collected from 1 November 2016 to 31 October 2020 at an hourly time step. The model parameters were optimised at the point scale using data from AWS-L at 5360 m a.s.l. over the year 2018/19. A multi-objective optimisation was employed, and the albedo aging and snow depth factors were selected as the most sensitive parameters and then calibrated. The model was validated both at the point scale with multiple AWS measurements (albedo and surface temperature recorded at 5360 and 5770 m a.s.l.) and at the glacier scale with annual point mass balance measurements obtained at various elevations. The validation indicates that the model effectively simulates the annual glacier-wide mass balance of Mera Glacier, with a simulated mean value of $-0.66 \text{ m w.e. a}^{-1}$ for 2016-20 compared to the observed value of $-0.74 \text{ m w.e. a}^{-1}$.

The SEB over Mera Glacier is dominated by radiative fluxes, which are responsible for almost all the energy available during the monsoon, the main melting season. From the pre-monsoon to the monsoon, with the increasing cloudiness, incoming shortwave radiation gradually decreases in intensity in favor of incoming longwave radiation thus maintaining a large amount of energy available for melt. Turbulent fluxes are only significant outside the monsoon. The sensible heat is an energy source at the surface whereas the latent heat flux is always negative. Sublimation is therefore an important ablation process, especially during the windy months of the post-monsoon and winter. Annually and at glacier scale, refreezing is a crucial process, because on average 44 % of meltwater refreezes, with a large positive gradient with altitude.

To investigate the sensitivity of glacier mass balance to changes in temperature and precipitation, we generated 180 different scenarios by shuffling our four-year dataset. We aggregated warm, cold, dry, or wet months alternatively, depending on the seasons. These scenarios allowed us to explore a wide range of conditions, from very dry and warm to very cold and wet. As a result, the glacier-wide mass balances of Mera Glacier ranged from -1.76 to $+0.54 \text{ m w.e. a}^{-1}$. The mass balance sensitivity to meteorological variables can be quantified from these synthetic scenarios. A temperature change of $+1 \text{ }^{\circ}\text{C}$ ($-1 \text{ }^{\circ}\text{C}$) results in a change of -

$0.75 \pm 0.17 (+0.93 \pm 0.18)$ m w.e. in glacier-wide mass balance, while a precipitation change of +20 % (-20 %) results in a change of $+0.52 \pm 0.10 (-0.60 \pm 0.11)$ m w.e. in mass balance. Compared to the classical approach, the sensitivity of the mass balance is more pronounced with temperature, but not significantly different with precipitation. Similar to other glaciers with summer accumulation, Mera Glacier is highly sensitive to both temperature and precipitation.

To evaluate the mass balance sensitivity to any meteorological variables, it is advantageous to generate scenarios based on real in-situ data. This not only helps to quantify these sensitivities more accurately but also to explore the inter-relationships between variables. Our study demonstrates, for instance, that temperature has a negative correlation with precipitation. Therefore, classical sensitivity approaches that alter temperature and precipitation independently are likely to be biased. It is worth noting that long-term high-quality datasets are necessary to apply such synthetic method approach. We are lucky enough to have a long-term dataset on Mera Glacier, but we encourage to maintain and develop similar observational networks on other glaciers in HKH, in order to compare glaciers and to assess whether sensitivities obtain locally on a glacier can be extrapolated regionally. Currently, we cannot be certain that this sensitivity is not specific to Mera Glacier.

Like any modelling, our approach has limitations inherent to the model used, the quality of input data, their spatial distribution, and the choice of initial conditions. These limitations are difficult to quantify, but our method allows us to provide an accuracy range for the results based on a 99 % confidence interval. A potential next step in this study would be to conduct an uncertainty analysis to assess the weight of all potential errors related to the model and data, as well as to evaluate the equifinality of the results. However, this is beyond the scope of the present study. Nonetheless, such an analysis would be valuable, as many modelling approaches encounter similar issues.

5.10 Supplementary material

Table S5.1. Monthly correlation coefficients (r^2) between the Mera La AWS and AWS-L hourly data with parameters used to linearly extrapolate the Mera La AWS data to AWS-L ($y = mx + c$). For SWin, the c value is 0 i.e., the correlation is forced to the origin, in order to keep night values at 0 W m^{-2} .

Variables	T			RH			u			SWin			LWin		
	r^2	m	c	r^2	m	c	r^2	m	c	r^2	m	c	r^2	m	C
all	0.92	0.90	-2.09	0.91	0.94	5.47	0.51	0.94	0.70	0.90	1.10	0	0.93	0.92	12.77
Jan	0.86	0.86	-3.07	0.82	0.86	4.94	0.41	0.80	1.62	0.95	0.93	0	0.77	0.77	37.72
Feb	0.90	0.86	-2.82	0.85	0.89	3.60	0.45	0.69	1.88	0.97	0.98	0	0.88	0.84	27.90
Mar	0.88	0.82	-2.83	0.79	0.87	3.28	0.37	0.79	1.61	0.96	1.08	0	0.82	0.78	38.44
Apr	0.81	0.72	-3.06	0.81	0.91	3.98	0.34	0.79	1.16	0.91	1.23	0	0.71	0.76	44.96
May	0.73	0.66	-2.19	0.78	0.93	3.73	0.22	0.64	1.31	0.87	1.26	0	0.73	0.81	37.50
Jun	0.65	0.59	-0.90	0.72	0.84	15.59	0.26	0.69	0.53	0.83	1.32	0	0.76	0.88	29.04
Jul	0.65	0.45	-0.10	0.31	0.45	53.71	0.09	0.49	0.55	0.83	1.27	0	0.61	0.78	64.50
Aug	0.64	0.44	-0.14	0.42	0.54	44.88	0.15	0.61	0.48	0.81	1.22	0	0.76	0.86	37.92
Sep	0.70	0.61	-1.03	0.64	0.72	28.11	0.15	0.45	0.55	0.84	1.15	0	0.78	0.97	1.67
Oct	0.80	0.79	-2.95	0.81	0.89	10.95	0.19	0.61	1.05	0.91	1.05	0	0.86	0.86	26.36
Nov	0.79	0.77	-3.53	0.74	0.81	10.53	0.25	0.59	1.75	0.95	0.96	0	0.83	0.80	35.77
Dec	0.89	0.84	-3.12	0.77	0.85	8.55	0.47	0.77	1.59	0.96	0.93	0	0.85	0.84	26.40

Table S5.2. Tested range and final values of the altitudinal gradients of air temperature, relative humidity, incoming longwave radiation and precipitation used to spatially distribute the meteorological forcing data

SN	Parameters	Max	Min	final value
1	Temperature gradient ($^{\circ}\text{C km}^{-1}$)	-4.2	-6.5	-5.7
2	Relative humidity gradient ($\% \text{ km}^{-1}$)	0	-20	-15
3	LWin gradient ($\text{W m}^{-2} \text{ km}^{-1}$)	0	-41	-25
4	Precipitation gradient (mm km^{-1} or $\% \text{ km}^{-1}$)			0

Table S5.3. Glacier-wide annual mass balance perturbations (m w.e.) with different magnitudes of meteorological variables from various studies done on HMA glaciers, always using the classical method, except our present study using the synthetic scenario approach. (refers to the sensitivities obtained from the literature, but multiplied or divided by a factor to make it comparable with other studies. For example, the mass balance sensitivity to a -10 % change in precipitation is multiplied by a factor 2, to make it comparable with a mass balance sensitivity to a -20 % change in precipitation.)*

Glacier Name, region	Region (ISM dominated, Y or N)	Study Period	T (-1 $^{\circ}\text{C}$)	T (+1 $^{\circ}\text{C}$)	P (-20 %)	P (+20 %)	Reference
Parlung No 4	southeast Tibetan Plateau, China (N)	1 Oct 2008 to 21 Sept 2013	+1.28	-1.28	-0.29	+0.29	Zhu et al. (2018)
Parlung No 4	southeast Tibetan Plateau, China (N)	Oct 2000 to Sept 2018	+0.44	-0.55	-0.86	+0.51	Arndt and Schneider (2023)
Parlung No 94	southeast Tibetan Plateau, China (N)	Oct 2000 to Sept 2018	+1.03	-1.14	-1.56	+0.89	Arndt and Schneider (2023)
Zhadang	western Nyainqentanglha Range, China (Y)	1 Oct 2008 to 21 Sept 2013	+1.30	-1.30	-0.52	+0.52	Zhu et al. (2018)
Zhadang	western Nyainqentanglha Range, China (Y)	Oct 2000 to Sept 2018	+1.68	-2.96	-2.34	+1.57	Arndt and Schneider (2023)
Mera	Central Himalaya, Nepal (Y)	Nov 2016 to Oct 2020	+0.93	-0.75	-0.60	+0.52	Present study
Trambau	Central Himalaya, Nepal (Y)	May 2016 to Oct 2018	NA	-0.90*	NA	+0.36*	Sunako et al. (2019)
Yala	Central Himalaya, Nepal (Y)	Oct 2000 to Sept 2018	+1.65	-3.18	-2.19	+1.25	Arndt and Schneider (2023)
Rikha Samba	Central Himalaya, Nepal (Y)	Oct 1974 to Sept 2021	+0.54	-0.69	-0.44	+0.35	Gurung et al. (2022)
Halji	Central Himalaya, Nepal (Y)	Oct 2000 to Sept 2018	+1.22	-1.33	-1.53	+1.07	Arndt and Schneider (2023)
Halji	Central Himalaya, Nepal (Y)	Jan 1982 to Apr 2019	+0.99	-1.43	-1.29	+0.76	Arndt et al. (2021)
Naimona'nyi	Central Himalaya, Nepal (Y)	Oct 2000 to Sept 2018	+0.47	-1.8	-1.46	+0.49	Arndt and Schneider (2023)
Naimona'nyi	western Himalaya, India (Y)	Oct 2010 to Sept 2018	+0.37	-0.37	-0.20*	+0.20*	Zhu et al. (2021)
Dokriani	western Himalaya, India (Y)	Nov 1979 to Oct 2020	+0.50	-0.50	-0.46	+0.46*	Srivastava and Azam (2022)
Chhota Shigri	western Himalaya, India (Y)	Nov 1979 to Oct 2020	+0.30	-0.30	-0.26	+0.26*	Srivastava and Azam (2022)
Chhota Shigri	western Himalaya, India (Y)	Oct 2000 to Sept 2018	+0.49	-0.53	-0.67	+0.53	Arndt and Schneider (2023)
Shruti Dhaka	western Himalaya, India (Y)	Oct 2015 to Sept 2017	+0.15	-0.25	-0.34*	+0.42*	Oulkar et al. (2022)

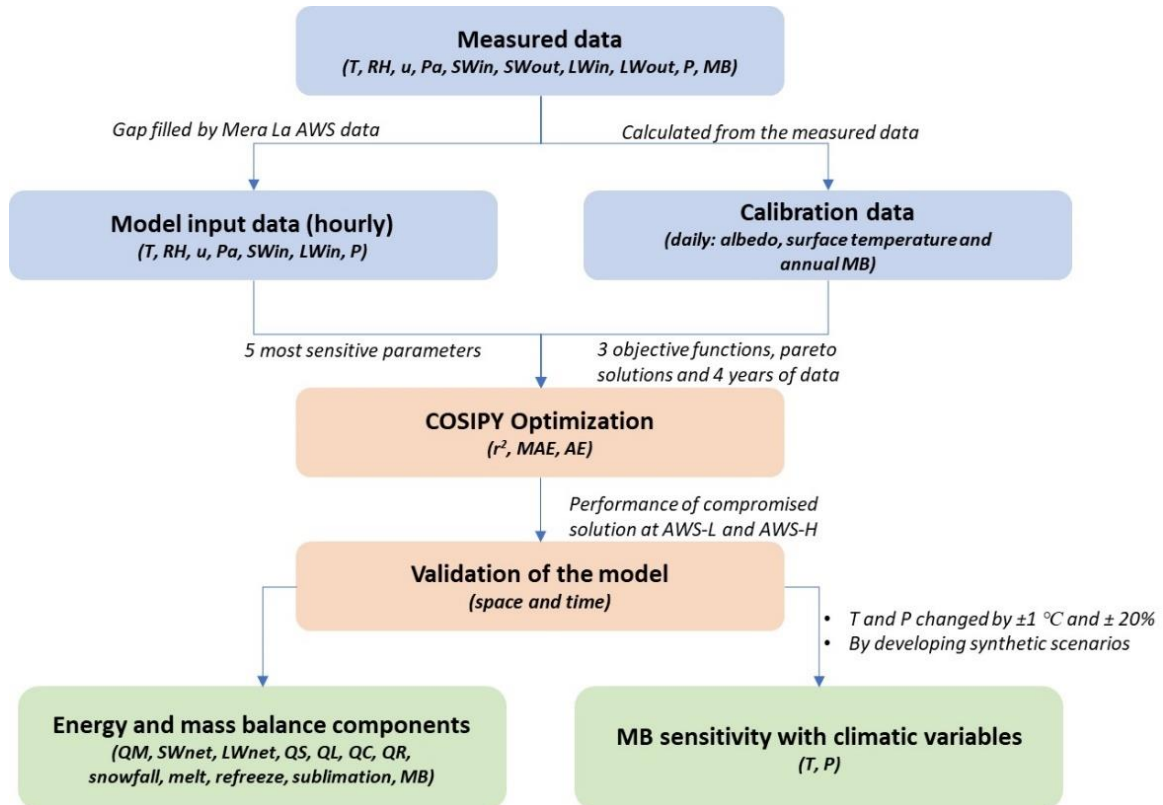


Figure S5.1. Flow chart describing the simplified sequential approach used in this study.

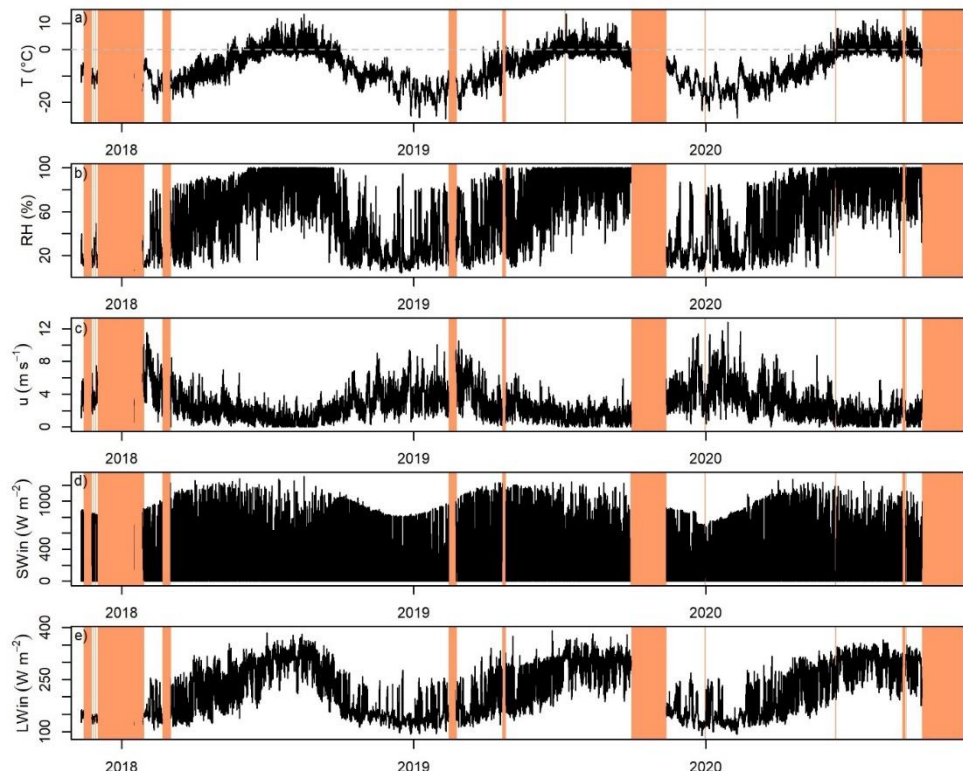


Figure S5.2. Hourly data of (a) air temperature (T), (b) relative humidity (RH), (c) wind speed (u), (d) incoming shortwave radiation ($SWin$), and (e) incoming longwave radiation ($LWin$) at AWS-H, from 10 November 2017 to 27 September 2020. Orange shaded areas indicate data gaps.

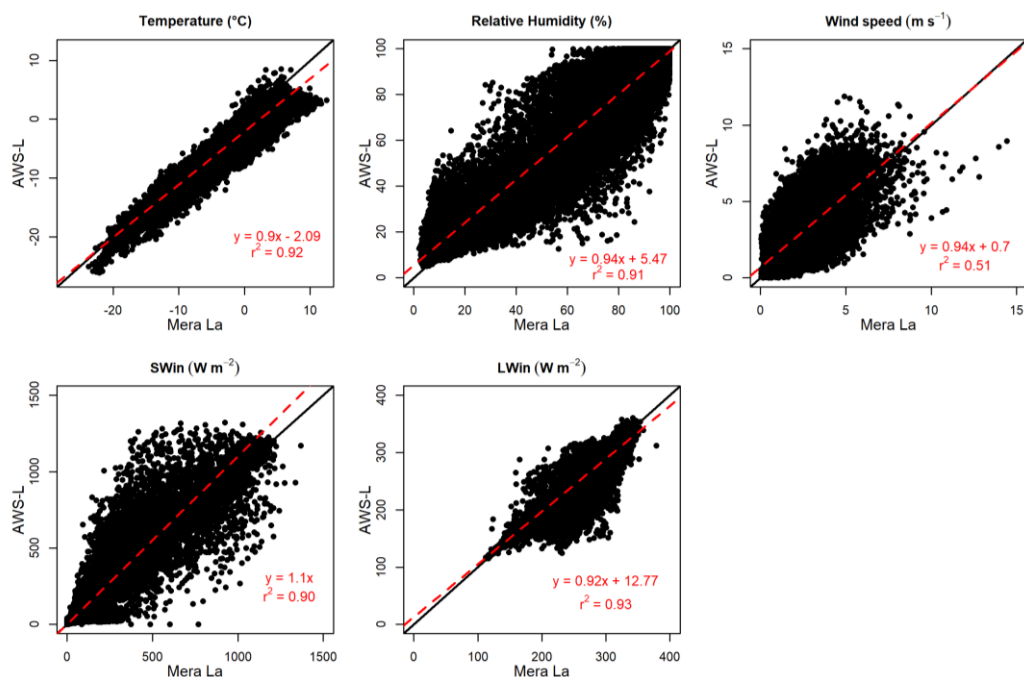


Figure S5.3. Hourly data comparison between Mera La and AWS-L. The red lines and equations are overall linear relationships between the two observed data, r^2 is the correlation coefficient, where the p -value is always significant ($p < 0.01$). Also shown in black the 1:1 line.

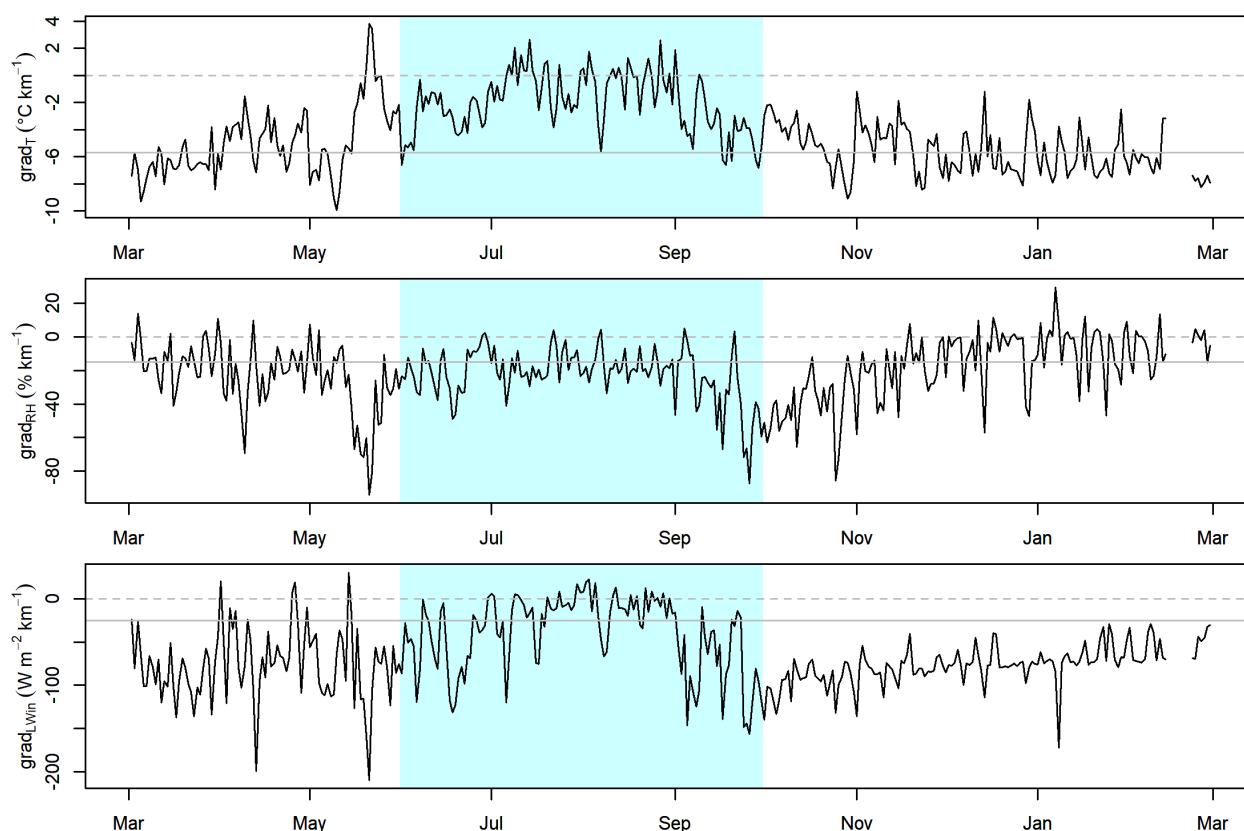


Figure S5.4. Mean daily altitudinal gradients of air temperature ($grad_T$), relative humidity ($grad_{RH}$), and longwave incoming radiation ($grad_{LWin}$), calculated from AWS-L and AWS-H data from 1 March 2018 to 28 February 2019. The horizontal grey lines represent the different values of altitudinal gradients used for the data distribution. The blue shaded area corresponds to the monsoon period.

Additional text related to Figure S5.4: Pressure data distribution method, altitudinal gradients of air temperature, relative humidity and incoming longwave radiation used in this study

The atmospheric pressure (Pa) has been interpolated using the barometric formula (eq. S5.1, S5.2):

$$SLP = \frac{Pa}{\left(1 - \frac{0.0065 * Z_{AWS-L}}{288.15}\right)^{5.255}} \quad (S5.1)$$

$$Pa_{elv} = SLP * \left(1 - \frac{0.0065 * Z_{elv}}{288.15}\right)^{5.255} \quad (S5.2)$$

Where SLP is the sea level pressure, Pa is the atmospheric pressure at the elevation of the AWS-L (Z_{AWS-L}), and Pa_{elv} is the pressure at any grid elevation (Z_{elv}).

The altitudinal gradients of air temperature, relative humidity and incoming longwave radiation are calculated using the data from AWS-L and AWS-H between 01 March 2018 and 28 February 2019. This particular period is chosen because there are almost no gaps at AWS-H (Figure S5.1) and because it covers one full year, allowing to compute annual and seasonal gradients. However, it is worth noting that during this period, a large portion of data at AWS-L (from 01 March 2018 to 24 November 2018) has been reconstructed with Mera La AWS. Using reconstructed data does not alter our analysis since we explore different gradients over a wide range of values. For air temperature, this range goes from the environmental lapse rate ($-6.5 \text{ }^\circ\text{C km}^{-1}$) to the mean annual temperature gradient observed from both AWSs ($-0.42 \text{ }^\circ\text{C km}^{-1}$). For the other variables, the range goes from the mean monsoonal observed gradient (-22 \% km^{-1} and $-41 \text{ Wm}^{-2} \text{ km}^{-1}$ for RH and LWin gradients, respectively) to 0 (no gradient) (Figure S5.3). Deriving dew point temperature gradients between AWS and converting dew point temperature to relative humidity at any glacier grid cell is more physical than directly using relative humidity gradients, but both approaches provide the same range of RH gradients (Figure S5.4). Twelve tests were conducted with different sets of gradients to ultimately determine the optimal set, which is $-5.7 \text{ }^\circ\text{C km}^{-1}$ for air temperature, -15 \% km^{-1} for relative humidity and $-25 \text{ W m}^{-2} \text{ km}^{-1}$ for incoming longwave radiation (Table S2).

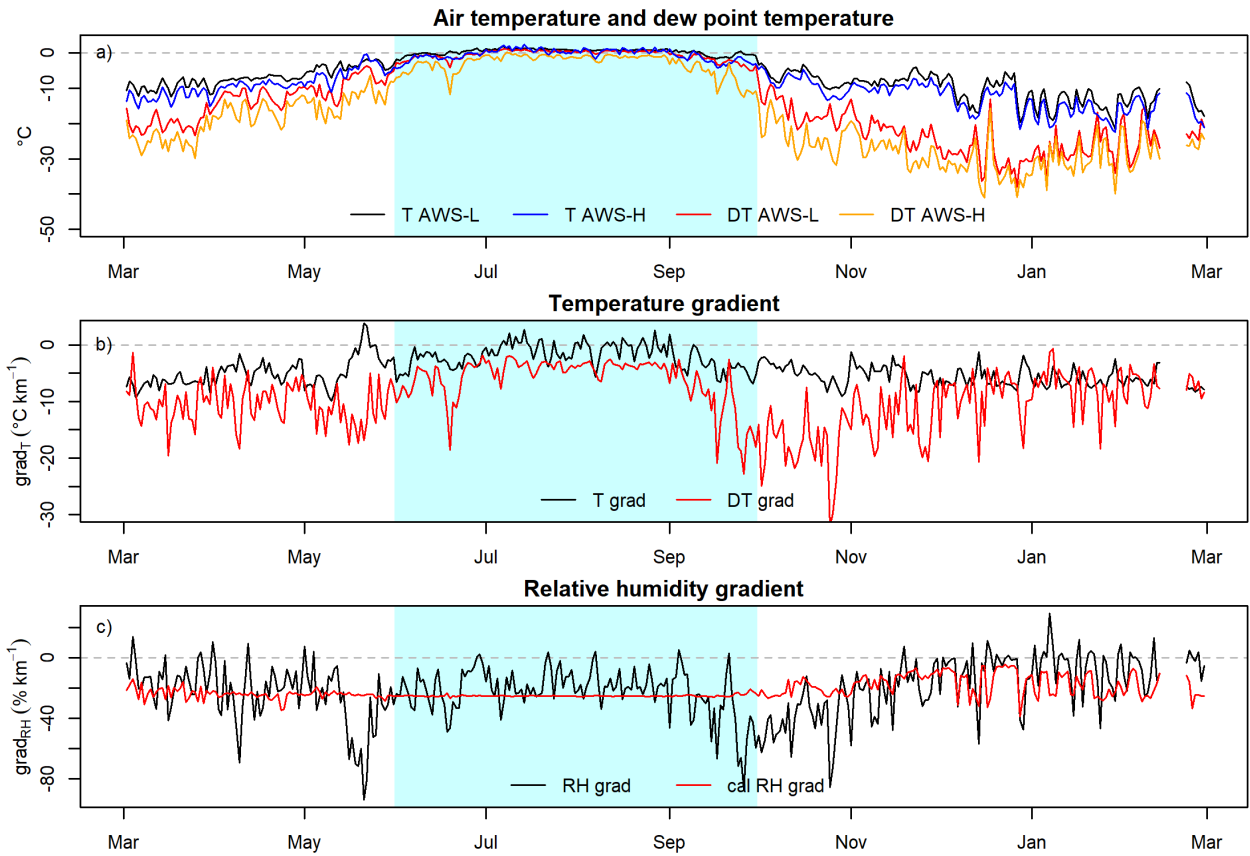


Figure S5.5. Mean daily temperature (T) and dew point temperature (DT) at AWS-L and AWS-H (top), calculated temperature and dew point temperature gradient (middle) and calculated relative humidity gradient from observation and dew point temperature (bottom) from the AWS-L and AWS-H from 1 March 2018 to 28 February 2019.

Additional text related to the section 5.5

Albedo

In COSIPY, the albedo (α) of the snow surface is calculated by the Oerlemans and Knap (1998) method. The albedo of snow (α_{sn}) depends upon how fast (t^* expressed in days) the fresh snow albedo (α_s) drops to firn albedo (α_f) after the last snowfall.

$$\alpha_{sn} = \alpha_f + (\alpha_s - \alpha_f) \exp\left(\frac{s}{t^*}\right) \quad (S5.3)$$

where s is the age of the snow layer from the last snowfall (in days). The overall snowpack thickness (d in m) impacts the albedo; if the snowpack is thin, the albedo must tend towards the albedo of ice (α_i). The full albedo can be written by introducing a characteristic snow depth scale d^* (in m) as

$$\alpha = \alpha_{sn} + (\alpha_i - \alpha_{sn}) \exp\left(\frac{-d}{d^*}\right) \quad (S5.4)$$

Densification

The snow volumetric mass (ρ_{sn} in kg m^{-3}) is a key characteristic of the snowpack. Following Essery et al. (2013), COSIPY calculates the snow volumetric mass to derive important snow properties such as thermal conductivity and liquid water content. Assuming that a rapid settlement of fresh snow occurs simultaneously with slow compaction by the load resisted by the viscosity (η), the rate of change in the volumetric mass as a function of time t , $\frac{d\rho_{sn}}{dt}$, of a snow layer with temperature T_{sn} and overlying mass M_{sn} is given by:

$$\frac{1}{\rho_{sn}} \frac{d\rho_{sn}}{dt} = \frac{M_{sn}g}{\eta} + c_1 \exp[-c_2(T_0 - T_{sn}) - c_3 \max(0, \rho_{sn} - \rho_0)] \quad (S5.5)$$

And the viscosity:

$$\eta = \eta_0 \exp[c_4(T_0 - T_{sn}) + c_5 \rho_{sn}] \quad (S5.6)$$

Values for the two physical constants and six parameters in equations (S5.3) and (S5.4) are given in Table S5.4 below.

Table S5.4. Physical constants and parameter values for snow compaction parameterisations.

equation	Parameters	Sources
----------	------------	---------

S5.5	$c_1 = 2.8 \times 10^{-6} \text{ s}^{-1}$, $c_2 = 0.042 \text{ K}^{-1}$, $c_3 = 0.046 \text{ m}^3 \text{ kg}^{-1}$ $\rho_0 = 150 \text{ kg m}^{-3}$ $T_0 = 273.15 \text{ K}$ melting point temperature $g = 9.81 \text{ m s}^{-2}$ acceleration due to gravity	(Anderson, 1976; Sauter et al., 2020; Essery et al., 2013; Boone, 2002)
S5.6	$c_4 = 0.081 \text{ K}^{-1}$, $c_5 = 0.018 \text{ m}^3 \text{ kg}^{-1}$ $\eta_0 = 3.7 \times 10^7 \text{ kg m}^{-1} \text{ s}^{-1}$	

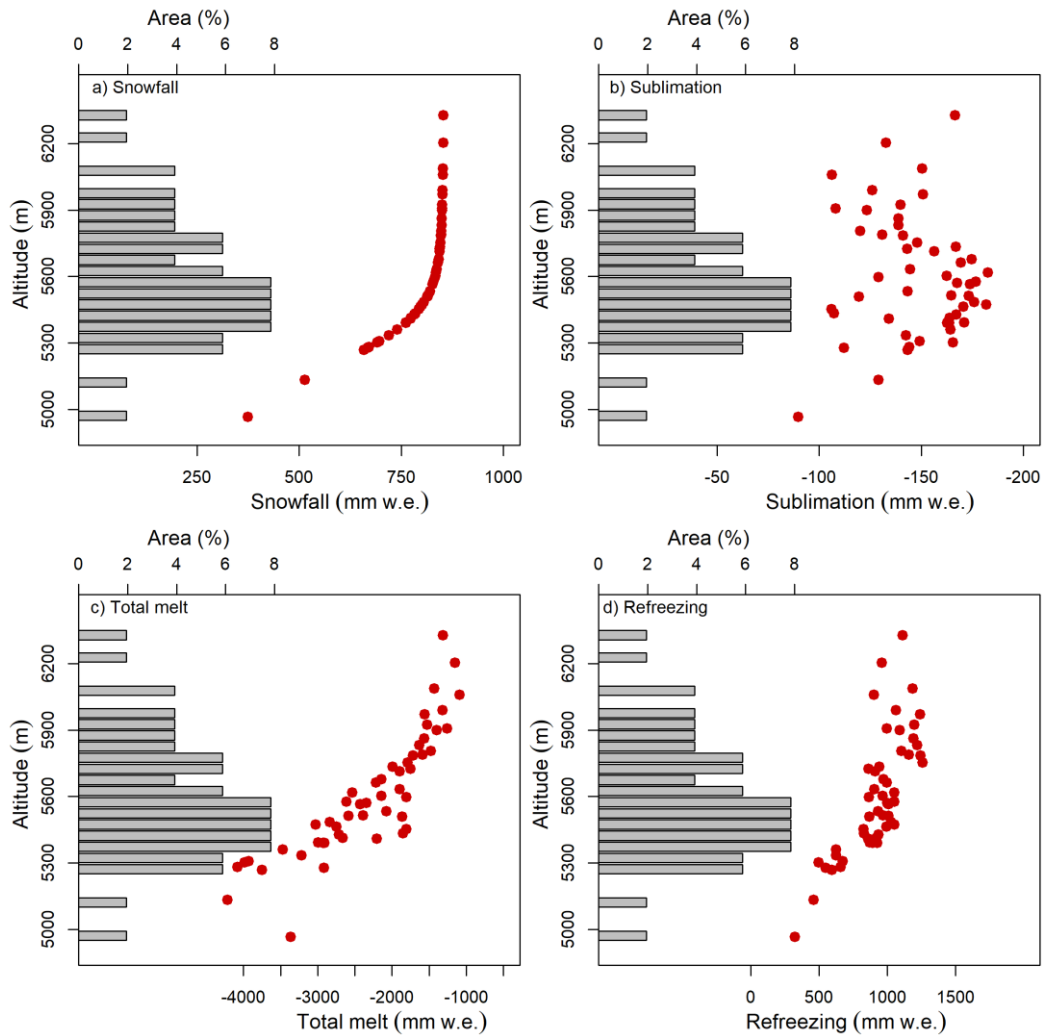
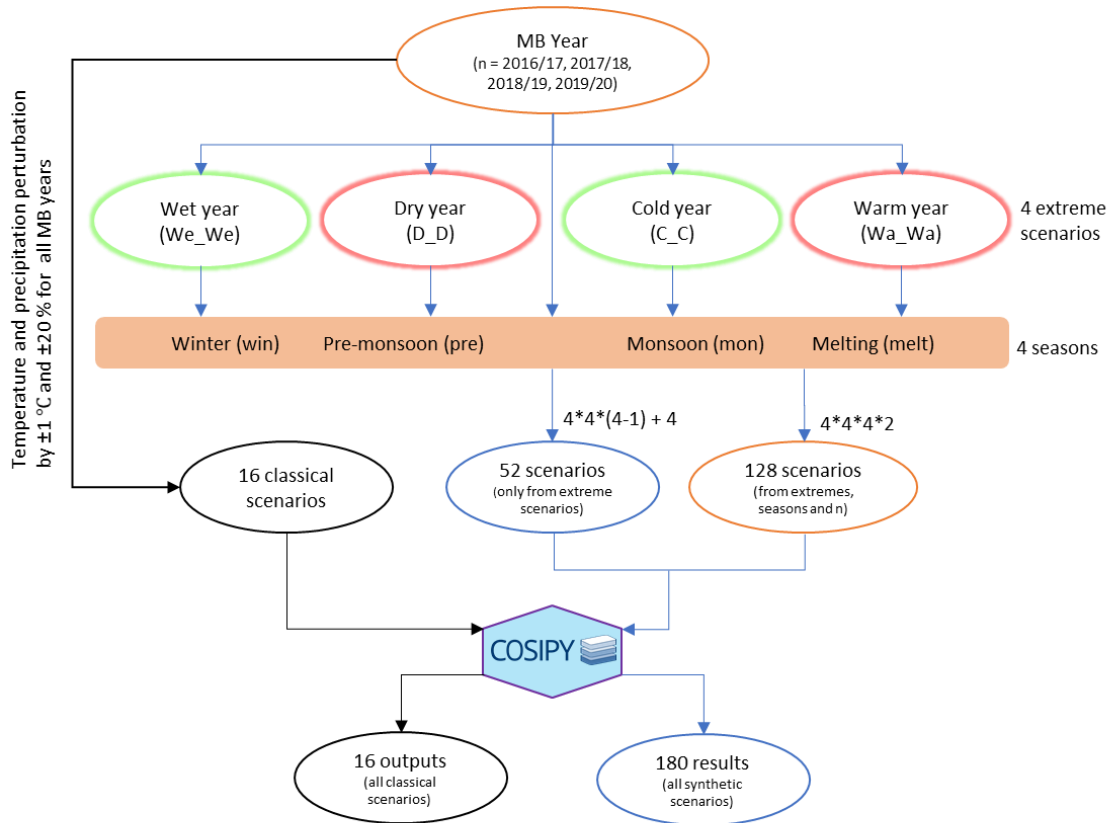


Figure S5.6. Total (a) snowfall, (b) sublimation, (c) melt and (d) refreezing (red dots) for each grid cell simulated by COSIPY for the 2018/19 period. Also shown is the glacier hypsometry (grey histograms) used in the model.



With mean, 4 results from classical scenarios, 180 results from synthetic scenarios

Figure S5.7. Flow chart illustrating the sequential approach used to develop and analyse mass balance sensitivity by both classical and synthetic methods.

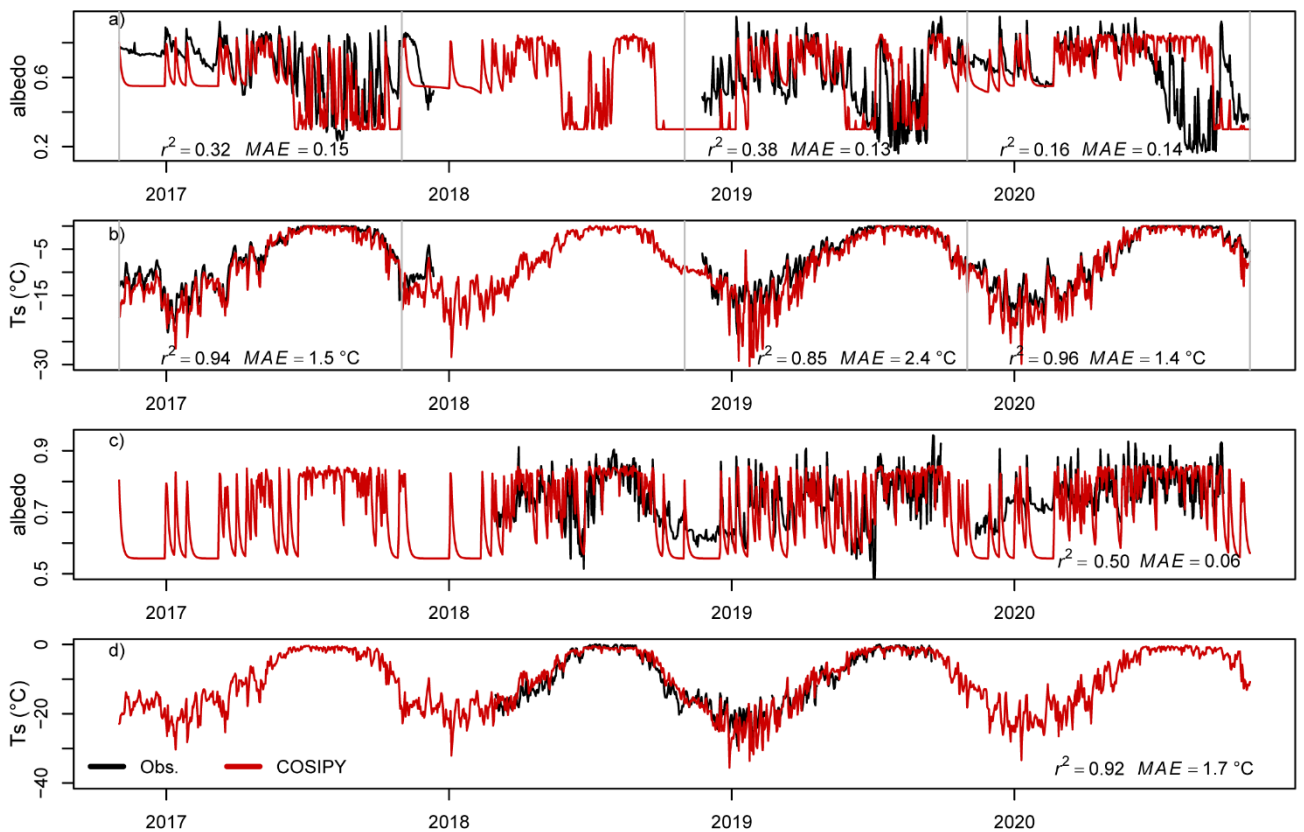
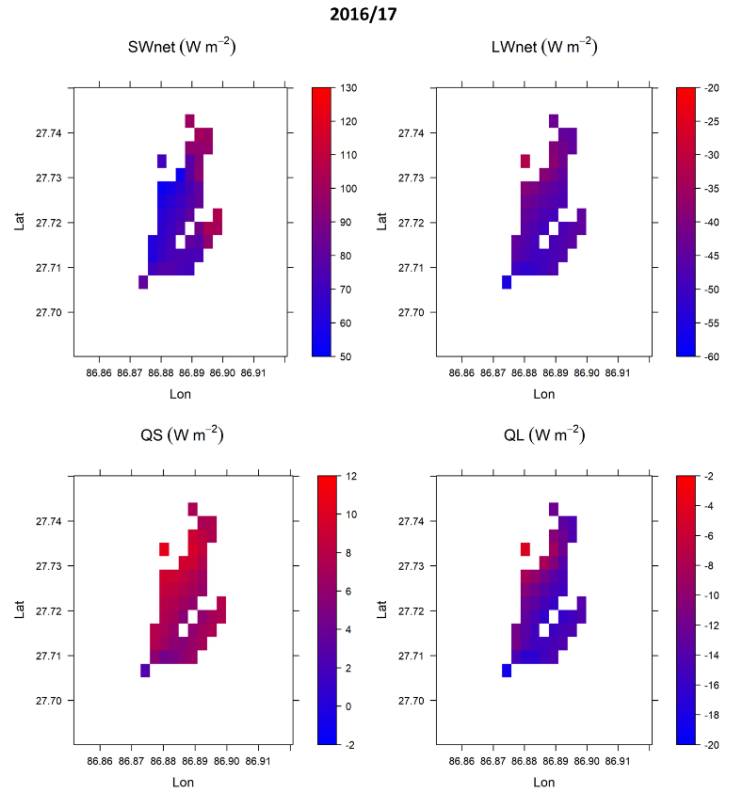


Figure S5.8. Mean daily observed and modelled albedo and surface temperature at AWS-L (a and b) and AWS-H (c and d) for the 2016-20 period. The metrics r^2 and MAE are calculated for each year at AWS-L (except 2017/18, because the data gap is too long) and for the 3-year 2017-20 period at AWS-H.

Figure S5.9. Distributed annual net shortwave radiation (SWnet), net longwave radiation (LWnet), sensible heat flux (QS), and latent heat flux (QL) in $W m^{-2}$ for the year 2016/17.



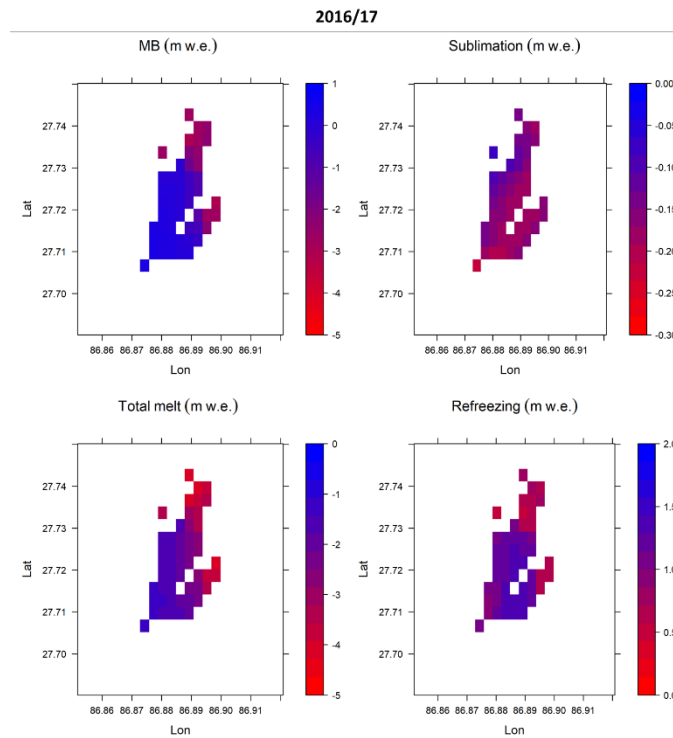


Figure S5.10. Distributed annual mass balance (MB), sublimation, total melt and refreezing in m.w.e. for the year 2016/17.

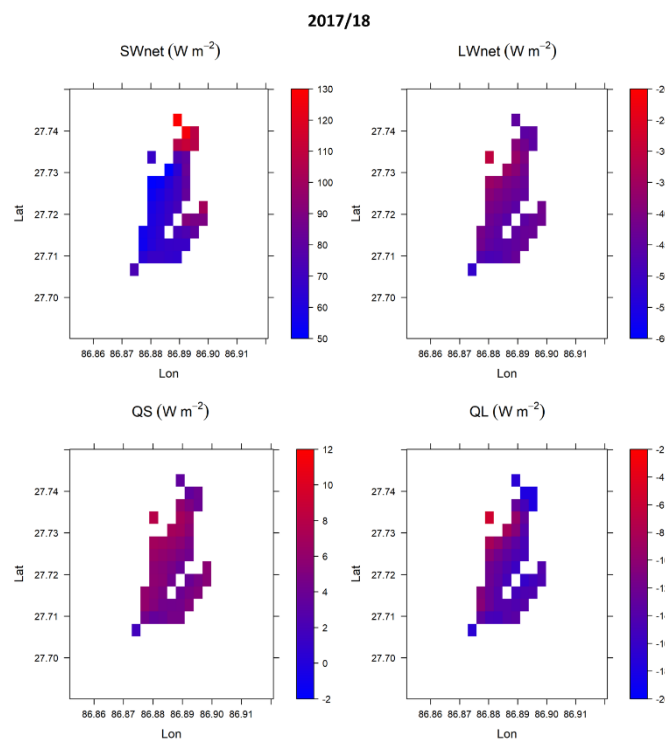


Figure S5.11. Same as Figure S5.9 for the year 2017/18

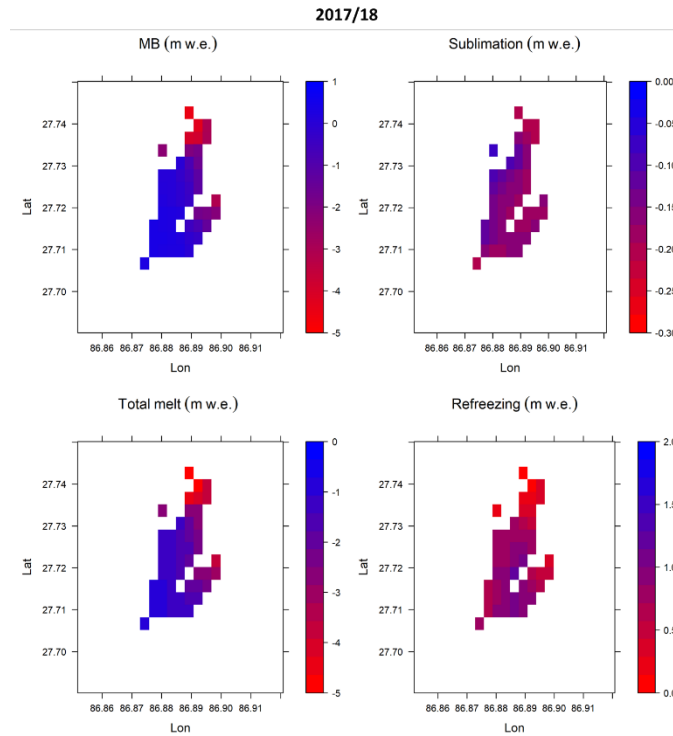


Figure S5.12. Same as Figure S5.10 for the year 2017/18

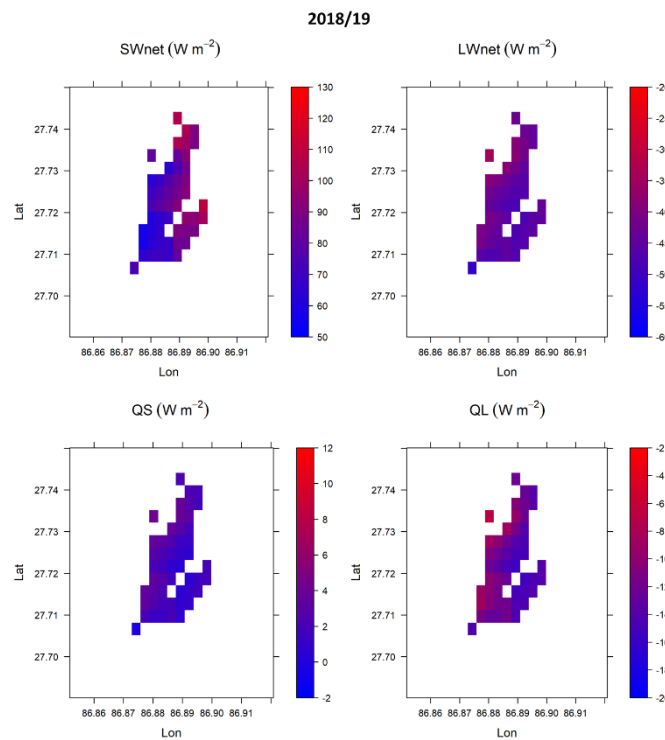


Figure S5.13. Same as Figure S5.9 for the year 2018/19

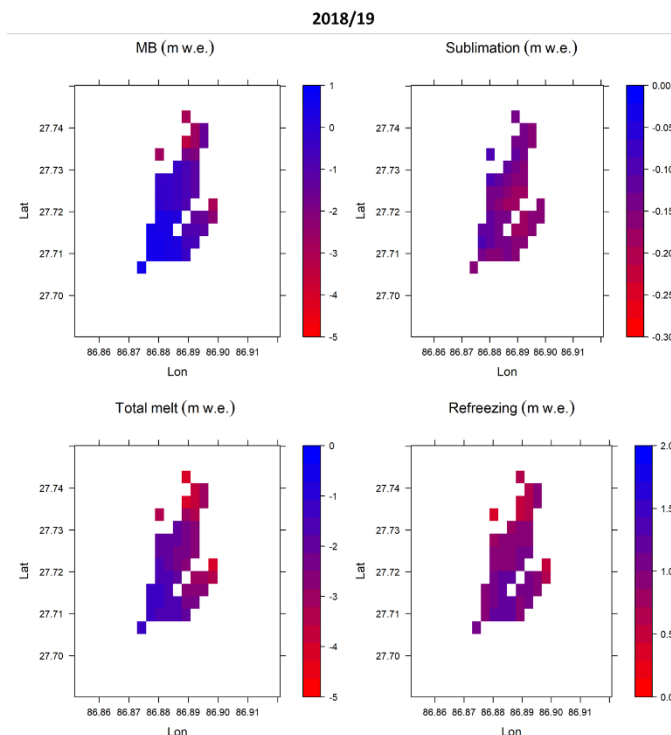


Figure S5.14. Same as Figure S5.10 for the year 2018/19

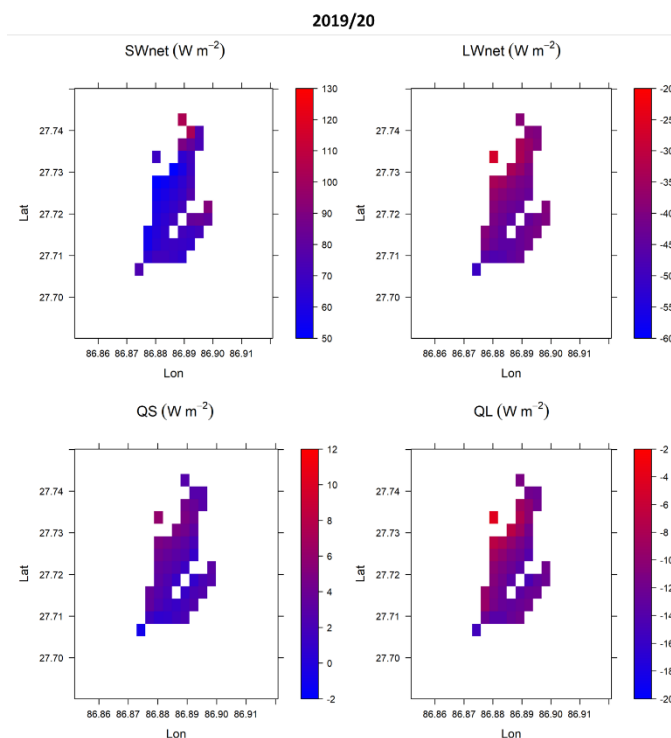


Figure S5.15. Same as Figure S5.9 for the year 2019/20

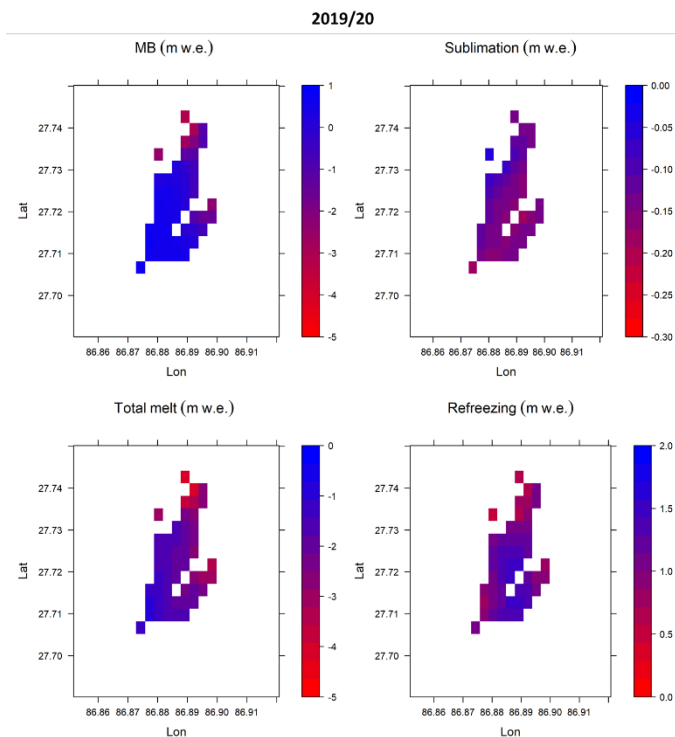


Figure S5.16. Same as Figure S5.10 for the year 2019/20

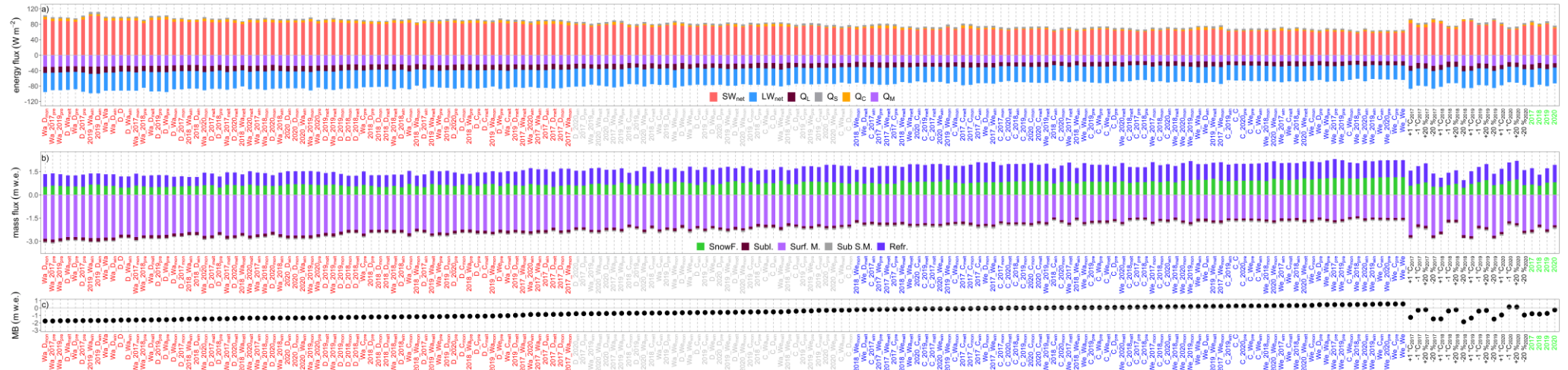


Figure S5.17. Glacier-wide (a) energy fluxes, (b) mass flux components, and (c) mass balance from the reference year (RY, in green on the x-axis) as well as all classical (in black) and synthetic (in red, grey and blue) scenarios. Synthetic scenarios are sorted in ascending order of glacier-wide mass balance, from the most negative (-1.76 m w.e.) to the most positive mass balance (0.54 m w.e.). The colour code of synthetic scenarios visualises the mass balance range: $MB < -0.80$ m w.e. (red); -0.80 m w.e. $\leq MB \leq -0.25$ m w.e. (grey) and -0.25 m w.e. $< MB$ (blue). SWnet = net shortwave radiation, LWnet = net longwave radiation, QL = latent heat flux, QS = sensible heat flux, QC = subsurface heat flux, QR = rain heat flux, QM = available melt energy at the surface, SnowF. = solid precipitation, Subl. = sublimation, Surf. M. = melt at surface Sub S. M. = subsurface melt and Refr. = refreezing. 2017, 2018, 2019 and 2020 are the mass balance years 2016/17, 2017/18, 2018/19 and 2019/20, respectively.

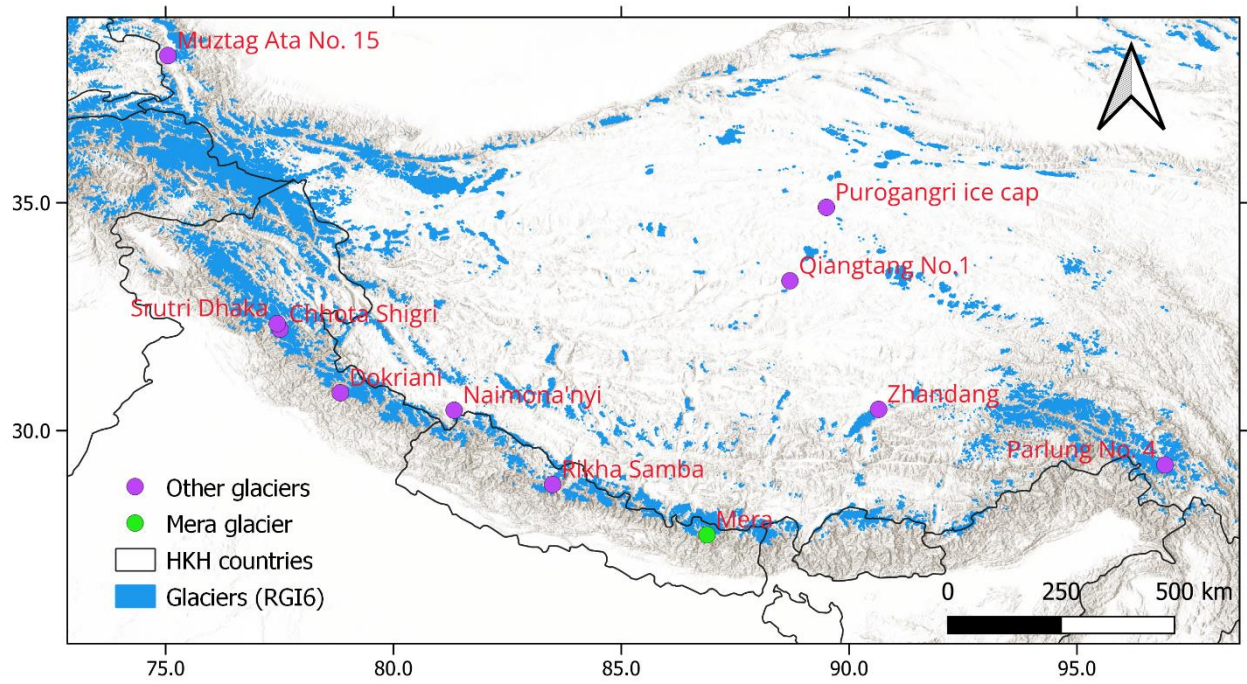


Figure S5.18. Location of glaciers where SEB studies have been conducted in HMA after 2014, and listed in Table 5.8.

Chapter 6

6 Conclusion and perspectives

The cryosphere plays a crucial role in the Himalaya-Karakoram region, particularly in the basins located in the drier parts of the range where a significant portion of fresh water comes from snow and glacier ice melt. While glaciological and meteorological measurements in this region began almost 55 years ago, many were intermittent and others started only in the last decade. Due to the limited measurements, the relationship between glacier mass balance and climate is still not well understood. With advances in remote sensing and the availability of DEMs from multiple sensors, geodetic mass balance methods have contributed to greatly enhancing our understanding of the region-wide glacier mass changes in the Himalaya-Karakoram region. However, there are significant limitations in understanding the mass balance processes and sensitivity. An explanation for the regional pattern of mass change is still missing. In-situ measurements and the analysis of climatic variables can contribute to the understanding of the mass balance processes, but this remains limited at local scale due to the difficulties of maintaining the instruments and conducting field measurements annually or sub-annually due to hard conditions and high altitude. Therefore, mass balance and sensitivity studies have been previously conducted for short time periods in the Himalaya-Karakoram region with limited in-situ data sets. The availability of reanalysis data such as ERA5, has greatly aided in understanding the climates, glacier energy, and mass balance patterns in this region (Arndt and Schneider, 2023). However, mass balance sensitivities derived from the reanalysis data are questionable due to the large biases found in meteorological variables even in the most resolved reanalysis, such as ERA5 Land and HARv2. Therefore, high-quality in-situ measurements are still needed to calibrate and validate surface energy balance models because of their high sensitivity to forcings.

This thesis relied on field data from the upper Dudh Koshi basin in the eastern part of the central Himalaya to advance the knowledge about local meteorology, and thus fill the knowledge gaps on glacier mass balance sensitivity to meteorological variables. At the same time, it also aimed to compare the reanalysis data with field measurements. The key findings are summarized below:

Key finding 1: towards a better description of the upper Dudh Koshi weather

The weather in the upper Dudh Koshi basin is generally spatially homogeneous in both Mera And Khumbu valleys at glacier elevations, except for the amount of precipitation. Winter is characterized by cold, windy, and dry conditions, with less than 10% of precipitation falling during this season. $SWin$ is at a minimum due to the lower solar angle and $LWin$ is due to lower atmospheric temperature and scant cloud coverage. In the pre-monsoon, wind speed decreases, and $SWin$ progressively increases due to the increase in solar angle and $LWin$ due to the rise in temperature and humidity. During the monsoon, $SWin$ is reduced due to overcast conditions, resulting in longwave radiation being at its peak. The weather is consistently warm and humid, with 70% of precipitation occurring during this period. Rain or snow occurs on 4 out of every 5 days,

with daily precipitation exceeding 1 mm w.e. on approximately 2 out of every 3 days. It is worth noting that precipitation mostly occurs during the late afternoon and night. The data from 2016 to 2020 shows that the Khare AWS receives 28% more precipitation than the Pyramid AWS despite being located at a similar elevation.

Key finding 2: meteorological variables from reanalysis are biased and should be bias corrected to run snow and ice surface energy balance models

Meteorological variables from the HARv2 and ERA5 Land datasets show a high correlation with the in-situ data sets at hourly, daily, monthly, and annual scales. Temperature performance varies across different time scales, from sub-daily to seasonal, with higher discrepancies during the daytime. Both gridded datasets represent the seasonal and daily cycles of specific humidity well, although there is still a large humid bias at Mera Summit. Overall, HARv2 is slightly closer to the observations than ERA5 Land for specific humidity. The performance of wind speed is highly variable. ERA5 Land underestimates wind speed at all sites and does not show any pronounced seasonality, while HARv2 overestimates wind speed by a factor of 1.5 to 3 for all sites located at approximately 5350 m a.s.l. Both reanalysis data sets overestimate precipitation at all sites, with a mean positive bias of 0.5-0.9 mm w.e. day⁻¹ at Pyramid for ERA5 Land and HARv2, respectively, and 2-3 times higher at Pheriche and Khare. Therefore, long-term reanalysis data sets has high potential to fill in gaps for glacier-climate studies in areas with limited meteorological data, but corrections from the in-situ measurements are needed.

Key finding 3: the importance of refreezing

The radiative fluxes are the main energy sources of Mera Glacier, where the turbulent heat fluxes are only significant outside the monsoon. Melting is the primary ablation process, while sublimation is significant during the windy months of the post-monsoon and winter. Refreezing is also a crucial mass balance process on Mera Glacier, with a large positive gradient with altitude. In our simulations, we estimate that a total of 44% of the meltwater being refrozen over the whole area of Mera Glacier.

Key finding 4: Mera Glacier mass balance is highly sensitive to both temperature and precipitation

The mass balance sensitivity to meteorological variables can be quantified from synthetic scenarios developed based on observed in-situ data. A temperature change of +1 °C (-1 °C) results in a change of -0.75 ± 0.17 ($+0.93 \pm 0.18$) m w.e. in glacier-wide mass balance. A +20 % (-20 %) change in precipitation results in a change of $+0.52 \pm 0.10$ (-0.60 ± 0.11) m w.e. in mass balance. Similar to other glaciers with summer accumulation regime, Mera Glacier is highly sensitive to both temperature and precipitation.

Perspectives

One of the main remaining question of this study is: to what extent the glacier mass balance sensitivity from Mera Glacier can be considered representative of the Khumbu region and beyond? Testing the findings in this study over other glaciers poses considerable difficulties. Working in the cryosphere of the Himalaya-Karakoram region is extremely challenging due to harsh climate conditions, rough terrain and high altitude. Collecting long-term continuous meteorological data at high altitudes is almost impossible in this region. Even for a single glacier, collecting multiple variables/parameters is challenging and requires significant effort, limiting the application of such as study over other glaciers in the region which may not have a dense measurement network. Furthermore, the impact of large-scale circulation systems such as ISM and sources of precipitation in the upper Dudh Koshi basin are not yet fully understood (Perry et al., 2020), and the mass balance results vary even over relatively short distances (Figure 2.9), requiring more studies.

Some future research directions based on the work from this thesis and my personal experience may be envisioned.

i) Importance of field measurements and use of reanalysis data

One of the significant findings of this thesis is that meteorological variables measured at different elevations at Mera Glacier indicate that they are not homogeneous with respect to altitude. For example, the range of temperature lapse rates varies greatly from daily to annually. The incoming shortwave and longwave radiation are affected by the water vapor ratio, that varies with altitude, and shading in different areas and elevations. Therefore, extrapolating radiative energy based on gradients is not reliable. Furthermore, the altitudinal precipitation gradient in mountain areas remain the largest unknown of hydrological studies (e.g., Immerzeel et al., 2015). For instance, precipitation increase above 3800 m a.s.l. in the Langtang Valley (Immerzeel et al., 2014), but it is still unclear what happens at glacier elevation (above 5000 m a.s.l.). Measuring meteorological data at multiple elevations and settings is key in order to better quantify temperature and precipitation gradients. This inturn is needed in order to better distribute the variables to acquire an in-depth understanding of the distributed energy and mass balance processes.

Second, where in-situ data exist only for short periods or are lacking, reanalysis data is useful for reconstructing historical glacier mass balance (Gurung et al., 2022; Arndt and Schneider, 2023). However, reanalysis data sets are gridded at coarse spatial resolution, posing limitations for glacier scale studies (Khadka et al., 2022). Therefore, downscaling the input long-term reanalysis dataset is needed to yield better results for site-specific long time-series studies (Gurung et al., 2022; Arndt et al., 2021; Sunako et al., 2019).

Thus, the in-situ measurements are very important in both of these aspects, so where the measurements have already started, they should be continued in the future and possibly expanded in the region where they have not yet been done.

ii) Expanding the energy balance and mass balance sensitivity study to multiple spatio-temporal scales

This energy balance study and mass balance sensitivity analysis, conducted over the last four years, have raised other important research questions. For example, *what are the different mass flux gradients in Mera Glacier?* In order to address these question, measurement of specific variables such as refreezing and sublimation at multiple sites would be helpful to gain a deeper understanding of the distributed mass balance processes.

Similarly, our results show that the mass balance of Mera Glacier is less sensitive to climatic variables than that of maritime glaciers in the region (Arndt and Schneider, 2023). This raises multiple questions, such as whether Mera Glacier is a continental or maritime glacier. It may also be the case that this glacier may be changing from a continental to a maritime glacier or that the geographical setting of Mera Glacier or the local climate is responsible.

Another key question is: What is the mass balance sensitivity of other glaciers in the upper Dudh Koshi basin? In order to answer this question, one possible approach is to expand the energy balance and sensitivity study conducted on Mera Glacier in this study. This can be done in two steps. First, in-situ data can be replaced by reanalysis data (downscaled/corrected) for the same period (2016-2020). This data can then be extended to past periods to conduct a long-term analysis, perhaps up to the 1950s. Second, studies can be expanded on other glaciers in the same region, such as Pokalde, west Changri Nup, and others from the Dudh Koshi basin. Additionally, we can expand mass balance sensitivity analysis by selecting glaciers like Arndt and Schneider (2023) throughout Himalaya-Karakoram to compare results from Sakai and Fujita (2017) and regional mass balance patterns (Shean et al., 2020).

Furthermore, the AR6 report of the IPCC (2021) mentions five possible future climate change projections. So, based on different projections, climatic scenarios can be used to predict future thinning and retreat. The analysis will provide an opportunity to understand how the dynamics of the Mera Glacier are adjusting to cumulative mass loss.

iii) **Ongoing and anticipated work on Mera Glacier and beyond**

Analysis (glacier melt, refreezing, sublimation)

As refreezing and sublimation contribute significantly to the mass balance of the Mera Glacier (Litt et al., 2019), studying these factors is crucial. Similarly, this thesis showed that refreeze and sublimation are two major mass balance components. Therefore, an analysis of snow water equivalent at AWS-H is being conducted using data collected by a HydrolInnova SnowFox (cosmic ray sensor). Additionally, we had an eddy-covariance-FlowCapt tower between November 2017 and November 2019 at the same site of AWS-H. The data has yet to be analyzed as it was beyond the scope of this thesis, but such data will provide insights into the sublimation rates in the accumulation area of Mera Glacier.

Measurements could be done on Mera

The ice temperature of Khumbu Glacier is ~ 2 °C higher than the mean annual air temperature in the Everest region (Miles et al., 2018). So, installing temperature sensors at different depths of Mera Glacier (at least 10 m or up to basal if possible)

would help in understanding the englacial structure of Mera Glacier, and in particular to determine whether this glacier is cold type or temperate.

Additional measurements could be envisioned on a big rocky ridge, we observed at 5800 m a.s.l. of Mera Glacier near the separation place of Mera and Naulek branches. Installing a timelapse camera at this location would allow monitoring the glacier on both branches and the whole valley, providing valuable information about glacier dynamics and the glacier mass changes in the area.

iv) **Other cryospheric research work**

Hydrological state and process

Climate change and increasing water demand, as well as comprehending the source of water flows in the Himalayas, emerge as a pivotal concern for evaluating water resource availability (Mimeau et al., 2019b). Hydrological processes could be studied by taking advantage of the current knowledge of mass balance and meteorological conditions in the Mera region. The basic idea is to use the atmospheric–cryospheric–hydrological model in the small catchment of Mera Glacier and compare it with other mountain basins with different precipitation and mass balance results in order to understand the spatial variability of mountain hydrology in the region. This would require some additional measurements such as discharge and gauge height, precipitation, and surface and subsurface temperatures at different locations.

Glacier-related hazards

Cryospheric cascading hazards have recently been observed in the Himalaya region (Pandey et al., 2021; Shrestha et al., 2023). Every year snow/glacier avalanches also takes up a lot of lives in the Himalaya region every year (Fujita et al., 2017; Acharya et al., 2023). The avalanche might be triggered by the instability created by melting and refreezing (Acharya et al., 2023). In addition, the number of potentially dangerous glacier lakes is increasing (Shrestha et al., 2023). If the temperature rises and climate change progresses as predicted or observed in the past, there could be more cryospheric hazards in the Himalayas (Sherpa et al., 2019). Therefore, there is a need the research to understand the physical mechanism of hazards, probability, and vulnerability so that it can work at the policy level.

Annex

Table A1. Different energy balance studies in HMA, including glacier name, location, study period, data type, and mass balance calculated from this model.

Paper	Title	Glacier name, region	Area (km ²)	Latitude(°)	Longitude (°)	Study period	Seasonal only	Data type	MB result (m w.e. s ⁻¹ /a ⁻¹)	Sensitivity analysis
(Kayastha et al., 1999)	Application of a mass-balance model to a Himalayan glacier	AX010, Central Himalaya	0.57	27.70	86.57	10 Jun - 24 Sept 1978	yes	AWS	-0.66	yes
(Fujita and Ageta, 2000)	Effect of summer accumulation on glacier mass balance on the Tibetan Plateau revealed by mass-balance model	Xiao Dongkemadi, Tibetan Plateau	1.77	33.07	92.08	Oct 1992- Oct 1993	no	AWS	+0.2	yes
(Jiang et al., 2010)	A distributed surface energy and mass balance model and its application to a mountain glacier in China	Qiyi, northern Tibetan Plateau	2.87	39.24	97.76	1 Jul-10 Oct 2007	yes	AWS	-0.604	yes
(Yang et al., 2011)	Summertime surface energy budget and ablation modeling in the ablation zone of a maritime Tibetan glacier	Parlung No. 4, southeast Tibetan Plateau	11.7	29.23	96.92	21 May - 8 September 2009	yes	AWS	-4.9	no
(Li et al., 2011)	Surface energy balance of Keqicar Glacier, Tianshan Mountains, China, during ablation period	Keqicar, Tuomuer region, southwest Tian Shan	83.6	41.66	80.16	16 Jun-5 Jul 2005	yes	AWS	-0.71	no
(Mölg et al., 2012)	The footprint of Asian monsoon dynamics in the mass and energy balance of a Tibetan glacier	Zhandang, central Tibetan Plateau		30.47	90.65	2009-2011	no	AWS	-0.154±0.043; -0.382±0.041	yes
(Zhang et al., 2013)	Energy and mass balance of Zhadang glacier surface, central Tibetan Plateau	Zhandang, central Tibetan Plateau	2	30.47	90.65	2009-2011	no	AWS	-1.97;-0.45	yes
(Azam et al., 2014a)	Processes governing the mass balance of Chhota Shigri Glacier (western Himalaya, India) assessed by point-scale surface energy balance measurements	Chhota Shigri, Western Himalaya	15.7	32.23	77.51	2012-2013	no	AWS	x	no
(Sun et al., 2014)	Ablation modeling and surface energy budget in the ablation zone of Laohugou glacier No. 12, western Qilian mountains	Laohugou glacier No. 12, Qilian mountains, China	20.4	39.47	96.55	1 June to 30 September 2011	yes	AWS	-1.703	yes
(Huintjes et al., 2015)	Evaluation of a coupled snow and energy balance model for Zhadang glacier, Tibetan Plateau, using glaciological measurements and time-lapse photography	Zhandang, central Tibetan Plateau	2	30.47	90.65	Oct 2001 - Sep 2011	no	HAR/AWS	-1.067±0.6	no
(Zhu et al., 2015)	Energy and mass-balance comparison between Zhadang and Parlung No. 4 glaciers on the Tibetan Plateau	Zhandang, central Tibetan Plateau	2	30.47	90.65	Aug 2010– Jul 2012	yes	AWS	-1.82	no
		Parlung No. 4, southeast Tibetan Plateau	11.7	29.23	96.92	Aug 2010– Jul 2012	yes	AWS	-4.5	no
(Huintjes et al., 2015)	Surface energy and mass balance at Purogangri ice cap, central Tibetan Plateau, 2001–2011	Purogangri ice cap, central Tibetan Plateau	400	34.90	89.50	2001-2011	no	HAR	-0.044	yes
(Wu et al., 2016)	Analysis of surface energy and mass balance in the accumulation zone of Qiyi Glacier, Tibetan Plateau in an ablation season	Qiyi, northern Tibetan Plateau	2.9	39.24	97.76	30 July – 9 October 2011	yes	AWS	-0.06	no
(Yang et al., 2017)	Comparison of the meteorology and surface energy fluxes of debris-free and debris-covered glaciers in the southeastern Tibetan Plateau	Parlung No. 4, southeastern Tibetan Plateau	11.7	29.25	96.93	Jun-Sep 2016	yes	AWS	x	no
(Sun et al., 2018)	The response of surface mass and energy balance of a continental glacier to climate variability, western Qilian Mountains, China	Laohugou Glacier No. 12	20.4	39.47	96.55	2009-2015	no	AWS	x	yes

(Zhu et al., 2018)	Differences in mass balance behavior for three glaciers from different climatic regions on the Tibetan Plateau	Parlung No. 4, southeastern Tibetan Plateau	11.86	29.25	96.93	1Oct 2008-21Sept 2013	no	AWS	-6.69	yes
		Zhandang, central Tibetan Plateau	1.8	30.47	90.65	1Oct 2008-21Sept 2014	no	AWS	-7.88	yes
		Muztag Ata No. 15	1.09	38.23	75.05	1Oct 2008-21Sept 2015	no	AWS	0.34	yes
(Li et al., 2018)	Glacier Energy and Mass Balance in the Inland Tibetan Plateau: Seasonal and Interannual Variability in Relation to Atmospheric Changes	Qiangtang No.1, inland Tibetan Plateau	1.84	33.29	88.70	1 November 2012- 31 October 2016	no	AWS	-0.089	no
(Litt et al., 2019)	Glacier ablation and temperature indexed melt models in the Nepalese Himalaya	Mera ablation Zone, Central Himalaya		27.72	86.90	2013-2017	yes	AWS	x	no
		Mera Summit, Central Himalaya		27.71	86.87	2013-2016	yes	AWS	x	no
		Yala, Central Himalaya		28.23	85.62	2014-2017	yes	AWS	x	no
(Li et al., 2019)	Energy and mass balance characteristics of the Guliya ice cap in the West Kunlun Mountains, Tibetan Plateau	Guliya ice cap, west Tibetan Plateau	111.4	35.26	81.46	Oct 2015-Sept 2016	no	AWS	-0.193 ± 0.042	yes
(Acharya and Kayastha, 2019)	Mass and Energy Balance Estimation of Yala Glacier (2011–2017), Langtang Valley, Nepal Anushilan	Yala, Central Himalaya	1.37	28.23	85.61	2011-2017	no	AWS	-0.81 ± 0.27	no
(Sunako et al., 2019)	Mass balance of Trambau Glacier, Rolwaling region, Nepal Himalaya: in-situ observations, long-term reconstruction and mass-balance sensitivity	Trambau, Central Himalaya	31.7	27.9	86.5	1980-2018	no	AWS/ERA-Interim	-0.65 ± 0.39	yes
(Zhu et al., 2020)	Mass balance of Muji Glacier, northeastern Pamir, and its controlling climate factors	Muji, northeastern Pamir	2.33	39.19	73.74	2011-2017	no	AWS	-0.276	yes
(Matthews et al., 2020)	Going to Extremes Installing the World's Highest Weather Stations on Mount Everest	South Col, Central Himalaya		27.98	86.93	Jun-Nov 2019	yes	AWS	x	no
		Camp II, Central Himalaya		27.98	86.90	2019	yes	AWS	x	no
(Singh et al., 2020)	Radiation and energy balance dynamics over a rapidly receding glacier in the central Himalaya	Pindari, Central Himalaya	9.6	30.26	79.99	Jun 2016- Jul 2017	no	AWS	x	no
(Wang et al., 2020a)	A Test Study of an Energy and Mass Balance Model Application to a Site on Urumqi Glacier No. 1, Chinese Tian Shan	Urumqi Glacier No. 1	1.56	43.12	86.81	Apr- Aug 2018	yes	AWS	-0.67 ± 0.03	
(Arndt et al., 2021)	Atmosphere Driven Mass-Balance Sensitivity of Halji Glacier, Himalayas	Hanji, Central Himalaya	1.9	30.27	81.47	1982-2019	no	AWS/ERA5L	-0.48±0.71	yes
(Liu et al., 2021)	Monsoon Clouds Control the Summer Surface Energy Balance on East Rongbuk Glacier (6,523 m Above Sea Level), the Northern of Mt. Qomolangma (Everest)	East Rongbuk, Central Himalaya		28.17	86.95	2005	yes	AWS	x	yes
(Zhu et al., 2021)	The Influence of Key Climate Variables on Mass Balance of Naimona'nyi Glacier on a North-Facing Slope in the Western Himalayas	Naimona'nyi, western Himalaya	7.34	30.45	81.33	Oct 2010-Sept 2018	no	AWS	-0.33	yes
(Guo et al., 2021)	Five-Year Analysis of Evaposublimation Characteristics and Its Role on Surface Energy Balance SEB on a Midlatitude Continental Glacier	August-one	2.4	39.01	98.90	2016-2020	no	AWS	x	no

(Li et al., 2022)	Summertime surface mass balance and energy balance of Urumqi Glacier No. 1, Chinese Tien Shan, modeled by linking COSIMA and in-situ measured meteorological records	Urumqi Glacier No. 1	1.52	43.1	86.81	1 May - 31 August 2018	yes	AWS	-0.77	yes
(Gurung et al., 2022)	A long-term mass-balance reconstruction (1974–2021) and a decadal in-situ mass-balance record (2011–2021) of Rikha Samba Glacier, central Himalaya	Rikha Samba, Central Himalaya	5.62	28.82	83.49	1974-2021	no	AWS/ERA5	-0.56 ± 0.27	yes
(Potocki et al., 2022)	Mt. Everest's highest glacier is a sentinel for accelerating ice loss	South Col, Central Himalaya		27.98	86.93	1950-2020	no	ERA5/AWS	~ -2	yes
(Oulkar et al., 2022)	Energy fluxes, mass balance, and climate sensitivity of the Sutri Dhaka Glacier in the western Himalaya	Sutri Dhaka, western Himalaya	20	32.35	77.45	2015-2017	no	AWS	-1.09 ± 0.31: -0.62 ± 0.19	yes
(Mandal et al., 2022)	11-year record of wintertime snow surface energy balance and sublimation at 4863 m a.s.l. on Chhota Shigri Glacier moraine (western Himalaya, India)	Chhota Shigri, western Himalaya		32.23	77.51	2009-2020	yes	AWS	X	no
(Srivastava & Azam, 2022)	Mass- and Energy-Balance Modeling and Sublimation Losses on Dokriani Bamak and Chhota Shigri Glaciers in Himalaya Since 1979	Dokriani, Central Himalaya	7.03	30.83	78.83	1979-2020	no	EAR5/AWS	-0.27 ± 0.32	yes
		Chhota Shigri, western Himalaya	15.5	32.23	77.51	1979-2020	no	EAR5/AWS	-0.31 ± 0.38	yes
(Conway et al., 2022)	Cloud forcing of surface energy balance from in-situ measurements in diverse mountain glacier environments	Chhota Shigri, western Himalaya		32.23	77.51	2012-2013	no	AWS	X	no
		Yala, Central Himalaya		28.23	85.62	2014-2018	no	AWS	X	no
		Mera Summit, Central Himalaya		27.706	86.87	2013-2016	no	AWS	X	no
		Naulek, Central Himalaya		27.72	86.89	2013-2017	no	AWS	X	no
(Shaw et al., 2022)s	Multi-decadal monsoon characteristics and glacier response in High Mountain Asia	Yala, Central Himalaya	1.5	28.23	85.61	1981-2019	no	AWS/WRF driven by ERA5	-0.59 ± 0.20	no
		Parlung No. 4, southeastern Tibetan Plateau	11.7	29.26	96.94	1981-2019	no		-0.55 ± 0.12	no
		Mugagangqiong, central Tibetan Plateau	1.9	32.25	87.49	1981-2019	no		-0.04 ± 0.09	no
(Fugger et al., 2022)	Understanding monsoon controls on the energy and mass balance of glaciers in the Central and Eastern Himalaya	Lirung, Central Himalaya	4	28.233	85.562	2014/5-2014/10	yes	AWS	X	no
		Langtang, Central Himalaya	37	28.279	85.722	2019/5-2019/10	yes	AWS	X	no
		Yala, Central Himalaya	1.4	28.235	85.613	2019/5-2019/10	yes	AWS	X	no
		Changri Nup, Central Himalaya	2.7	27.993	86.78	2016/5-2016/10	yes	AWS	X	no
		24 K, southeastern Tibetan Plateau	2	29.761	95.72	2016/6-2016/9	yes	AWS	X	no
		Parlung No. 4, southeastern Tibetan Plateau	11	29.25	96.93	2016/5-2016/10	yes	AWS	X	no

		Hailuogou, southeastern Tibetan Plateau	24.1	29.56	101.97	2008/5-2008/10	yes	AWS	X	no
(Kronenberg et al., 2022)	Long-term firn and mass balance modelling for Abramov glacier, Pamir Alay	Abramov, Pamir Alay	24	39.62	71.56	1968-2020	no	AWS/ERA5	-0.27	no
(Liu et al., 2023)	Cold-Season Surface Energy Balance on East Rongbuk Glacier, Northern Slope of Mt. Qomolangma (Everest)	East Rongbuk, Central Himalaya	41.7	28.17	86.95	2007-2008	yes	AWS	x	no
(Arndt and Schneider, 2023)	Spatial pattern of glacier mass balance sensitivity to atmospheric forcing in High Mountain Asia	Batysh Sook, Tein Shan	1	41.79	77.75	2001-2018	no	ERA5 land	-1.46	yes
		Zhadang, central Tibetan Plateau	1.5	30.47	90.64	2001-2018	no	ERA5 land	-1.44	yes
		Urumqi Glacier No. 1, Tein Shan	1.6	43.11	86.81	2001-2018	no	ERA5 land	-2.95	yes
		Yala, Central Himalaya	2.1	28.24	85.62	2001-2018	no	ERA5 land	-1.16	yes
		Halji glacier (HAL)	2.3	30.26	81.47	2001-2018	no	ERA5 land	-2.85	yes
		Bayi Ice Cap, northwestern Tibetan Plateau	2.6	39.02	98.89	2001-2018	no	ERA5 land	-0.5	yes
		Parlung No. 94, southeastern Tibetan Plateau	2.8	29.39	96.98	2001-2018	no	ERA5 land	0.71	yes
		Keli Yanghe source, Kunlung	3.7	36.7	77.86	2001-2018	no	ERA5 land	0.53	yes
		Naimona'nyi, western Himalaya	7.3	30.46	81.32	2001-2018	no	ERA5 land	-0.64	yes
		Parlung No. 4, southeastern Tibetan Plateau	11.9	29.23	96.92	2001-2018	no	ERA5 land	1.19	yes
		Chhota Shigri, Western Himalaya	16.8	32.22	77.51	2001-2018	no	ERA5 land	-0.65	yes
		Abramov, Pamir Alay	21.3	39.61	71.57	2001-2018	no	ERA5 land	-0.8	yes
		Guliya Ice Cap, Kunlung	111.4	35.26	81.46	2001-2018	no	ERA5 land	0.28	yes
		Muztagh Ata, Pamir	293.4	38.24	75.19	2001-2018	no	ERA5 land	-0.14	yes
Purogangrilce cap, central Tibetan Plateau	397.8	33.91	89.14	2001-2018	no	ERA5 land	-1.49	yes		
Siachen, Karakoram	1078	35.43	76.89	2001-2018	no	ERA5 land	0.36	yes		

7 References

- Acharya, A. and Kayastha, R. B.: Mass and Energy Balance Estimation of Yala Glacier (2011-2017), Langtang Valley, Nepal, *mdpi Water*, 11, <https://doi.org/10.3390/w11010006>, 2019.
- Acharya, A., Steiner, J. F., Walizada, K. M., Ali, S., Zakir, Z. H., Caiserman, A., and Watanabe, T.: Review article: Snow and ice avalanches in high mountain Asia – scientific, local and indigenous knowledge, *Nat. Hazards Earth Syst. Sci.*, 23, 2569–2592, <https://doi.org/10.5194/nhess-23-2569-2023>, 2023.
- Ageta, Y. and Higuchi, K.: Estimation of mass balance components of a summer-accumulation type glacier in the Nepal Himalaya., *Geogr. Ann. Ser. A*, 66 A, 249–255, <https://doi.org/10.1080/04353676.1984.11880113>, 1984.
- Ageta, Y., Ohata, T., Tanaka, Y., Ikegami, K., and Higuchi, K.: Mass Balance of Glacier AX010 in Shorong Himal, East Nepal during the Summer Monsoon Season Glaciological Expedition of Nepal, Contribution No. 66, *J. Japanese Soc. Snow Ice*, 41, 34–41, https://doi.org/10.5331/SEPPYO.41.SPECIAL_34, 1980.
- Alduchov, O. A. and Eskridge, R. E.: Improved Magnus form approximation of saturation vapor pressure. / *Appl Meteor.*, 35, 601–609., 1996.
- Alford, D. and Armstrong, R.: Nepal glaciers and rivers The role of glaciers in stream flow from the Nepal Himalaya Nepal glaciers and rivers Nepal glaciers and rivers, *Cryosph. Discuss*, 4, 469–494, 2010.
- Anderson, E. A.: A point energy and mass balance model of a snow cover, Tech. Report, Natl. Weather Serv. (NWS), United States, 1976.
- Angchuk, T., Ramanathan, A., Bahuguna, I. M., Mandal, A., Soheb, M., Singh, V. B., Mishra, S., and Vatsal, S.: Annual and seasonal glaciological mass balance of Patsio Glacier, western Himalaya (India) from 2010 to 2017, *J. Glaciol.*, 67, 1137–1146, <https://doi.org/10.1017/JOG.2021.60>, 2021.
- Arndt, A. and Schneider, C.: Spatial pattern of glacier mass balance sensitivity to atmospheric forcing in High Mountain Asia, *J. Glaciol.*, 1–18, <https://doi.org/10.1017/JOG.2023.46>, 2023.
- Arndt, A., Scherer, D., and Schneider, C.: Atmosphere driven mass-balance sensitivity of Halji glacier, Himalayas, *Atmosphere (Basel)*, 12, <https://doi.org/10.3390/ATMOS12040426>, 2021.
- Autin, P., Sicart, J. E., Rabatel, A., Soruco, A., and Hock, R.: Climate Controls on the Interseasonal and Interannual Variability of the Surface Mass and Energy Balances of a Tropical Glacier (Zongo Glacier, Bolivia, 16°S): New Insights From the Multi-Year Application of a Distributed Energy Balance Model, *J. Geophys. Res. Atmos.*, 127, 1–21, <https://doi.org/10.1029/2021JD035410>, 2022.
- Azam, M. F.: Climate-Glacier relationship in the monsoon-arid transition zone : A Case study in Himachal Pradesh, India, 177 pp., 2014.

- Azam, M. F., Wagnon, P., Vincent, C., Ramanathan, A., Favier, V., Mandal, A., and Pottakkal, J. G.: Processes governing the mass balance of Chhota Shigri Glacier (western Himalaya, India) assessed by point-scale surface energy balance measurements, *Cryosph.*, 8, 2195–2217, <https://doi.org/10.5194/tc-8-2195-2014>, 2014a.
- Azam, M. F., Wagnon, P., Vincent, C., Ramanathan, A., Linda, A., and Singh, V. B.: Reconstruction of the annual mass balance of Chhota Shigri glacier, Western Himalaya, India, since 1969, *Ann. Glaciol.*, 55, 69–80, <https://doi.org/10.3189/2014AoG66A104>, 2014b.
- Azam, M. F., Wagnon, P., Berthier, E., Vincent, C., Fujita, K., and Kargel, J. S.: Review of the status and mass changes of Himalayan-Karakoram glaciers, *J. Glaciol.*, 64, 61–74, <https://doi.org/10.1017/jog.2017.86>, 2018.
- Azam, M. F., Kargel, J. S., Shea, J. M., Nepal, S., Haritashya, U. K., Srivastava, S., Maussion, F., Qazi, N., Chevallier, P., Dimri, A. P., Kulkarni, A. V., Cogley, J. G., and Bahuguna, I. M.: Glaciohydrology of the Himalaya-Karakoram, *Science* (80-.), 3668, eabf3668, <https://doi.org/10.1126/science.abf3668>, 2021.
- Bajracharya, S. R., Maharjan, S. B., Shrestha, F., Bajracharya, O. R., and Baidya, S.: Glacier Status in Nepal and Decadal Change from 1980 to 2010 Based on Landsat Data, ICIMOD, <https://doi.org/10.53055/ICIMOD.591>, 2014.
- Bamber, J. L. and Rivera, A.: A review of remote sensing methods for glacier mass balance determination, *Glob. Planet. Change*, 59, 138–148, <https://doi.org/10.1016/j.gloplacha.2006.11.031>, 2007.
- Baral, P., Kayastha, R. B., Immerzeel, W. W., Pradhananga, N. S., Bhattarai, B. C., Shahi, S., Galos, S., Springer, C., Joshi, S. P., and Mool, P. K.: Preliminary results of mass-balance observations of Yala Glacier and analysis of temperature and precipitation gradients in Langtang Valley, Nepal, *Ann. Glaciol.*, 55, 9–14, <https://doi.org/10.3189/2014AOG66A106>, 2014.
- Baudouin, J., Herzog, M., and Petrie, C.: Cross-validating precipitation datasets in the Indus River basin, 2020.
- Beraud, L., Cusicanqui, D., Rabatel, A., Brun, F., Vincent, C., and Six, D.: Glacier-wide seasonal and annual geodetic mass balances from Pléiades stereo images: application to the Glacier d'Argentière, French Alps, *J. Glaciol.*, 69, 525–537, <https://doi.org/10.1017/JOG.2022.79>, 2023.
- Berthier, E. and Brun, F.: Karakoram geodetic glacier mass balances between 2008 and 2016: persistence of the anomaly and influence of a large rock avalanche on Siachen Glacier, *cambridge.org*, 65, 494–507, <https://doi.org/10.1017/jog.2019.32>, 2019.
- Berthier, E., Belart, J., Floriciou, D., Gardner, A. S., Gourmelen, N., Hugonnet, R., Jakob, L., Käab, A., Krieger, L., Pálsson, F., Paul, F., Treichler, D., Wouters, B., and Zemp, M.: Measuring glacier mass changes from space - a review, *Reports Prog. Phys.*, 1–55, <https://doi.org/10.1088/1361-6633/acaf8e>, 2023.
- Blau, M. T., Turton, J. V., Sauter, T., and Mölg, T.: Surface mass balance and energy balance of the 79N Glacier (Nioghalvfjærdsfjorden, NE Greenland) modeled by linking COSIPY and Polar

- WRF, J. *Glaciol.*, 1–15, <https://doi.org/10.1017/jog.2021.56>, 2021.
- Bolch, T., Kulkarni, A., Kääb, A., Huggel, C., Paul, F., Cogley, J. G., Frey, H., Kargel, J. S., Fujita, K., Scheel, M., Bajracharya, S., and Stoffel, M.: The state and fate of himalayan glaciers, *Science* (80-.), 336, 310–314, <https://doi.org/10.1126/science.1215828>, 2012.
- Bolch, T., Shea, J. M., Liu, S., Azam, F. M., Gao, Y., Gruber, S., Immerzeel, W. W., Kulkarni, A., Li, H., Tahir, A. A., Zhang, G., and Zhang, Y.: Status and Change of the Cryosphere in the Extended Hindu Kush Himalaya Region, in: *The Hindu Kush Himalaya Assessment*, Springer International Publishing, 209–255, https://doi.org/10.1007/978-3-319-92288-1_7, 2019.
- Bollasina, M., Bertolalani, L., and Tartari, G.: Meteorological observations at high altitude in the Khumbu Valley, Nepal Himalayas, 1994-1999, *Bulletin of Glaciological Research*, 19, 1–12 pp., 2002.
- Bonasoni, P., Laj, P., Marinoni, A., Sprenger, M., Angelini, F., Arduini, J., Bonafè, U., Calzolari, F., Colombo, T., Decesari, S., Di Biagio, C., di Sarra, A. G., Evangelisti, F., Duchi, R., Facchini, M., Fuzzi, S., Gobbi, G. P., Maione, M., Panday, A., Roccatò, F., Sellegri, K., Venzac, H., Verza, G., Villani, P., Vuillermoz, E., and Cristofanelli, P.: Atmospheric Brown Clouds in the Himalayas: first two years of continuous observations at the Nepal Climate Observatory-Pyramid (5079 m), *Atmos. Chem. Phys.*, 10, 7515–7531, <https://doi.org/10.5194/acp-10-7515-2010>, 2010.
- Bonekamp, P. N. J., de Kok, R. J., Collier, E., and Immerzeel, W. W.: Contrasting Meteorological Drivers of the Glacier Mass Balance Between the Karakoram and Central Himalaya, *Front. Earth Sci.*, 7, 107, <https://doi.org/10.3389/feart.2019.00107>, 2019.
- Bookhagen, B. and Burbank, D. W.: Topography, relief, and TRMM-derived rainfall variations along the Himalaya, *Geophys. Res. Lett.*, 33, <https://doi.org/10.1029/2006GL026037>, 2006.
- Bookhagen, B. and Burbank, D. W.: Toward a complete Himalayan hydrological budget: Spatiotemporal distribution of snowmelt and rainfall and their impact on river discharge, *J. Geophys. Res. Earth Surf.*, 115, <https://doi.org/10.1029/2009JF001426>, 2010.
- Boone, A.: Boone A. Description du schema de neige ISBA-ES (Explicit Snow). Centre National de Recherches Météorologiques, Météo-France, Toulouse, Available from <http://www.cnrn.meteo.fr/IMG/pdf/snowdoc.pdf>, 2002.
- Braithwaite, R. J. and Raper, S. C. B.: Estimating equilibrium-line altitude (ELA) from glacier inventory data, *Ann. Glaciol.*, 50, 127–132, <https://doi.org/10.3189/172756410790595930>, 2009.
- van den Broeke, M. R. and Bintanja, R.: The surface energy balance of antarctic snow and blue ice, 1995.
- Brun, F., Dumont, M., Wagnon, P., Berthier, E., Azam, M. F., Shea, J. M., Sirguey, P., Rabatel, A., and Ramanathan, A.: Seasonal changes in surface albedo of Himalayan glaciers from MODIS data and links with the annual mass balance, *Cryosphere*, 9, 341–355, <https://doi.org/10.5194/tc-9-341-2015>, 2015.
- Brun, F., Berthier, E., Wagnon, P., Kääb, A., and Treichler, D.: A spatially resolved estimate of High Mountain Asia glacier mass balances from 2000 to 2016, *Nat. Geosci.*, 10, 668–673,

<https://doi.org/10.1038/ngeo2999>, 2017.

Brun, F., Wagnon, P., Berthier, E., Jomelli, V., Maharjan, S. B., Shrestha, F., and Kraaijenbrink, P. D. A.: Heterogeneous Influence of Glacier Morphology on the Mass Balance Variability in High Mountain Asia, *J. Geophys. Res. Earth Surf.*, **124**, 1331–1345, <https://doi.org/10.1029/2018JF004838>, 2019.

Brunello, C. F., Andermann, C., Marc, O., Schneider, K. A., Comiti, F., Achleitner, S., and Hovius, N.: Annually Resolved Monsoon Onset and Withdrawal Dates Across the Himalayas Derived From Local Precipitation Statistics, *Geophys. Res. Lett.*, **47**, e2020GL088420, <https://doi.org/10.1029/2020GL088420>, 2020.

Cao, B., Gruber, S., Zheng, D., and Li, X.: The ERA5-Land Soil-Temperature Bias in Permafrost Regions, <https://doi.org/10.5194/tc-2020-76>, 2020.

Clauzel, L., Ménégoz, M., Gilbert, A., Gagliardini, O., Six, D., Gastineau, G., and Vincent, C.: Sensitivity of Glaciers in the European Alps to Anthropogenic Atmospheric Forcings: Case Study of the Argentière Glacier, *Geophys. Res. Lett.*, **50**, e2022GL100363, <https://doi.org/10.1029/2022GL100363>, 2023.

Cogley, J. G., Hock, R., Rasmussen, L. A., Arendt, A. A., Bauder, A., Braithwaite, R. J., Jansson, P., Kaser, G., Möller, M., Nicholson, L., and M., Z.: Glossary of glacier mass balance and related terms, (IHP-VII Tech. Doc. Hydrol. Int. Hydrol. Program., 2011.

Conway, J. P., Abermann, J., Andreassen, L. M., Azam, M. F., Cullen, N. J., Fitzpatrick, N., Giesen, R. H., Langley, K., MacDonell, S., Mölg, T., Radić, V., Reijmer, C. H., and Sicart, J.-E.: Cloud forcing of surface energy balance from in situ measurements in diverse mountain glacier environments, *Cryosph.*, **16**, 3331–3356, <https://doi.org/10.5194/tc-16-3331-2022>, 2022.

Cuffey, K. M. J. and Paterson, W. S. B.: *The Physics of Glacier*, 1–23 pp., 2010.

Dee, D. P., Uppala, S. M., Simmons, A. J., Berrisford, P., Poli, P., Kobayashi, S., Andrae, U., Balmaseda, M. A., Balsamo, G., Bauer, P., Bechtold, P., Beljaars, A. C. M., van de Berg, L., Bidlot, J., Bormann, N., Delsol, C., Dragani, R., Fuentes, M., Geer, A. J., Haimberger, L., Healy, S. B., Hersbach, H., Hólm, E. V., Isaksen, I., Kållberg, P., Köhler, M., Matricardi, M., McNally, A. P., Monge-Sanz, B. M., Morcrette, J. J., Park, B. K., Peubey, C., de Rosnay, P., Tavolato, C., Thépaut, J. N., and Vitart, F.: The ERA-Interim reanalysis: Configuration and performance of the data assimilation system, *Q. J. R. Meteorol. Soc.*, **137**, 553–597, <https://doi.org/10.1002/qj.828>, 2011.

DHM: Observed Climate Trend Analysis in the Districts and Physiographic Regions of Nepal (1971-2014)., Kathmandu, 2017.

Dobhal, D. P., Mehta, M., and Srivastava, D.: Influence of debris cover on terminus retreat and mass changes of Chorabari Glacier, Garhwal region, central Himalaya, India, *J. Glaciol.*, **59**, 961–971, <https://doi.org/10.3189/2013JOG12J180>, 2013.

Dobhal, D. P., Pratap, B., Bhambri, R., and Mehta, M.: Mass balance and morphological changes of Dokriani Glacier (1992–2013), Garhwal Himalaya, India, *Quat. Sci. Adv.*, **4**, 100033, <https://doi.org/10.1016/J.QSA.2021.100033>, 2021.

- Edwards, T. L., Nowicki, S., Marzeion, B., Hock, R., Goelzer, H., Seroussi, H., Jourdain, N. C., Slater, D. A., Turner, F. E., Smith, C. J., McKenna, C. M., Simon, E., Abe-Ouchi, A., Gregory, J. M., Larour, E., Lipscomb, W. H., Payne, A. J., Shepherd, A., Agosta, C., Alexander, P., Albrecht, T., Anderson, B., Asay-Davis, X., Aschwanden, A., Barthel, A., Bliss, A., Calov, R., Chambers, C., Champollion, N., Choi, Y., Cullather, R., Cuzzone, J., Dumas, C., Felikson, D., Fettweis, X., Fujita, K., Galton-Fenzi, B. K., Gladstone, R., Golledge, N. R., Greve, R., Hattermann, T., Hoffman, M. J., Humbert, A., Huss, M., Huybrechts, P., Immerzeel, W., Kleiner, T., Kraaijenbrink, P., Le clec'h, S., Lee, V., Leguy, G. R., Little, C. M., Lowry, D. P., Malles, J. H., Martin, D. F., Maussion, F., Morlighem, M., O'Neill, J. F., Nias, I., Pattyn, F., Pelle, T., Price, S. F., Quiquet, A., Radić, V., Reese, R., Rounce, D. R., Rückamp, M., Sakai, A., Shafer, C., Schlegel, N. J., Shannon, S., Smith, R. S., Straneo, F., Sun, S., Tarasov, L., Trusel, L. D., Van Breedam, J., van de Wal, R., van den Broeke, M., Winkelmann, R., Zekollari, H., Zhao, C., Zhang, T., and Zwinger, T.: Projected land ice contributions to twenty-first-century sea level rise, *Nat.* 2021 5937857, 593, 74–82, <https://doi.org/10.1038/s41586-021-03302-y>, 2021.
- Eeckman, J., Chevallier, P., Boone, A., Neppel, L., De Rouw, A., Delclaux, F., and Koirala, D.: Providing a non-deterministic representation of spatial variability of precipitation in the Everest region, *Hydrol. Earth Syst. Sci.*, 21, 4879–4893, <https://doi.org/10.5194/HESS-21-4879-2017>, 2017.
- Essery, R., Morin, S., Lejeune, Y., and B Ménard, C.: A comparison of 1701 snow models using observations from an alpine site, *Adv. Water Resour.*, 55, 131–148, <https://doi.org/10.1016/j.advwatres.2012.07.013>, 2013.
- Favier, V., Wagnon, P., Chazarin, J. P., Maisincho, L., and Coudrain, A.: One-year measurements of surface heat budget on the ablation zone of Antizana Glacier 15, Ecuadorian Andes, *J. Geophys. Res. Atmos.*, 109, <https://doi.org/10.1029/2003JD004359>, 2004.
- Førland, E. J., Allerup, P., Dahlström, B., Elomaa, E., Jo´nsson, T., Madsen, H., Jaakko, P., Rissanen, P., Vedin, H., and Vejen, F.: Manual for operational correction of Nordic precipitation data, DNMI-Reports, [https://doi.org/Report Nr. 24/96](https://doi.org/Report%20Nr.%2024/96), DNMI, P.O. Box 43, Blindern, Oslo, Norway, 1996.
- Fugger, S., Fyffe, C. L., Fatichi, S., Miles, E., Mccarthy, M., and Shaw, T. E.: Understanding monsoon controls on the energy and mass balance of glaciers in the Central and Eastern Himalaya, *Cryosph.*, 16, 1631–1652, <https://doi.org/https://doi.org/10.5194/tc-16-1631-2022>, 2022.
- Fujii, Y., Nakawo, M., and Shrestha, M.: Mass balance studies of the glaciers in hidden valley, Mukut Himal, *J. Japanese Soc. Snow Ice*, 38(Special, 17–21, 1976.
- Fujita, K.: Effect of precipitation seasonality on climatic sensitivity of glacier mass balance, *Earth Planet. Sci. Lett.*, 276, 14–19, <https://doi.org/10.1016/j.epsl.2008.08.028>, 2008a.
- Fujita, K.: Influence of precipitation seasonality on glacier mass balance and its sensitivity to climate change, *Ann. Glaciol.*, 48, 88–92, 2008b.
- Fujita, K. and Ageta, Y.: Effect of summer accumulation on glacier mass balance on the Tibetan Plateau revealed by mass-balance model, *J. Glaciol.*, 46, 244–252, <https://doi.org/10.3189/172756500781832945>, 2000.

- Fujita, K., Kadota, T., Rana, B., Kayastha, R., and Ageta, Y.: Shrinkage of Glacier AX010 in Shorong region, Nepal Himalayas in the 1990s, *Bull. Glaciol.*, 18, 51–54, 2001.
- Fujita, K., Inoue, H., Izumi, T., Yamaguchi, S., Sadakane, A., Sunako, S., Nishimura, K., Immerzeel, W. W., Shea, J. M., Kayastha, R. B., Sawagaki, T., Breashears, D. F., Yagi, H., and Sakai, A.: Anomalous winter-snow-amplified earthquake-induced disaster of the 2015 Langtang avalanche in Nepal, *Nat. Hazards Earth Syst. Sci.*, 17, 749–764, <https://doi.org/10.5194/nhess-17-749-2017>, 2017.
- Gautam, C. and Mukherjee, B.: Synthesis of glaciological studies on Tipra Bank Glacier Bhyundar Ganga Basin, district Chamoli, Uttar Pradesh (F.S. 1980-1988) Geological Survey of India, Northern Region, Lucknow, 1992.
- Giese, A., Boone, A., Wagnon, P., and Hawley, R.: Incorporating moisture content in surface energy balance modeling of a debris-covered glacier, *Cryosph.*, 14, 1555–1577, <https://doi.org/10.5194/tc-14-1555-2020>, 2020.
- Gregory, J. M. and Oerlemans, J.: Simulated future sea-level rise due to glacier melt based on regionally and seasonally resolved temperature changes, *Nat.* 1998 3916666, 391, 474–476, <https://doi.org/10.1038/35119>, 1998.
- GSI, (Geological Survey of India): Annual general report, Part 8. Volume 144, Volume 124, 2011.
- Guo, S., Chen, R., Han, C., Liu, J., Wang, X., and Liu, G.: Five-Year Analysis of Evaposublimation Characteristics and Its Role on Surface Energy Balance SEB on a Midlatitude Continental Glacier, *Wiley Online Libr.*, 8, 2021.
- Gurung, T. R., Kayastha, R. B., Fujita, K., Joshi, S. P., Sinisalo, A., and Kirkham, J. D.: A long-term mass-balance reconstruction (1974–2021) and a decadal in situ mass-balance record (2011–2021) of Rikha Samba Glacier, central Himalaya, *J. Glaciol.*, 1–14, <https://doi.org/10.1017/JOG.2022.93>, 2022.
- Ham, J.: Useful equations and tables in micrometeorology, *Wiley Online Libr.*, 2005.
- Hamm, A., Arndt, A., Kolbe, C., Wang, X., Thies, B., Boyko, O., Reggiani, P., Scherer, D., Bendix, J., and Schneider, C.: Intercomparison of gridded precipitation datasets over a sub-region of the Central Himalaya and the Southwestern Tibetan Plateau, *Water* 2020, Vol. 12, Page 3271, 12, 3271, <https://doi.org/10.3390/w12113271>, 2020.
- Hansen, J., Sato, M., Ruedy, R., Lo, K., Lea, D. W., and Medina-Elizade, M.: Global temperature change, *Proc. Natl. Acad. Sci. U. S. A.*, 103, 14288–14293, https://doi.org/10.1073/PNAS.0606291103/SUPPL_FILE/06291FIG9.PDF, 2006.
- Hantel, M., Ehrendorfer, M., and Haslinger, A.: Climate sensitivity of snow cover duration in Austria, *Int. J. Climatol.*, 20, 615–640, [https://doi.org/10.1002/\(SICI\)1097-0088\(200005\)20:6<615::AID-JOC489>3.0.CO;2-0](https://doi.org/10.1002/(SICI)1097-0088(200005)20:6<615::AID-JOC489>3.0.CO;2-0), 2000.
- Hersbach, H., Bell, B., Berrisford, P., Hirahara, S., Horányi, A., Muñoz-Sabater, J., Nicolas, J., Peubey, C., Radu, R., Schepers, D., Simmons, A., Soci, C., Abdalla, S., Abellan, X., Balsamo, G., Bechtold, P., Biavati, G., Bidlot, J., Bonavita, M., De Chiara, G., Dahlgren, P., Dee, D., Diamantakis, M., Dragani, R., Flemming, J., Forbes, R., Fuentes, M., Geer, A., Haimberger, L.,

- Healy, S., Hogan, R. J., Hólm, E., Janisková, M., Keeley, S., Laloyaux, P., Lopez, P., Lupu, C., Radnoti, G., de Rosnay, P., Rozum, I., Vamborg, F., Villaume, S., and Thépaut, J. N.: The ERA5 global reanalysis, *Q. J. R. Meteorol. Soc.*, 146, 1999–2049, <https://doi.org/10.1002/qj.3803>, 2020.
- Hock, R.: A distributed temperature-index ice- and snowmelt model including potential direct solar radiation, *J. Glaciol.*, 45, 101–111, <https://doi.org/10.3189/S0022143000003087>, 1999.
- Hock, R.: Glacier melt: A review of processes and their modelling, *Prog. Phys. Geogr.*, 29, 362–391, <https://doi.org/10.1191/0309133305pp453ra>, 2005.
- Hock, R. and Holmgren, B.: A distributed surface energy-balance model for complex topography and its application to Storglaciären, Sweden, *J. Glaciol.*, 51, 25–36, <https://doi.org/10.3189/172756505781829566>, 2005.
- Hrudya, P. H., Varikoden, H., and Vishnu, R.: A review on the Indian summer monsoon rainfall, variability and its association with ENSO and IOD, *Meteorol. Atmos. Phys.*, 133, 1–14, <https://doi.org/10.1007/S00703-020-00734-5/METRICS>, 2021.
- Huang, X., Zhou, T., Turner, A., Dai, A., Chen, X., Clark, R., Jiang, J., Man, W., Murphy, J., Rostron, J., Wu, B., Zhang, L., Zhang, W., and Zou, L.: The Recent Decline and Recovery of Indian Summer Monsoon Rainfall: Relative Roles of External Forcing and Internal Variability, *J. Clim.*, 33, 5035–5060, <https://doi.org/10.1175/JCLI-D-19-0833.1>, 2020.
- Hugonnet, R., McNabb, R., Berthier, E., Menounos, B., Nuth, C., Girod, L., Farinotti, D., Huss, M., Dussaillant, I., Brun, F., and Käab, A.: Accelerated global glacier mass loss in the early twenty-first century, *Nature*, 592, 726–731, <https://doi.org/10.1038/s41586-021-03436-z>, 2021.
- Huintjes, E.: Energy and mass balance modelling for glaciers on the Tibetan Plateau - Extension, validation and application of a coupled snow and energy balance model, 2014.
- Huintjes, E., Sauter, T., Schröter, B., Maussion, F., Yang, W., Kropáček, J., Buchroithner, M., Scherer, D., Kang, S., and Schneider, C.: Evaluation of a Coupled Snow and Energy Balance Model for Zhadang Glacier, Tibetan Plateau, Using Glaciological Measurements and Time-Lapse Photography, *Arctic, Antarct. Alp. Res.*, 47, 573–590, <https://doi.org/10.1657/AAAR0014-073>, 2015a.
- Huintjes, E., Neckel, N., Hochschild, V., and Schneider, C.: Surface energy and mass balance at Purogangri ice cap, central Tibetan Plateau, 2001–2011, *J. Glaciol.*, 61, 1048–1060, <https://doi.org/10.3189/2015JOG15J056>, 2015b.
- Huss, M.: Density assumptions for converting geodetic glacier volume change to mass change, *Cryosph.*, 7, 877–887, <https://doi.org/10.5194/tc-7-877-2013>, 2013.
- Hussain, A., Cao, J., Hussain, I., Begum, S., Akhtar, M., Wu, X., Guan, Y., and Zhou, J.: Observed Trends and Variability of Temperature and Precipitation and Their Global Teleconnections in the Upper Indus Basin, Hindukush-Karakoram-Himalaya, *Atmos.* 2021, Vol. 12, Page 973, 12, 973, <https://doi.org/10.3390/ATMOS12080973>, 2021.
- Immerzeel, W. W., Van Beek, L. P. H., and Bierkens, M. F. P.: Climate change will affect the

asian water towers, *Science* (80-.), 328, 1382–1385, <https://doi.org/doi:10.1126/science.1183188>, 2010.

Immerzeel, W. W., Petersen, L., Ragettli, S., and Pellicciotti, F.: The importance of observed gradients of air temperature and precipitation for modeling runoff from a glacierized watershed in the Nepalese Himalayas, *Water Resour. Res.*, 50, 2212–2226, <https://doi.org/10.1002/2013WR014506>, 2014.

Immerzeel, W. W., Wanders, N., Lutz, A. F., Shea, J. M., and Bierkens, M. F. P.: Reconciling high-altitude precipitation in the upper Indus basin with glacier mass balances and runoff, *Hydrol. Earth Syst. Sci.*, 19, 4673–4687, <https://doi.org/10.5194/hess-19-4673-2015>, 2015.

Immerzeel, W. W., Lutz, A. F., Andrade, M., Bahl, A., Biemans, H., Bolch, T., Hyde, S., Brumby, S., Davies, B. J., Elmore, A. C., Emmer, A., Feng, M., Fernández, A., Haritashya, U., Kargel, J. S., Koppes, M., Kraaijenbrink, P. D. A., Kulkarni, A. V., Mayewski, P. A., Nepal, S., Pacheco, P., Painter, T. H., Pellicciotti, F., Rajaram, H., Rupper, S., Sinisalo, A., Shrestha, A. B., Viviroli, D., Wada, Y., Xiao, C., Yao, T., and Baillie, J. E. M.: Importance and vulnerability of the world's water towers, *Nature*, 577, 364–369, <https://doi.org/10.1038/s41586-019-1822-y>, 2020.

IPCC, I. P. on C. C.: Changing State of the Climate System, *Clim. Chang. 2021 – Phys. Sci. Basis*, 287–422, <https://doi.org/10.1017/9781009157896.004>, 2021.

Jackson, M., Azam, M. F., Baral, P., Benestad, R., Brun, F., Muhammad, S., Pradhananga, S., Shrestha, F., Steiner, J. F., and Thapa, A.: Consequences of climate change for the cryosphere in the Hindu Kush Himalaya, *Water, ice, Soc. Ecosyst. Hindu Kush Himalaya An outlook*, ICIMOD, 17–71, <https://doi.org/https://doi.org/10.53055/ICIMOD.1030>, 2023.

Jiang, X., Wang, N. L., He, J. Q., Wu, X. B., and Song, G. J.: A distributed surface energy and mass balance model and its application to a mountain glacier in China, *Chinese Sci. Bull.*, 55, 2079–2087, <https://doi.org/10.1007/s11434-010-3068-9>, 2010.

Johnson, E. and Rupper, S.: An Examination of Physical Processes That Trigger the Albedo-Feedback on Glacier Surfaces and Implications for Regional Glacier Mass Balance Across High Mountain Asia, *Front. Earth Sci.*, 8, <https://doi.org/10.3389/FEART.2020.00129/FULL>, 2020.

Kattel, D. B., Yao, T., Yang, K., Tian, L., Yang, G., and Joswiak, D.: Temperature lapse rate in complex mountain terrain on the southern slope of the central Himalayas, *Theor. Appl. Climatol.*, 113, 671–682, <https://doi.org/10.1007/S00704-012-0816-6>, 2013.

Kaul, M.: Mass balance of Liddar glaciers, *Trans. Inst. Indian Geogr*, 8, 95–111, 1986.

Kayastha, R. B., Ohata, T., and Ageta, Y.: Application of a mass-balance model to a Himalayan glacier, *J. Glaciol.*, 45, 559–567, <https://doi.org/10.3189/s002214300000143x>, 1999.

Khadka, A., Matthews, T., Perry, L. B., Koch, I., Wagnon, P., Shrestha, D., Sherpa, T. C. G., Aryal, D., Tait, A., Sherpa, T. C. G., Tuladhar, S., Baidya, S. K., Elvin, S., Elmore, A. C., Gajurel, A., and Mayewski, P. A.: Weather on Mount Everest during the 2019 summer monsoon, *Weather*, 76, 205–207, <https://doi.org/10.1002/wea.3931>, 2021.

Khadka, A., Wagnon, P., Brun, F., Shrestha, D., Lejeune, Y., and Arnaud, Y.: Evaluation of ERA5-Land and HARv2 reanalysis data at high elevation in the upper Dudh Koshi basin (Everest

- region, Nepal), *J. Appl. Meteorol. Climatol.*, 61, 931–954, <https://doi.org/10.1175/jamc-d-21-0091.1>, 2022.
- Khanal, S., Lutz, A. F., Kraaijenbrink, P. D. A., van den Hurk, B., Yao, T., and Immerzeel, W. W.: Variable 21st Century Climate Change Response for Rivers in High Mountain Asia at Seasonal to Decadal Time Scales, *Water Resour. Res.*, 57, e2020WR029266, <https://doi.org/10.1029/2020WR029266>, 2021.
- Kirkham, J. D., Koch, I., Saloranta, T. M., Litt, M., Stigter, E. E., Møen, K., Thapa, A., Melvold, K., and Immerzeel, W. W.: Near real-time measurement of snow water equivalent in the Nepal Himalayas, *Front. Earth Sci.*, 7, 1–18, <https://doi.org/10.3389/feart.2019.00177>, 2019.
- Kochendorfer, J., Nitu, R., Wolff, M., Mekis, E., Rasmussen, R., Baker, B., Earle, M. E., Reverdin, A., Wong, K., Smith, C. D., Yang, D., Roulet, Y.-A., Buisan, S., Laine, T., Lee, G., Aceituno, J. L. C., Alastrué, J., Isaksen, K., Meyers, T., Brækkan, R., Landolt, S., Jachcik, A., and Poikonen, A.: Analysis of single-Alter-shielded and unshielded measurements of mixed and solid precipitation from WMO-SPICE, *Hydrol. Earth Syst. Sci.*, 21, 3525–3542, <https://doi.org/10.5194/hess-21-3525-2017>, 2017.
- Koul, M. N. and Ganjoo, R. K.: Impact of inter- and intra-annual variation in weather parameters on mass balance and equilibrium line altitude of Naradu Glacier (Himachal Pradesh), NW Himalaya, India, *Clim. Change*, 99, 119–139, <https://doi.org/10.1007/S10584-009-9660-9>/METRICS, 2010.
- Kraaijenbrink, P. D. A., Bierkens, F. P., Lutz, A. F., and Immerzeel, W. W.: Impact of a global temperature rise of 1.5 degrees Celsius on Asia's glaciers, *nature.com*, <https://doi.org/10.1038/nature23878>, 2017.
- Kronenberg, M., Van Pelt, W., Machguth, H., Fiddes, J., Hoelzle, M., and Pertziger, F.: Long-term firn and mass balance modelling for Abramov glacier, Pamir Alay, *Cryosph. Discuss.*, 2022.
- Laha, S., Kumari, R., Singh, S., Mishra, A., Sharma, T., Banerjee, A., Nainwal, H. C., and Shankar, R.: Evaluating the contribution of avalanching to the mass balance of Himalayan glaciers, *Ann. Glaciol.*, 58, 110–118, <https://doi.org/10.1017/AOG.2017.27>, 2017.
- Lee, J.-Y., Marotzke, J., Bala, G., Milinski, S., Yun, K.-S., Ribes, A., Ruane, A. C., Kumar Kanikicharla Qatar, K., Kattsov, V., Kimoto, M., Marotzke, J., Bala, G., Cao, L., Corti, S., Dunne, J., Engelbrecht, F., Fischer, E., Fyfe, J., Jones, C., Maycock, A., Mutemi, J., Ndiaye, O., Panickal, S., Zhou, T., Pirani, A., Connors, S., Péan, C., Berger, S., Caud, N., Chen, Y., Goldfarb, L., Gomis, M., Huang, M., Leitzell, K., Lonnoy, E., Matthews, J., Maycock, T., Waterfield, T., Yelekçi, O., Yu, R., and Zhou, B.: Future Global Climate: Scenario-based Projections and Near-term Information, *Phys. Sci. basis. Contrib. Work. Gr. I to sixth Assess. Rep. Intergov. panel Clim. Chang.* Cambridge Univ. Press., 553–672, <https://doi.org/10.1017/9781009157896.006>, 2021.
- Lejeune, Y., L'hôte, Y., Etchevers, P., Wagnon, P., Chazarin, J.-P., and Chevallier, P.: Constitution d'une base de données météorologiques sur un site andin de haute altitude : le site du Charquini, 4795 m, Bolivie, 318, 2007a.
- Lejeune, Y., Wagnon, P., Bouilloud, L., Chevallier, P., Etchevers, P., Martin, E., Sicart, J. E., and Habets, F.: Melting of Snow Cover in a Tropical Mountain Environment in Bolivia: Processes

- and Modeling, *J. Hydrometeorol.*, 8, 922–937, <https://doi.org/10.1175/JHM590.1>, 2007b.
- Li, H., Wang, P., Li, Z., Jin, S., and He, J.: Summertime surface mass balance and energy balance of Urumqi Glacier No. 1, Chinese Tien Shan, modeled by linking COSIMA and in-situ measured meteorological records, *Clim. Dyn.*, <https://doi.org/10.1007/s00382-022-06571-z>, 2022.
- Li, J., Liu, S., Zhang, Y., and Shangguan, D.: Surface Energy Balance of Keqicar Glacier, Tianshan Mountains China During Ablation Period.Pdf, *Sci. Cold Arid Reg.*, 3, <https://doi.org/10.3724/SP.J.1226.2011.00197>, 2011.
- Li, S., Yao, T., Yang, W., Yu, W., and Zhu, M.: Glacier energy and mass balance in the inland Tibetan Plateau: Seasonal and interannual variability in relation to atmospheric changes, *Wiley Online Libr.*, 123, 6390–6409, <https://doi.org/10.1029/2017JD028120>, 2018.
- Li, S., Yao, T., Yu, W., Yang, W., and Zhu, M.: Energy and mass balance characteristics of the Guliya ice cap in the West Kunlun Mountains, Tibetan Plateau, *Cold Reg. Sci. Technol.*, 159, 71–85, <https://doi.org/10.1016/j.coldregions.2018.12.001>, 2019.
- Lindsey, R. and Dahlman, L.: Climate change: Global temperature, *Clim. gov.*, 2020.
- Litt, M., Shea, J., Wagnon, P., Steiner, J., Koch, I., and Stigter, E. E.: Glacier ablation and temperature indexed melt models in the Nepalese Himalaya, *Nat. Sci. Rep.*, 2019.
- Liu, S., XIE, Z., SONG, G., MA, L., and AGETA, Y.: Mass balance of Kangwure (flat-top) Glacier on the north side of Mt. Xixiabangma, China, *Bull. glacier Res.*, 37–43, 1996.
- Liu, W., Zhang, D., Qin, X., van den Broeke, M. R., Jiang, Y., Yang, D., and Ding, M.: Monsoon Clouds Control the Summer Surface Energy Balance on East Rongbuk Glacier (6,523 m Above Sea Level), the Northern of Mt. Qomolangma (Everest), *J. Geophys. Res. Atmos.*, 126, 1–24, <https://doi.org/10.1029/2020JD033998>, 2021.
- Liu, W., Yang, X., van den Broeke, M. R., Huai, B., Yang, D., Zhang, D., Qin, X., Yue, P., Wang, H., and Ding, M.: Cold-Season Surface Energy Balance on East Rongbuk Glacier, Northern Slope of Mt. Qomolangma (Everest), *J. Geophys. Res. Atmos.*, 128, e2022JD038101, <https://doi.org/10.1029/2022JD038101>, 2023.
- Lutz, A., Immerzeel, W., Shrestha, A., and Bierkens, M.: Consistent increase in High Asia's runoff due to increasing glacier melt and precipitation, *Nat. Clim. Chang.* 2014, 4, 587–592, 2014.
- Lyon-Caen, H. and Molnar, P.: Gravity anomalies, flexure of the Indian plate and the evolution of the Himalaya and Ganga Basin, *Tectonics*, 4, 513–538, 1985.
- Mandal, A., Angchuk, T., Azam, M. F., Ramanathan, A., Wagnon, P., Soheb, M., and Singh, C.: 11-year record of wintertime snow surface energy balance and sublimation at 4863 m a.s.l. on Chhota Shigri Glacier moraine (western Himalaya, India), *Cryosph.*, <https://doi.org/10.5194/tc-2021-386>, 2022.
- Marzeion, B., Jarosch, A. H., and Hofer, M.: Past and future sea-level change from the surface mass balance of glaciers, *Cryosphere*, 6, 1295–1322, <https://doi.org/10.5194/TC-6-1295-2012>, 2012.

- Marzeion, B., Champollion, N., Haeberli, W., Langley, K., Leclercq, P., and Paul, F.: Observation-Based Estimates of Global Glacier Mass Change and Its Contribution to Sea-Level Change, 107–132, https://doi.org/10.1007/978-3-319-56490-6_6, 2017.
- Marzeion, B., Hock, R., Anderson, B., Bliss, A., Champollion, N., Fujita, K., Huss, M., Immerzeel, W. W., Kraaijenbrink, P., Malles, J. H., Maussion, F., Radić, V., Rounce, D. R., Sakai, A., Shannon, S., van de Wal, R., and Zekollari, H.: Partitioning the Uncertainty of Ensemble Projections of Global Glacier Mass Change, *Earth's Futur.*, 8, e2019EF001470, <https://doi.org/10.1029/2019EF001470>, 2020.
- Massoud, E., Lim, Y., Andrews, L., and Giroto, M.: Connecting Global Modes of Variability to Climate in High Mountain Asia, Preprints, <https://doi.org/https://doi.org/10.20944/preprints202311.0749.v1>, 2023.
- Matthews, T., Perry, L. B., Koch, I., Aryal, D., Khadka, A., Shrestha, D., Abernathy, K., Elmore, A. C., Seimon, A., Tait, A., Elvin, S., Tuladhar, S., Baidya, S. K., Potocki, M., Birkel, S. D., Kang, S., Sherpa, T. C., Gajurel, A., and Mayewski, P. A.: Going to Extremes: Installing the World's Highest Weather Stations on Mount Everest, *Bull. Am. Meteorol. Soc.*, 101, E1870–E1890, <https://doi.org/10.1175/BAMS-D-19-0198.1>, 2020.
- Maussion, F., Scherer, D., Finkelnburg, R., Richters, J., Yang, W., Yao, T., Scherer, D., and Yang, W.: WRF simulation of a precipitation event over the Tibetan Plateau, China-An assessment using remote sensing and ground observations CAS project View project Variability and Trends in Water Balance Components of Benchmark Drainage Basins on the Tibetan Plat, *Hydrol. Earth Syst. Sci.*, 15, 1795–1817, <https://doi.org/10.5194/hess-15-1795-2011>, 2011.
- Maussion, F., Scherer, D., Mölg, T., Collier, E., Curio, J., and Finkelnburg, R.: Precipitation Seasonality and Variability over the Tibetan Plateau as Resolved by the High Asia Reanalysis, *J. Clim.*, 27, 1910–1927, <https://doi.org/10.1175/JCLI-D-13-00282.1>, 2014.
- Miles, E., McCarthy, M., Dehecq, A., Kneib, M., Fugger, S., and Pellicciotti, F.: Health and sustainability of glaciers in High Mountain Asia, *Nat. Commun.*, 12, 1–10, <https://doi.org/10.1038/s41467-021-23073-4>, 2021.
- Miles, E. S., Steiner, J. F., and Brun, F.: Highly variable aerodynamic roughness length (z_0) for a hummocky debris-covered glacier, *J. Geophys. Res. Atmos.*, 122, 8447–8466, <https://doi.org/10.1002/2017JD026510>, 2017.
- Miles, K. E., Hubbard, B., Quincey, D. J., Miles, E. S., Sherpa, T. C., Rowan, A. V., and Doyle, S. H.: Polythermal structure of a Himalayan debris-covered glacier revealed by borehole thermometry, *Sci. Reports* 2018 81, 8, 1–9, <https://doi.org/10.1038/s41598-018-34327-5>, 2018.
- Mimeau, L., Esteves, M., Jacobi, H.-W., and Zin, I.: Evaluation of Gridded and In Situ Precipitation Datasets on Modeled Glacio-Hydrologic Response of a Small Glacierized Himalayan Catchment, *journals.ametsoc.org*, 20, 1103–1121, <https://doi.org/10.1175/JHM-D-18-0157.1>, 2019a.
- Mimeau, L., Esteves, M., Zin, I., Jacobi, H.-W. W., Brun, F., Wagnon, P., Koirala, D., and Arnaud, Y.: Quantification of different flow components in a high-altitude glacierized catchment (Dudh

- Koshi, Himalaya): some cryospheric-related issues, *Hydrol. Earth Syst. Sci.*, 23, 3969–3996, <https://doi.org/10.5194/hess-23-3969-2019>, 2019b.
- Mishra, R., Kumar, A., and Singh, D.: Long term monitoring of mass balance of Hamtah Glacier, Lahaul and Spiti district, Himachal Pradesh, *Geolo Surv India*, 147, 230–232, 2014.
- Moazzam, M. F. U., Thakuri, S., Rahman, G., and Lee, B. G.: Unravelling the elevation-dependent warming in the Indus Basin, *Phys. Chem. Earth, Parts A/B/C*, 133, 103514, <https://doi.org/10.1016/J.PCE.2023.103514>, 2024.
- Mölg, T., Maussion, F., Yang, W., and Scherer, D.: The footprint of Asian monsoon dynamics in the mass and energy balance of a Tibetan glacier, *Cryosph.*, 6, 1445–1461, <https://doi.org/10.5194/tc-6-1445-2012>, 2012.
- Mölg, T., Maussion, F., and Scherer, D.: Mid-latitude westerlies as a driver of glacier variability in monsoonal High Asia, *Nat. Clim. Chang.*, 4, 68–73, <https://doi.org/10.1038/nclimate2055>, 2014.
- Mu, Y., Nepal, S. K., and Lai, P.-H.: Tourism and sacred landscape in Sagarmatha (Mt. Everest) National Park, Nepal, *Pilgr. beyond Off. Sacred*, 82–99, <https://doi.org/10.4324/9781003007821-5>, 2020.
- Muñoz-Sabater, J., Dutra, E., Agustí-Panareda, A., Albergel, C., Arduini, G., Balsamo, G., Boussetta, S., Choulga, M., Harrigan, S., Hersbach, H., Martens, B., Miralles, D. G., Piles, M., Rodríguez-Fernández, N. J., Zsoter, E., Buontempo, C., and Thépaut, J. N.: ERA5-Land: A state-of-the-art global reanalysis dataset for land applications, *Earth Syst. Sci. Data*, 13, 4349–4383, <https://doi.org/10.5194/ESSD-13-4349-2021>, 2021.
- Nepal, S.: Impacts of climate change on the hydrological regime of the Koshi river basin in the Himalayan region, *J. Hydro-environment Res.*, 10, 76–89, 2016.
- Nepal, S., Neupane, N., Belbase, D., Pandey, V. P., and Mukherji, A.: Achieving water security in Nepal through unravelling the water-energy-agriculture nexus, *Int. J. Water Resour. Dev.*, 37, 67–93, <https://doi.org/10.1080/07900627.2019.1694867>, 2021.
- Nicholson, L. I., Prinz, R., Mölg, T., and Kaser, G.: Micrometeorological conditions and surface mass and energy fluxes on Lewis Glacier, Mt Kenya, in relation to other tropical glaciers, *Cryosph.*, 7, 1205–1225, <https://doi.org/10.5194/TC-7-1205-2013>, 2013.
- Oerlemans, J.: A projection of future sea level, *Clim. Change*, 15, 151–174, <https://doi.org/10.1007/BF00138850/METRICS>, 1989.
- Oerlemans, J.: Climate sensitivity of glaciers in southern Norway: application of an energy-balance model to Nigardsbreen, Hellstugubreen and Alftobreen, *J. Glaciol.*, 38, 223–232, <https://doi.org/10.1017/S0022143000003634>, 1992.
- Oerlemans, J. and Fortuin, J. P. F.: Sensitivity of Glaciers and Small Ice Caps to Greenhouse Warming, *Science (80-.)*, 258, 115–117, <https://doi.org/10.1126/SCIENCE.258.5079.115>, 1992.
- Oerlemans, J. and Knap, W.: A 1 year record of global radiation and albedo in the ablation zone

- of Morteratschgletscher, Switzerland, *J. Glaciol.*, 44, 231–238, <https://doi.org/10.1017/S0022143000002574>, 1998.
- Oerlemans, J. and Reichert, B. K.: Relating glacier mass balance to meteorological data by using a seasonal sensitivity characteristic, *J. Glaciol.*, 46, 1–6, <https://doi.org/10.3189/172756500781833269>, 2000.
- Oerlemans, J., Björnsson, H., Kuhn, M., Obleitner, F., Palsson, F., Smeets, C. J. P. P., Vugts, H. F., and De Wolde, J.: Glacio-meteorological investigations on Vatnajökull, Iceland, Summer 1996: An overview, *Boundary-Layer Meteorol.*, 92, 3–24, <https://doi.org/10.1023/A:1001856114941>, 1999.
- Ohmura, A., Kasser, P., and Funk, M.: Climate at the Equilibrium Line of Glaciers, *J. Glaciol.*, 38, 397–411, <https://doi.org/10.3189/S0022143000002276>, 1992.
- Oke, T.: *Boundary layer climates*, 2002.
- Orsolini, Y., Wegmann, M., Dutra, E., Liu, B., Balsamo, G., Yang, K., De Rosnay, P., Zhu, C., Wang, W., Senan, R., and Arduini, G.: Evaluation of snow depth and snow cover over the Tibetan Plateau in global reanalyses using in situ and satellite remote sensing observations, *Cryosphere*, 13, 2221–2239, <https://doi.org/10.5194/TC-13-2221-2019>, 2019.
- Oulkar, S. N., Thamban, M., Sharma, P., Pratap, B., Singh, A. T., Patel, L. K., Pramanik, A., and Ravichandran, M.: Energy fluxes, mass balance, and climate sensitivity of the Sutri Dhaka Glacier in the western Himalaya, *Front. Earth Sci.*, 0, 1298, <https://doi.org/10.3389/FEART.2022.949735>, 2022.
- Palzett, A., Huamei, L., Wang, J., and Appel, E.: Palaeomagnetism of Cretaceous to Tertiary sediments from southern Tibet: Evidence for the extent of the northern margin of India prior to the collision with Eurasia, *Tectonophysics*, 259, 259–84, 1996.
- Pandey, P., Chauhan, P., Bhatt, C. M., Thakur, P. K., Kannaujia, S., Dhote, P. R., Roy, A., Kumar, S., Chopra, S., Bhardwaj, A., and Aggrawal, S. P.: Cause and Process Mechanism of Rockslide Triggered Flood Event in Rishiganga and Dhauliganga River Valleys, Chamoli, Uttarakhand, India Using Satellite Remote Sensing and in situ Observations, *J. Indian Soc. Remote Sens.*, 49, 1011–1024, <https://doi.org/10.1007/S12524-021-01360-3/METRICAL>, 2021.
- Pareto, V.: *Manual of political economy*, Macmillan, London, 1971.
- Pepin, N., Bradley, R. S., Diaz, H. F., Baraer, M., Caceres, E. B., Forsythe, N., Fowler, H., Greenwood, G., Hashmi, M. Z., Liu, X. D., Miller, J. R., Ning, L., Ohmura, A., Palazzi, E., Rangwala, I., Schöner, W., Severskiy, I., Shahgedanova, M., Wang, M. B., Williamson, S. N., and Yang, D. Q.: Elevation-dependent warming in mountain regions of the world, *Nat. Clim. Chang.* 2015 5, 5, 424–430, <https://doi.org/10.1038/nclimate2563>, 2015.
- Perry, L. B., Matthews, T., Guy, H., Koch, I., Khadka, A., Elmore, A. C., Shrestha, D., Tuladhar, S., Baidya, S. K., Maharjan, S., Wagnon, P., Aryal, D., Seimon, A., Gajurel, A., and Mayewski, P. A.: Precipitation Characteristics and Moisture Source Regions on Mt. Everest in the Khumbu, Nepal, *One Earth*, 3, 594–607, <https://doi.org/10.1016/j.oneear.2020.10.011>, 2020.
- Pfeffer, W. T., Arendt, A. A., Bliss, A., Bolch, T., Graham, J., Gardner, A. S., Hagen, J.-O., Hock,

- R., Kaser, G., Kienholz, C., Miles, E. S., Moholdt, G., Mölg, N., Mölg, M., Paul, F., Radic, V., Radic, R., Rastner, P., Raup, B. H., Rich, J., Sharp, M. J., and Consortium, R.: The Randolph Glacier Inventory: a globally complete inventory of glaciers, <https://doi.org/10.3189/2014JoG13J176>, 2014.
- Potocki, M., Mayewski, P. A., Matthews, T., Perry, L. B., Schwikowski, M., Tait, A. M., Korotkikh, E., Clifford, H., Kang, S., Sherpa, T. C., Singh, P. K., Koch, I., and Birkel, S.: Mt. Everest's highest glacier is a sentinel for accelerating ice loss, *npj Clim. Atmos. Sci.*, 5, 1–8, <https://doi.org/10.1038/s41612-022-00230-0>, 2022.
- Prasad, B.: Economic Dynamics of Tourism in Nepal: A VECM Approach, *Appl. Econ.*, 34, 877–884, <https://doi.org/10.1080/00036840110058923>, 2014.
- Prinz, R., Nicholson, L. I., Mölg, T., Gurgiser, W., and Kaser, G.: Climatic controls and climate proxy potential of Lewis Glacier, Mt. Kenya, *Cryosph.*, 10, 133–148, <https://doi.org/10.5194/tc-10-133-2016>, 2016.
- Pritchard, H. D.: Article Asia's shrinking glaciers protect large populations from drought stress, *Nature*, <https://doi.org/10.1038/s41586-019-1240-1>, 2019.
- Pugh, L. G. C. E.: Notes on Temperature and Snow Conditions in the Everest Region in Spring 1952 and 1953, cambridge.org, n.d.
- Ragetti, S., Pellicciotti, F., Immerzeel, W. W., Miles, E. S., Petersen, L., Heynen, M., Shea, J. M., Stumm, D., Joshi, S., and Shrestha, A.: Unraveling the hydrology of a Himalayan catchment through integration of high resolution in situ data and remote sensing with an advanced simulation model, *Adv. Water Resour.*, 78, 94–111, 2015.
- Raina, V. K.: Himalayan glaciers: a state-of-art review of glacial studies, glacial retreat and climate change., in: *Himal. Glaciers State-Art Rev. Glacial Stud. Glacial Retreat Clim. Change*, 2009.
- Raina, V. K., Kaul, M. K., and Singh, S.: Mass-Balance Studies of Gara Glacier, *J. Glaciol.*, 18, 415–423, <https://doi.org/10.3189/S0022143000021092>, 1977.
- A 'Ticking Bomb': Understanding the 2023 Glacial Lake Outburst Flood (GLOF) in Sikkim Himalaya: <https://blogs.egu.eu/divisions/cr/2023/11/02/a-ticking-bomb-understanding-the-2023-glacial-lake-outburst-flood-glof-in-sikkim-himalaya/>.
- Ren, G., Zhan, Y., Ren, Y., Wen, K., Zhang, Y., Sun, X., Zhang, P., Zheng, X., Qin, Y., Zhang, S., and He, J.: Observed changes in temperature and precipitation over Asia, 1901-2020, *Clim. Res.*, 90, 31–43, <https://doi.org/10.3354/cr01713>, 2023.
- Rodrigo, J. S., Buchlin, J. M., van Beeck, J., Lenaerts, J. T. M., and van den Broeke, M. R.: Evaluation of the antarctic surface wind climate from ERA reanalyses and RACMO2/ANT simulations based on automatic weather stations, *Clim. Dyn.*, 40, 353–376, <https://doi.org/10.1007/s00382-012-1396-y>, 2013.
- Romshoo, S. A., Abdullah, T., Murtaza, K. O., and Bhat, M. H.: Direct, geodetic and simulated mass balance studies of the Kolahoi Glacier in the Kashmir Himalaya, India, *J. Hydrol.*, 617, 129019, <https://doi.org/10.1016/J.JHYDROL.2022.129019>, 2023.

- Rounce, D. R., Hock, R., and Shean, D. E.: Glacier Mass Change in High Mountain Asia Through 2100 Using the Open-Source Python Glacier Evolution Model (PyGEM), *Front. Earth Sci.*, 7, <https://doi.org/10.3389/FEART.2019.00331>, 2020.
- Roxy, M. K., Ritika, K., Terray, P., Murtugudde, R., Ashok, K., and Goswami, B. N.: Drying of Indian subcontinent by rapid Indian Ocean warming and a weakening land-sea thermal gradient, *Nat. Commun.* 2015 61, 6, 1–10, <https://doi.org/10.1038/ncomms8423>, 2015.
- Rye, C. J., Willis, I. C., Arnold, N. S., and Kohler, J.: On the need for automated multiobjective optimization and uncertainty estimation of glacier mass balance models, *J. Geophys. Res. Earth Surf.*, 117, 2005, <https://doi.org/10.1029/2011JF002184>, 2012.
- Sakai, A. and Fujita, K.: Contrasting glacier responses to recent climate change in high-mountain Asia, *Sci. Rep.*, 7, 1–8, <https://doi.org/10.1038/s41598-017-14256-5>, 2017.
- Sakai, A., Nuimura, T., Fujita, K., Takenaka, S., Nagai, H., and Lamsal, D.: Climate regime of Asian glaciers revealed by GAMDAM glacier inventory, *Cryosph.*, 9, 865–880, <https://doi.org/10.5194/tc-9-865-2015>, 2015.
- Salerno, F., Guyennon, N., Thakuri, S., Viviano, G., Romano, E., Vuillermoz, E., Cristofanelli, P., Stocchi, P., Agrillo, G., Ma, Y., and Tartari, G.: Weak precipitation, warm winters and springs impact glaciers of south slopes of Mt. Everest (central Himalaya) in the last 2 decades (1994–2013), *Cryosph.*, 9, 1229–1247, <https://doi.org/10.5194/tc-9-1229-2015>, 2015.
- Sangewar, C. V. and Siddiqui, M. A.: Thematic compilation of mass balance data on glaciers of Satluj catchment in Himachal Himalaya, *Geol. Surv. India*, (Unpub.), 2007.
- Sauter, T., Arndt, A., and Schneider, C.: COSIPY v1.3 – an open-source coupled snowpack and ice surface energy and mass balance model, *Geosci. Model Dev.*, 13, 5645–5662, <https://doi.org/10.5194/gmd-13-5645-2020>, 2020.
- Schauwecker, S., Rohrer, M., Huggel, C., Endries, J., Montoya, N., Neukom, R., Perry, B., Salzmann, N., Schwarb, M., and Suarez, W.: The freezing level in the tropical Andes, Peru: An indicator for present and future glacier extents, *J. Geophys. Res. Atmos.*, 122, 5172–5189, <https://doi.org/10.1002/2016JD025943>, 2017.
- Schneider, T., Bischoff, T., and Haug, G. H.: Migrations and dynamics of the intertropical convergence zone, *Nat.* 2014 5137516, 513, 45–53, <https://doi.org/10.1038/nature13636>, 2014.
- Shaw, T. E., Miles, E. S., Chen, D., Jouberton, A., Kneib, M., Fugger, S., Ou, T., Lai, H., Fujita, K., Yang, W., Fatichi, S., and Pellicciotti, F.: Multi-decadal monsoon characteristics and glacier response in High Mountain Asia, *Environ. Res. Lett.*, 17, 104001, <https://doi.org/10.1088/1748-9326/AC9008>, 2022.
- Shea, J. M., Wagnon, P., Immerzeel, W. W., Biron, R., Brun, F., and Pellicciotti, F.: A comparative high-altitude meteorological analysis from three catchments in the Nepalese Himalaya, *Int. J. Water Resour. Dev.*, 31, 174–200, <https://doi.org/10.1080/07900627.2015.1020417>, 2015a.
- Shea, J. M., Immerzeel, W. W., Wagnon, P., Vincent, C., and Bajracharya, S.: Modelling glacier

- change in the Everest region, Nepal Himalaya, *Cryosph.*, 9, 1105–1128, <https://doi.org/10.5194/tc-9-1105-2015>, 2015b.
- Shean, D. E., Bhushan, S., Montesano, P. M., Rounce, D. R., Arendt, A., and Osmanoglu, B.: A Systematic, Regional Assessment of High Mountain Asia Glacier Mass Balance, *Front. Earth Sci.*, 7, 363, <https://doi.org/10.3389/feart.2019.00363>, 2020.
- Shekhar, M. S., Rao, N., Paul, S., Bhan, S. C., Singh, G. P., and Singh, A.: Winter precipitation climatology over Western Himalaya: Altitude and Range wise study, *J. Ind. Geophys. Union*, 21, 148–152, 2017.
- Sherpa, S. and Wengel, Y.: *The Sherpas and Their Original Identity*, Cambridge Sch. Publ., 2023.
- Sherpa, S. F., Wagnon, P., Brun, F., Berthier, E., Vincent, C., Lejeune, Y., Arnaud, Y., Kayastha, R. B., and Sinisalo, A.: Contrasted surface mass balances of debris-free glaciers observed between the southern and the inner parts of the Everest region (2007–15), *J. Glaciol.*, 63, 637–651, <https://doi.org/10.1017/jog.2017.30>, 2017.
- Sherpa, S. F., Shrestha, M., Eakin, H., and Boone, C. G.: Cryospheric hazards and risk perceptions in the Sagarmatha (Mt. Everest) National Park and Buffer Zone, Nepal, *Nat. Hazards*, 96, 607–626, <https://doi.org/10.1007/S11069-018-3560-0/METRICS>, 2019.
- Sherpa, T. C., Matthews, T., Perry, L. B., Thapa, A., Singh, P. K., Khadka, A., Koch, I., Pelto, M., Panday, P., Aryal, D., Shrestha, D., Kang, S., and Mayewski, P. A.: Insights from the first winter weather observations near Mount Everest’s summit, *Weather*, 1–5, <https://doi.org/10.1002/wea.4374>, 2023.
- Shi, Y. and Liu, S.: Estimation on the response of glaciers in China to the global warming in the 21st century, *Chinese Sci. Bull.*, 45, 668–672, <https://doi.org/10.1007/BF02886048/METRICS>, 2000.
- Shrestha, A., Wake, C., Mayewski, P., and Dibb, J.: Maximum temperature trends in the Himalaya and its vicinity: an analysis based on temperature records from Nepal for the period 1971–94, *J. Clim.*, 12, 2775–2786, <https://doi.org/https://doi.org/10.1175/1520->, 1999.
- Shrestha, D., Singh, P., and Nakamura, K.: Spatiotemporal variation of rainfall over the central Himalayan region revealed by TRMM Precipitation Radar, *J. Geophys. Res. Atmos.*, 117, 22106, <https://doi.org/10.1029/2012JD018140>, 2012.
- Shrestha, F., Steiner, J. F., Shrestha, R., Dhungel, Y., Joshi, S. P., Inglis, S., Ashraf, A., Wali, S., Walizada, K. M., and Zhang, T.: A comprehensive and version-controlled database of glacial lake outburst floods in High Mountain Asia, *Earth Syst. Sci. Data*, 15, 3941–3961, <https://doi.org/10.5194/ESSD-15-3941-2023>, 2023.
- Sicart, J. E., Hock, R., Ribstein, P., and Chazarin, J. P.: Sky longwave radiation on tropical Andean glaciers: Parameterization and sensitivity to atmospheric variables, *J. Glaciol.*, 56, 854–860, <https://doi.org/10.3189/002214310794457182>, 2010.
- Singh, N., Singhal, M., Chhikara, S., Karakoti, I., Chauhan, P., and Dobhal, D. P.: Radiation and energy balance dynamics over a rapidly receding glacier in the central Himalaya, *Int. J. Climatol.*, 40, 400–420, <https://doi.org/10.1002/joc.6218>, 2020.

- Soheb, M., Ramanathan, A., Angchuk, T., Mandal, A., Kumar, N., and Lotus, S.: Mass-balance observation, reconstruction and sensitivity of Stok glacier, Ladakh region, India, between 1978 and 2019, *J. Glaciol.*, 66, 627–642, <https://doi.org/10.1017/jog.2020.34>, 2020.
- Srivastava, D., Sangewar, C. V., Kaul, M. K., and Jamwal, K. S.: Mass balance of Rulung Glacier_a Trans-Himalayan glacier, Indus basin, Ladak. *Proc. Symp. Snow, Ice and Glacier*, March 1999, *Geol. Surv. India, Spec. Publ.*, 53, 41–46, 2001.
- Srivastava, S. and Azam, M. F.: Mass- and Energy-Balance Modeling and Sublimation Losses on Dokriani Bamak and Chhota Shigri Glaciers in Himalaya Since 1979, *Front. Water*, 4, 1–21, <https://doi.org/10.3389/frwa.2022.874240>, 2022.
- Steiner, J. F. and Pellicciotti, F.: Variability of air temperature over a debris-covered glacier in the Nepalese Himalaya, *Ann. Glaciol.*, 57, 295–307, <https://doi.org/10.3189/2016AOG71A066>, 2016.
- Stevens, S. F.: Sherpas, Tourism, and Cultural Change in Nepal’s Mount Everest Region, *J. Cult. Geogr.*, 12, 32–58, 1991.
- Stigter, E. E., Litt, M., Steiner, J. F., Bonekamp, P. N. J., Shea, J. M., Bierkens, M. F. P., and Immerzeel, W. W.: The Importance of Snow Sublimation on a Himalayan Glacier, *Front. Earth Sci.*, 6, <https://doi.org/10.3389/feart.2018.00108>, 2018.
- Stumm, D., Joshi, S. P., Gurung, T. R., and Silwal, G.: Mass balances of Yala and Rikha Samba glaciers, Nepal, from 2000 to 2017, *Earth Syst. Sci. Data*, 13, 3791–3818, <https://doi.org/10.5194/essd-13-3791-2021>, 2021.
- Sun, W., Qin, X., Du, W., Liu, W., Liu, Y., Zhang, T., Xu, Y., Zhao, Q., Wu, J., and Ren, J.: Ablation modeling and surface energy budget in the ablation zone of Laohugou glacier No. 12, western Qilian mountains, China, *Ann. Glaciol.*, 55, 111–120, <https://doi.org/10.3189/2014Aog66A902>, 2014.
- Sun, W., Qin, X., Wang, Y., Chen, J., Du, W., Zhang, T., and Huai, B.: The response of surface mass and energy balance of a continental glacier to climate variability, western Qilian Mountains, China, *Clim. Dyn.*, 50, 3557–3570, <https://doi.org/10.1007/s00382-017-3823-6>, 2018.
- Sunako, S., Fujita, K., Sakai, A., and Kayastha, R. B.: Mass balance of Trambau Glacier, Rolwaling region, Nepal Himalaya: In-situ observations, long-term reconstruction and mass-balance sensitivity, *J. Glaciol.*, 65, 605–616, <https://doi.org/10.1017/jog.2019.37>, 2019.
- Tetzner, D., Thomas, E., Geosciences, C. A.-, and 2019, U.: A Validation of ERA5 Reanalysis Data in the Southern Antarctic Peninsula—Ellsworth Land Region, and Its Implications for Ice Core Studies, *mdpi.com*, 2019.
- Thakuri, S., Salerno, F., Smiraglia, C., Bolch, T., D’Agata, C., Viviano, G., and Tartari, G.: Tracing glacier changes since the 1960s on the south slope of Mt. Everest (central Southern Himalaya) using optical satellite imagery, *Cryosph.*, 8, 1297–1315, <https://doi.org/10.5194/tc-8-1297-2014>, 2014.
- Thakuri, S., Dahal, S., Shrestha, D., Guyennon, N., Ramano, E., and Colombo, N.: Elevation-

- dependent warming of maximum air temperature in Nepal during 1976–2015, *Atmos. Res.*, 228, 261–269, <https://doi.org/https://doi.org/10.1016/j.atmosres.2019.06.006>, 2019.
- Thayyen, R. J. and Gergan, J. T.: Role of glaciers in watershed hydrology: A preliminary study of a “himalayan catchment,” *Cryosphere*, 4, 115–128, <https://doi.org/10.5194/tc-4-115-2010>, 2010.
- Thibert, E., Blanc, R., Vincent, C., and Eckert, N.: Glaciological and volumetric mass-balance measurements: Error analysis over 51 years for Glacier de Sarennes, French Alps, *J. Glaciol.*, 54, 522–532, <https://doi.org/10.3189/002214308785837093>, 2008.
- Treichler, D.: Measuring mountain glaciers and snow with a spaceborne laser, Elsevier Inc., 389–401 pp., <https://doi.org/10.1016/J.RSE.2017.01.022>, 2017.
- Tshering, P. and Fujita, K.: First in situ record of decadal glacier mass balance (2003–2014) from the Bhutan Himalaya, *Ann. Glaciol.*, 57, 289–294, <https://doi.org/10.3189/2016AOG71A036>, 2016.
- Ueno, K., Toyotsu, K., Bertolani, L., and Tartari, G.: Stepwise Onset of Monsoon Weather Observed in the Nepal Himalaya, *journals.ametsoc.org*, 136, 2507–2522, <https://doi.org/10.1175/2007MWR2298.1>, 2008.
- Valdiya, K. .: Emergence and evolution of Himalaya: reconstructing history in the light of recent studies, *Prog. Phys. Geogr.*, 26, 360–399, 2002.
- Veldhuijsen, S. B. M., De Kok, R. J., Stigter, E. E., Steiner, J. F., Saloranta, T. M., and Immerzeel, W. W.: Spatial and temporal patterns of snowmelt refreezing in a Himalayan catchment, *J. Glaciol.*, 68, 369–389, <https://doi.org/10.1017/jog.2021.101>, 2022.
- Vincent, C.: Influence of climate change over the 20th Century on four French glacier mass balances, *J. Geophys. Res. Atmos.*, 107, ACL 4-1, <https://doi.org/10.1029/2001JD000832>, 2002.
- Wagnon, P., Lafaysse, M., Lejeune, Y., Maisincho, L., Rojas, M., and Chazarin, J. P.: Understanding and modeling the physical processes that govern the melting of snow cover in a tropical mountain environment in Ecuador, *J. Geophys. Res. Atmos.*, 114, 19113, <https://doi.org/10.1029/2009JD012292>, 2009.
- Wagnon, P., Vincent, C., Arnaud, Y., Berthier, E., Vuillermoz, E., Gruber, S., Ménégoz, M., Gilbert, A., Dumont, M., Shea, J. M., Stumm, D., and Pokhrel, B. K.: Seasonal and annual mass balances of Mera and Pokalde glaciers (Nepal Himalaya) since 2007, *Cryosphere*, 7, 1769–1786, <https://doi.org/10.5194/tc-7-1769-2013>, 2013.
- Wagnon, P., Brun, F., Khadka, A., Berthier, E., Shrestha, D., Vincent, C., Arnaud, Y., Six, D., Dehecq, A., Ménégoz, M., and Jomelli, V.: Reanalysing the 2007–19 glaciological mass-balance series of Mera Glacier, Nepal, Central Himalaya, using geodetic mass balance, *J. Glaciol.*, 67, 117–125, <https://doi.org/10.1017/jog.2020.88>, 2021.
- Wang, C., Graham, R. M., Wang, K., Gerland, S., and Granskog, M. A.: Comparison of ERA5 and ERA-Interim near-surface air temperature, snowfall and precipitation over Arctic sea ice: effects on sea ice thermodynamics and evolution, *Cryosph.*, 13, 1661–1679, <https://doi.org/10.5194/tc-13-1661-2019>, 2019a.

- Wang, P., Li, Z., Schneider, C., Li, H., Hamm, A., Jin, S., Xu, C., Li, H., Yue, X., and Yang, M.: A Test Study of an Energy and Mass Balance Model Application to a Site on Urumqi Glacier No. 1, Chinese Tian Shan, *Water* 2020, Vol. 12, Page 2865, 12, 2865, <https://doi.org/10.3390/W12102865>, 2020a.
- Wang, R., Liu, S., Shangguan, D., Radić, V., and Zhang, Y.: Spatial Heterogeneity in Glacier Mass-Balance Sensitivity across High Mountain Asia, *Water*, 11, 776, <https://doi.org/10.3390/W11040776>, 2019b.
- Wang, X., Tolksdorf, V., Otto, M., and Scherer, D.: WRF-based dynamical downscaling of ERA5 reanalysis data for High Mountain Asia: Towards a new version of the High Asia Refined analysis, *Wiley Online Libr.*, 41, 743–762, <https://doi.org/10.1002/joc.6686>, 2020b.
- Wester, P., Mishra, A., Mukherji, A., and Shrestha, A. B.: *The Hindu Kush Himalaya assessment: mountains, climate change, sustainability and people*, 2019.
- WGMS: *Fluctuations of Glaciers Database*. World Glacier Monitoring Service (WGMS), Zurich, Switzerland, 2024.
- Wohlfahrt, G., Albin, H., Georg, N., Katharina, S., Enrico, T., and Peng, Z.: On the energy balance closure and net radiation in complex terrain, *Agric. For. Meteorol.*, 226, 37–49, <https://doi.org/10.1016/j.agrformet.2016.05.012>, 2016.
- Wu, X., He, J., Jiang, X., and Wang, N.: Analysis of surface energy and mass balance in the accumulation zone of Qiyi Glacier, Tibetan Plateau in an ablation season, *Environ. Earth Sci.*, 75, 1–13, <https://doi.org/10.1007/S12665-016-5591-8/FIGURES/9>, 2016.
- Yamamoto, M. K., Ueno, K. ', and Nakamura, K.: Comparison of Satellite Precipitation Products with Rain Gauge Data for the Khumb Region, Nepal Himalayas, *J. Meteorol. Soc. Japan*, 89, 597–610, <https://doi.org/10.2151/jmsj.2011-601>, 2011.
- Yan, L. and Liu, X.: Has climatic warming over the Tibetan Plateau paused or continued in recent years, *J. Earth, Ocean Atmos. Sci.*, 1, 13–28, 2014.
- Yancheva, G., Nowaczyk, N. R., Mingram, J., Dulski, P., Schettler, G., Negendank, J. F. W., Liu, J., Sigman, D. M., Peterson, L. C., and Haug, G. H.: Influence of the intertropical convergence zone on the East Asian monsoon, *Nat.* 2006 4457123, 445, 74–77, <https://doi.org/10.1038/nature05431>, 2007.
- Yang, W., Guo, X., Yao, T., Yang, K., Zhao, L., Li, S., Zhu, M., Yang, W., Guo, X., Yao, T., Yang, K., Zhao, L., Li, S., and Zhu, M.: Summertime surface energy budget and ablation modeling in the ablation zone of a maritime Tibetan glacier, *J. Geophys. Res. Atmos.*, 116, 14116, <https://doi.org/10.1029/2010JD015183>, 2011.
- Yang, W., Yao, T., Zhu, M., and Wang, Y.: Comparison of the meteorology and surface energy fluxes of debris-free and debris-covered glaciers in the southeastern Tibetan Plateau, *J. Glaciol.*, 63, 1090–1104, <https://doi.org/10.1017/jog.2017.77>, 2017.
- Yao, T., Thompson, L., Yang, W., Yu, W., Gao, Y., Guo, X., Yang, X., Duan, K., Zhao, H., Xu, B., Pu, J., Lu, A., Xiang, Y., Kattel, D. B., and Joswiak, D.: Different glacier status with atmospheric circulations in Tibetan Plateau and surroundings, *Nat. Clim. Chang.*, 2, 663–667,

<https://doi.org/10.1038/nclimate1580>, 2012.

Yao, T., Bolch, T., Chen, D., Gao, J., Immerzeel, W., Piao, S., Su, F., Thompson, L., Wada, Y., Wang, L., Wang, T., Wu, G., Xu, B., Yang, W., Zhang, G., and Zhao, P.: The imbalance of the Asian water tower, *Nat. Rev. Earth Environ.*, 3, 618–632, <https://doi.org/10.1038/s43017-022-00299-4>, 2022.

Yapo, P. O., Gupta, H. V., and Sorooshian, S.: Multi-objective global optimization for hydrologic models, *J. Hydrol.*, 204, 83–97, [https://doi.org/10.1016/S0022-1694\(97\)00107-8](https://doi.org/10.1016/S0022-1694(97)00107-8), 1998.

Zemp, M., Thibert, E., Huss, M., Stumm, D., Rolstad Denby, C., Nuth, C., Nussbaumer, S. U., Moholdt, G., Mercer, A., Mayer, C., Joerg, P. C., Jansson, P., Hynek, B., Fischer, A., Escher-Vetter, H., Elvehøy, H., and Andreassen, L. M.: Reanalysing glacier mass balance measurement series, *Cryosph.*, 7, 1227–1245, <https://doi.org/10.5194/tc-7-1227-2013>, 2013.

Zemp, M., Huss, M., Thibert, E., Eckert, N., McNabb, R., Huber, J., Barandun, M., Machguth, H., Nussbaumer, S. U., Gärtner-Roer, I., Thomson, L., Paul, F., Maussion, F., Kutuzov, S., and Cogley, J. G.: Global glacier mass changes and their contributions to sea-level rise from 1961 to 2016, *Nature*, 568, 382–386, <https://doi.org/10.1038/s41586-019-1071-0>, 2019.

Zhang, G., Kang, S., Fujita, K., Huintjes, E., Xu, J., Yamazaki, T., Haginoya, S., Wei, Y., Scherer, D., Schneider, C., and Yao, T.: Energy and mass balance of Zhadang glacier surface, central Tibetan Plateau, *J. Glaciol.*, 59, 137–148, <https://doi.org/10.3189/2013JoG12J152>, 2013.

Zhang, J., Wu, T., Xin, X., Lu, Y., Yan, J., Zhang, F., Liu, L., and Zhao, H.: Surface Air Temperature Trend Over the Tibetan Plateau in CMIP6 and Its Constraint in Future Projection, *J. Geophys. Res. Atmos.*, 128, e2023JD039527, <https://doi.org/10.1029/2023JD039527>, 2023.

Zhu, M., Yao, T., Yang, W., Maussion, F., Huintjes, E., and Li, S.: Energy- and mass-balance comparison between Zhadang and Parlung No. 4 glaciers on the Tibetan Plateau, *J. Glaciol.*, 61, 595–607, <https://doi.org/10.3189/2015JOG14J206>, 2015.

Zhu, M., Yao, T., Yang, W., Xu, B., Wu, G., and Wang, X.: Differences in mass balance behavior for three glaciers from different climatic regions on the Tibetan Plateau, *Clim. Dyn.*, 50, 3457–3484, <https://doi.org/10.1007/s00382-017-3817-4>, 2018.

Zhu, M., Yao, T., Xie, Y., Xu, B., Yang, W., and Yang, S.: Mass balance of Muji Glacier, northeastern Pamir, and its controlling climate factors, *J. Hydrol.*, 590, 125447, <https://doi.org/10.1016/j.jhydrol.2020.125447>, 2020.

Zhu, M., Yang, W., Yao, T., Tian, L., Thompson, L. G., and Zhao, H.: The Influence of Key Climate Variables on Mass Balance of Naimona'nyi Glacier on a North-Facing Slope in the Western Himalayas, *J. Geophys. Res. Atmos.*, 126, <https://doi.org/10.1029/2020JD033956>, 2021.

Zhu, M., Yao, T., Yang, W., Wu, G., Li, S., Zhao, H., and Thompson, L. G.: Possible Causes of Anomalous Glacier Mass Balance in the Western Kunlun Mountains, *J. Geophys. Res. Atmos.*, 127, e2021JD035705, <https://doi.org/10.1029/2021JD035705>, 2022.

Zolles, T., Maussion, F., Peter Galos, S., Gurgiser, W., and Nicholson, L.: Robust uncertainty assessment of the spatio-temporal transferability of glacier mass and energy balance models, *Cryosph.*, 13, 469–489, <https://doi.org/10.5194/TC-13-469-2019>, 2019.

Zuo, Z. and Oerlemans, J.: Contribution of glacier melt to sea-level rise since AD 1865: A regionally differentiated calculation, *Clim. Dyn.*, 13, 835–845, <https://doi.org/10.1007/S003820050200/METRICS>, 1997.